Faculdade de Engenharia da Universidade do Porto

Predicting in-silico structural response of dental restorations

Gabriela Afonso Ribeiro Caldas

Masters on Biomedical Engineering

Supervisor: Prof. Jorge Américo Oliveira Pinto Belinha, PhD
Co-Supervisor: Prof. Renato Manuel Natal Jorge, PhD

June, 2018

MEB - MESTRADO EM ENGENHARIA BIOMÉDICA   *2017/2018*

A Dissertação intitulada

"Predicting In-Silico Structural Response of Dental Restorations"

foi aprovada em provas realizadas em 02-07-2018

o júri

Presidente Prof. Doutor José Alberto Peixoto Machado da Silva
Professor Associado do Departamento de Engenharia Eletrotécnica e de Computadores da
FEUP - U.Porto

Doutor Jorge Américo Oliveira Pinto Belinha
Investigador Pós-Doutoramento do Instituto de Ciência e Inovação em Engenharia Mecânica e
Engenharia Industrial da U. Porto - INEGI - U.Porto

Prof. Doutor Raul Duarte Salgueiral Gomes Campilho
Professor do Instituto Superior de Engenharia do Porto do Instituto Politécnico do Porto

O autor declara que a presente dissertação (ou relatório de projeto) é da sua exclusiva autoria e foi escrita sem qualquer apoio externo não explicitamente autorizado. Os resultados, ideias, parágrafos, ou outros extratos tomados de ou inspirados em trabalhos de outros autores, e demais referências bibliográficas usadas, são corretamente citados.

Autor - Gabriela Afonso Ribeiro Caldas

Faculdade de Engenharia da Universidade do Porto

Resumo

A perda dentária tem um impacto negativo na qualidade de vida, prejudicando o desempenho no trabalho e em atividades diárias. Assim, muitos pacientes têm o desejo de substituir dentes em falta, o que pode ser feito através de uma variedade de restaurações dentárias, como é o caso de pontes dentárias adesivas. As pontes adesivas, também conhecidas como pontes de Maryland, são um tipo de prótese fixa em que o dente pôntico (dente falso) é anexado a uma estrutura que por sua vez é cimentada nos dentes pilares, ou seja, os dentes adjacentes ao espaço do dente em falta e que irão servir de suporte.

Assim, neste projeto, é proposto o estudo da resposta estrutural biomecânica de uma ponte dentária adesiva utilizando técnicas computacionais de discretização avançadas, como métodos sem malha, o que permitirá obter conclusões práticas relevantes e demonstrar que os métodos sem malha são uma técnica numérica alternativa.

Para tal, foi estudado o efeito de diferentes adesivos e da sua espessura, assim como o uso de pontes de três unidades ou de duas unidades, na resistência mecânica de uma ponte dentária adesiva. Simulações biomecânicas do biossistema adesivo/dente em modelos bidimensionais (2D) e tridimensionais (3D) foram realizadas usando três métodos numéricos: Método dos Elementos Finitos (FEM), "Radial Point Interpolation Method" (RPIM) e "Natural Neighbour Radial Point Interpolation Method" (NNRPIM). Análises elasto-estáticas e elasto-plásticas foram realizadas, e os resultados mostraram que tanto o adesivo como a sua espessura influenciam a distribuição de tensões ao longo da ponte. O uso de um único dente de suporte aumenta o risco da prótese falhar. Adicionalmente, os resultados obtidos para os métodos sem malha aproximam-se dos resultados obtidos para o FEM.

Abstract

The loss of teeth has a negative impact on the individual's quality of life, adversely affecting performance at work and in daily activities. Thus, many patients have the desire to replace missing teeth, which can be done through a variety of treatment alternatives, such as adhesive dental bridges. Adhesive bridges, also known as Maryland bridges, are a type of fixed prosthesis in which the pontic tooth is attached to a structure that is cemented on the abutment teeth (teeth adjacent to the space of the missing tooth, serving as support pillars).

This work proposes to study the biomechanical structural response of an adhesive dental bridge using advanced discretization computational techniques, such as meshless methods, which will allow to obtain relevant practical conclusions and to show that meshless methods are a solid alternative numerical technique.

Therefore, it was studied the effect of different resin-cements, the adhesive's thickness and the use of a two-retainer design or a single-retainer design on the mechanical resistance of an adhesive dental bridge. Biomechanical simulations of the adhesive/tooth biosystem in two dimensional (2D) and three dimensional (3D) settings were performed using three numerical methods: Finite Element Method (FEM), Radial Point Interpolation Method (RPIM) and Natural Neighbour Radial Point Interpolation Method (NNRPIM). Elasto-static and nonlinear-elasto-plastic analysis were performed, and the results show that both adhesive's thickness and resin-cement influence the stress concentration. The single-retainer design increases the risk of debonding. In addition, the results obtained using meshless methods agree with FEM.

Agradecimentos

Um sincero obrigada ao Prof. Jorge Belinha por todo o apoio e ajuda ao longo da realização deste projeto. Obrigada pelas reuniões semanais, pelos conselhos, pela amizade, por responder à mesma pergunta mais do que uma vez e por muito básica que fosse e pela paciência, mesmo quando mandava incontáveis emails.

Às minhas amigas, Teresa, Helena e Catarina, pelos trabalhos em conjunto, pela partilha de conhecimento, pelo apoio e por ficarem a tomar conta das minhas análises enquanto ia almoçar. Mas também aos meus amigos Isabel e João que me acompanharam ao longo destes 5 anos de faculdade, mesmo quando o tempo não era muito. Estiveram sempre comigo e foi ao vosso lado que partilhei as melhores experiências que recordarei para sempre.

Um enorme obrigada aos meus pais, Susana e Vasco, por todo o apoio, carinho, motivação, força e paciência, mesmo nos meus momentos de maior frustração. Esta etapa concluída com sucesso é graças a vocês que sempre me incentivaram a estudar, a ir mais longe e a dar o melhor de mim.

Ao meu namorado, Pedro, que apesar de não me ter acompanhado ao longo de todo o meu percurso na faculdade, apareceu na melhor altura possível. Obrigada por me teres ensinado a ser mais positiva, por teres lido os meus enormes textos em inglês e teres dado as tuas opiniões mais sinceras, por partilhares comigo a tua tese e simplesmente por seres quem és.

Gabriela Afonso Ribeiro Caldas

x

x

Institutional acknowledgments

Gabriela Afonso Ribeiro Caldas

Contents

List of figures

List of tables

List of abbreviations and symbols

Abbreviations

2D	Two-dimensional
3D	Three-dimensional
AFPD	Adhesive Fixed Partial Denture
CT	Computed Tomography
CAD	Computer Aided Design
CAT	Computational Axial Tomography
DICOM	Digital Imaging and Communications in Medicine
FEM	Finite Element Method
FEMAS	Finite Element and Meshless Method Analysis Software
FPD	Fixed Partial Denture
FRC	Fibre Reinforced Composite
FEUP	Faculdade de Engenharia da Universidade do Porto
MR	Magnetic Resonance
NNRPIM	Natural Neighbour Radial Point Interpolation Method
PDL	Periodontal Ligament
RBF	Radial Basis Function
RPIM	Radial Point Interpolation Method
STL	Stereolithography
TMJ	Temporomandibular Joint

Symbols

E	Young's modulus
υ	Poisson ration

Chapter 1

Introduction

Age is directly related to tooth loss. Therefore, aging is one of the main factors contributing to the large number of teeth lost in the world population. As such, although presently the number of teeth lost per patient is decreasing, due to improvements in dental health care, it is expected that in the next decades the total number of teeth lost will continue to increase, due to the aging population [1]. In addition to the aging population, there are also oral diseases that significantly affect dental health, leading to tooth loss, as is the case of dental caries and periodontitis. In 2010, the overall prevalence of periodontitis was 743 million individuals and dental caries was 3.054 million individuals [2]. Regarding its treatment economic cost, oral diseases are the fourth more expensive and, in 2010, their overall economic burden was 372,9 thousand million euros [3].

Failure of a dental restoration may cause even more problems for the patient than missing teeth. Therefore, there are a variety of options that should be considered and analysed. This work focuses on a specific type of dental restoration, the adhesive dental bridges.

Adhesive dental bridges are a type of fixed prosthesis that allows the replacement of one or more missing teeth. The replaced tooth, called pontic, is supported by the adjacent teeth, named abutment. Thus, for the application of this restoration, it is necessary a solid/robust abutment [4]. This type of prosthesis is distinguished from others due to the conservation of dental structures and their reversibility [5,6].

However, these bridges are associated with failure due to debonding between the retainer wing and the cement or between the cement and the dental surface, to the fracture of the abutment tooth and delamination of the veneering material of the framework [7,8].

There are several factors that should be considered and whose optimization may improve the mechanical resistance of adhesive dental bridges, also known as Maryland Bridges. It is important to consider the design of the bridge, its thickness, height and angle of the axial surface extensions [9]. Another relevant factor is the materials used, both in the retainer wing and in the adhesive. The selection of the abutment teeth is also relevant as they will be submitted to higher loads, transmitted through the bridge, and as such should have the ability to support those same loads. Not only the health of the abutment teeth is important, but also the number of abutment teeth, since multiple abutments are more likely to debond due to differential movements [6].

Numerical-experimental approaches serve as comprehensive methodologies of in vitro research for the study of complex mechanical behaviour of prostheses and surrounding structures.

In this project, it is proposed to study the biomechanical structural response of an adhesive dental bridge. To perform the biomechanical analysis of a tooth restoration, it is necessary to build a numerical model representing the real biomechanical structure. Due to the complexity of the structural system composing the assembly of "restored tooth"/" natural teeth"/" mandibular bone", the numerical model construction must be obtained with 3D segmentation techniques. This project aims to study a tooth restoration using advanced discretization computational techniques, such as meshless methods. The 3D model of the mandibular bone and existent teeth will be obtained from available orthopantomography images. Then, the restored tooth and the adhesive bridge will be built in a CAD software. In the end, the 3D complete model will be studied using a meshless academic software and the relevant variable fields (displacement/stress/strain fields) will be obtained and analysed. Several materials will be considered in the simulation, allowing to register their performance and obtain relevant practical conclusions.

The advanced numerical methods discretize the problem domain into a nodal cloud without any preestablished relations. This nodal distribution can be used directly by the meshless technique to define the geometric domain of the problem under analysis, easing the discretization step. This natural advantage of meshless methods is a true asset in biomechanics. Furthermore, the literature shows that meshless methods are capable to deliver accurate solutions [10]. Thus, it is expected with this work to demonstrate that meshless methods are an alternative and efficient numerical technique.

During the elaboration of this master's thesis it was possible to present the work intitled *"The numerical analysis of a resin-bonded bridge using finite element method"* in the 11° edition of IJUP Conference (Encontro de investigação jovem Universidade do Porto - Young research meeting of University of Porto). It was also possible the participation in the V International Conference on Biodental Engineering (BIODENTAL-2018), which gave rise to the publication of four papers intitled: *"Numerical analysis of support structures on an adhesive dental bridge"*; *"Predicting in-silico structural response of dental restorations using meshless methods"*; *"Comparing the stress distribution between atrophic maxillary rehabilitation techniques using FEM"*; and *"The numerical analysis of 4-On-Pillars technique using meshless methods"*. All this four works were accepted for a book chapter and are in press.

1.1 – Motivation

Adhesive dental bridges have been considered as a method of replacing missing teeth, when it is necessary to preserve dental structures, since its introduction in 1973 by Rochette. They are already used for the replacement of both anterior and posterior teeth [9]. However, there are still some concerns in using these bridges, which require a more complex geometry design and have a low retention rate. This low retention rate between the retainer wing and the abutment tooth leads to debonding, which is the main cause of failure of this type of dental restoration [11,7]. Thus, this was one of the motivations of this work.

Computational biomechanics allows the numerical simulation of complex problems and, in this case, may help to study the resistance of dental bridges. The Finite Element Method (FEM) is one of the most used discrete numerical methods, however there are other methods that

have been successfully used, such as meshless methods [10]. As it can be seen in Figure 1.1 (the data was obtained through a research on *Scopus* database: www.scopus.com), these advanced discrete methods have not yet been widely used in dentistry, once the number of papers is reduced. For the study of adhesive dental bridges, this method was never applied. As such, another motivation of this work was to understand the level of performance of these methods in the structural analysis of adhesive dental bridges, enhancing the state-of-the-art of meshless methods.
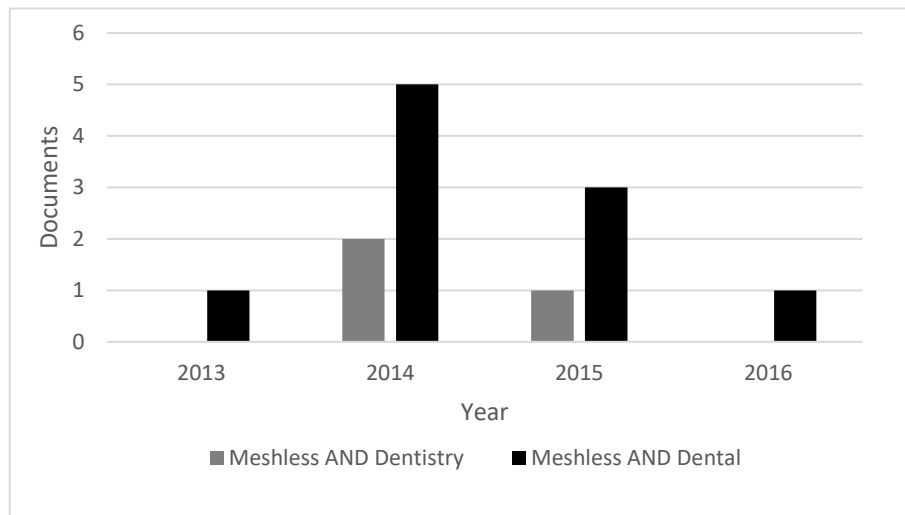
Figure 1.1 - Number of documents published through the years, in the subjects indicated. The data was obtained through a research on *Scopus* database (www.scopus.com) assuming as keywords the subjects indicated in the graph.

1.2 - Objectives

One of the main objectives of this project is to study the adhesive forces of the cement bonding the adhesive dental bridge to the palatal surface of the nearby teeth and, consequently, understand how to increase the mechanical resistance of this type of dental restoration. Another major goal is the validation of the meshless method, as a way of simulating and studying the behaviour of dental restorations.

To achieve these main objectives, other secondary objectives have been established:

- Simulate the materials used as adhesive (whose material properties were experimentally obtained);
- Compare the results obtained experimentally with the computational solution, to validate the mathematical model used;
- Study numerically the structural behaviour of the retainer wing (materials, thickness and design);
- Simulate the overall teeth/restoration system;
- Attain numerically of the best combination of resin-cement, adhesive's thickness and design that allows to achieve a higher mechanical resistance to the dental bridge.

1.3 - Document structure

This thesis is organized in several chapters, beginning with Chapter 1 that presents the motivation that led to the development of this work, as well as the main objectives. In Chapter 2 it is presented all the anatomy concepts that contribute to a better understanding of the mandible/tooth biosystem. Chapter 3 presents some of the existing options for replacement of missing teeth are explained, emphasizing dental bridges that are the focus of this work. In Chapter 3 it is also presented a socioeconomic analysis to understand the impact of dental health on the population. In Chapter 4 and Chapter 5 are explained the mathematical models that will be applied throughout the dissertation, as well as an introduction to the basic notions of solids mechanics. Chapter 6 presents the elato-plastic formulation used in this work. In Chapter 7 it is presented a review on the state of the art of Meshless methods and Numerical Simulation in dental medicine. Chapter 8 and Chapter 9 present all the numerical simulations performed, with the respective results and discussion. The main conclusions of this work are stated and some recommendations for future work in this topic are given in Chapter 10 .

Chapter 2

Mandible/tooth biosystem

In this chapter are presented anatomy concepts of the mandible/tooth biosystem.

2.1 – Bone tissue

There are different classifications for bone tissues and bone structure/shape. Thus, regarding the structure/shape, there are four main classes, based on their shape: long, short, flat or irregular. The description of each one of these types of bone is found in the diagram of Figure 2.1.

Each of these bones referred above, as well as the entire skeletal system, have different functions [10,12]:

1. **Support:** support the soft tissues and provide attachment points for the tendons of skeletal muscle.
2. **Protection:** provide protection to the internal organs and soft tissues.
3. **Movement assistance:** the bones, muscles, tendons, ligaments and joints work in a combined way, generating and transferring forces to move certain parts of the body, or even the whole body.
4. **Storage and release of minerals:** bone tissue stores various minerals, mainly calcium and phosphorus. When necessary, the bone release minerals in the blood to keep constant the critical mineral balance (homeostasis) and distribute the minerals to other parts of the body.
5. **Production of blood cells:** contains red bone marrow, which produces blood cells.
6. **Storage of triglycerides:** contains yellow bone marrow, which stores triglycerides (fats), a potential chemical energy source.

Flat Bone:
Are generally thin, provide considerable protection and extensive muscle attachment surfaces. Include the cranial bones that protect the brain; the breastbone (sternum) and ribs, which protect the organs in the chest; and the scapulae (shoulder blades).

Short Bone:
Are nearly equal in length and width and are a little cube-shaped. Examples of short bones include most of the bones of the wrist and ankle.

Irregular Bone:
Have complex shapes and cannot be grouped in any other categorie. Such bones including vertebrae and facial bones.

Long Bone:
Have longer length than width and consist of a shaft and a variable number of ends. Long bones include the thigh (femur), leg (tibia and fibula), arm (humerus), forearm (radius and ulna) and fingers (phalanges).

Figure 2.1 - Bone shape major groups.

The extracellular matrix is composed of 25 % water, 25 % collagen fibres and 50 % crystallized minerals. As these minerals are deposited in the structure formed by collagen fibres, they crystallize, and the tissue hardens, this process is called calcification [12]. Bone hardness depends on the crystallized minerals, which confers the bone high values of ultimate strength on compression. Flexibility depends on the collagen fibres, giving high values of modulus of elasticity and ultimate strength in tension [10].

2.1.1 - Bone quality and bone density

The bone is an organ which can change in relation to many factors, according to Wolff: *"Every change in the form and function of bone or of its function alone is followed by certain definite changes in the internal architecture, and equally definite alteration in its external conformation, in accordance with mathematical laws"* [13]. So, this tissue can change in relation to its function or because of mechanical influence, and these changes are also observed in the maxilla and mandibula. These two structures have different biomechanical functions: (1) the mandibula corresponds to a force absorption unit and by this, when teeth are present, the outer layer of cortical bone is denser and thicker, as well as the trabecular bone; (2) the maxilla corresponds to a force distribution unit, so all stresses applied to the maxilla are transferred by the zygomatic arch and the palate away from the brain and orbit. In this way, the maxilla has a thinner layer of cortical bone and a denser trabecular bone [13].

Bone quality is related to the proportion and the structure of the cortical and trabecular bone tissue and can be classified into four groups: 1 to 4 or type groups I to IV, explained in Figure 2.2 [14].

Type I: homogeneous cortical bone;
Type II: thick cortical bone with marrow cavity;
Type III: thin cortical bone with dense trabecular bone of good strength;
Type IV: very thin cortical bone with low density trabecular bone of poor strength.
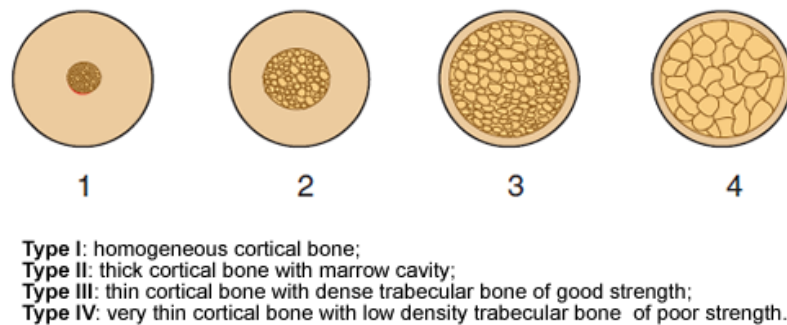
Figure 2.2 - Bone quality index [13].

Bone density is related to the strength of the bone to microfracture and can be categorized, once again, into four groups: D1 to D4, being D1 the stronger the and D4 the weakest [13]. These four groups, showed in Figure 2.3, vary in both macroscopic cortical and trabecular bone types.

D1: dense cortical;
D2: Porous cortical and coarse trabecular;
D3: Porous cortical (thin) and fine trabecular;
D4: Fine trabecular.
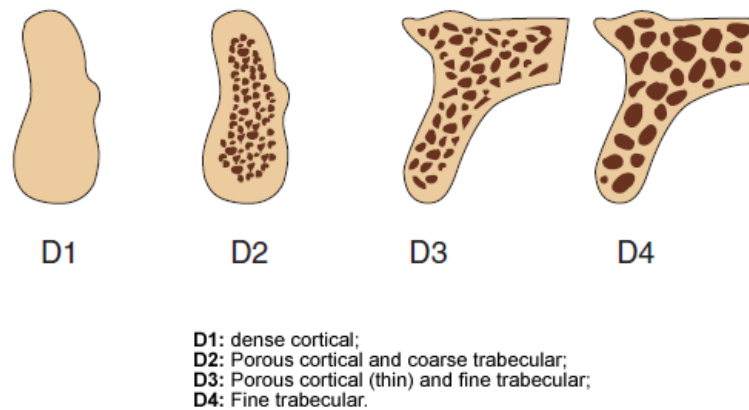
Figure 2.3 - Bone density [13].

The bone type D1 is a homogeneous and dense cortical bone and presents several advantages for implant dentistry. It is most often found in anterior mandible with moderate to severe resorption. This bone density displays a force greater than any other type, but it has fewer blood vessels than the other three types, so it is more dependent on the periosteum to its nutrition [14].

Bone density D2 is the most common observed in the mandible, specifically on the anterior mandible (from first premolar to first premolar) [13].

In D3 bone the trabecula are approximately 50% weaker than those in bone D2. This type of bone is more often found in the anterior maxilla and posterior regions of the mouth in either arch [14].

The D4 has little bone density and little or no cortical crestal bone, so it is the opposite of D1. D4 may be up to 10 times weaker than D1. It is more often found in the posterior region of the maxilla and it is rarely observed in the mandible [14].

So, to resume: anterior mandible is mostly D2 bone, posterior mandible and anterior maxilla are D3 bone and posterior maxilla is D4 [13].

The Young's modulus of a material correlates the material strain with its internal stress state. Generally, for bone tissue the Young's modulus can be correlated with the bone's apparent density [13]. The types 1 and 2 offer high Young's modulus, while types 3 and 4 have a thin cortex and low Young's modulus with low trabecular density [15].
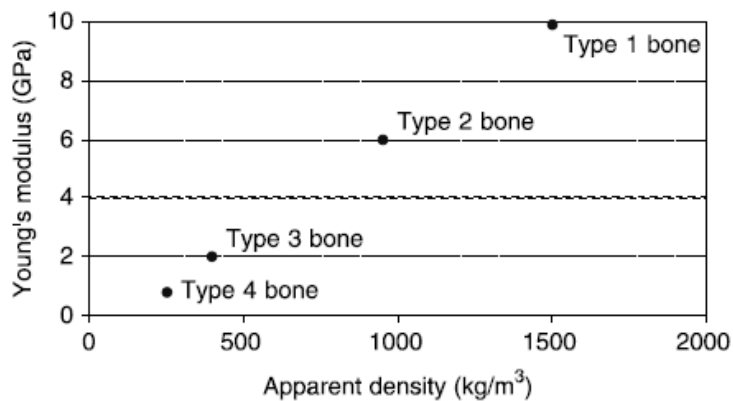
Figure 2.4 - Correlation between Young's modulus and apparent bone density of different bone types [15].

Since different types of bone have different mechanical properties, its biomechanical behaviour will also be different, and this will affect the ability of the bone to support physiological loads. The poor bone quality type 4 promoted major failures of dental implants, due to its reduced binding capacity of the implant in the bone [16].

2.2 - Mandible/tooth biosystem

The brief description presented in this subchapter can be found with more detail in the following references: [17], [5] and [18].

2.2.1 - Mandible

The mandible, as seen in Figure 2.5 is located inferiorly in the facial skeleton, is the largest, strongest and lowest bone in the face. It serves as reception of the lower teeth, within the alveolar process. The holes in the jaws that contain the roots of the teeth are called tooth sockets or dental alveoli. The alveolar process is a thickened ridge of bone that contains the teeth and the dental alveoli. The mandible consists in a horizontal portion convexed forwards (positioned anteriorly) - the body - and two vertical portions that ascend posteriorly - the ramus. These structures, the body and the ramus, link together in a near right angle. The mandible articulates on either side with temporal bone, forming the TMJ (temporomandibular joint) [17].
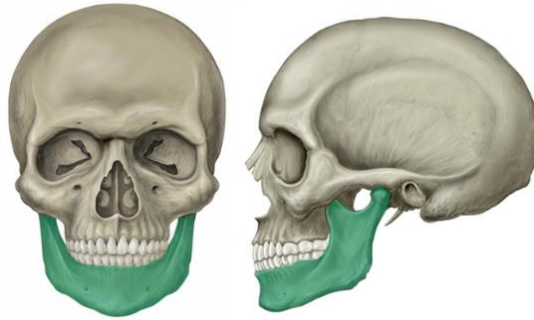
Figure 2.5 - Anterior and lateral views of the mandible within the facial skeleton.

The body has two surfaces and two borders: external and internal surfaces separated by upper and lower borders. So, it has the alveolar border (superior), that contains 16 sockets to hold the lower teeth, and the base (inferior), that corresponds to the site of attachment for the digastric muscle medially.

In the midline of the body there is a mark, the mandibular symphysis. This is a small ridge of bone that represents the merger of the two halves of the jaw during development. The symphysis encloses a triangular eminence – the mental protuberance - which forms the shape of the chin. Lateral to the mental protuberance is the mental foramen (below the second premolar tooth on either side), which acts as a passageway for neurovascular structures [17].

A foramen corresponds to any opening through which neurovascular structures can travel. The mandible is marked by two foramina. The mandibular foramen that is located on the internal surface of the ramus and serves as a conduit for the inferior alveolar nerve and inferior alveolar artery. They travel through the mandibular foramen, into the mandibular canal, and exit at the mental foramen. The mental foramen, located on the external surface of the mandibular body, allows the inferior alveolar nerve and artery to exit the mandibular canal. When the inferior alveolar nerve passes through the mental foramen, it becomes the mental nerve (innervates the skin of the lower lip and the front of the chin).

Each rami project perpendicularly upwards from the angle of the mandible (showed in Figure 2.7) and has two surfaces (lateral and medial), four borders (superior, inferior, anterior and posterior) and two processes (coronoid and condylar). In the lower part of the lateral surface there is the oblique ridge and in the medial surface there is the mandibular foramen (located midway between the anterior and posterior borders), that acts as passageway for neurovascular structures. The inferior border is continuous with the mandibular body and meets the posterior border of the ramus at the angle. The superior border is surmounted in front by the coronoid process and behind by the condylar process.

In Figure 2.8, the condylar process is situated posteriorly and articulates with the temporal bone to form the TMJ. The coronoid process is the site of attachment of the temporalis muscle. The posterior border extends from the condyle to the angle and is convex backwards above and concave below. The anterior border extends from the edge of the coronoid process to the external oblique line and is thin above and thicker below. The neck supports the head and it is the site of attachment of the lateral pterygoid muscle [17].
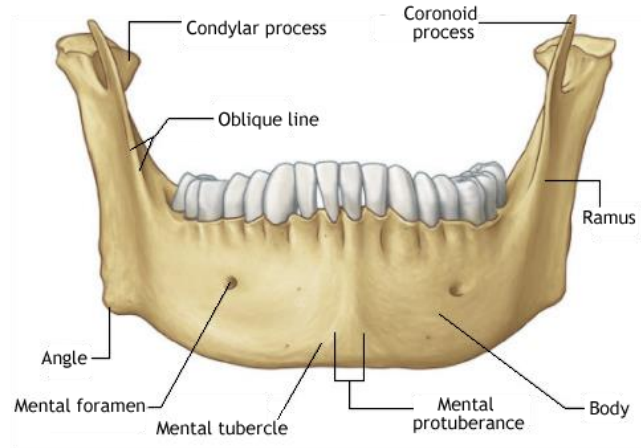
Figure 2.6 - Anterior view of an adult mandible [17].
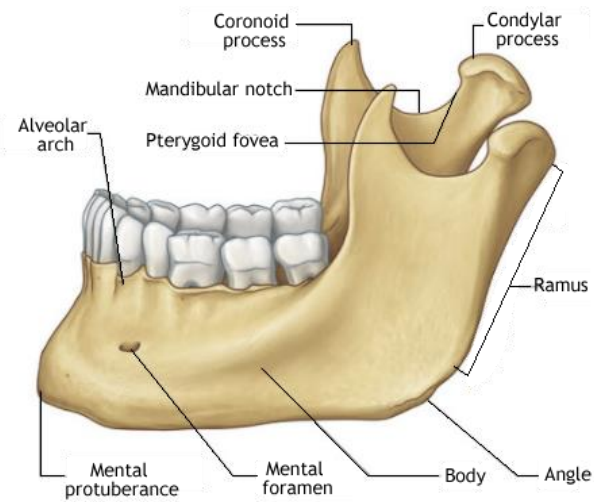
Figure 2.7 - Lateral view of the mandible [17].
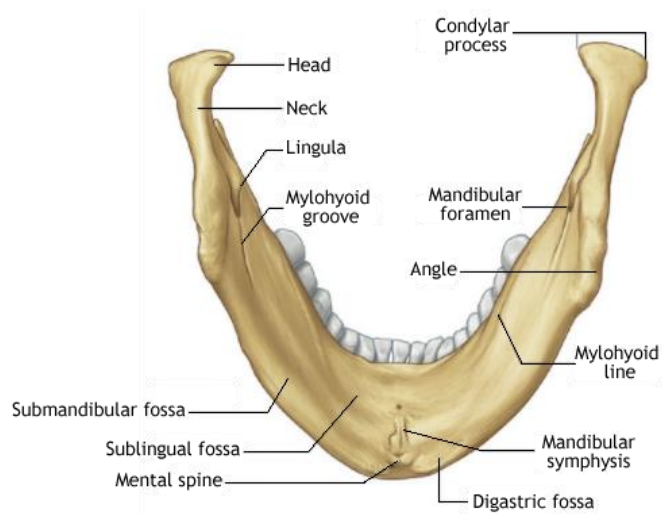
Figure 2.8 - Inferior view of the mandible [17].

2.2.2 - Teeth

The teeth are the hardest substances in the human body. A tooth is divided into crown and root. The crown is covered by enamel and the root by cementum. So, the different parts of a tooth include:

1. **Enamel:** the hardest, white outer part of the tooth. It is a highly crystalline structure since it is constituted by 95-98 % inorganic component by mass. The inorganic component comprises 86-95% hydroxyapatite by volume. The organic component comprises 1-2 %, while water contributes 4-12 % [18].

2. **Dentin:** A layer underlying the enamel. Dentin is made of living cells, which secrete a hard-mineral substance. It comprises 45-50 % inorganic hydroxyapatite crystals, with 30 % organic matrix and 25 % water. Dentin consists of: (1) Intertubular dentin: the primary structural component, comprising hydroxyapatite embedded in a collagen matrix; (2) Peritubular dentin: provides a collagen-free hyper mineralised tubular wall; and (3) Dentinal tubules: filled with extended processes of odontoblasts (cells responsible for the formation of dentin), which form the interface between the dentin and the pulp [18].

3. **Pulp:** The softer, living inner structure of teeth. Blood vessels and nerves run through the pulp of the teeth. The pulp is contained within a rigid chamber of dentin. It function is to produce dentin and it also has a sensory role [5].

4. **Cementum:** A layer of connective tissue that binds the roots of the teeth firmly to the gums and jawbone. It covers the whole surface of the root and attaches the fibres of the Periodontal Ligament (PDL) to the tooth. So, it has an important role on the maintenance of the periodontal health. There are two types of cementum: (1) cellular cementum, which contains cells called cementocytes (whose function is to nourish the avascular cementum via the surrounding vascular PDL); and (2) acellular cementum, which does not contain cells. First formed cementum is usually the acellular type, so this covers the cervical two-thirds of the root. Cellular type is formed later, so it covers the apical third and normally overlaps the acellular type. The cementum alters in response to the functional requirements of the tooth [5].

5. **Periodontal tissue:** it consists of the gingiva, covering the alveolar processes, and the PDL. It has dense bundles of fibres which run from the cementum lining the root surface to the alveolar bone to which the fibres are attached. The PDL helps hold the teeth tightly against the jaw. It is made up of connective tissue and contains collagen fibres. This tissue also contains blood vessels, that supply the ligament with nutrients, and nerves, that are responsible for controlling the amount of force used while chewing. There are two main types of collagen fibres of the PDL: (1) interstitial fibres, randomly arranged throughout the PDL, supporting the blood vessels and nerves; and (2) principal fibres, denser than the previous fibres mentioned and run from cementum to bone, holding the tooth firmly in its socket [5].
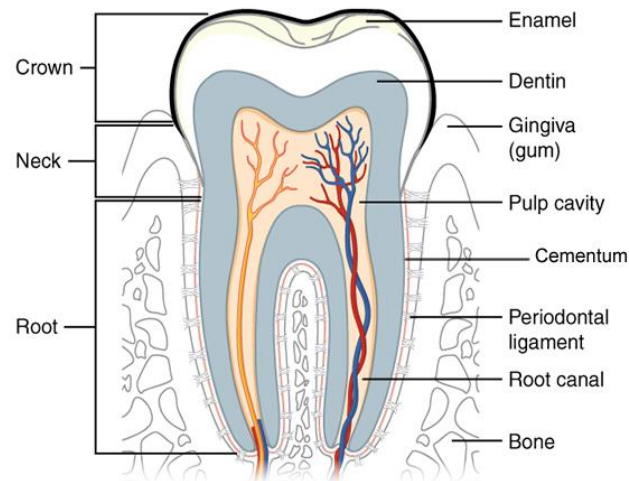
Figure 2.9 - Tooth structure.

The teeth are connected to the walls of the dental alveoli and anchored in the jaws by the PDL and the cementum.

The gums (gingiva) cover and protect the ligament and the neck of the tooth and are usually the only visible part of the periodontium. It consists of mucosal tissue and surrounds the teeth providing a seal around them, once it is tightly bound to the underlying bone which helps resist the friction of food passing over the teeth. The gingiva can be divided into the following areas [5]:

1. **Free marginal gums:** the edge of the gums surrounding the teeth. It has about 1.5 mm wide in health. The collagen fibres of the free gingiva are arranged in three main groups: (1) circular fibres, these form a collar around the neck of the tooth holding the free gingiva tightly against it; (2) gingival fibres, these originate from the cementum of the cervical part of the root and fan outwards into the free gingiva; and (3) transeptal fibres, these run from the cervical cementum on the distal side of the one root to the cementum on the mesial aspect of the next tooth.
2. **Attached gum:** The attached gums are continuous with the marginal gum. It is firm, resilient, and tightly bound to the underlying periosteum of alveolar bone. It has variable width.
3. **Interdental gum:** The interdental gum lies between adjacent teeth.
4. **The gingival crevice or sulcus:** leading from the marginal gingiva to the junctional epithelium.

The junctional epithelium (JE) is adjacent to the tooth and corresponds to the part of gingiva which attaches the connective tissue to the tooth surface. It has 2-3 mm wide around the tooth. It creates the firm attachment of the soft gingival tissue to hard tooth tissue, once JE attaches to enamel by basal lamina and intercellular hemidesmosomes (cells responsible for the attachment of one cell to the extracellular matrix). It is permeable, so it serves as a pathway for diffusion of the metabolic products of plaque bacteria such as toxins, chemotactic agents and antigens. When gingiva is inflamed, the JE has many polymorphonuclear leucocytes (PMNs) moving through it towards the sulcus. These form an important part of the defence mechanism and so the JE has an important role in the maintenance of periodontal health [5].

A normal adult mouth has 32 teeth:
- **8 Incisors:** The four teeth on the upper and lower jaws located in the middle;
- **4 Canines:** The pointed teeth located just beside the incisors, one of each side upwards and downwards;
- **8 Premolars:** Teeth between the canines and molars;
- **8 Molars:** Flat teeth in the rear of the mouth, best at grinding food;
- **4 third molars or wisdom teeth:** These are often surgically removed to prevent displacement of other teeth.
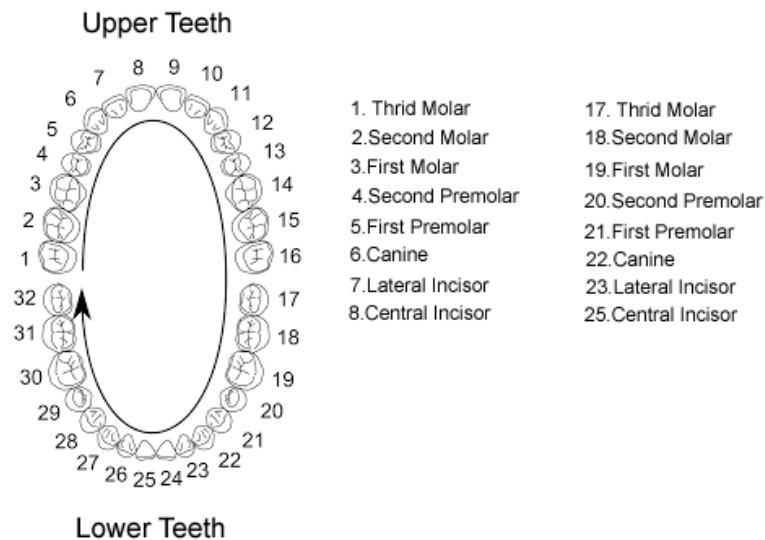
Figure 2.10 - Adult dentition.

2.3 - Nomenclature of dental anatomy

The crowns of the incisors and canines have four surfaces and a ridge (the incisal surface), and the crowns of the premolars and molars have five surfaces [19].

In the incisors and canines there are:
- **Facial surface:** in this case it calls labial surface and corresponds to the surface towards lip;
- **Lingual surface:** surface towards tongue;
- **Proximal surfaces:** it includes mesial surface, that corresponds to surfaces towards midline, and distal surface, that corresponds to surfaces away from midline;
- **Incisal surface:** surfaces of the incisors and canine that meet teeth from the opposite jaws during closing.

In the premolars and molars there are:
- **Facial surface:** in this case it calls buccal surface and corresponds to the surface towards cheek;
- **Lingual surface:** surface towards tongue;
- **Proximal surfaces:** it includes mesial surface, that corresponds to surfaces towards midline, and distal surface, that corresponds to surfaces away from midline.
- **Occlusal surface:** surfaces of the premolars and molars that meet teeth from the opposite jaws during closing.
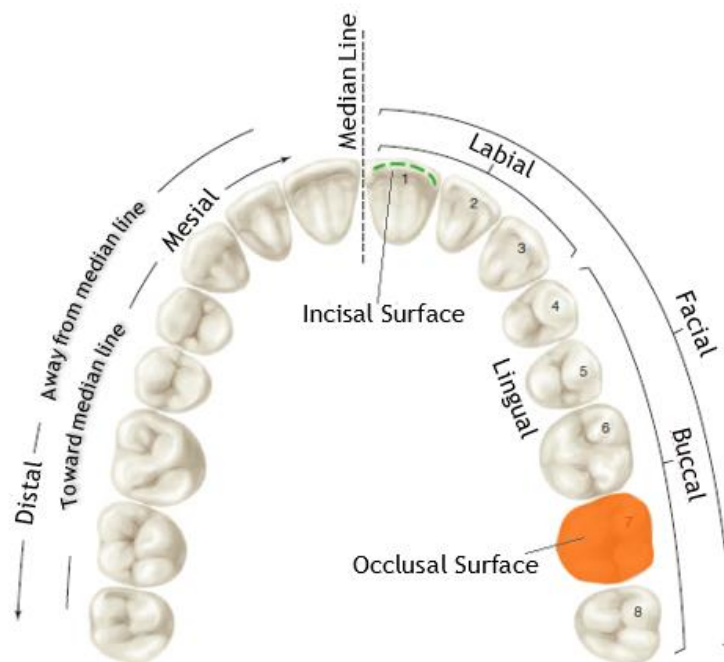
Figure 2.11 - Surfaces and ridges [19].

To study an individual tooth, it is necessary to become familiar with additional terms:
- **Cusp:** elevation on the crown making up a divisional part of the occlusal surface;
- **Tubercle:** smaller elevation on some portion of the crown produced by an extra formation of enamel, creating derivations from the typical form;
- **Cingulum:** the lingual lobe of an anterior teeth;
- **Ridge:** linear elevation on the surface of a tooth and is named according to its location, particularly the marginal ridges correspond to those rounded borders of the enamel that form the mesial and distal margins of the occlusal surfaces of premolars and molars and the mesial and distal margins of the lingual surfaces of the incisors and canines;
- **Triangular ridges:** descend from the cusps of molars and premolars towards the centre of the occlusal surface. When two triangular ridges come together, they form a transverse ridge;
- **Fossa:** irregular depression or concavity. A pit is a small pinpoint depression.

To describe a tooth, the crowns and roots can be divided into thirds, line angles and point angles, all described in Figure 2.13, Figure 2.14 and Figure 2.15, respectively.
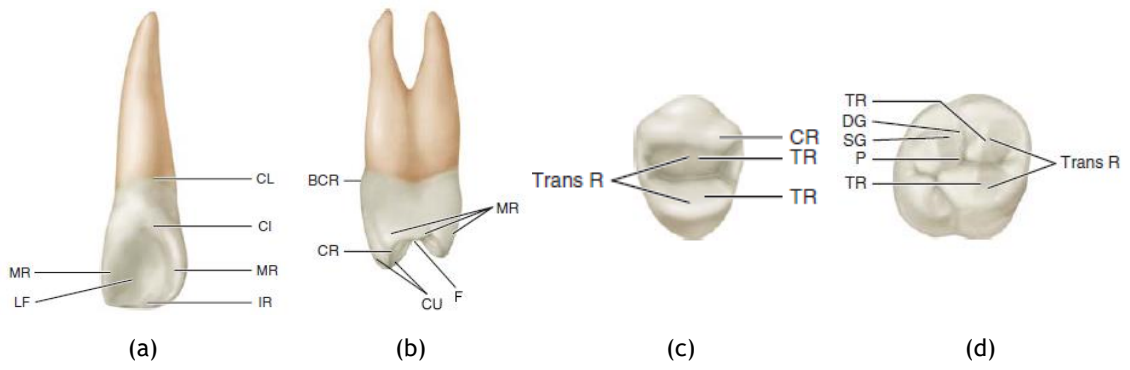
Figure 2.12 - Other landmarks important to describe teeth: (a) maxillary right lateral incisor: CL – cervical line; CI- cingulum; MR – marginal ridge; IR – incisal ridge; LF – lingual fossa. (b) mesial view of a maxillary right first premolar: CR – cusp ridge; BCR – buccocervical ridge; MR – marginal ridge; CU - cusp; F – fissure. (c) Occlusal view of maxillary right first premolar: Tran R – transverse ridge; TR – transverse ridge; CR – cusp ridge. (d) Occlusal view of a maxillary right first molar: P – pit; Tran R – transverse ridge; TR – transverse ridge [19].
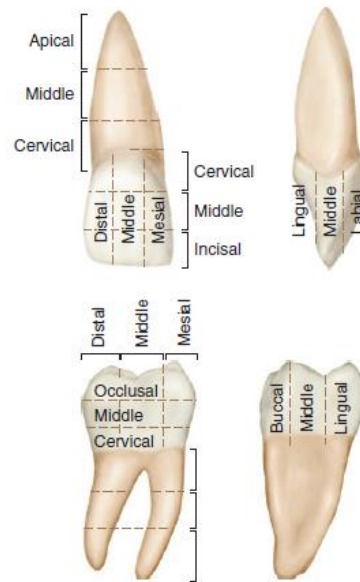
Figure 2.13 - Division of teeth into thirds [19].
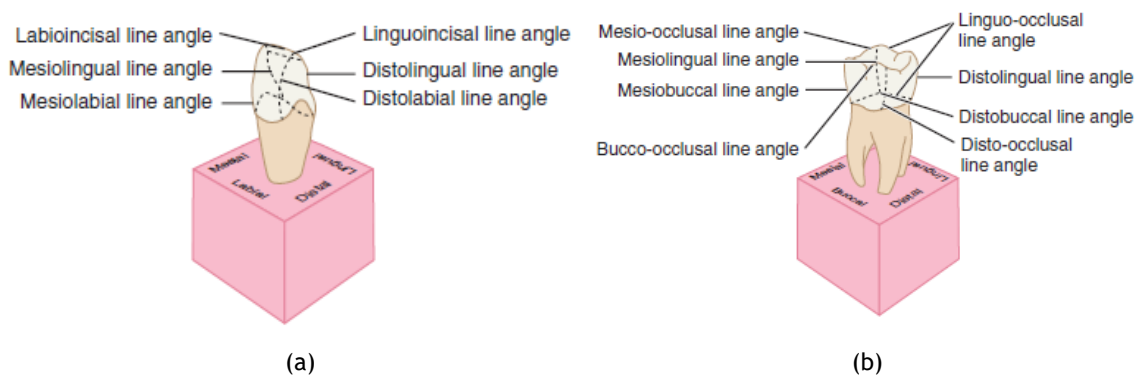
Figure 2.14 - Line angles: (a) line angles of an anterior tooth; (b) Line angles of a posterior tooth [19].
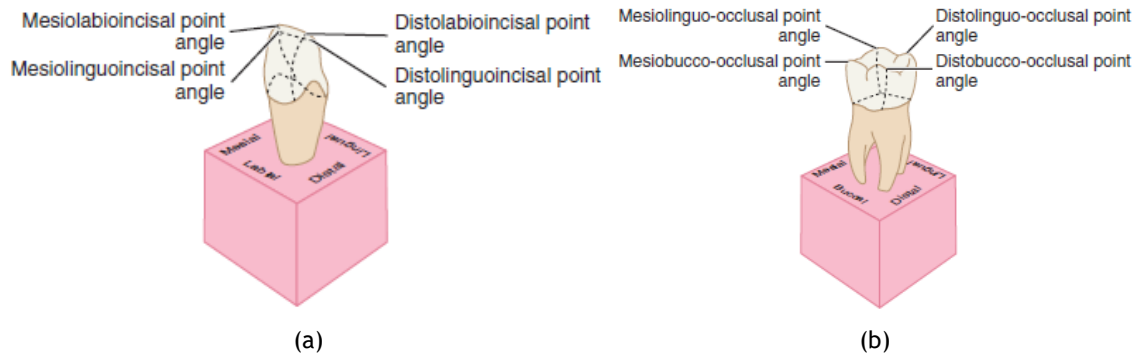
Figure 2.15 - Point angles: (a) Point angles of an anterior tooth; (b) Point angles of a posterior tooth [19].

The brief description presented in this subchapter can be found with more detail in [19].

Chapter 3

Dental restorations

Implants have come a long way, and since the beginning of mankind, humans have used implants to replace missing teeth. In some cases, these substitutions were made after the death of the person, aiming to improve the smile in the underworld. In about 2500 BC, the ancient Egyptians tried to stabilize teeth using a golden wire. This was an attempt to replace an upper jaw of an Egyptian King. About of 2000 years later, in 500 BC, Etruscan civilization (area now known as Tuscany) used animal teeth to replace their own teeth [20]. Nowadays, oral problems persist and, globally, it was reported that in 2010 oral conditions affected 3.9 billion people, with untreated cavities being de most prevalent and severe periodontitis the sixth most prevalent [2]. Around the world, about 30% of individuals in group age from 65 to 74 years old have no natural teeth [21].

3.1 - Socioeconomic analysis

Loss of teeth has a negative impact on quality of life, since it can interfere with chewing, aesthetics, speaking and social skills of the patient. In our present society good aesthetics is very important. Thus, naturally, the loss of a tooth can lead to low self-esteem, compromising the individual's ability to socialize, adversely affecting his/her performance at work and in daily activities.

The teeth may be lost for congenital reasons or due to a disease, but there also some factors that contribute to tooth loss, like demographic, behavioural and attitudinal factors [22].

According to the literature, the age is directly related to the loss of teeth. Therefore, the ageing population is one of the main factors to consider. A study performed from 1988 to 1991, in the United States, found that only 30 % of the patients had 28 teeth. The followed-up study occurred from 1999 to 2004 and it was verified that the average number of teeth lost was 2 for the group of 20 to 39 years of age, and 9 in adults with more than 60 years. The biggest transition from an intact dental arch to an edentulous arch occurred in the group of 35 to 54 years of age. Although the number of missing teeth per patient is apparently declining, due to improvements in oral care, the total number of missing teeth will continue to increase due to the aging of the population [1].

There are also several diseases than can lead to tooth loss, which will decrease oral health, that is essential to overall health and quality of life. Dental caries and periodontal disease are leading causes of tooth loss. As it is possible to see in Figure 3.1, tooth decay (dental caries) is the most prevalent condition affecting 44 % of the world population and severe periodontitis is not very far, affecting 11% of the world population [2].
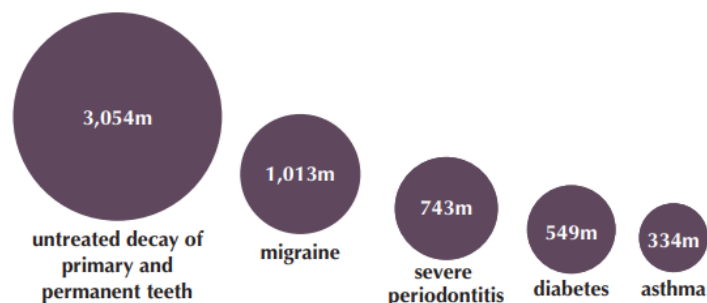
Figure 3.1 - Estimated number of people affected by common diseases in 2010 [2].

The economic impact of oral diseases is still not very clear due to the lack of comprehensive and comparable international statistics on oral diseases. However according to the World Health Organization, oral diseases are the fourth more expensive to treat [21]. It was estimated an annual cost of €79 billion in the 27 European Union member states as seen in Figure 3.2.
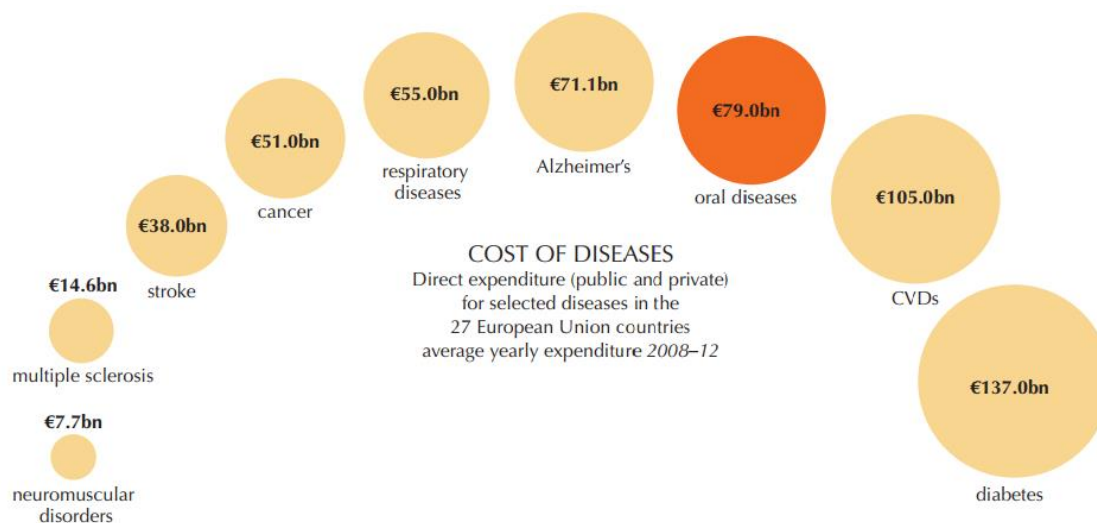
Figure 3.2 - Direct costs of different diseases in the 27 European Union countries, average from 2008 to 2012 [2].

The overall economic burden of dental diseases accounted for US$442 billion (€372,9 thousand million) in 2010, of which [3]:

- US$298 billion (€251,41 thousand million) were assigned to direct treatment costs, corresponding to an average of 4.6 % of global health expenditures: 83 % of direct treatment costs were attributable to the high-income countries;
- US$144 billion (€121.49 thousand million) for indirect costs: in that, US$63.03 billion (€53.17 thousand million) (44 %) was attributed to severe tooth loss, US$53.99 billion (€45.54 thousand million) (37 %) to severe periodontitis, US$25.14 billion (€21.20 thousand million) (17 %) to untreated caries in permanent teeth and

US$2.09 billion (€1.76 thousand million) (1 %) to untreated caries in deciduous teeth.

These findings indicated that oral conditions have a global significant impact and even with the improvements of health treatment costs and productivity, loses are still very high.

According to the barometer of oral health in Portugal of 2017, only 32.4 % of Portuguese population (3.240 million people) possesses a full dentition (more details in Figure 3.3), which means that 68 % of Portuguese population (6.800 million people) lack at least one natural teeth [23].

| 32.4 % | 37.8 % | 10.8 % | 12.9 % | 6.2 % |
| Have all teeth | Missing 1 to 5 teeth | Missing 6 to 8 teeth | Missing more than 8 teeth | Missing all teeth |

Figure 3.3 - Statistics of missing teeth in Portugal, in 2017 [23].

Of those who have lack of natural teeth, only 42.6 % (2.896 million people) have replacement teeth (more details in Figure 3.4).

| | 2015 | 54.0% | 41.3% | 4.7% |
| | 2014 | 56.1% | 36.2% | 7.7% |

| 57.4% | 35.8% | 6.7% |
| Nothing to replace | Prosthesis or dentures | Fixed teeth |
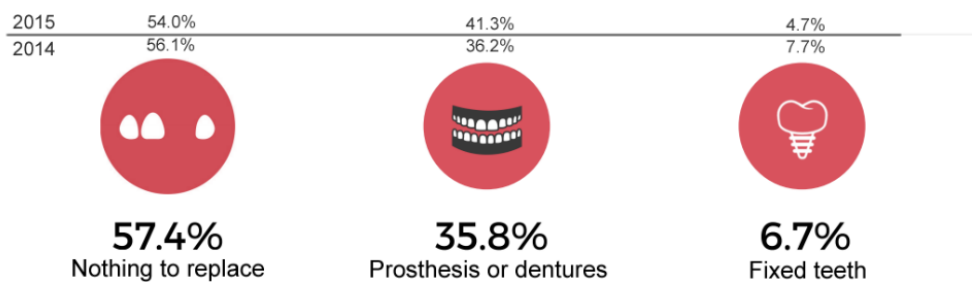
Figure 3.4 - Statistics demonstrating how Portuguese replace their missing teeth [23].

So is possible to conclude that 11% of Portuguese live without more than 6 teeth and without replacements.

In Portugal, costs with oral healthcare, in 2010 and 2012, were €720 million and €750 million, respectively. With an annual growth rate of 2 %, costs with oral healthcare can reach €880 million [24].

Countries around the world have tried to increase emergency hospital admissions for dental problems and to implement oral healthcare programs to better provide equitable access to oral healthcare but this is a challenge. In USA, admissions have doubled in the last 10 years and the related costs are US$2.7 billion (€2.27 thousand million) [2]. In Portugal, almost 6.500 patients were treated by dentists in health primary care of the national health system (SNS), integrated since July 2016 in a pilot project that will now be extended to more health centres.

3.2 - Dental restorations

Missing teeth do not always need to be replaced, but if it is the patient's best interest and if it is a viable option, there are a variety of treatment alternatives.

The patient can opt for orthodontic treatment, that can be: preventive (by preventing problems that were detected while the patient was still a child by the application of dental appliances), interceptive treatments (using fixed dental appliances) or corrective treatments (trying to correct a problem that is already installed). Orthodontic treatments have the advantage of not having long-term maintenance requirements.

Mobile prostheses can replace a full arcade, and these do not require the existence of healthy teeth. These types of restorations are versatile, allowing to manage extensive tooth loss, significant alveolar resorption or large soft-tissue or osseous defects [4].

Fixed prostheses are usually recommended to those who have lost one or more teeth, but still possess some in his mouth, once the crown that is going to replace the missing tooth needs other teeth as a pillar to be fixed.

The patient can opt for an implant (represented in Figure 3.5), which can replace a tooth or even a complete arcade. This technique consists in the insertion of a pin into the bone and, then, placing in the top of the pin an artificial tooth, known as crown. This technique can be used to stabilize both fixed and removable prostheses. Implants can also be used in dental bridges, serving as abutment teeth in screw-retained implant-stabilized bridges [4].

Implant supported restoration

Single unit crown

Cement retained

Implant abutment with holding

screw in position
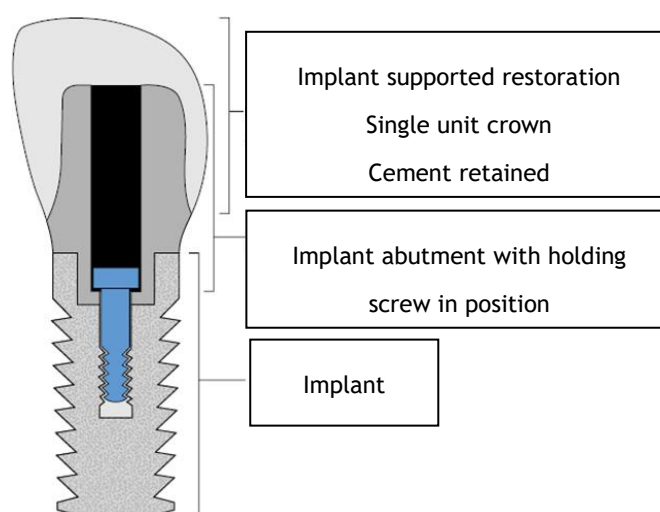
Implant

Figure 3.5 - Basic components of an implant [18].

With implants, the dentist just replaces a single tooth, getting a strong and permanent result. However, in the event of the neighbouring teeth have many problems and need rebuilding or if the tooth has been lost long ago (which means that probably the bone and gum will have receded), it is recommended the dental bridge. A bridge is a type of fixed prosthesis that serves to fill one or more missing teeth supported by natural teeth. To use these types of restorations it is important the presence of solid/robust abutments and good oral hygiene habits (so that in long term the abutments do not get compromised) [4]. There are three types of dental bridges [18]:

1. **Conventional bridges:** these appear before the development of adhesive techniques and therefore these types of bridges consist in reducing the natural teeth placing a crown. The pontic tooth is placed in the lack between the prepared

abutment teeth and is attached to the crowns that where placed in the abutments. So, this is a method that requires a significant tooth preparation [4].

2. **Adhesive bridges**: described forward.

3. **Hybrid bridges:** corresponds to a combination of the two types mentioned above. However, it should be avoided since it is difficult to use both conventional cements and adhesive resins at the same time.

These types of bridges described previously can also be divided, according to the level of support provided by adjacent teeth [5]:

1. **Fixed-fixed bridges:** all joints are either soldered or cast in one piece, rigidly connecting all the abutment teeth.

2. **Fixed-movable bridges:** this type of bridge incorporates a stress-redistributing device which allows limited movement at one of the joints between the pontic(s) and the retainer(s). The fixed end of the bridge has a rigid connector with the major retainer that is usually distal to the pontic. The minor retainer houses the movable joint and does not require as much retention as the major retainer. The movable joint gives support to the pontic against vertical occlusal forces and allows minimal movement in response to lateral forces, so there is less torsional stress on the adhesive part of the bridge. This type of bridges places additional stress on the fixed part of the bridge and therefore strong abutments are necessary. It allows independent tooth movement and the use of divergent abutments.

3. **Cantilever bridges:** used when there are adjacent teeth on only one side of the missing tooth or teeth. So, the tooth to be restored will be suspended with support on one side. For this reason, multiple abutments are often used.

4. **Spring Cantilever bridges:** in this type of bridges the abutment is at some distance from the pontic. The pontic is supported by a metal bar (which should follow a wide curve) that connects the abutment to the pontic and is in contact with the palatal mucosa. It is supported by tooth and tissue and is only indicated in the maxilla.

5. **Compound bridges:** corresponds to a combination of the different types mentioned above.

These types of bridges are represented in Figure 3.6 and Figure 3.7.

(a)   (b)   (c)   (d)
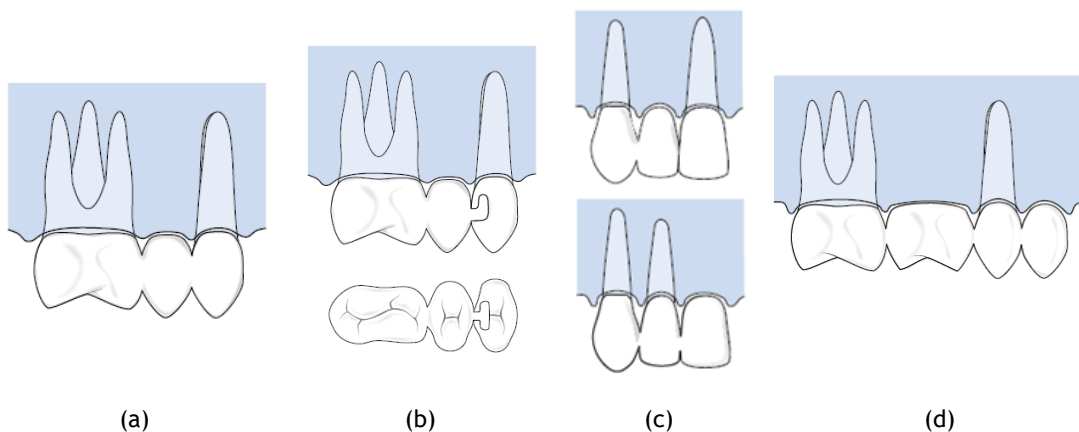
Figure 3.6 - Schematic representation of different types of bridges: (a) fixed-fixed bridge; (b) fixed-movable bridge; (c) cantilever bridge with a single abutment (top image) and double abutment (bottom image); (d) compound bridge with fixed-fixed bridge and cantilever bridge [18].

Figure 3.7 - Spring cantilever bridge [5].

In Table 3.1 there is a comparison between FPDs and removable dentures.

Table 3.1 – Comparison of advantages and disadvantages of FPDs with removable partial dentures [25].

Fixed partial dentures	Removable partial dentures
Advantages:	Advantages:
• The tooth substitutes appear more natural • Fell more natural • Superior stability when chewing hard foods • Minimal soft tissue coverage • Not easily removed	• Generally, less expensive • Minimal tooth preparation • Longer edentulous spans can be restored • Replacement of missing alveolar ridge tissues is possible • Can be removed for cleaning and adjustments or repairs
Disadvantages:	Disadvantages:
• More expensive • More suitable for short spans • Extensive tooth preparation is usual • Abutments must be in good alignment and functionally adequate	• Clasps may be unattractive • Designs may be bulky, complicated and plaque-retentive • May cause gagging • Retention and stability may be problematic

More information about the treatment options described above can be found with more detail in [4], [5] and [18].

3.2.1 – Adhesive bridges

Adhesive bridges were first described in 1973 by Rochette that demonstrated the ability to bond cast metal alloys to teeth. He used perforated retainers, demonstrated in Figure 3.8, made of cast gold and the retention was generated micromechanically by resin cement [26]. However, this type of restoration had limited longevity and to address this problem, in 1980, the University of Maryland developed a type of electrochemical etching, giving origin to the term 'Maryland bridge' [6].
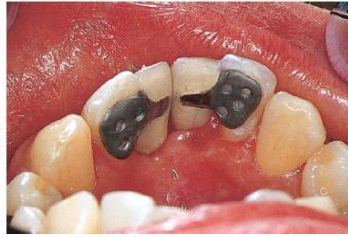
Figure 3.8 - Two cantilever Rochette bridges [5].

Adhesive bridges are a type of fixed prosthesis in which the pontic tooth is attached to a structure that is cemented on the abutment teeth (adjacent teeth to the space of the missing tooth and that will serve as a support). This method requires minimal tooth reparation.

This type of restorations distinguishes from the others because it is a conservative method, it can be placed quickly, it is economical, is accepted by the patients and it is versatile [5]. Another advantage is that it is reversible and does not compromise the abutment tooth. Therefore, it can be used as a provisory restoration, which is good for example for young patients who, for some reason, lost a tooth. In these cases, an implant might not be a viable option once the growth of the mouth is still on going. So, adhesive bridges can be used without damaging the abutment teeth [6]. However, it has some disadvantages such as: it requires sound abutments, it is unsuitable for long spans and occasionally occurs debonding [4,5].

There are several factors that should be considered to try to improve the resistance of dental bridges. It is important to consider the bridge design, which includes the choice of the type of the bridge. Cantilevers and fixed-movable bridges are the preferred designs, once debonding of one retainer in a fixed-fixed bridge is common, which may lead to caries in the retainer that debonded [5]. Another important aspect of the bridge design are the biomechanical aspects of the retainer as the thickness, height and angle of the axial surface extensions [9]. It is also important to choose the correct abutments and the correct number of abutments. It is known that bridges with multiple abutments are more likely to debond due to the differential movements. Besides that, it is important to investigate the endodontic and periodontal health of the abutments [6].

Other important factor is the kind of materials used. Adhesive bridges can be made on a substructure of metal alloy veneered with a composite. The metal alloys rigidity makes them ideal for the retainers since they can be used without the risk of flexing [6]. However, the use of a metal framework has one major disadvantage. Due to translucency of teeth, abutments started to have a greyish appearance, and this was not aesthetically acceptable. So, other materials started to be used, like all-ceramic, which offer an increased biocompatibility, lower plaque accumulation and a more aesthetic result. However, one disadvantage with the use of these materials is the required dimensions for the connector to allow sufficient strength and rigidity. Therefore, other type of materials was considered, such as: FRC (Fibre Reinforced Composite), like glass fibres, ultra-high molecular weight polyethylene and Kevlar fibres (which allows better adhesion of the luting agent to the framework, lower cost and better aesthetic). The fibres can be arranged either in one direction (unidirectionally) or in different directions to one another (bidirectional fibres). This is an important characteristic that should be selected to improve the mechanical resistance of the bridge [27]. In Table 3.2 is a comparison of the different materials mentioned and in Figure 3.9, Figure 3.10 and Figure 3.11 there are real cases of adhesive bridges with different materials.

Table 3.2 - Comparison of different materials for retainer wing of an adhesive bridge [27].

Resin-bonded bridge type	Advantages	Disadvantages
Fibre-reinforced composite	• Relatively good aesthetics • Better adhesion of the luting agent to the framework • Direct manufacturing possible (lower cost) • Possible to repair with addition of composite resin/fibres	• Unsure long-term prognosis • Wear of the composite resin material • Framework fracturing difficult to repair • Unstable aesthetics • More extensive preparation required • Adequate thickness required, bulky
All-ceramic	• Superb aesthetics • Biocompatible • Reduced plaque accumulation	• High failure risk • Unsure long-term prognosis • Impossible to repair • Least minimally invasive • Adequate thickness required, bulky • High laboratory cost
Metal-ceramic	• Long-term clinical data available • Most minimally invasive • Simple rebonding • Suits a cantilever design • With more extensive preparation the success becomes more predictable	• Medium aesthetics • Metal unpopular

Figure 3.9 - Resin-bonded bridge with metal retainer's wings, applied to a young patient with developmentally missing lateral incisors [6].

Figure 3.10 - All-ceramic resin-bonded bridge [27].

Figure 3.11 - FRC resin-bonded bridge [28].

Bond strength is higher to enamel and so increasing the available area of enamel for bonding and reducing the functional stress on the resin composite lute, through vertical groves, can increase resistance to debonding forces [5,6].

The success rate of resin-bonded FPDs varies from study to study:

- 76 % after 5 years for bridges with cast metal framework [7];
- Survival rate is only 40 % for mandibular prostheses [9];
- Survival rate of 75 % and a functional survival rate of 93 % after a follow-up period of 24-63 months for resin-bonded, glass fibre-reinforced composite [8];
- Survival rate of 73 % after 5 years for inlay glass fibre-reinforced FPDs [8];
- 95 % survival rate within a period of 2.8-4.3 years for prostheses with high-volume of fibre-reinforced composite substructure [8];
- 25 % survival rate for bridges on a metal alloy substructure after 15 months [11].

In fact, probably these differences in survival rates are due to differences in the conditions of the studies. However, with these different studies it is possible to extract that the most common reasons for failures are:

- Debonding of the cast metal framework from the luting cement or debonding of the luting cement from the enamel surface [7];
- Fracture of the pontic [8];
- Delamination of the veneering material from the framework [8].

(a)

(b)

(c)
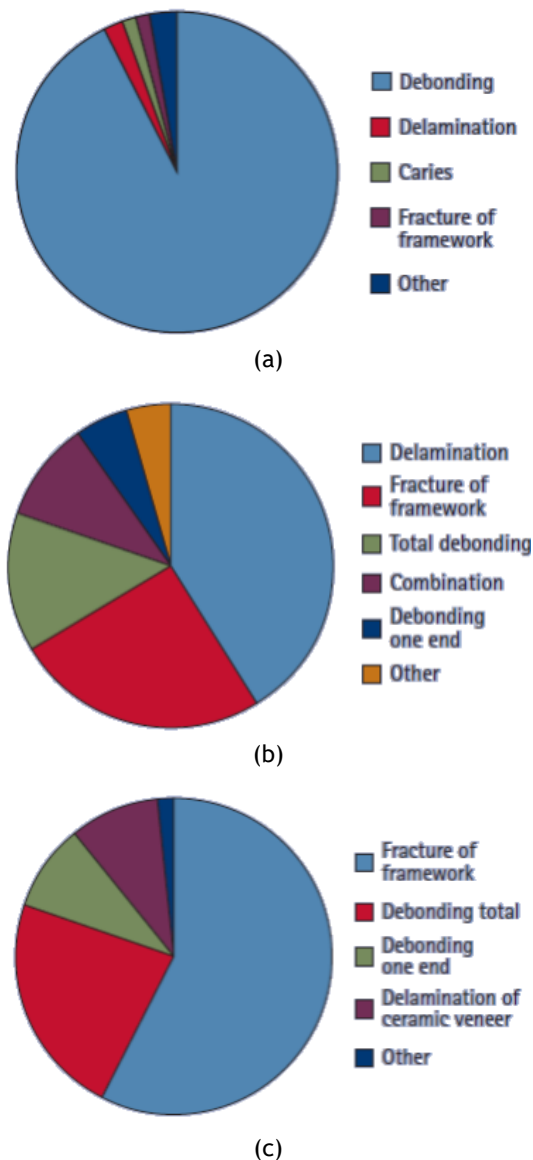
Figure 3.12 - Reasons for failure of adhesive bridges: (a) reasons for failure in metal dental bridges; (b) reasons for failure in FRC dental bridges; (c) reasons for failure in ceramic dental bridges [27].

Once again, there can be a variety of reasons for failure of dental bridges. Thus, attempting to better understand the survival rates and the reasons of failure, several studies, listed in Table 3.3, were analysed, aiming to find common factors.

Analysing Table 3.3:

- In [7], prostheses were examined after periods of 6 months for up 24 months. No framework fractures were observed and two prostheses debonded during the follow-up time, of which one was due to improper occlusal adjustment and the other due to unknown reasons;

- The other three studies presented in Table 3.3 were a literature review of a total of 49 studies: 25 studies on metal-framed, 17 studies on fibre-reinforced and 7 studies on all-ceramic resin-bonded bridges. It was possible to conclude that all types of resin-bonded bridges provide an effective short- to medium-term option, with all-ceramic performing least well and having the least favourable mode of

failure. The methods of failures were different for different bridges with metal frameworks performing the best over time.

Table 3.3 - Studies that analysed survival rates of different adhesive bridges.

Year		1997-1998	1996-2008	1997-2010	1996-2012
Type of study		Clinical	Review	Review	Review
Follow-up time (mean)		14 months	4.95 years	3.1 years	4.33 years
Number of patients	Male	11	4 260	500	192
	Female	20			
Type of bridge		Continuous unidirectional glass fibre reinforcement	Metal-framed	Fibre-reinforced composite	All-ceramic resin-bonded bridges
Number of abutments Mean (min/max)	Maxilla	2.6 (2/5)	-	-	-
	Mandible	3.3 (2/5)			
Number of pontics Mean (min/max)	Maxilla	1.5 (1/3)	-	-	-
	Mandible	1.8 (1/3)			
Location	Maxilla Anterior	9	68.2% were placed in maxilla and 38.7% were in the posterior regions.	61% were in the maxilla and 75% in the posterior region.	58% were in the maxilla and 55% in the posterior regions.
	Maxilla Posterior	8			
	Mandible Anterior	10			
	Mandible Posterior	4			
Results		93% probability of survival at 24 months	82.8% estimated survival after 3 years	88.5% success after 3 years	72.54% success after 3 years
Reference		[7]	[27]	[27]	[27]

3.2.2 - Adhesion

Adhesion is the process of bonding dissimilar materials by attraction of atoms or molecules. In this process there is the formation of an adhesive joint. In the adhesive joint, the initial substrate is called the adherend and the material producing the interface is called adhesive [29]. Normally, most of adhesive joint involve two interfaces showed in Figure 3.13: (1) cement/tooth interface, that can be with dentin or enamel and (2) cement/restoration interface [30]. There are two types of adhesion: (1) chemical, that involves bonding at an

atomic or molecular level and (2) mechanical, that involves the interlocking of one phase into the surface of the other phase [29]. In many cases both chemical and mechanical bonding occur together, and the chemical bonding is desirable at both interfaces, but the type of bonding will depend on the materials and the cements used [29,30].
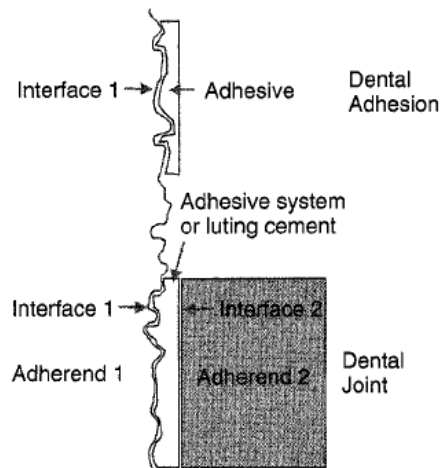
Figure 3.13 - Adhesive systems [29].

Adhesive techniques can be used for: (1) restoration of carious cavities; (2) aesthetic correction of dental anomalies; (3) bonding of ceramic or metal to tooth substance (like in dental bridges); (4) cementation of crowns; (5) splinting (technique used to support, protect and immobilize teeth that have been loosened, replanted, fractured or subjected to certain endodontic surgical procedures); (6) repair of fractures restorations [18].

To create the adhesive layer there are many steps to be followed and there are involved several components that are called bonding agents. Therefore, the implementation of all these steps should ensure that: the surface of the substrate is clean; the adhesive wets the substrate well; the interface includes the sufficient physical, chemical and/or mechanical strength (to resist intraoral forces of debonding); and the adhesive is well cured under the conditions recommend for use. If all these requirements are verified, the chances of forming an optimally bonded interface are higher [29].

However, keeping the surface of the substrate clean in the patient's mouth until the adhesive is applied is a challenge because dental surfaces in the oral environment contain a pellicle of materials from saliva and components from food. Besides that, once the surface is clean, it is more likely to adsorb material from the surrounding air, which will decrease the energy for bonding. So, the surfaces must be clean, removing these materials, and then it must be protected. In addition, if enamel and dentin are prepared with rotary instruments, a layer of debris, called smear layer, will be formed and will compromise the process of adhesion and so it must be removed. The conditioning of enamel can be achieved using mild acids, such as phosphoric acid (30-40 % in a gel form), applied for a period no less than 15 seconds (like demonstrated in Figure 3.14), resulting in dissolution and removal of approximately 10 μm of the surface organic component of enamel and leaving a microporous layer of 5–50 μm. Then, enamel is washed for 10-20 seconds. The conditioning of dentin can be achieved using a range of acids for varying periods of time, but it always should be avoided extreme demineralization of the dentin. The acids used include 10–40 % phosphoric acid, 2.5 % nitric acid, 10 % citric or maleic acids and 1.6–3.5 % oxalic acid [18].

Figure 3.14 – Etching with phosphoric acid [31].

When adhesive is finally applied to a substrate, it must wet properly the surface, which is demonstrated by a small contact angle and spreading of the adhesive onto the substrate. These will allow to produce an intimate material approximation without entrapped air or other intervening materials. A good flow and lower viscosity can be achieved by adding solvent to the adhesive [29].

The final step is the adhesive curing (polymerizing), which can be accomplished by chemical reactions initiated by visible light [29].

Clean dentin is hydrophilic, thus it will be better wetted by an adhesive that is also hydrophilic. On the other hand, composites that constitute the retainer wing are hydrophobic. Thus, the adhesion of these two layers (with different characteristics) can be improved using an intermediate layer of a compound that is hydrophilic in one end and hydrophobic on the other end [29].

Adhesive techniques have several advantages, some of which are: (1) less invasive tooth preparation (because of the reduced need for mechanical retention or stabilization of the restoration); (2) reduction in microleakage; (3) possible better stress transmission to tooth substance; and (4) improved aesthetic treatment options. The quality of bonding depends on: the materials used; the functional loads applied to the tooth; and the restoration and the effects of repeated thermocycling [18].

Despite the advantages referred, there are cases in which occurs debonding. The adhesive bonds are weakened by stresses caused by differences in thermal expansion coefficients and dimensional changes during the setting of the adhesive [29]. When an adhesive bond is weakened, it can occur debonding, which occurs by a process of crack formation. These cracks will grow and propagate, and will contribute to stress concentrations within the substrates, leading to joint failure. Since tooth and restorative substrates are much stronger than the bond strength of the restorations, cracks will generally form in the bonded interface zone [29].

There are two types of failures: (1) adhesive, that can occur between the cement/tooth interface or cement/restoration interface and (2) cohesive, that occur within the intermediate cement layer or the underlying tooth substrate. Most common failures are adhesive in the cement/tooth interface due to weak dentine bond [30].

Examples of defects are trapped air bubbles and zones of poor wetting. The joint's resistance to failure depends on the extent of defects [29].

3.3 - Materials

For dental materials it was assumed that these are brittle, which means that when subjected to stress, they break without plastic deformation. In Figure 3.15 it is possible to see this type of behaviour for dentin. In Table 3.4, there are all the dental materials that were considered, with the respective mechanical properties.
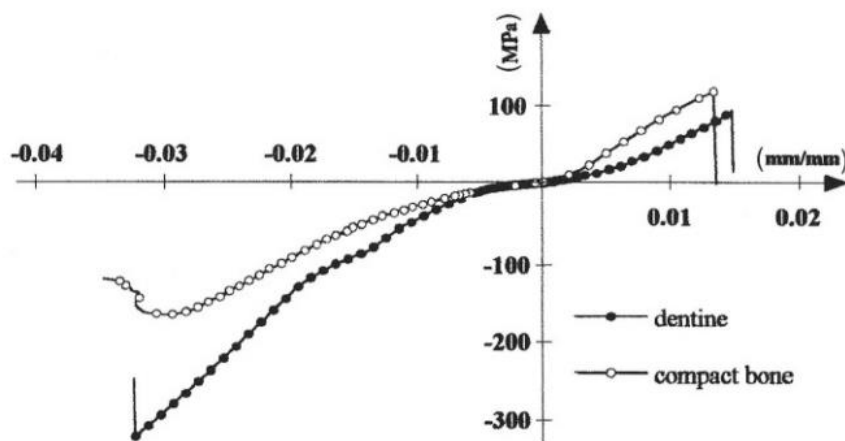
Figure 3.15 - Typical stress-strain curves for dentin and compact bone [32].

Table 3.4 - Dental materials considered, with the respective properties.

Materials	Dentin	Enamel	Pulp
Density (Kg/mm³)	$2.14 \cdot 10^{-6}$	$2.97 \cdot 10^{-6}$	-
Young's modulus E (GPa)	14.7	84.1	0.0200
Poisson ratio υ	0.31	0.33	0.45
Maximum stress, to tension (MPa)	50	10	-
Maximum stress, to compression (MPa)	234	262	-
Reference	[33]	[33]	[34]

In Table 3.5, it is possible to observe the mechanical properties of the most common materials considered for the retainer wing and the crown. The mechanical properties of the metallic materials (Type IV gold, Titanium Alloy, Co-Cr alloy) were obtained from the experimental tests documented in [35], Figure 3.16(a). Thus, using the experimental results, the experimental curves were adjusted with a bilinear elasto-plastic law, Figure 3.16(b). Due to lack of data, it was considered that all materials have the same elasto-plastic behaviour when submitted to compression and to traction.

(a)   (b)
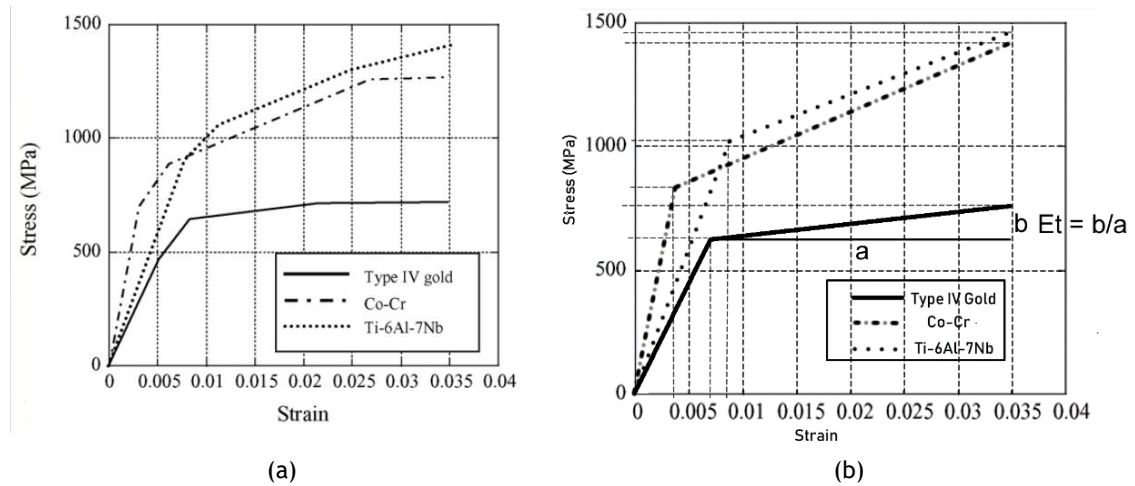
Figure 3.16 - Stress-strain curves of different materials [35].

Table 3.5 - Selected materials for the dental bridge with the respective properties (traction).

Materials	Retainer wing				Crown and Retainer wing
	Type IV gold	Titanium Alloy	Co-Cr alloy	FRC (Glass fibre)	Zirconia
Young's Modulus - E (GPa)	92.6	115.8	229.1	X: 39 Y: 12 Z: 12	245
Poisson's Ratio υ	0.33	0.33	0.33	X: 0.35 Y: 0.11 Z: 0.11	0.26
Yield stress (MPa)	630.2	1021.7	836.35	-	-
Plastic Modulus (MPa)	4650	16377	18284	-	-
Elastic strain limit	0.007	0.0085	0.0035	-	-
Ultimate stress (MPa)	760.4	1455.7	1412.3	-	900-1200 (2000[1])
Reference	[35]	[35]	[35]	[36]	[37,38]

For the adhesive, three materials were considered. Within the scope of this work, these materials were tested in laboratory, through compression tests. So, it was possible to obtain the graphics showed in Figure 3.17(a). Once again, the experimental curves were adjusted to a bilinear elasto-plastic law, as represented in Figure 3.17(b). The materials and respective properties are represented in Table 3.6. It was assumed that these adhesives have the same Poisson's ratio as the Epoxy Resins. Additionally, due to lack of experimental data (since the experimental test was only a compression test), it is considered that these adhesive materials possess the same mechanical properties in traction and compression.

---

[1] Ultimate stress to compression.
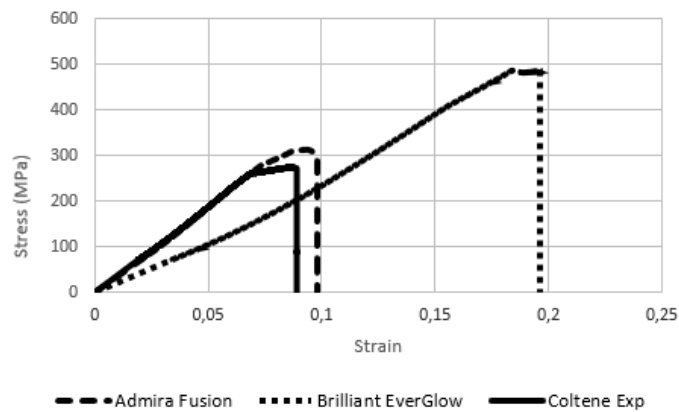
(a)
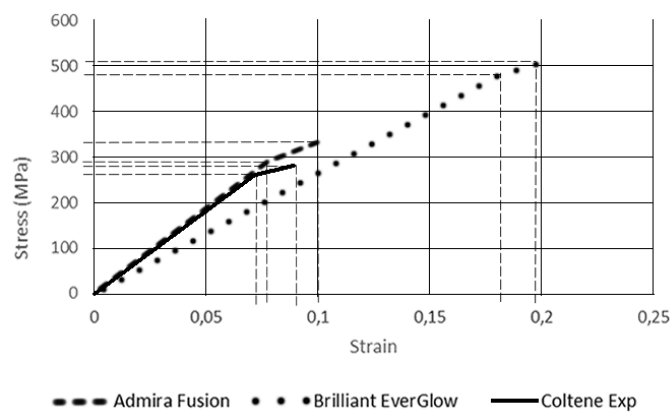
(b)

Figure 3.17 - Compression tests of different adhesives.

Table 3.6 - Adhesive tested and respective obtained properties.

Materials	Adhesive		
	Admira Fusion VOCO	Brilliant COLTÈNE	NC COLTÈNE
Young's Modulus – E (GPa)	3.6	2.3	2.3
Poisson ratio υ	0.3	0.3	0.3
Yield Stress (MPa)	290	480	260
Plastic Modulus (MPa)	1739	2532	1111
Elastic Strain Limit	0.077	0.1815	0.0725
Ultimate Stress (MPa)	330	520	280
Ultimate Strain	0.1	0.1973	0.0905

3.4 - Comparison of different methods

Replacement of a missing tooth is desirable to improve appearance, masticatory function or speech or even to prevent harmful changes in dental arches, like resorption of the alveolar bone (which exacerbates the resultant tissue deficit), overeruption or tilting/drifting of teeth. If the patient decides to replace the missing teeth, an appropriate treatment must be selected

by the dentist. To select the best treatment, the dentist must assess the patient's condition (considering the medical, dental and social history), perform a clinical oral and radiographic examination, perform articulated study costs, evaluate trial dentures/diagnostic wax-up and discusses options [4]. When indicated, and if the patient desires, replacement of missing teeth can be accomplished with different treatments, mentioned in Table 3.7 and Table 3.8.

Table 3.7 - Comparison of different restorative treatments [4].

	RPD	Adhesive bridge	Conventional bridge	Implant-fixed prosthesis
Dentist's skill level	Competent/ Advanced	Competent/ Advanced	Competent/ Advanced	Advanced
Technical support	Competent/ Advanced	Competent/ Advanced	Advanced	Advanced
Maintenance	High	Low	Low	Low
Duration of treatment	Moderate	Short	Short/moderate	Long
May preserve bone	No	No	No	Yes
Replaces soft tissues	Yes	No	No	No
Mucosal support	Partial	No	No	No
Tooth preparation	Yes, minimal	Yes, minimal	Yes	No
Subjective prosthesis security	Usually acceptable	Very high	Very high	Very high
Aesthetic potential	Good	Good	Good	Good
Bulk	Moderate/ Considerable	Minimal	Minimal	Minimal
Initial cost	Low/ Moderate/ High	Moderate/ High	Moderate/high/ Very high	High/very high
Recurrent cost	Moderate	Low	Low	Low
Functional life	Moderate	Good	Very good	Prosthesis very good. Implant extremely good
Modification of prosthesis	Straightforward /Impossible	Very difficult/ Impossible	Very difficult/ Impossible	Bridge difficult. Implants impossible

Table 3.8 - Advantages and disadvantages of different restorative treatments [5].

Type of treatment	Advantages	Disadvantages
Conventional bridgework	• Fixed • Good aesthetics • Medium-term predictability is good for short-span bridges • Good control of occlusion possible • Minimal compromise of oral hygiene	• Involves tooth preparation which can result in pulp death • Failure due to de-cementation and caries of abutment teeth may lead to further tooth loss • Moderately expensive • Highly operator-dependent • Requires lengthy clinical time and temporary restorations • Irreversible
Resin-bonded bridgework	• Minimal or no preparation • Good aesthetics if ideal spacing exists • Less expensive than conventional bridges • Consequences of failure are relatively small	• Lack of predictability • Average life span 5–7 years • Requires high operator technique and enamel surface area for bonding • Change in colour/translucency of abutment teeth due to presence of retainer • May interfere with occlusion • Debonding may lead to reduction in life span
Removable partial dentures	• Replaces multiple teeth in multiple sites • Mucosa and/or teeth support • Generally, do not require extensive preparation of abutment teeth • May be designed to accommodate future tooth loss • Replaces missing soft tissue and provides soft tissue support • Aesthetics may be very good • Low cost	• Patient acceptance may be poor • Connectors cover soft tissue such as palate and gingiva • Coverage of gingival margins will lead to plaque retention and increase periodontal disease and caries • Aesthetics compromised by retentive elements such as clasps • Moderate maintenance requirements and durability
Implant-retained prostheses	• Fixed or removable • Independent of natural teeth for retention of crowns, etc. • No dental caries reduced or altered response to dental plaque • High level of predictability • Good maintenance of supporting bone	• Requires the presence of adequate bone quantity and quality • Involves surgical procedures • High operator technique • High initial expense and lengthy treatment time • Moderate maintenance requirements especially for removable or extensive fixed prostheses

Chapter 4

Numerical methods

The mechanical simulation is very important not only in the aerospace industry, civil engineering and automotive industry, but also in health. The biomedical research has proved to be expensive and ethically questionable, due to human or animal trials. As such, numerical methods allowing the development of virtual models and simulation processes became a solid alternative, allowing to save time, money and permitting the analysis of complex problems with a difficult analytical solution [39].

This chapter starts with a brief explanation of FEM, exhibiting its advantages and disadvantages. Then it is presented a brief state-of-the-art of meshless methods, with an explanation of two numerical methods: RPIM e NRRPIM.

4.1 - FEM

FEM is a technique that gives the solution of a complex mechanical problem. This method is characterized by the domain discretization into multiple subdomains called finite elements. Thus, this means that a complex problem is simplified by splitting the problem domain into smaller and simpler domains. For each one of the finite elements the field variables are interpolated by simple functions, the shape functions [40].

The process of modelling with FEM is divided into several steps. The first step is to represent the geometry digitally. Through images obtained from a Computed Tomography (CT) or a Magnetic Resonance (MR) it is possible to obtain virtual models anatomically accurate. It is also necessary to define the properties of the materials considered, as well as the load cases and boundary conditions. The material properties influence the distribution of stresses and deformations in a structure. The materials can be considered isotropic, transversely isotropic, anisotropic and orthotropic. In most studies, the materials are considered homogeneous, linear and with elastic behaviour characterized by two constants: Young's modulus and Poisson coefficient [40].

Then, it is necessary to create a mesh to divide the entire domain into elements. The process of creating the mesh with its elements and their respective nodes is defined as the discretization step of the process. The type, the arrangement and the total number of elements has impact on the accuracy of the results, as shown in Figure 4.1 [41]. These elements can be

irregular and may have different properties, allowing the discretization of structures composed of different materials. Finally, the desired settings can be simulated with accuracy and the results analysed.
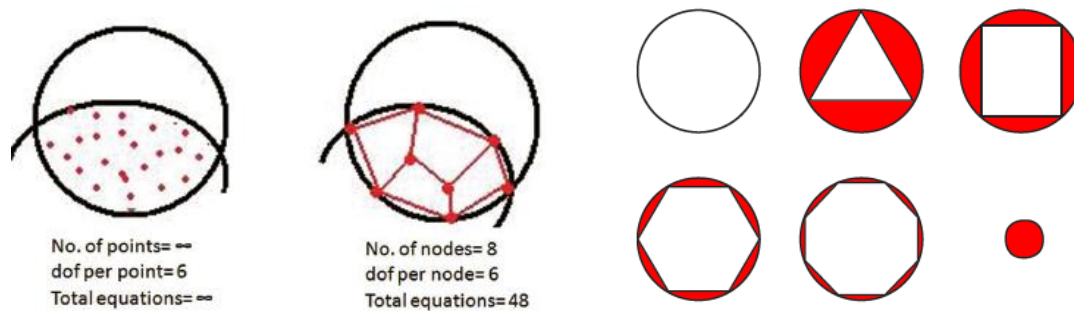
Figure 4.1 – Creation of a mesh and demonstration of its influence on the discretization error [42].

The FEM combined with the theory of elasticity allow to predict several variable fields, such as displacement, strain and stress fields. These solution fields depend on the assumptions made in the modelling of the structure under study, such as the structure geometry, the properties of the materials considered, the essential and natural boundary conditions and, in the case of dentistry, the bone-implant interfaces, for example [40]. The FEM was developed in the 60's to resolve structural problems in aerospace industry, but it has been applied in many other areas such as biomedical engineering [40].

The FEM was applied for the first time in biomechanics in 1972 for the analysis of mechanical behaviour of skeleton parts. The application of this method in biomechanics allowed to understand the process of bone remodelling, assess the risk of fractures and designing possible solutions [43].

In the biomedical engineering field this method can be used to study a great range of topics, such as: percutaneous heart valves, human lumbar spine, bone remodelling, tissue modelling, among others [16].

This method has several advantages. It allows to predict (and interpolate) the stress/strain state of virtually any point inside the geometric 3D model [16,44]. Additionally, FEM provides quick solutions and results can be obtained with a reasonable degree of accuracy [42].

4.2 - Meshless methods

The meshless methods were developed to address some of the limitations of FEM, mainly related to the difficulties in the mesh generation [45].

The main difference between FEM and meshless methods is that in the latter, the domain of the problem is discretized in arbitrarily distributed nodes without any pre-established relation between them. Nodal connectivity is established by influence-domains, so field functions are approximated within an influence-domain, rather than an element. In meshless methods, influence-domains must overlap each other. These advanced numerical methods comprise three phases: the construction of the shape function, the formulation and the integration [10].

Meshless methods can be divided into two categories: approximation meshless methods and interpolation meshless methods [45].

The first meshless methods developed were approximation methods. These methods use approximation functions, as they allow to obtain smoother solutions. The influence-domains were obtained through fixed radial searches and the background integration mesh (used to integrate the integral-differential equations that govern the study of a physical phenomenon) was constructed through integration cells, independent on the nodal distribution. For this reason, these methods inherited the FEM integration scheme [46].

The first meshless approximation method was the Smoothed-Particle Hydrodynamics (SPH), developed for astronomy and this was the origin of the Reproducing Kernel Particle Method (RKPM) [46]. One of the oldest methods is the Diffuse Element Method (DEM). This method uses the Moving Least Square approximants (MLS), proposed by Lancaster and Salkauskas, in the construction of the approximation function. Belytschko evolved DEM by developing one of the most popular meshless methods, the Element Free Galerkin Method (EFGM) [47].

However, these approximation methods present a limitation in the imposition of essential and natural boundary conditions, due to the lack of the delta Kronecker property, for which the interpolation methods were developed. Several interpolation methods have been developed, such as the Point Interpolation Method (PIM), the Radial Point Interpolation Method (RPIM), the Natural Neighbour Finite Element Method (NNFEM) and the Natural Element Method (NEM) [47].

The RPIM had its origin in the PIM, through the addition of an extra functional base, an RBF (Radial Basis Function). The combination of NEM and RPIM originated the Natural Neighbour Radial Point Interpolation Method (NNRPIM) [10].

An issue that causes a lot of discussion is the dependency and the construction of a background mesh for integration purposes. This means that some meshless methods are not a truly meshless discretization method since they require a secondary mesh: the background integration mesh. Some of these methods are the EFGM and the RPIM. Alternatively, other meshless method formulations are capable to construct the integration mesh and to impose the nodal connectivity using only the nodal distribution, being truly meshless methods. Some of these techniques are the NNRPIM and the Natural Radial Element Method (NREM) [45,47].

The meshless methods used in this work are the RPIM and the NNRPIM. Next, a brief explanation of both techniques is presented.

4.2.1 - Meshless generic procedure

In meshless methods, the first step should be the study of the geometry of the problem and establish a solid domain, its boundaries and boundary conditions, as shown in Figure 4.2(a) [10].

Then, the solid domain must be numerically discretized by a nodal set, with regular or irregular distribution, as shown in Figure 4.2(b) and Figure 4.2(c), respectively. It is necessary to consider that the nodal discretization has a direct effect on the result of the numerical analysis, affecting the performance of the method. As such, a uniform nodal distribution leads to more accurate results. In meshless methods, no information about the relationship between nodes is required. The only information required is the spatial location of each discrete node in the problem domain, and it is important to note that the nodal distribution does not form a mesh [10].
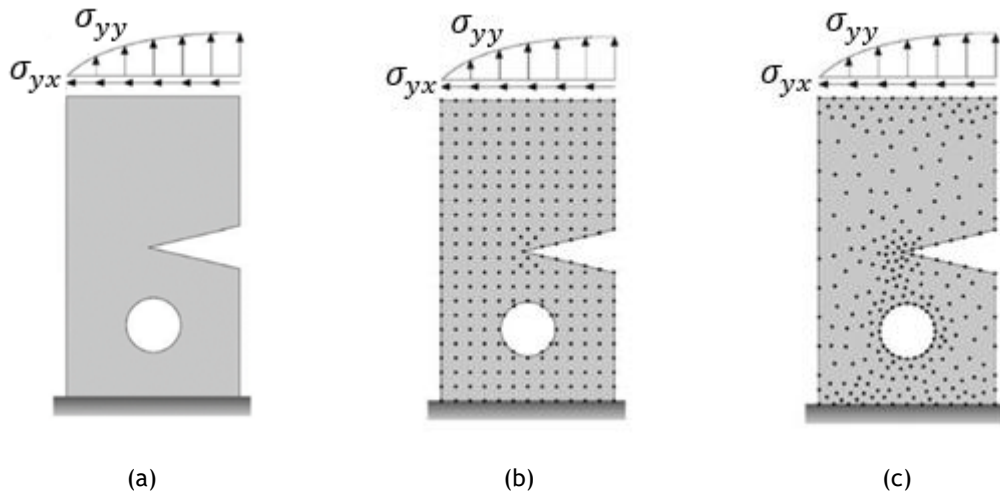
Figure 4.2 - Nodal discretization of the domain of the problem: (a) solid domain with the natural and essential boundaries; (b) regular nodal discretization; (c) irregular nodal discretization [10].

After discretization of the problem domain, nodal connectivity can be imposed through influence-domains or Voronoï diagrams. Next, a background integration mesh is created, with the use of Gaussian integration meshes being adjusted to the problem domain. Other methods, such as nodal integration, may be used through the Voronoï diagrams to obtain the integration weight of each node [10].

Then, it is possible to obtain the field variables under study using approximation or interpolation functions, based on the combination of RBFs with polynomial basis functions. The interpolation functions have an important property - delta Kronecker property - so the obtained function passes through all nodes inside the influence-domain. This property allows the use of the same simple FEM techniques to impose boundary conditions [10].

Thus, meshless methods require the combination of three parts: nodal connectivity, numerical integration scheme, and shape functions. These three parts will be explained for both RPIM and NNRPIM formulations in the next sections. However, since it is simple to represent 2D domains, the sections regarding the nodal connectivity, numerical integration and interpolation functions will present (both for the RPIM and NNRPIM formulations) only the 2D case. Nevertheless, the presented concepts are easily extended to higher dimensional spaces, as shown in [10].

4.2.2 - Nodal connectivity

4.2.2.1 - RPIM

After initial nodal discretization of the problem domain, it is necessary to impose nodal connectivity between all nodes. Therefore, to find nodal connectivity it is necessary to overlap the influence-domain of each node [10].

Influence-domains are found by searching for enough nodes within a given area or volume and can have a fixed or variable size, as well as may take different shapes. In Figure 4.3(a) and Figure 4.3(b) are represented two types of fixed size domains, a rectangular and a circular one, respectively. Varying the shape, or the size, a different nodal connectivity is obtained. In addition, the initial nodal spatial distribution will influence the influence-domains leading to a

different number of nodes. These factors will affect the final solution of the problem and may cause loss of precision in the numerical analysis [10].

To overcome these problems, RPIM relies on influence-domains with variable size, but with a constant number of nodes within the domain, as shown in Figure 4.3(c). RPIM uses the Galerkin weak formulation to obtain the discrete equation system. The shape functions are constructed using a polynomial basis and an RBF. A radial search is carried out, using as centre a point of interest x_I to find the n closest nodes. This process is illustrated in Figure 4.3(c) being perceptible the presence of constant nodal connectivity [10].

(a)   (b)   (c)
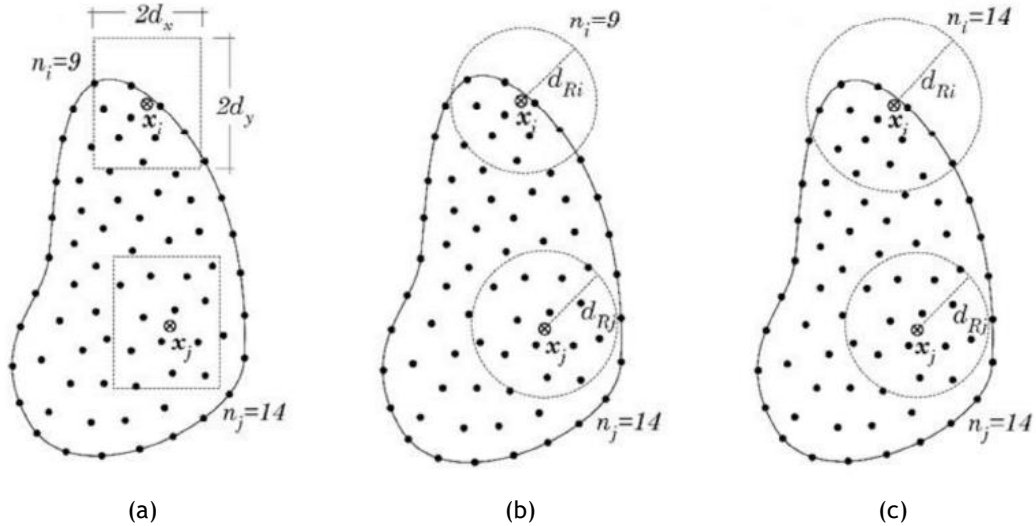
Figure 4.3 - Examples of different types of influence-domains: (a) influence-domain with fixed size and rectangular shape; (b) influence-domain with fixed size and circular shape; (c) influence-domain with variable size and circular shape [10].

4.2.2.2 - NNRPIM

In NNRPIM, the nodal connectivity employs the concept of natural neighbour, being obtained through the Voronoï diagram in the discrete domain [48]. This diagram is composed of Voronoï cells, in which a single node is identified [49].

The problem domain - $\Omega \subset \mathbb{R}^2$ - is circumscribed by a physical limit $\Gamma \in \Omega$. This domain is discretized in several arbitrarily distributed nodes - $N = \{n_0, n_1,..., n_N\} \in \mathbb{R}^2$ - which express the following coordinates: $X = \{x_0, x_1,... , x_N\}$, com $x_i \in \mathbb{R}^2$.

The Voronoï diagram of N constitutes the partition of the domain defined by Ω in closed and convex sub regions V_i. Each of these subregions V_i is associated with a node n_i. Thus, all points within V_i are closer to n_i than any other node, $n_j \in N \wedge i \neq j$. For $x_i \in \mathbb{R}^2$, the Voronoï cell is defined by [10]:

$$V_i := \{x_I \in \ \Omega \ \subset \mathbb{R}^2 : \|x_I - x_i\| \ < \|x_J - x_j\|, \quad \forall \, i \neq j\} \tag{4.1}$$

In which x_I corresponds to the interest point and $\|\cdot\|$ to the distance between the interest point and the nodes defined by the coordinates x_i and x_j [10].

The Voronoï diagram is determined by:

$$V = \{V_1, V_{2,\dots,} V_N\} \tag{4.2}$$

The Voronoï diagram is obtained through a similar process as shown in Figure 4.4 [10].

(a)

(b)

(c)

(d)

(e)

(f)
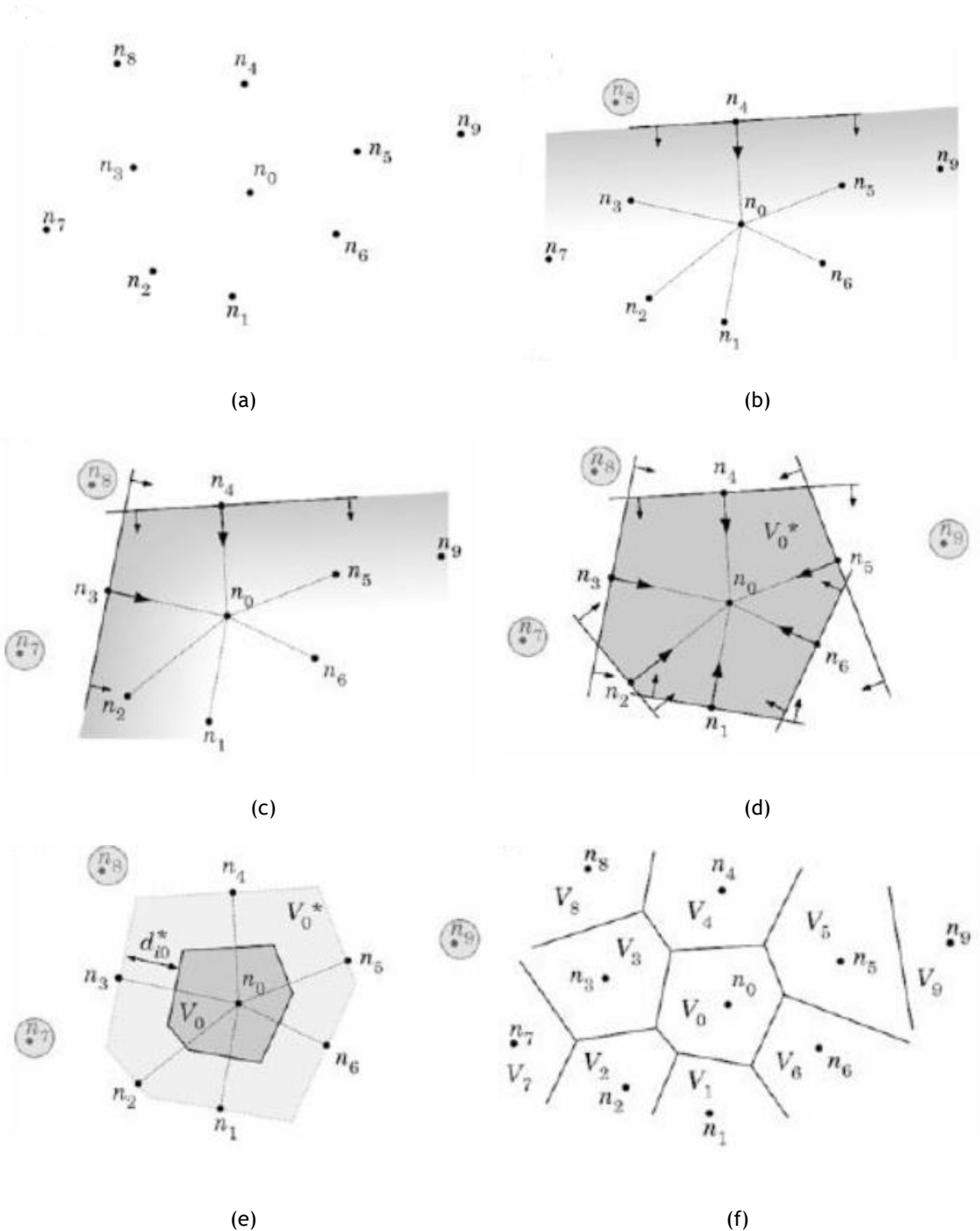
Figure 4.4 – (a) Initial node set; (b) first trial plane; (c) second trial plane; (d) provisional Voronoï cell; (e) Voronoï cell from node n_0; (f) Voronoï diagram [10].

In Figure 4.4(a) is presented a nodal set in a 2D dimension, demonstrating the process of determining the Voronoï cell of node n_0. First the neighbouring nodes are chosen [10]. All other nodes that were not included in this initial provisional selection are excluded, and one of the

selected nodes is then chosen as the potential neighbour, as is the case of node n_4 in Figure 4.4(b). Then the vector $\boldsymbol{u_{40}}$ is defined:

$$u_{40} = \frac{(x_0 - x_4)}{\|x_0 - x_4\|} \tag{4.3}$$

Where $\boldsymbol{u_{40}} = \{u_{40}, v_{40}, w_{40}\}$. Subsequently, a plane is established. Nodes that do not meet the following conditions are excluded:

$$u_{40}x + v_{40}y + w_{40}z \geq (u_{40}x_4 + v_{40}y_4 + w_{40}z_4) \tag{4.4}$$

This whole process is repeated for each node belonging to the initial set of nodes, as shown in Figure 4.4(c), to select the natural neighbours of node n_0. Thus, the provisional Voronoï cell is obtained, which is converted into a definitive one as shown in Figure 4.4(d) and Figure 4.4(e). The distance between node n_0 and the border of the Voronoï cell is given by:

$$d_{oi}^* = \frac{d_{oi}}{2} = \frac{\|x_0 - x_i\|}{2} \tag{4.5}$$

The other Voronoï cells are obtained through a similar process as shown in Figure 4.4(f) [10].

Thus, in NNRPIM is considered a new concept of nodal connectivity, influence-cell concept. These influence cells are built based on the Voronoï diagram and the nodal connectivity is effectively imposed by the overlap of the influence-cells. These cells are composed of n nodes capable of interpolating the point of interest [47].

There are two types of influence-cells. The first-degree influence-cells, represented in Figure 4.5(a), are established when a point of interest x_I begins to search the direct neighbouring nodes, following the Natural Neighbour Voronoï Construction. The second-degree influence-cells, shown in Figure 4.5(b), are established when a point of interest x_I searches neighbouring nodes similarly to first degree influence-cells and, then, taking into account the Voronoï diagram, the natural neighbours of the first neighbours of x_I are attached to the influence-cell [47]. As the size of the second degree influence-cell is superior to the size of the first degree influence-cell, it is expected that using second degree influence-cells allow to obtain more accurate approximations [10].

(a) (b)
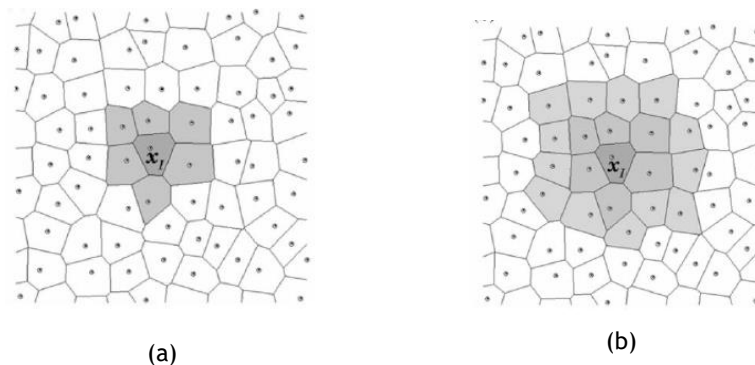
Figure 4.5 – (a) First-degree influence-cell; (b) Second-degree influence-cell [10].

4.2.3 - Numerical integration

4.2.3.1 - RPIM

For numerical integration, RPIM uses the Gauss-Legendre quadrature scheme. First, a background mesh is created. This background integration mesh can be built using integration cells fitted to the solid domain, as shown in Figure 4.6(a), or a blind regular grid, as shown in Figure 4.6(b). In the case of an integration mesh fitted to the solid domain no further treatment is required. However, if a blind regular grid is used, the integration points outside the solid domain have to be removed [10].

| (a) | (b) |
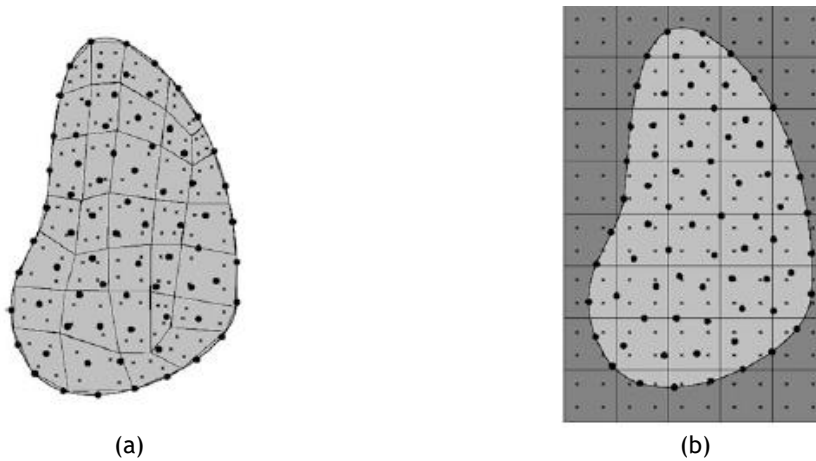
Figure 4.6 – (a) Fitted background mesh; (b) Regular grid integration mesh [10].

After setting the integration cells, each cell is filled with integration points, respecting the Gauss-Legendre quadrature rule. These same cells can be triangular or quadrilateral [10].

Following Figure 4.7, a cell in the grid is selected. This cell, which in this case is a quadrilateral, is transformed into an isoparametric square and the integration points are distributed in that same square. In the example a 2x2 square was used.

| (a) | (b) | (c) |
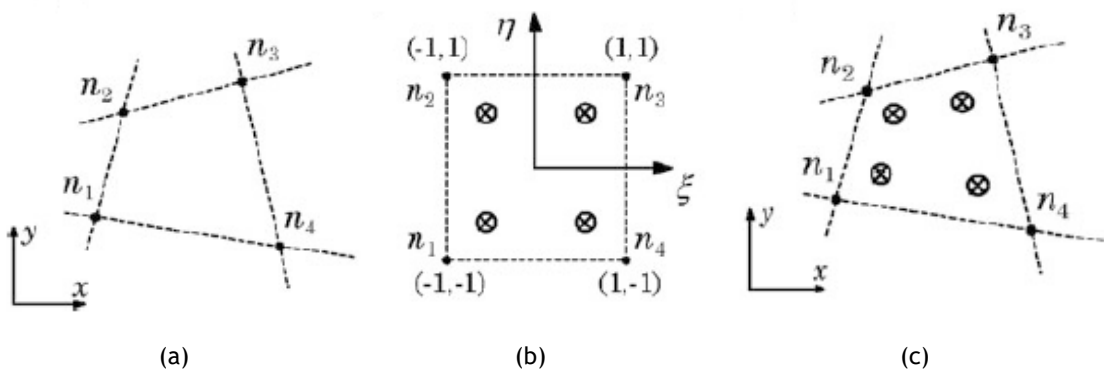
Figure 4.7 – (a) Initial grid-cell; (b) Isoparametric square with integration points; (c) Initial quadrature cell with integration points [10].

Then, the Cartesian coordinates of the quadrature points are obtained using isoparametric interpolation functions, N_i, for quadrilaterals:

$$N_1(\xi,\eta) = \frac{1}{4}(1-\xi)(1-\eta)$$
$$N_2(\xi,\eta) = \frac{1}{4}(1-\xi)(1+\eta)$$
$$N_3(\xi,\eta) = \frac{1}{4}(1+\xi)(1+\eta)$$
$$N_4(\xi,\eta) = \frac{1}{4}(1+\xi)(1-\eta)$$

(4.6)

Or for triangles:

$$N_1(\xi,\eta) = 1 - \xi - \eta$$
$$N_2(\xi,\eta) = \eta$$
$$N_3(\xi,\eta) = \xi$$

(4.7)

The Cartesian coordinates are given by:

$$x = \sum_{i=1}^{m} N_i(\xi,\eta) \cdot x_i$$
$$y = \sum_{i=1}^{m} N_i(\xi,\eta) \cdot y_i$$

(4.8)

In which, m represents the number of nodes inside the grid-cell and x_i and y_i the Cartesian coordinates of the nodes that defined the integration cell.

The integration weight of the quadrature point is obtained by multiplying the isoparametric weight of the quadrature point with the Jacobian matrix determinant of the respective grid-cell:

$$[J] = \begin{bmatrix} \dfrac{\partial x}{\partial \xi} & \dfrac{\partial x}{\partial \eta} \\ \dfrac{\partial y}{\partial \xi} & \dfrac{\partial y}{\partial \eta} \end{bmatrix}$$

(4.9)

The tables presented next give the location and the weights of the isoparametric integration points for quadrilaterals and triangles:

Table 4.1 – Integration points and corresponding weights for quadrilaterals isoparametric cells.
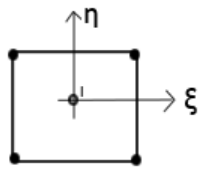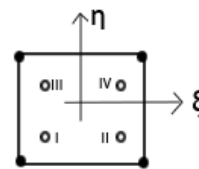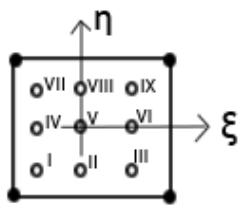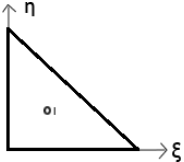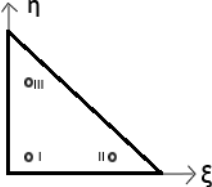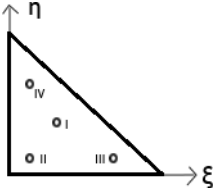
Gauss-Legendre Point	ξ	η	Weight
I	0	0	4
I	$-\dfrac{1}{\sqrt{3}}$	$-\dfrac{1}{\sqrt{3}}$	1
II	$+\dfrac{1}{\sqrt{3}}$	$-\dfrac{1}{\sqrt{3}}$	1
III	$-\dfrac{1}{\sqrt{3}}$	$+\dfrac{1}{\sqrt{3}}$	1
IV	$+\dfrac{1}{\sqrt{3}}$	$+\dfrac{1}{\sqrt{3}}$	1
I	$-\sqrt{\dfrac{3}{5}}$	$-\sqrt{\dfrac{3}{5}}$	$\dfrac{25}{81}$
II	0	$-\sqrt{\dfrac{3}{5}}$	$\dfrac{40}{81}$
III	$+\sqrt{\dfrac{3}{5}}$	$-\sqrt{\dfrac{3}{5}}$	$\dfrac{25}{81}$
IV	$-\sqrt{\dfrac{3}{5}}$	0	$\dfrac{40}{81}$
V	0	0	$\dfrac{25}{81}$
VI	$+\sqrt{\dfrac{3}{5}}$	0	$\dfrac{40}{81}$
VII	$-\sqrt{\dfrac{3}{5}}$	$+\sqrt{\dfrac{3}{5}}$	$\dfrac{25}{81}$
VIII	0	$+\sqrt{\dfrac{3}{5}}$	$\dfrac{40}{81}$
IX	$+\sqrt{\dfrac{3}{5}}$	$+\sqrt{\dfrac{3}{5}}$	$\dfrac{25}{81}$

Table 4.2 - Integration points and corresponding weights for triangles isoparametric cells.

Gauss-Legendre Points	ξ	η	Weight	
I	$\dfrac{1}{3}$	$\dfrac{1}{3}$	$\dfrac{1}{2}$	
I	$\dfrac{1}{6}$	$\dfrac{1}{6}$	$\dfrac{1}{6}$	
II	$\dfrac{2}{3}$	$\dfrac{1}{6}$	$\dfrac{1}{6}$	
III	$\dfrac{1}{6}$	$\dfrac{2}{3}$	$\dfrac{1}{6}$	
I	$\dfrac{1}{3}$	$\dfrac{1}{3}$	$-\dfrac{27}{96}$	
II	$\dfrac{1}{5}$	$\dfrac{1}{5}$	$\dfrac{25}{96}$	
III	$\dfrac{3}{5}$	$\dfrac{1}{5}$	$\dfrac{25}{96}$	
IV	$\dfrac{1}{5}$	$\dfrac{3}{5}$	$\dfrac{25}{96}$	

4.2.3.2 - NNRPIM

NNRPIM also uses the Galerkin weak form, therefore a background integration mesh is likewise required. As there is no information beyond the spatial location of each node that discretizes the problem domain, it is necessary to establish: nodal connectivity, integration points and shape functions. Through the construction of the Voronoï diagram is possible to obtain an integration mesh that is defined considering the nodal distribution [10,47].

Thus, the area of each Voronoï cell is subdivided into several sub-areas using the Delaunay triangulation, shown in Figure 4.8 [10].

(a) (b)
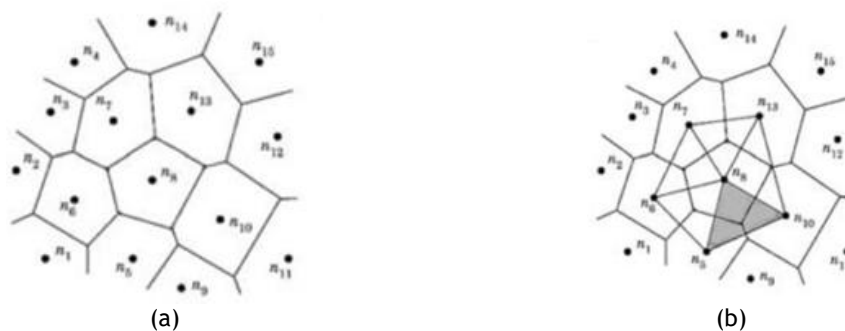
Figure 4.8 – (a) Initial Voronoï diagram; (b) Delaunay triangulation [10].

In the Voronoï cell are identified the corners of the polygon, P_{Ii}, and the middle points, M_{Ii}, between n_I and each neighbour node n_i are determined, like is demonstrated in Figure 4.9. Thus, the Voronoï cells are divided into k quadrilateral sub-cells, S_{Ii}. The number of quadrilateral sub-cells created is equal to the number of natural neighbours of node n_I.
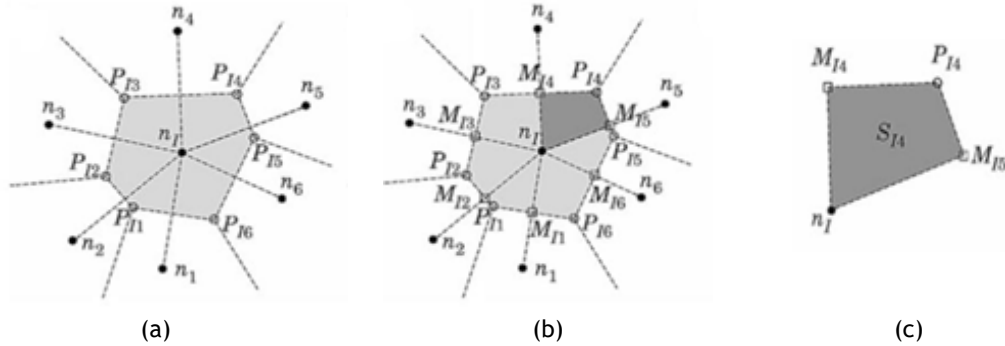
Figure 4.9 – (a) Voronoï cell and respective intersection points, P_{Ii}; (b) Middle points, M_{Ii}, and the respective generated quadrilaterals; (c) Quadrilateral [10].

If the N nodes are distributed in an irregular way, the sub-cells created are quadrilateral, however if the nodes are distributed in a regular way, then the sub-cells will have a triangular shape, like shown in Figure 4.10.
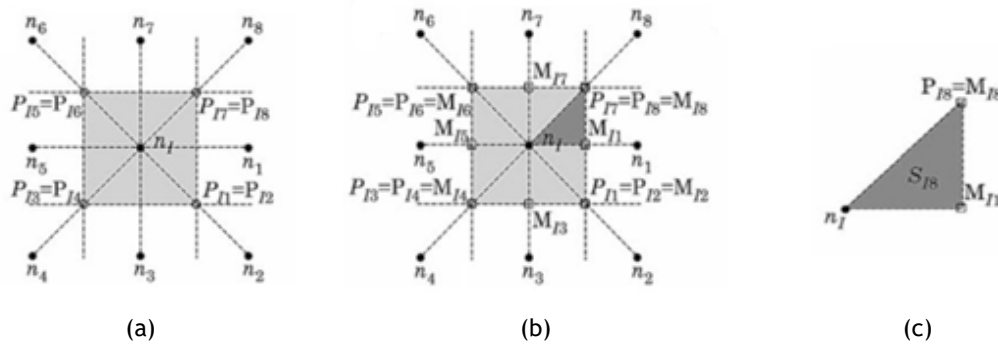
Figure 4.10 – (a) Voronoï cell and respective intersection points, P_{Ii}; (b) Middle points, M_{Ii}, and the respective generated triangles; (c) Triangle [10].

Therefore, the Voronoï cell area of interest point x_I, A_{V_I}, is divided into k sub-cells S_{Ii}, each with an area $A_{S_{Ii}}$. Hence, the area of the Voronoï cell is equal to the sum of the area of each sub-cell, as indicated by the equation:

$$A_{V_I} = \sum_{i=1}^{k} A_{S_{Ii}}, \quad \forall_{A_{S_{Ii}}} \geq 0 \tag{4.10}$$

It is known that the Voronoï cell set is a partition, without gaps, of the domain. In this sense, the same can be asserted for the set of sub-cells. Numerical integration is then performed using the Gauss-Legendre numerical integration [47].

To obtain the simplest integration scheme, using triangular and quadrilateral sub-cells, a single point is placed in the centre of each of the sub-cells. Then, the spatial location of each

integration point is determined in each sub-cell as shown in Figure 4.11. In this case, the integration weight is the area of the corresponding sub-cell.
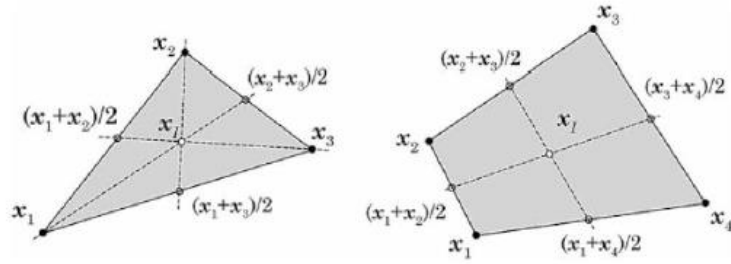
Figure 4.11 - Triangular and quadrilateral shapes and the respective integration points [10].

However, it is possible to add more integration points, for which the previously obtained sub-cells are again divided, through the crossing of the centre point, already determined, with the middle points of the edges of the sub-cell considered. This process is illustrated in Figure 4.12. The formed cells are then quadrilateral, and the Gauss-Legendre numerical integration is applied to the formed sub-quadrilaterals to obtain the integration points [47].
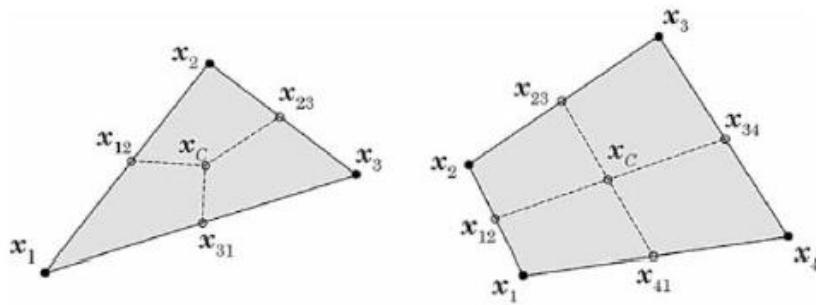
Figure 4.12 - Division in quadrilaterals of the sub-cells [10].

In Figure 4.13 different integration schemes are presented for the triangular and quadrilateral subcells.

The background integration mesh that discretizes the problem domain is then defined by repeating the above process for the Voronoï cells, N, which constitute the Voronoï diagram.
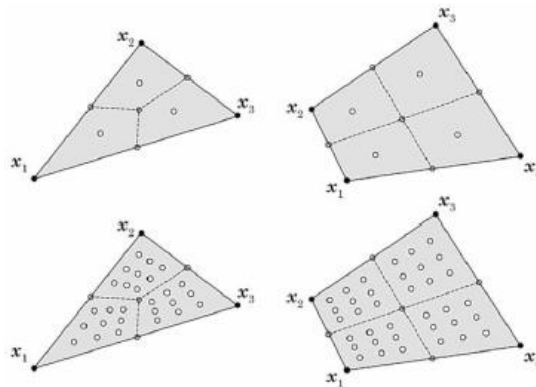
Figure 4.13 - Triangular and rectangular shape and respective integration points, x_I, using the Gauss-Legendre integration scheme [10].

In the context of this work only one integration point will be included by sub-area, $A_{S_{Ii}}$. Several published studies found in the literature on NNRPIM demonstrate that the use of an integration point by sub-area $A_{S_{Ii}}$ is sufficient to accurately integrate integral-differential equations [47,49].

For 2D and 3D nodal meshes a detailed description of the implementation of nodal connectivity and the construction of the integration mesh is presented in the work [47].

4.2.4 - Interpolation functions

As previously mentioned, in meshless methods, the problem domain is discretized in a nodal mesh, which may have a regular or irregular distribution. Due to the absence of elements and to facilitate the construction of the shape functions, it is necessary to apply an interpolation method based on the local nodal domain [10].

Both RPIM and NNRPIM use the same procedure for interpolation functions, using the RPI technique [50], combining RBF and polynomial base functions.

The interpolation functions considering both methods, RPIM and NNRPIM, possess the delta Kronecker property:

$$\varphi_i(x_j) = \delta_{ij} \tag{4.11}$$

Where δ_{ij} is the delta Kronecker, for which δ_{ij}=1 if $i = j$ and δ_{ij}=0 if $i \neq j$. Thus, this property allows to use direct imposition techniques to numerically apply the essential boundary conditions in the stiffness matrix.

Considering a function $u(x_I)$ defined in the domain Ω, which is discretized by a set of n nodes. It is assumed that only the nodes within the influence-cell of the point of interest considered have an effect on $u(x_I)$. The value of the function $u(x_I)$, defined in the domain $\Omega \subset \mathbb{R}^2$, at the point of interest x_I, is given by the following expression:

$$u(x_I) = \sum_{i=1}^{n} R_i(x_I) \cdot a_i(x_I) + \sum_{j=1}^{m} p_j(x_I) \cdot b_j(x_I) = \{R(x_I)^T, p(x_I)^T\} \begin{Bmatrix} a(x_I) \\ b(x_I) \end{Bmatrix} \tag{4.12}$$

Where $R_i(x_I)$ is the RBF, n the number of nodes inside the influence-cell of x_I, $p_j(x_I)$ is the polynomial function and $a_i(x_I)$ and $b_j(x_I)$ are the constant coefficients associated with the respective functions mentioned [49].

Normally, $m < n$ to guarantee a stable function.

The vectors in equation (4.12) can be represented as:

$$R(x_I) = \{R_1(x_I), R_2(x_I), \dots R_n(x_I)\}^T$$
$$P(x_I) = \{p_1(x_I), p_2(x_I), \dots p_m(x_I)\}^T$$
$$a(x_I) = \{a_1(x_I), a_2(x_I), \dots a_n(x_I)\}^T \tag{4.13}$$
$$b(x_I) = \{b_1(x_I), b_2(x_I), \dots b_m(x_I)\}^T$$

The distance between the relevant node x_I and the neighbour node x_i corresponds to the variable established in the RBF, given by r_{Ii}=$\|x_i - x_I\|$. Several RBFs were studied and developed

in [51], being the most common the Multiquadrics (MQ) functions, initially proposed by Hardy [51]. The general formulation of MQ-RBF is:

$$R(r_{Ii}) = (r_{Ii}^2 + c^2)^p \tag{4.14}$$

Where c and p are two parameters that take a value close to 0 and 1, respectively, to obtain accurate results [10]. The non-constant coefficients a and b need to be determined. The polynomial basis functions used have the following monomial term as:

$$\boldsymbol{p}(\mathbf{x})^T = [1, x, y, x^2, xy, y^2, \dots] \tag{4.15}$$

Having in consideration equation (4.12) for each node inside the influence-cell and admitting an extra equation, $\sum_{i=1}^{n} p_j(x_i)a_i(x_i) = 0$, to guarantee a unique solution [47], a system of equations is obtained:

$$\begin{bmatrix} \boldsymbol{u}_s \\ 0 \end{bmatrix} = \begin{bmatrix} \boldsymbol{R} & \boldsymbol{P} \\ \boldsymbol{P}^T & 0 \end{bmatrix} \begin{Bmatrix} \boldsymbol{a} \\ \boldsymbol{b} \end{Bmatrix} = \boldsymbol{M} \begin{Bmatrix} \boldsymbol{a} \\ \boldsymbol{b} \end{Bmatrix} \tag{4.16}$$

Where:

$$\boldsymbol{u}_s = \{u_1, u_2, \dots u_n\}^T \tag{4.17}$$

$$\boldsymbol{R} = \begin{bmatrix} R(r_{11}) & R(r_{21}) & \cdots & R(r_{1n}) \\ R(r_{21}) & R(r_{22}) & \cdots & R(r_{2n}) \\ \vdots & \vdots & & \vdots \\ R(r_{n1}) & R(r_{n2}) & \cdots & R(r_{nm}) \end{bmatrix} \tag{4.18}$$

The constant polynomial basis is defined as:

$$\boldsymbol{P} = \begin{bmatrix} 1 & 1 & \cdots & 1 \end{bmatrix}^T \tag{4.19}$$

For the 2D problem, the polynomial basis is represented as:

$$\boldsymbol{P} = \begin{bmatrix} 1 & 1 & \cdots & 1 \\ x_1 & x_2 & \cdots & x_n \\ y_1 & y_2 & \cdots & y_n \end{bmatrix}^T \tag{4.20}$$

Notice that is a 3D problem, the polynomial function can be expressed as:

$$\boldsymbol{P} = \begin{bmatrix} 1 & 1 & \cdots & 1 \\ x_1 & x_2 & \cdots & x_n \\ y_1 & y_2 & \cdots & y_n \\ z_1 & z_2 & \cdots & z_n \end{bmatrix}^T \tag{4.21}$$

Therefore, is possible to determine the non-constant coefficients a and b with the following equation:

$$\begin{Bmatrix} a \\ b \end{Bmatrix} = \begin{bmatrix} R & P \\ P^T & 0 \end{bmatrix}^{-1} \begin{Bmatrix} u_s \\ 0 \end{Bmatrix} \Rightarrow \begin{Bmatrix} a \\ b \end{Bmatrix} = M^{-1} \begin{Bmatrix} u_s \\ 0 \end{Bmatrix} \tag{4.22}$$

Replacing in equation (4.12):

$$u(x_I) = \{R(x_I)^T \; p(x_I)^T\} \, M^{-1} \begin{Bmatrix} u_s \\ 0 \end{Bmatrix} = \varphi(x_I) \begin{Bmatrix} u_s \\ 0 \end{Bmatrix} \tag{4.23}$$

Lastly, the interpolation function in the interest point, $\varphi(x_I)$, can be determined using:

$$\varphi(x_I) = \{R(x_I)^T, p(x_I)^T\} \, M^{-1} = \{ \varphi_1(x_I), \varphi_2(x_I), \dots, \varphi_n(x_I)\} \tag{4.24}$$

In the literature is possible to find studies about the construction and the most important properties of the RPI functions [50,47].

Chapter 5

Solid mechanics

Solid Mechanics is based on the study of deformations and relative displacements of solids, under the action of forces or loads. Thus, the main objective of this field of study is to understand the relationship between stress and strain and the relationship between strain and displacements [10].

It is known that different applied loads will give rise to different behaviours. Therefore, in this chapter, the concepts of stress and strain are presented, explaining the considered equilibrium and the constitutive equations [10].

5.1 - Fundamentals

Considering the configuration of the structure of each solid material as well as its characteristics, it is possible to predict the behaviour of each solid through its stress-strain curve.

In this work, for the initial studies the solids were considered linear-elastic, i.e., the relationship between stress and strain is assumed to be linear. In this case, after removal of the applied load, the solid returns to its initial form. Another important feature is that this study assumes a static nature, which means that only static loads were considered and applied. This indicates that the stresses, deformations and displacements obtained are not time dependent.

The materials can be classified into two types: isotropic and anisotropic. The former has different properties in each direction. Thus, the deformation caused by a load applied in one direction is not the same as that caused by the same load, but in a different direction. In the case of isotropic materials, only two independent material properties are required, Young's Modulus (E) and Poisson ratio (v) [10].

Therefore, when the deformation is analysed, the consequent change in the configuration of the solid body is defined by the stress and strain, being necessary to ensure that stress tensor and strain tensor, are referred in the same deformed state. The symmetric tensor of the Cauchy stresses represents the stresses of a current configuration. For a three-dimensional problem, the stress state is defined as:

$$\Lambda = \begin{bmatrix} \sigma_{xx} & \tau_{xy} & \tau_{xz} \\ \tau_{yx} & \sigma_{yy} & \tau_{yz} \\ \tau_{zx} & \tau_{zy} & \sigma_{zz} \end{bmatrix} \tag{5.1}$$

Voigt notation expresses tensors in column vectors, reducing their order. Therefore, the stress tensor, (5.1), is transformed into stress vector, $\boldsymbol{\sigma}$:

$$\boldsymbol{\sigma} = \{\sigma_{xx} \quad \sigma_{yy} \quad \sigma_{zz} \quad \tau_{xy} \quad \tau_{yz} \quad \tau_{zx}\}^T \tag{5.2}$$

Stress can be divided into two components, the normal stress, which is perpendicular to the plane in question, indicated by the letter σ and the shear stress, which is tangential to the plane in which it acts, denoted by the letter τ [52].

The strain tensor $\boldsymbol{E}$ is reduced to the strain vector $\boldsymbol{\varepsilon}$:

$$\boldsymbol{\varepsilon} = \{\varepsilon_{xx} \quad \varepsilon_{yy} \quad \varepsilon_{zz} \quad \gamma_{xy} \quad \gamma_{yz} \quad \gamma_{zx}\}^T \tag{5.3}$$

As previously stated, solids have two types of behaviour. In isotropic materials, the relation between stress and strain of a solid domain is given by the following constitutive equation, denominated Hooke's Law:

$$\boldsymbol{\sigma} = \boldsymbol{c}\boldsymbol{\varepsilon} \tag{5.4}$$

In which $\boldsymbol{c}$ is the constitutive matrix, given by $\boldsymbol{c} = \boldsymbol{s}^{-1}$, being $\boldsymbol{s}$ the compliance elasticity matrix. For 3D cases, considering anisotropic materials, in a plane stress formulation, $\boldsymbol{s}$ can be expressed as:

$$\boldsymbol{s} = \begin{bmatrix} \dfrac{1}{E_{xx}} & -\dfrac{v_{yx}}{E_{yy}} & -\dfrac{v_{zx}}{E_{zz}} & 0 & 0 & 0 \\ -\dfrac{v_{yx}}{E_{xx}} & \dfrac{1}{E_{yy}} & -\dfrac{v_{zy}}{E_{zz}} & 0 & 0 & 0 \\ -\dfrac{v_{xz}}{E_{xx}} & -\dfrac{v_{yz}}{E_{yy}} & \dfrac{1}{E_{zz}} & 0 & 0 & 0 \\ 0 & 0 & 0 & \dfrac{1}{G_{xy}} & 0 & 0 \\ 0 & 0 & 0 & 0 & \dfrac{1}{G_{yz}} & 0 \\ 0 & 0 & 0 & 0 & 0 & \dfrac{1}{G_{zx}} \end{bmatrix} \tag{5.5}$$

Where E_{ii} corresponds to Young's modulus, v_{ij} is the Poisson ratio and G_{ij} is the distortion modulus of the material in direction i and j.

Considering the following displacements field, for each point of the solid:

$$\boldsymbol{u}\,(x,y,z) = \begin{Bmatrix} u(x,y,z) \\ v(x,y,z) \\ w(x,y,z) \end{Bmatrix} \tag{5.6}$$

The strain components can be calculated with the following expressions:

$$\begin{Bmatrix} \varepsilon_{xx} \\ \varepsilon_{yy} \\ \varepsilon_{zz} \\ \gamma_{xy} \\ \gamma_{xz} \\ \gamma_{yz} \end{Bmatrix} = \begin{Bmatrix} \dfrac{\partial u}{\partial x} \\ \dfrac{\partial v}{\partial y} \\ \dfrac{\partial w}{\partial z} \\ \dfrac{\partial v}{\partial x} + \dfrac{\partial u}{\partial y} \\ \dfrac{\partial w}{\partial x} + \dfrac{\partial u}{\partial z} \\ \dfrac{\partial w}{\partial y} + \dfrac{\partial v}{\partial z} \end{Bmatrix} \tag{5.7}$$

As in stress, strain is also represented by two types. The letter ε represents the normal strain representing the relative change of length of a certain line segment. The shear strain is represented by the letter γ, which represents the change in angle of two previously perpendicular line segments [52].

The strain vector can be obtained through the combination of a partial differential operator and the displacements field, $\boldsymbol{u}$:

$$\boldsymbol{\varepsilon} = \boldsymbol{Lu} \tag{5.8}$$

Where $\boldsymbol{L}$ is given by:

$$\boldsymbol{L} = \begin{bmatrix} \dfrac{\partial}{\partial x} & 0 & 0 & \dfrac{\partial}{\partial y} & 0 & \dfrac{\partial}{\partial z} \\ 0 & \dfrac{\partial}{\partial y} & 0 & \dfrac{\partial}{\partial x} & \dfrac{\partial}{\partial z} & 0 \\ 0 & 0 & \dfrac{\partial}{\partial z} & 0 & \dfrac{\partial}{\partial y} & \dfrac{\partial}{\partial x} \end{bmatrix}^{T} \tag{5.9}$$

Considering an infinitesimal element, the equilibrium equations for a 3D example are obtained:

$$\frac{\partial \sigma_{xx}}{\partial x} + \frac{\partial \tau_{xy}}{\partial y} + \frac{\partial \tau_{xz}}{\partial z} + F_x = 0$$
$$\frac{\partial \tau_{yx}}{\partial x} + \frac{\partial \sigma_{yy}}{\partial y} + \frac{\partial \tau_{yz}}{\partial z} + F_y = 0 \tag{5.10}$$
$$\frac{\partial \tau_{zx}}{\partial x} + \frac{\partial \tau_{zy}}{\partial y} + \frac{\partial \sigma_{zz}}{\partial z} + F_z = 0$$

In which F_x, F_y and F_z correspond to the body forces in x, y and z directions, respectively.

5.2 - Strong form and weak form

The system of partial differential equations governing a physical phenomenon can be defined as strong form equations. This formulation allows to obtain the exact solution,

however, it has some limitations. Solving this type of equation is often a rather difficult task, particularly in problems of more complex engineering geometry.

Thus, the weak form based on a discrete system of equations is established, being stated for each integration point. Although it presents a lower consistency, it has the capacity to produce equations of more stable algebraic systems [10].

5.2.1 - Galerkin weak form

In this work, the system of discrete equations is obtained by applying the Galerkin weak form, a variational method based on energy minimization.

Considering a body in a domain Ω and bounded by Γ, where $\Gamma \in \Omega \colon \Gamma_u \cup \Gamma_t = \Gamma \wedge \Gamma_u \cap \Gamma_t = \phi$, in which Γ_u corresponds to the essential boundary conditions and Γ_t to the natural boundary conditions. The external forces $\bar{t}$ are applied to the surface of the body where the natural boundary conditions are applied, and the displacements are constrained on the surface where the essential boundary conditions are applied, as shown in Figure 5.1.
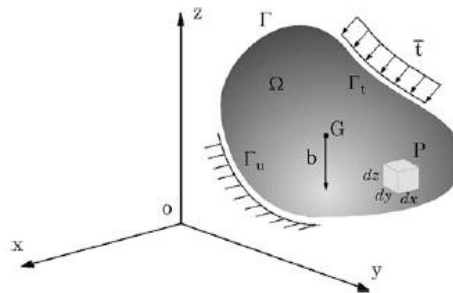
Figure 5.1 – Continuous solid subject to volume forces and external forces [10].

The equilibrium equations that govern the linear elasto-static problem are established as follows:

$$\nabla \mathbf{\Lambda} + \mathbf{b} = 0 \tag{5.11}$$

In which, ∇ is the nabla operator, $\mathbf{b}$ is the body force per volume unit and $\mathbf{\Lambda}$ is the Cauchy stress tensor, already referred previously. The natural boundary follows a condition - $\nabla \mathrm{n} = \bar{t}$ in Γ_t – and the essential boundary follows another condition - $\mathrm{u} = \bar{u}$ in Γ_u, where $\bar{u}$ corresponds to the displacement imposed at the essential boundary Γ_u.

Resorting to Galerkin weak form, the real solution is the one that minimizes the Langrangian functional, established by:

$$L = T - U - W_f \tag{5.12}$$

Where T corresponds to kinetic energy, U corresponds to strain energy and W_f is the work produced by the external forces. Kinetic energy T is defined as:

$$T = \frac{1}{2} \int_\Omega \rho \dot{\boldsymbol{u}}^T \dot{\boldsymbol{u}} \, d\Omega \tag{5.13}$$

Where Ω represents the solid volume, $\dot{\boldsymbol{u}}$ is the first derivative of displacement with respect to time and ρ is solid mass density. For elastic materials, the strain energy is given by:

$$U = \frac{1}{2} \int_{\Omega} \boldsymbol{\varepsilon}^T \boldsymbol{\sigma} \, d\Omega \tag{5.14}$$

Where $\boldsymbol{\varepsilon}$ is the strain vector and $\boldsymbol{\sigma}$ is the stress vector. The work performed by external forces is represented by:

$$W_f = \int_{\Omega} \boldsymbol{u}^T \boldsymbol{b} \, d\Omega + \int_{\Gamma_t} \boldsymbol{u}^T \bar{\boldsymbol{t}} \, d\Gamma_t \tag{5.15}$$

Where $\boldsymbol{u}$ correspond to displacement, $\boldsymbol{b}$ is the body forces and Γ_t is the traction boundary where forces $\bar{\boldsymbol{t}}$ are applied. Therefore, Galerkin weak form is expressed as:

$$L = \frac{1}{2} \int_{\Omega} \rho \dot{\boldsymbol{u}}^T \dot{\boldsymbol{u}} \, d\Omega - \frac{1}{2} \int_{\Omega} \boldsymbol{\varepsilon}^T \boldsymbol{\sigma} \, d\Omega + \int_{\Omega} \boldsymbol{u}^T \boldsymbol{b} \, d\Omega + \int_{\Gamma_t} \boldsymbol{u}^T \bar{\boldsymbol{t}} \, d\Gamma_t \tag{5.16}$$

Equation (5.16) can be minimized:

$$\delta \int_{t_1}^{t_2} \left[\frac{1}{2} \int_{\Omega} \rho \dot{\boldsymbol{u}}^T \dot{\boldsymbol{u}} d\Omega - \frac{1}{2} \int_{\Omega} \boldsymbol{\varepsilon}^T \boldsymbol{\sigma} d\Omega + \int_{\Omega} \boldsymbol{u}^T \boldsymbol{b} d\Omega + \int_{\Gamma_t} \boldsymbol{u}^T \bar{\boldsymbol{t}} d\Gamma_t \right] dt = 0 \tag{5.17}$$

Moving the variation operator δ inside the integrals:

$$\int_{t_1}^{t_2} \left[\frac{1}{2} \int_{\Omega} \delta(\rho \dot{\boldsymbol{u}}^T \dot{\boldsymbol{u}}) d\Omega - \frac{1}{2} \int_{\Omega} \delta(\boldsymbol{\varepsilon}^T \boldsymbol{\sigma}) \, d\Omega + \int_{\Omega} \delta \boldsymbol{u}^T \boldsymbol{b} \, d\Omega + \int_{\Gamma_t} \delta \boldsymbol{u}^T \bar{\boldsymbol{t}} \, d\Gamma_t \right] dt = 0 \tag{5.18}$$

The function integrated in the second integral can also be represented as:

$$\delta(\boldsymbol{\varepsilon}^T \boldsymbol{\sigma}) = \delta \boldsymbol{\varepsilon}^T \boldsymbol{\sigma} + \boldsymbol{\varepsilon}^T \delta \boldsymbol{\sigma} \tag{5.19}$$

In which $\boldsymbol{\varepsilon}^T \delta \boldsymbol{\sigma} = (\boldsymbol{\varepsilon}^T \delta \boldsymbol{\sigma})^T = \delta \boldsymbol{\sigma}^T \boldsymbol{\varepsilon}$. Using Hooke´s law and the symmetry property of material matrix, $\boldsymbol{c}^T = \boldsymbol{c}$, is possible to obtain:

$$\delta \boldsymbol{\sigma}^T \boldsymbol{\varepsilon} = \delta(\boldsymbol{c}\boldsymbol{\varepsilon})^T \boldsymbol{\varepsilon} = \delta \boldsymbol{\varepsilon}^T \boldsymbol{c}^T \boldsymbol{\varepsilon} = \delta \boldsymbol{\varepsilon}^T \boldsymbol{c} \boldsymbol{\varepsilon} = \delta \boldsymbol{\varepsilon}^T \boldsymbol{\sigma} \tag{5.20}$$

Therefore, equation (5.19) is replaced with:

$$\delta(\boldsymbol{\varepsilon}^T \boldsymbol{\sigma}) = 2\delta \boldsymbol{\varepsilon}^T \boldsymbol{\sigma} \tag{5.21}$$

And so, equation (5.18) can be expressed as:

$$-\rho \int_{\Omega} (\delta \boldsymbol{u}^T \ddot{\boldsymbol{u}}) d\Omega - \int_{\Omega} \delta \boldsymbol{\varepsilon}^T \boldsymbol{\sigma} \, d\Omega + \int_{\Omega} \delta \boldsymbol{u}^T \boldsymbol{b} \, d\Omega + \int_{\Gamma_t} \delta \boldsymbol{u}^T \bar{\boldsymbol{t}} \, d\Gamma_t = 0 \tag{5.22}$$

Considering stress-strain relation, $\boldsymbol{\sigma} = \boldsymbol{c\varepsilon}$, and strain-displacement relation, $\boldsymbol{\varepsilon} = \boldsymbol{Lu}$, equation (5.22) can be defined as:

$$\int_\Omega (\delta \boldsymbol{Lu})^T \boldsymbol{c}(\boldsymbol{Lu})d\Omega - \int_\Omega \delta \boldsymbol{u}^T \boldsymbol{b}\, d\Omega - \int_{\Gamma_t} \delta \boldsymbol{u}^T \bar{\boldsymbol{t}}\, d\Gamma_t + \int_\Omega \rho(\delta \boldsymbol{u}^T \ddot{\boldsymbol{u}})d\Omega = 0 \tag{5.23}$$

Which corresponds to Galerkin weak form, described in terms of displacement, which is helpful for solid mechanical problems. In static problems, the fourth term of equation (5.23) is removed.

5.3 - Discrete equation system

The discrete equation system for meshless methods is obtained based on the principle of virtual work. The field variables can be obtained through interpolation functions, already mentioned in section 4.2.4. For a 3D case, the field of displacements $\boldsymbol{u}$ can be obtained at an integration point $\boldsymbol{x}_I$ by the following equation:

$$u(\boldsymbol{x}_I) = \sum_{i=1}^{n} \varphi_i(\boldsymbol{x}_I)u(\boldsymbol{x}_i) \tag{5.24}$$

Where $\varphi_i(\boldsymbol{x}_I)$ is the meshless approximation or interpolation function and $u(\boldsymbol{x}_i)$ is the nodal displacement vector of n nodes belonging to the influence-domain of integration point $\boldsymbol{x}_I$.

Interpolated virtual displacement is obtained using test (shape) functions,

$$\delta u(\boldsymbol{x}_I) = \sum_{i=1}^{n} \varphi_i(\boldsymbol{x}_I)\delta u_i \tag{5.25}$$

Where $\delta u_i = \delta u(\boldsymbol{x}_i)$ is the nodal virtual displacements.

Combining equation (5.23) with (5.25):

$$\int_\Omega \boldsymbol{L}\left(\sum_{i=1}^{n} \varphi_i(\boldsymbol{x}_I)\delta u_i\right)^T \boldsymbol{cL}\left(\sum_{i=1}^{n} \varphi_i(\boldsymbol{x}_I)u_i\right)d\Omega$$
$$- \int_\Omega \left(\sum_{i=1}^{n} \varphi_i(\boldsymbol{x}_I)\delta u_i\right)^T \boldsymbol{b}\, d\Omega - \int_{\Gamma_t} \left(\sum_{i=1}^{n} \varphi_i(\boldsymbol{x}_I)\delta u_i\right)^T \bar{\boldsymbol{t}}\, d\Gamma = 0 \tag{5.26}$$

The previous equation can be rewritten as a matrix equation. Considering that it is possible to define the matrix of approximation/interpolation functions for the point of interest $\boldsymbol{x}_I$ as:

$$\boldsymbol{H}(\boldsymbol{x}_I) = \begin{bmatrix} \varphi_1(\boldsymbol{x}_I) & 0 & 0 & \varphi_2(\boldsymbol{x}_I) & 0 & 0 & \cdots & \varphi_n(\boldsymbol{x}_I) & 0 & 0 \\ 0 & \varphi_1(\boldsymbol{x}_I) & 0 & 0 & \varphi_2(\boldsymbol{x}_I) & 0 & \cdots & 0 & \varphi_n(\boldsymbol{x}_I) & 0 \\ 0 & 0 & \varphi_1(\boldsymbol{x}_I) & 0 & 0 & \varphi_2(\boldsymbol{x}_I) & \cdots & 0 & 0 & \varphi_n(\boldsymbol{x}_I) \end{bmatrix} \tag{5.27}$$

Equation (5.26) can now be rewritten as follows:

$$\delta \boldsymbol{u}^T \int_\Omega \left[(\boldsymbol{H}(\boldsymbol{x_I}))^T \boldsymbol{L}^T \right] \boldsymbol{c}[\boldsymbol{LH}(\boldsymbol{x_I})] d\Omega \boldsymbol{u} - \delta \boldsymbol{u}^T \int_\Omega (\boldsymbol{H}(\boldsymbol{x_I}))^T \boldsymbol{b} \, d\Omega - \delta \boldsymbol{u}^T \int_{\Gamma^t} (\boldsymbol{H}(\boldsymbol{x_I}))^T \bar{\boldsymbol{t}} \, d\Gamma = 0 \qquad (5.28)$$

Considering $\boldsymbol{u}$ as the nodal displacement vector of all n nodes inside the influence-domain, it can be written:

$$\boldsymbol{u} = \{u_1, v_1, w_1, u_2, v_2, w_2 \dots u_n, v_n, w_n\}^T \qquad (5.29)$$

Remembering the partial differential operator matrix $\boldsymbol{L}$, the deformability matrix $\boldsymbol{B}(\boldsymbol{x_I})$ can be defined, for the interest point $\boldsymbol{x_I}$, as the multiplication between $\boldsymbol{L}$ and $\boldsymbol{H}(\boldsymbol{x_I})$:

$$\boldsymbol{B}(\boldsymbol{x_I}) = \boldsymbol{LH}(\boldsymbol{x_I}) = \begin{bmatrix} \dfrac{\partial \varphi_i(\boldsymbol{x_I})}{\partial x} & 0 & 0 & \dfrac{\partial \varphi_i(\boldsymbol{x_I})}{\partial y} & 0 & \dfrac{\partial \varphi_i(\boldsymbol{x_I})}{\partial z} \\[2mm] 0 & \dfrac{\partial \varphi_i(\boldsymbol{x_I})}{\partial y} & 0 & \dfrac{\partial \varphi_i(\boldsymbol{x_I})}{\partial x} & \dfrac{\partial \varphi_i(\boldsymbol{x_I})}{\partial z} & 0 \\[2mm] 0 & 0 & \dfrac{\partial \varphi_i(\boldsymbol{x_I})}{\partial z} & 0 & \dfrac{\partial \varphi_i(\boldsymbol{x_I})}{\partial y} & \dfrac{\partial \varphi_i(\boldsymbol{x_I})}{\partial x} \end{bmatrix}_i^T \qquad (5.30)$$

For $i = 1,2,3, \dots, n$, i.e., to the order of nodes inside the influence-domain. Therefore, matrix $\boldsymbol{B}(\boldsymbol{x_I})$ is composed by all n matrices $\boldsymbol{B}_i(\boldsymbol{x_I})$, one for each node inside the influence-domain.

Finally, equation (5.28) developed, substituting $\boldsymbol{LH}(\boldsymbol{x_I})$ by $\boldsymbol{B}(\boldsymbol{x_I})$:

$$\delta \boldsymbol{u}^T \left[\int_\Omega (\boldsymbol{B}(\boldsymbol{x_I}))^T \boldsymbol{cB}(\boldsymbol{x_I}) d\Omega \boldsymbol{u} - \int_\Omega (\boldsymbol{H}(\boldsymbol{x_I}))^T \boldsymbol{b} \, d\Omega - \int_{\Gamma_t} (\boldsymbol{H}(\boldsymbol{x_I}))^T \bar{\boldsymbol{t}} \, d\Gamma \right] = 0 \qquad (5.31)$$

Resulting in:

$$\int_\Omega (\boldsymbol{B}(\boldsymbol{x_I}))^T \boldsymbol{cB}(\boldsymbol{x_I}) \, d\Omega \boldsymbol{u} - \int_\Omega (\boldsymbol{H}(\boldsymbol{x_I}))^T \boldsymbol{b} \, d\Omega - \int_{\Gamma^t} (\boldsymbol{H}(\boldsymbol{x_I}))^T \bar{\boldsymbol{t}} \, d\Gamma = 0 \qquad (5.32)$$

This leads to the local static equilibrium equation for the influence-domain since the first integral of equation (5.32) corresponds to the local stiffness matrix, $\boldsymbol{K_I}$, and the other two integrals correspond to $\boldsymbol{f_I}^b$ and $\boldsymbol{f_I}^t$, respectively, and can be grouped constituting the local force vector $\boldsymbol{F_I}$.

Then, considering the nodal connectivity, the previous local matrices must be assembled, leading to the global discrete system of equations:

$$\boldsymbol{K}.\boldsymbol{u} = \boldsymbol{F} \qquad (5.33)$$

Where $\boldsymbol{K}$ is the local stiffness matrix, $\boldsymbol{u}$ is the nodal displacement vector and $\boldsymbol{F}$ is the global force vector.

Chapter 6

Elasto-plastic formulation

In this chapter, it is briefly explained the concept of elasto-plastic material, as well as the elasto-plastic formulation used within this work and the non-linear solution method used to solve the equations derived from this formulation.

6.1 - Elasto-plastic definition

When a growing force is applied, a tension is generated in the material causing a deformation that increases with the applied force. For most materials, this response is initially elastic, that is, the deformation vanishes when the force stops acting. After the material elastic limit, an increase in force will cause irreversible deformation, also known as a plastic deformation. If this force is maintained, the material will deform until it breaks. The maximum value of stress before rupture is called Ultimate Stress.

The relationship between stress and strain in the elastic range is defined by the Young's Modulus (E), which is a measure of the stiffness of a solid material. The elastic behaviour of a material can be described using the Hooke's law.

In the plastic range, the relationship between stress and strain is defined by the Plastic Modulus (E_t). To describe the stress-strain relation after plastic deformation, a plastic constitutive tensor needs to be established.

A material with an elasto-plastic behaviour is one who possesses both elastic and plastic properties.

In Figure 6.1, it is possible to observe the stress-strain curve that translates the typical elasto-plastic behaviour. If the material exhibited simply a linear-elastic behaviour, strain would increase proportionally with stress, following the dashed line until point A. An elastic-plastic material will exhibit elastic behaviour only until a certain point, marked as σ_y in this figure and called Yield Stress. If this point is exceeded, the material will start to experience plastic deformation. Therefore, the strain increases more rapidly than in the elastic region. When the material reaches point B, it does not return to the origin, but to point 0^*, possessing now irreversible deformations. After the material reaches point B, it has experienced a phenomenon called hardening, i.e., the material will need increasingly higher stresses to have further deformations. In this way, point B is the new Yield Point, denominated σ^*_y in the figure.
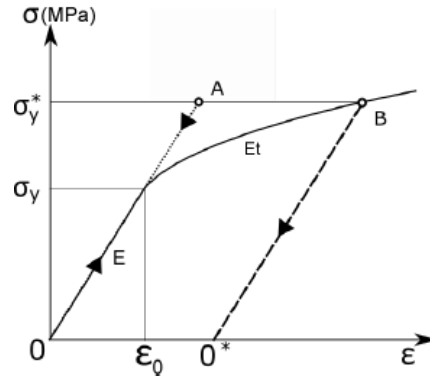
Figure 6.1 - Stress-strain curve.

6.2 - Elasto-plastic formulation

To characterize the non-linear behaviour of an elastic-plastic material, three points need to be addressed [53]:

(1) A Yield criterion, showing the stress level in terms of the stress tensor and indicating the beginning of the plastic regime;

(2) A flow rule, characterizing how the deformation relates to stress after plastification;

(3) A hardening criterion describing the interdependency between the yield criterion and the plastic deformation [54].

The Yield stress defines the beginning of the plastic deformation, and it is defined as:

$$F(\boldsymbol{\sigma}, k) = f(\boldsymbol{\sigma}) - \sigma_y(k) = 0 \tag{6.1}$$

In which $\boldsymbol{\sigma}$ corresponds to the stress tensor and k to the hardening parameter. The yield surface $F(\boldsymbol{\sigma}, k)$ depends on the magnitude of the load applied and of the hardening parameter. The yield function is the scalar function $f(\boldsymbol{\sigma})$ and the yield stress, the stress limit for the elastic regime, is represented as $\sigma_y(k)$.

According to this yield criterion, if the material's stress state at a certain point is $f(\boldsymbol{\sigma}) < \sigma_y(k)$, then the material is being governed by the linear equations of the theory of elasticity [55]. On the other hand, if $f(\boldsymbol{\sigma}) = \sigma_y(k)$, then the material reached yielding, i.e., it will enter the plastic regime and start to experience plastic deformations. In this work, it was used the von Mises yield criterion [56], which is defined as:

$$f(\boldsymbol{\sigma}) = \bar{\sigma} = \frac{\sqrt{2}}{2} \left[(\sigma_{xx} - \sigma_{yy})^2 + (\sigma_{yy} - \sigma_{zz})^2 + (\sigma_{zz} - \sigma_{xx})^2 + 6(\tau_{xy}^2 + \tau_{yz}^2 + \tau_{zx}^2) \right]^{0.5} \tag{6.2}$$

This yield function can be rewritten as the following:

$$f(\boldsymbol{\sigma}) = \bar{\sigma} = \left[\sigma_{xx}^2 + \sigma_{yy}^2 + \sigma_{zz}^2 + \sigma_{xx}\sigma_{yy} + \sigma_{yy}\sigma_{zz} + \sigma_{zz}\sigma_{xx} + 3\tau_{xy}^2 + 3\tau_{yz}^2 + 3\tau_{zx}^2 \right]^{0.5} \tag{6.3}$$

In this work, it was considered the associated flow rule since it associates the plastic flow with the yield criterion. The Prandtl-Reuss flow rule defines that the plastic strain is determined as:

$$d\boldsymbol{\varepsilon}_p = d\lambda \frac{\partial f}{\partial \boldsymbol{\sigma}} = d\lambda \boldsymbol{a} \tag{6.4}$$

Where $d\lambda$ corresponds to the plastic rate multiplier and $\boldsymbol{a}$ to the flow vector, normal to the adopted yield function, f, defined previously. The flow vector can be presented as $a = \partial f / \partial \boldsymbol{\sigma}$, where:

$$\boldsymbol{a} = \left\{ \frac{\partial f}{\partial \sigma_{xx}} \quad \frac{\partial f}{\partial \sigma_{yy}} \quad \frac{\partial f}{\partial \sigma_{zz}} \quad \frac{\partial f}{\partial \sigma_{xy}} \quad \frac{\partial f}{\partial \sigma_{yz}} \quad \frac{\partial f}{\partial \sigma_{zx}} \right\}^T \tag{6.5}$$

Considering Hooke's law, the relation between the stress rate $d\boldsymbol{\sigma}$ and the elastic strain rate $d\boldsymbol{\varepsilon}_e$ is assumed as:

$$d\boldsymbol{\sigma} = \boldsymbol{c}d\boldsymbol{\varepsilon}_e = \boldsymbol{c}(d\boldsymbol{\varepsilon} - d\boldsymbol{\varepsilon}_p) \tag{6.6}$$

In which $d\boldsymbol{\varepsilon}$ corresponds to the total strain rate and $d\boldsymbol{\varepsilon}_p$ to the plastic strain rate. By considering the Prandtl-Reuss flow rule and assuming that the yield surface $F(\boldsymbol{\sigma}, k)$ only depends on the magnitude of the applied principal stresses and of the hardening parameter k, the previous equation can be rewritten as:

$$d\boldsymbol{\sigma} = \boldsymbol{c}(d\boldsymbol{\varepsilon} - d\lambda \boldsymbol{a}) \tag{6.7}$$

The stress must not pass beyond the yield surface in order to occur plastic flow, therefore the following relation is established:

$$dF = \frac{\partial f}{\partial \boldsymbol{\sigma}} d\boldsymbol{\sigma} - \frac{\partial \sigma_Y}{\partial k} = \boldsymbol{a}^T d\boldsymbol{\sigma} - A d\lambda = 0 \tag{6.8}$$

In which A corresponds to the hardening parameter [54], dependent on the hardening rule and defined as:

$$A = \frac{1}{d\lambda} \frac{\partial \sigma_Y}{\partial k} dk \tag{6.9}$$

Combining equation (6.7) with equation (6.8) it is obtained:

$$d\lambda = \frac{\boldsymbol{a}^T \boldsymbol{c} d\boldsymbol{\varepsilon}}{\boldsymbol{a}^T \boldsymbol{c} \boldsymbol{a} + A} \tag{6.10}$$

Once again, combining equation (6.6) with equation (6.10), the stress rate can be rewritten as the following:

$$d\boldsymbol{\sigma} = \boldsymbol{c}d\boldsymbol{\varepsilon} - \frac{\boldsymbol{a}^T \boldsymbol{c} d\boldsymbol{\varepsilon}}{\boldsymbol{a}^T \boldsymbol{c} \boldsymbol{a} + A} \cdot \boldsymbol{c}\boldsymbol{a} = \left(\boldsymbol{c} - \frac{\boldsymbol{c}\boldsymbol{a}\boldsymbol{a}^T \boldsymbol{c}}{\boldsymbol{a}^T \boldsymbol{c} \boldsymbol{a} + A} \right) d\boldsymbol{\varepsilon} = \boldsymbol{c}_t d\boldsymbol{\varepsilon} \tag{6.11}$$

Where $\boldsymbol{c}_t$ corresponds to the tangential constitutive matrix. In this work the work hardening hypothesis is employed [54] considering the associated flow rule to define explicitly the

hardening parameter A. As all of the materials studied in this work will be considered as having a "linear elastic" – "linear plastic" hardening behaviour, the hardening parameter A can be defined as [54]:

$$A = \frac{E_{T0}}{1 - \frac{E_{T0}}{E_0}}$$

(6.12)

Where E_0 corresponds to the Elastic Modulus and E_{T0} to the tangential modulus in the reference direction.

In this work, the material behaviour is modelled as an incremental relation between the incremental stress vector and the strain increment, using the "backward-Euler" procedure [57] to force the stress back to the yield surface, as demonstrated in Figure 6.2. Within this methodology, which solves the nonlinear equations acting on the level of the Gauss points, it is not required to determine the intersection point of the incremental load with the yield surface, point A. Thus, after the incremental load application, and for each Gauss point, it is verified if the achieved stress state is inside or outside the yield surface [53]. The algorithm is called if the stress state is outside the yield surface, like point B. This point must be pushed back to point C, on the yield surface. To perform the returning of the stress state to the yield surface, the implemented algorithm starts with a predictor, simulating that point B is on the surface of a 'forward' yield function f_B, consequently avoiding the computing of the intersection point A [53]. The flow vector is calculated from point B, $\boldsymbol{a}_B$, being the yield function in point B defined by $f_B = \bar{\sigma}_B - \sigma^*{}_Y$, where $\sigma^*{}_Y$ is the updated yield stress. Next, using equation (6.7), an estimation of the stress in point C is obtained [53]:

$$\boldsymbol{\sigma}_C = \boldsymbol{\sigma}_B - d\lambda c \boldsymbol{a}_B$$

(6.13)
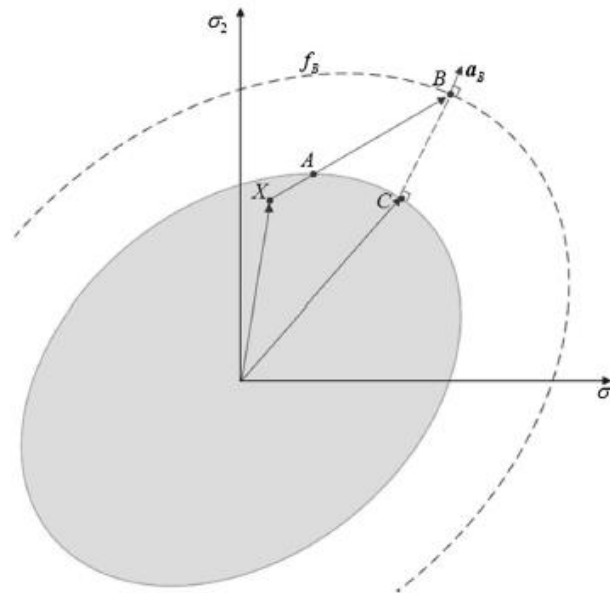
Figure 6.2 - Backward-Euler scheme [53].

To correctly obtain the stress in point C, it should be used the flow vector on point C, a_C. However, a_C cannot be directly obtained with only the data from points X and B. Hence, the information from point B must be employed to estimate point C. This process continues iteratively until C is satisfactorily approximated, concluding the process [53].

Within discrete numerical methods, an elasto-plastic problem is solved considering increments of load. For a load increment that produces an elastic response of the material, the discrete system of equations is solved. Once the material reaches the elastic limit, the stiffness matrix needs to be updated to consider the effects of plastic deformation.

The calculation of the non-linear solution was performed through the incremental-iterative full Newton-Rapson solution algorithm [54]. Therefore, the stiffness matrix is calculated in each iteration. A diagram of the algorithm implemented in the software used for this work can be seen in Figure 6.3.
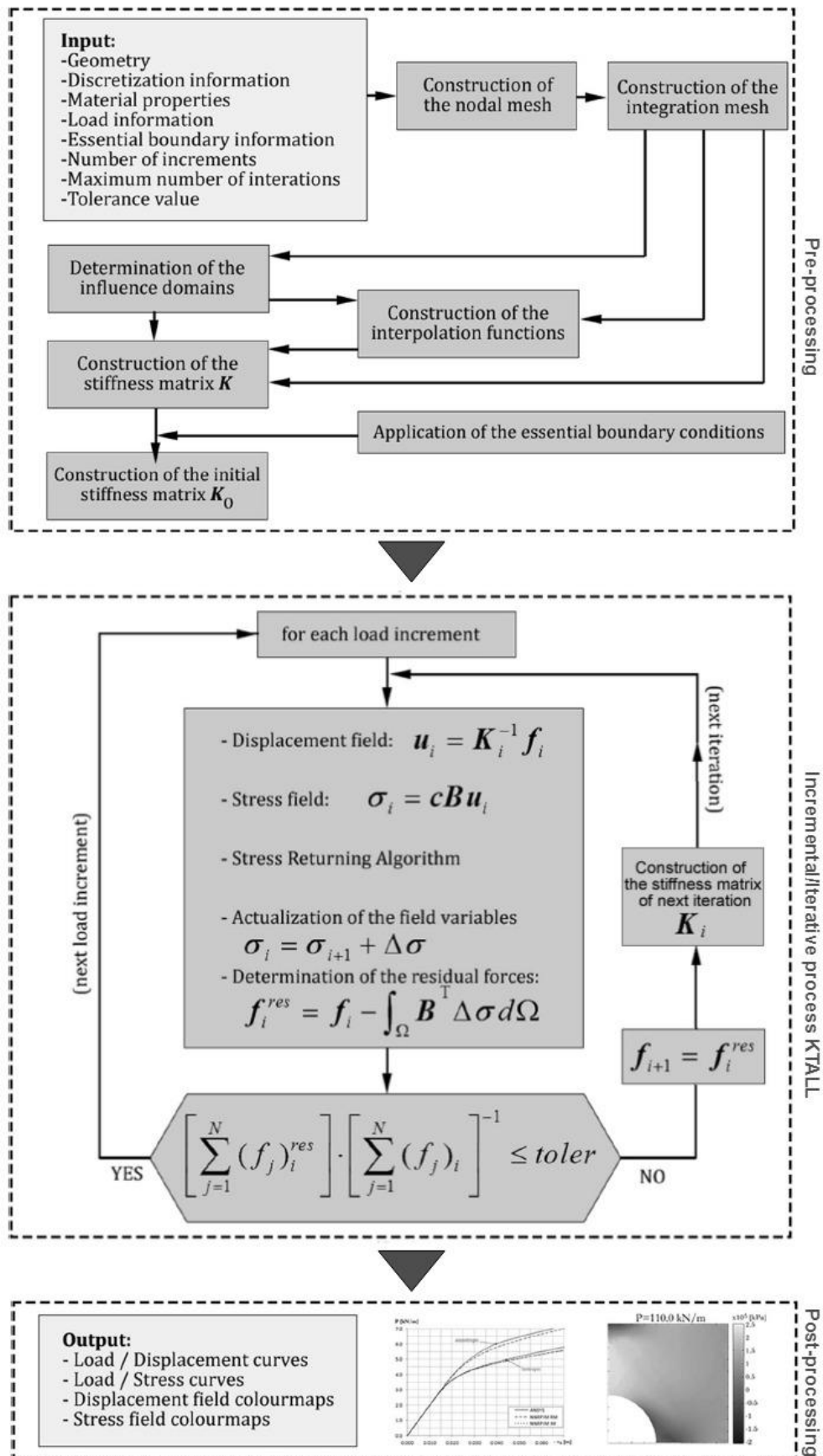
Figure 6.3 – NNRPIM and KTALL algorithm (adapted from [53]).

Chapter 7

State-of-the-art

7.1 - FEM

FEM was initially developed to solve aeronautic structural problems. However, in just six decades, it was applied to most of physical problems, allowing to solve complex problems (impossible to solve using classical analytical approaches). The graph depicted in Figure 7.1 was obtained through a research on *Scopus* database, using different keywords. It can be verified that, regardless of the keywords used ('FEM AND Dentistry' or 'FEM AND Dental'), the number of papers, using FEM in dentistry, follows a growing trend over the years, which indicates that this is still a subject of considerable interest, with many unanswered questions and interesting topics to investigate. Even when the search is narrowed to a more specific area of dentistry ('FEM AND Dental Restorations'), there are still a growth of published papers.
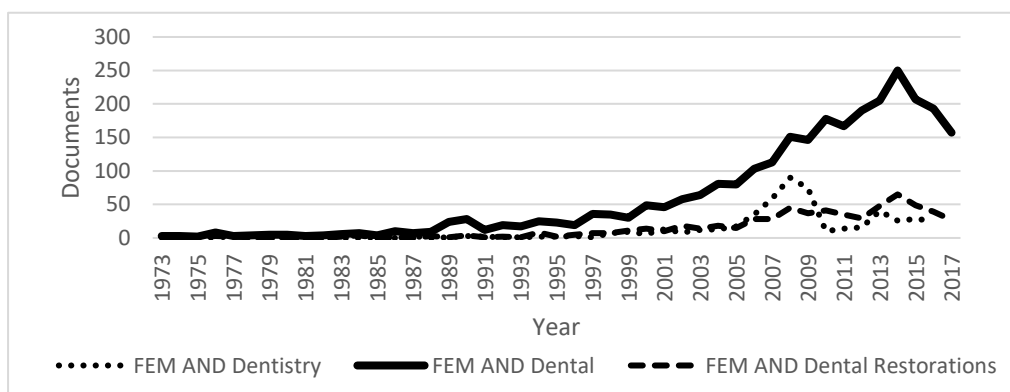
Figure 7.1 - Number of documents published through the years, in the subjects indicated. The data was obtained through a research on *Scopus* database (www.scopus.com) assuming as keywords the subjects indicated in the graph.

This mathematical method was first introduced in dental medicine in the early 1970s by Farah's. Farah, Craig and Sikarskie (1973), presented a study of firsts molars restored with a gold crown, the models were presented in its axisymmetric form. In this work, two methods, the photoelastic method and FEM, were used to study the stress distribution. These two methods were compared favourably, and it was concluded that together they allowed a better understanding of the distribution of stresses in dental restorations [58].

7.1.1 - Geometrical models

7.1.1.1 - Two-dimensional

The first models were 2D simplifications of reality. The simplification was due to the low computation capacity of computers, which did not allow a high number of calculations. From 1970 to 1990, one of the main focuses was the validation of this method. Since many geometrical simplifications were still made, such could lead to mathematical errors [16].

Thresher and Saito (1973), by analysing the stresses in a 2D model of maxillary central incisor, concluded, among other things, that FEM proved its validity as a tool for the study of teeth. However, a 3D model would be more adequate to study complex structures, such as the human teeth [59]. Despite that, Farah, Hood and Craig (1975) realized that the main advantage of using a 2D model is that the magnitude, direction and location of the load are repeatable, and the varying thickness is easily altered, which makes the results easily reproducible. Another advantage of using this mathematical method to study materials used in dental restorations, is that the results obtained depend on the mechanical properties of the materials considered, thus reflect the behaviour of the materials [60].

Yettram, Wright and Pickard (1976) verified that FEM is ideal for the examination of the structural behaviour of teeth [61].

The model used by Reinhardt et al. (1983), who performed a plane-strain analysis to understand the effect of loss of alveolar bone (i.e. the loss of bone support) in the magnitude and distribution of the stresses obtained, is represented in Figure 7.2 [62]. With this figure is possible to demonstrate the accuracy of the models used at the time. FEM proved its validity and its advantage, since it allowed to obtain more detailed information on the stress state in non-homogeneous bodies [62].
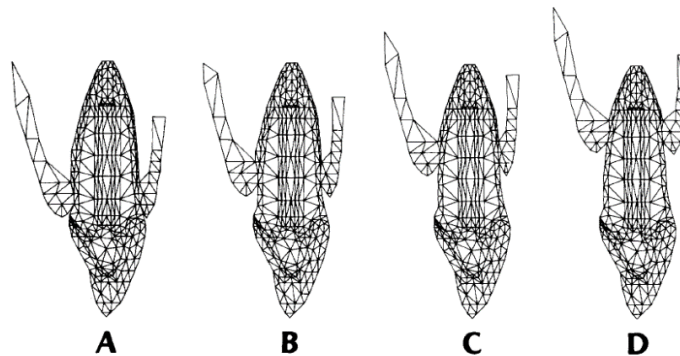
Figure 7.2 - Models used in [62]: 2D models partitioned into triangular elements with increase loss of crestal bone height from A to D.

7.1.1.2- Three-dimensional with CT

Khera et al. (1988) were pioneers on 3D modelling. The authors constructed a 3D human mandible based on a 2D model. This 2D model was obtained and then it was performed a projection of several pictures in a magnifying monitor, given origin to a 3D model. Lastly, an axial Z-axis was defined [63].

During the decade of 1990-2000, with the strong development of imaging technologies, it was then possible to develop 3D models. Using images obtained by CT, it became possible to obtain stacks of sectional geometries of human jaws. These geometries were digitized and reconstructed into the 3D models [16]. The images obtained with CT produce DICOM formatted images, which can be imported into a 3D software platform to develop the 3D models.

In [64] is documented a review of published papers with complete maxillary/mandibular FE models and regional FE analysis, i.e., 3D jaws models and tooth models. When modelling regional FE models, there were found 2D, 3D and axisymmetric models (types of FE models presented in Figure 7.3). Although 3D models are more realistic, it requires more computational capacity. Thus, in many cases, it can be justified the use of 2D modelling. Axisymmetric modulation is an option that combines 3D stress conditions with the simplicity and efficiency of a 2D model, but it limits the options for geometry and boundary conditions. With this analysis, the authors concluded that the advancements previously mentioned were in fact very useful to provide models with improved geometric accuracy. Therefore, with these advancements, many authors started to use 3D models, like: (1) Toparli et al. (2000), that studied the influence of temperature on the behaviour of different restorations, using a 3D model of a restored maxillary second premolar subjected to thermal loads, simulating the presence of hot and cold liquids in the mouth [65]; and (2) Jones et al. (2001), that developed a 3D model of a maxillary incisor with the aim of studying tooth movements when these are subjected to orthodontic loads. Comparing the results obtained numerically with the results obtained experimentally, the authors concluded that the FEM approach may be valid for the study of orthodontics [66].
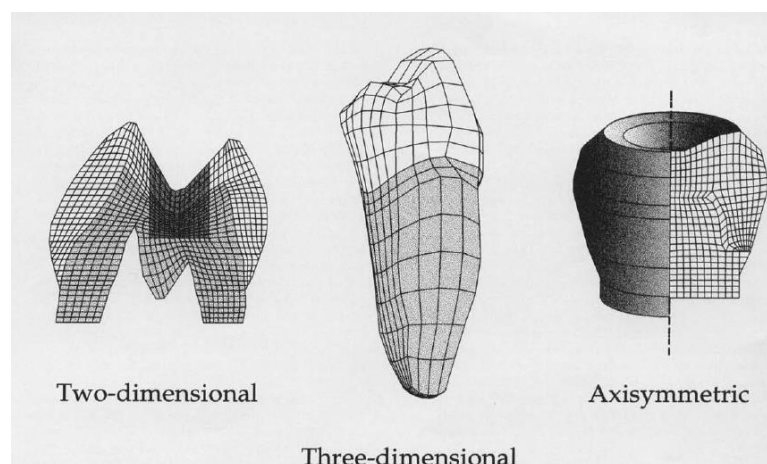
Figure 7.3 - Different types of FE tooth models [64].

7.1.1.3- Three-dimensional with µCT

Between 2000-2010, improvements on software capability allowed the development of 3D models increasingly complex and with more detail. The use of µCT images contributed to these advances in the representation of complex structures, such as dental structures. It has also become possible to represent interfaces between different tissues [16].

So, through the µCT images, Verdonschot et al. (2001) developed a 3D model of a premolar with a cusp-replacing resin composite restoration. For this, the tooth was scanned by µCT, then the different visible materials were identified through 2D contours. These contours were

stacked generating a 3D structure which, lastly, was meshed. A process identic to the one followed in this article is demonstrated in Figure 7.4, but to a different tooth [67].

Magne (2007) developed a model of a mandibular molar. For this, an intact mandibular molar was digitized using µCT, then the different materials were identified through the difference between pixel density, and the 3D structures were automatically created in the form of masks. The enamel and dentin were then separately converted into STL files [39].
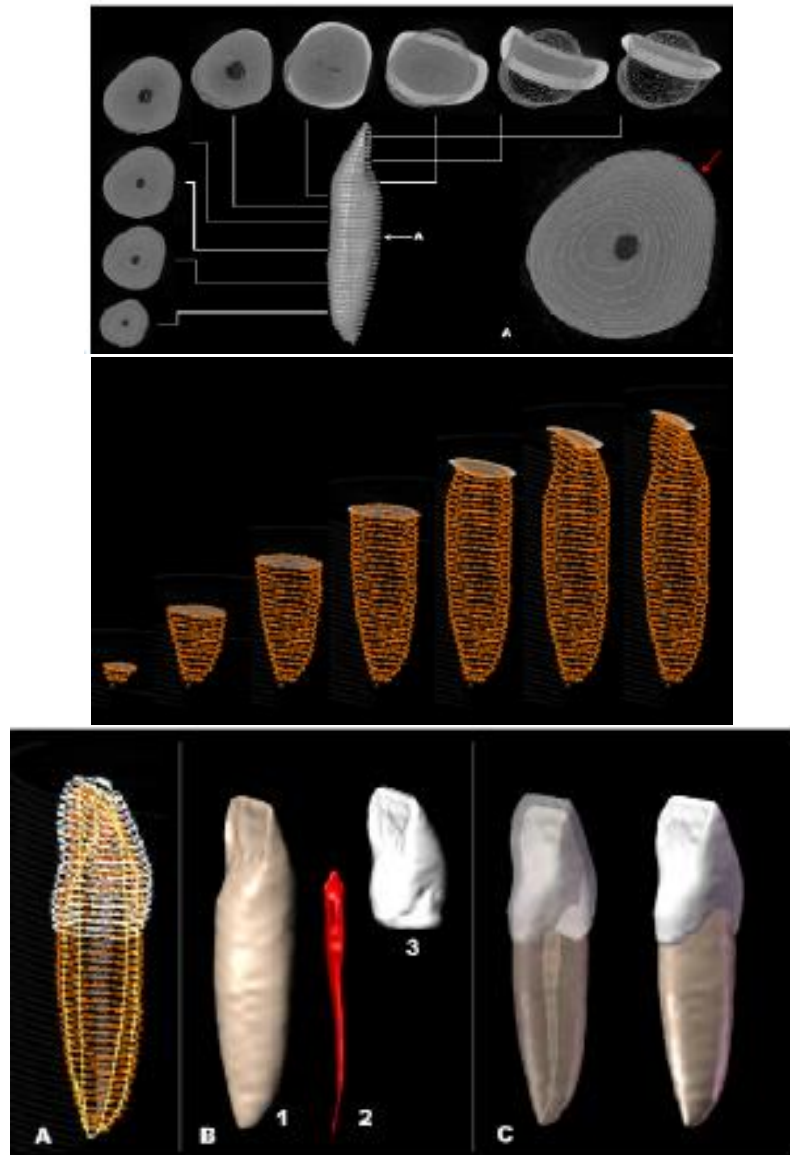
Figure 7.4 - Process of developing a 3D model of a maxillary central incisor through the µCT images [16].

7.1.1.4- Three-dimensional with CAD

Between 2000-2010, increased mathematical functions in 3D CAD have also contributed to advances in the representation of complex structures, such as dental structures. With CAD programs it was possible to build solid 3D models, which were then converted to FE programs for meshing and analysis [16].

The previous referred study of Magne (2007), which developed a model of a mandibular molar through µCT images, used Boolean operations with CAD objects to simulate a fixed cylindrical base, different cavity preparations and restorations. This process is shown in Figure 7.5 [39].

(a)   (b)
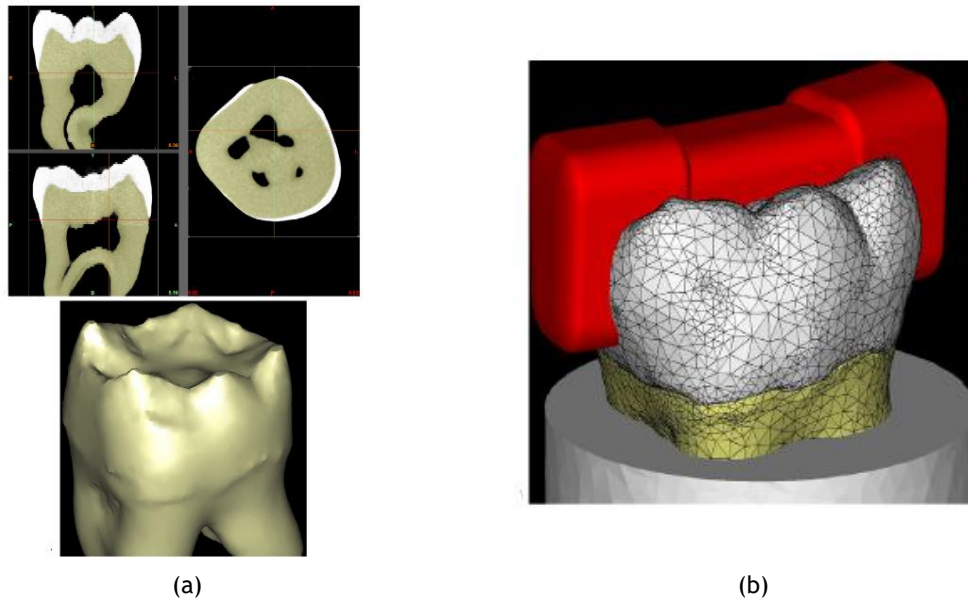
Figure 7.5 - Process of developing a 3D model of a mandibular molar through the µCT images: (a) CT-scan data in three different cross-sectional views of the tooth and 3D representation of dentin as result of segmentation; (b) CAD objects used to simulate a cylindrical stone base and different cavity designs (red inserts) [39].

The use of CAD programs during this decade and in the present, is widely applied in restorative dentistry, contributing to the study of different options of dental treatment, such as: crowns supported by implants [68]; glass-fibre post system (simulating for instance different support bone conditions, i.e., different levels of alveolar bone) [69]; removable thermoplastic appliances (RTAs) to treat malocclusion problems (in which the use of CAD tools allows to create a layer completely congruent with the tooth crown surfaces) [70]; and class II MOD (Mesial/Occlusal/Distal) dental restorations [71].

7.1.2 - Three-dimensional structures

As previously seen, with the advancement of software capability it was possible to develop more complex 3D structures. During the decade of 2000 to 2010, it was recognized the importance of considering the complete dentition and all the materials that constitute the tooth in a biomechanical simulation, to correctly predict the stress-strain fields.

Thresher and Saito (1973), analysed the stresses in a maxillary central incisor, subject to lateral loads at the tip. They used triangular elements in a plane-strain, to understand the differences in stress distributions along different sections in homogeneous and non-homogeneous models, as well as to determine how the load is carried by the tooth and distributed to the surrounding bone structures. The results obtained demonstrate the importance of considering all the materials that constitute the tooth [59].

Field et al. (2009), carried out a study on orthodontic treatments, considering two models: (1) a model of a single tooth, a mandibular canine; and (2) a model considering adjacent teeth, i.e., consisting of mandibular incisor, canine and first molar. The mandibular bone and orthodontic hardware, consisting of brackets, adhesive and wire, were included in both models. With this study it was possible to verify the importance of considering the effect of adjacent teeth, since simplified models containing only one tooth did not consider the effect of tooth-tooth contacts [72].

7.1.3 - Meshing techniques

Despite the evolution of 2D models to 3D models that occurred between 1990 and 2000, allowing a more realistic representation of human geometries, the manual and semi-automatic meshing process was still in gradual development [16]. In the previously mentioned review papers (in section 7.1.1.2 of this manuscript, which contains published articles with complete maxillary/mandibular FE models and regional FE analysis), the element size used in these 3D jaws models and tooth models was relatively large due to the immature meshing techniques that characterize this decade [64]. However, the FEM's gradual development contributed to more robust studies, such the work of Hübsch et al. (1993), that applied the FEM to simulate polymer tooth fillings (being these addition-curing polymers) that may shrink in the placement process [73].

During this decade, validation was required to verify the accuracy of stress-strain estimations and its association with the models mesh density [16]. Winkler et al. (2000) developed a study to understand the process of shrinkage of resin composites during the polymerization, which causes stresses at the interface between the resin and the cavity walls. This study was performed experimentally and using FEM. The authors focused on verifying surface deformations, and the plots obtained experimentally were compared favourably with the results obtained through FEM, thus validating this approach [74]. Palamara et al. (2000), studied the variations in strains in enamel of a tooth subjected to different patterns of occlusal loading, using a 3D model of a mandibular second premolar and strain gage placed on extracted teeth. The results obtained through the two methods used were in full agreement, thus validating the FEM [75].

Between 2000-2010, with the software advancements, there was an increase in CPU computing power, which allowed to improve the meshing process as well as it permitted to enhance the automeshing capability. Superior computing power coupled with a precise mesh, allowed to improve the calculation of mechanical fields, such as stress, strain and energy [16]. An example of these advancements is the work done by Magne (2007), already referred in sections 7.1.1.3 and 7.1.1.4, in which automatic meshing was used to reduce the amount and improve the quality of triangular elements that constituted the mesh without damaging the geometry of this model [39].

Currently, after segmentation, it is necessary to correct irregularities, or defects that may occur from scanning and segmentation, and smooth surfaces without affecting the accuracy of the model. This smoothing process demonstrated in Figure 7.6, allows to decrease file size, meshing time, mesh density and solution times [16].
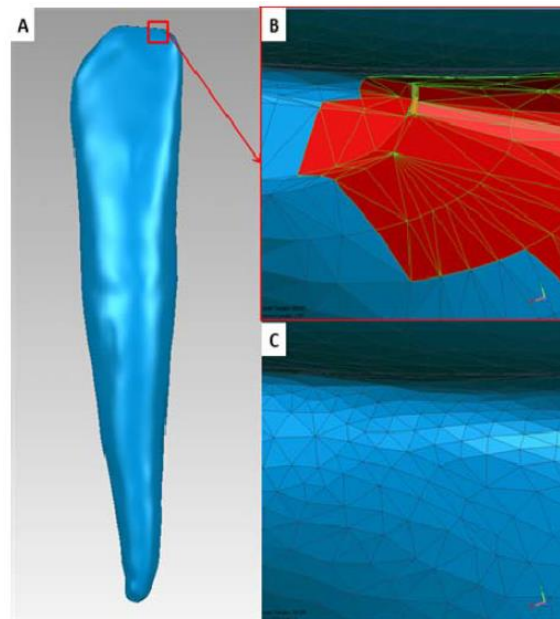
Figure 7.6 - Smoothing process [16].

7.1.4- Structural analysis

7.1.4.1- Static analysis

The nature of loading governs the kind of analysis to be performed on the structure. Static loads vary slowly. Thus, it can be assumed that static loads remain constant and there is no significant variation in the structural response with time.

An example of a static analysis is the work done by Mattos et al. (2012), which studied restored teeth with post-and-core systems to understand if adhesive reconstruction can restore the original biomechanical behaviour of weakened roots. To do so, the authors applied a 100 N load on the palatal surface of the models considered. To simulate an occlusal contact area, the force was applied at an angle of 130° from the long axis of the tooth and distributed over four nodes [76].

7.1.4.2 - Dynamic analysis

In addition to the evolution of 2D models for 3D models that occurred between 1990 and 2000 (see section 7.1.1.2), specific solvers (e.g., poroelasticity, homogenization theory, dynamic response) were also developed, being adapted from the engineering area to study dental problems involving heterogeneous structures and time-dependent properties [16].

Dynamic loads are transient loads that vary significantly with time, thus the structural response needs to be calculated at every time instant. Examples of a dynamic analysis are thermal and mechanical loading and fatigue analysis. An example of a dynamic analysis is demonstrated in Figure 7.7, in which is clearly seen that the results obtained varied with time.
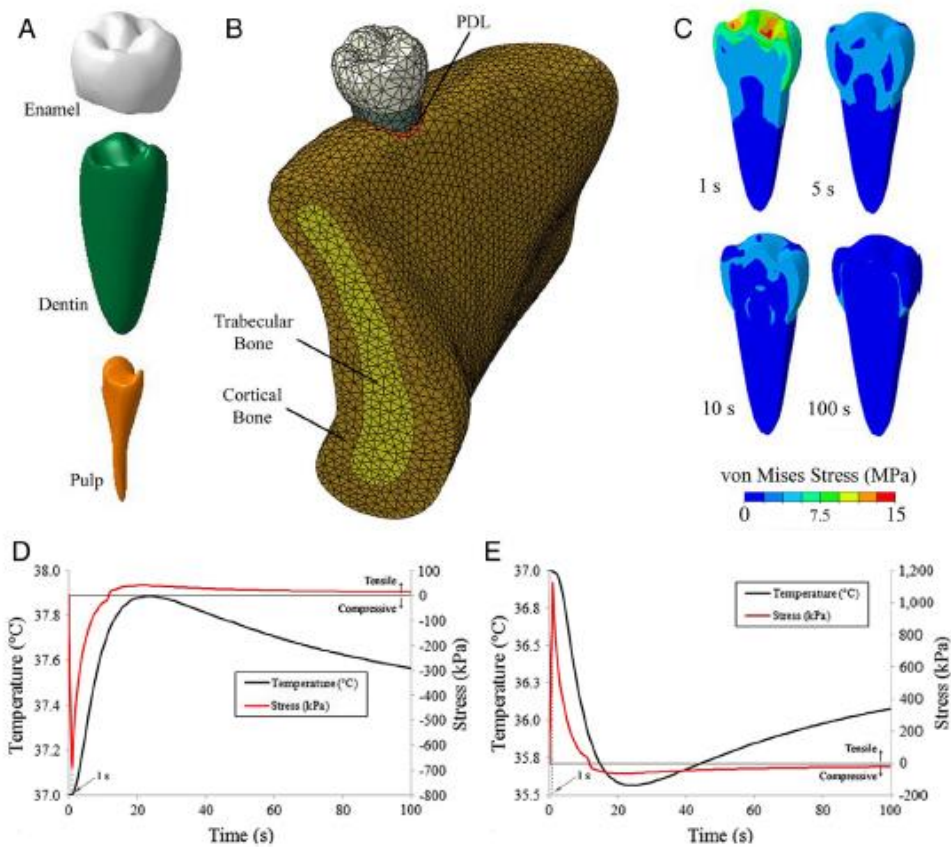
Figure 7.7 - Type of results obtained when performing a dynamic analysis [77].

Several authors focus on the influence of temperature on tooth pain sensation mechanism, different types of restorations and materials. Considering this effect allows a more realistic analysis, since it permits, for example, to simulate the daily intake of hot or cold beverages [65,77].

Fatigue analysis focuses on damage accumulation and allows to understand where the crack will grow and propagate. Some authors performed this type of analysis on different types of restorations and materials, to predict the fatigue lifetime before crack [78,79]. These studies are relevant because the inclusion of the fatigue analysis considers the dynamic nature of the masticatory forces, thus making the studies more realistic.

Silva et al. (2013), studied two different impact situations (frontal and vertical impact) through a transient dynamic analysis in which the loading force was applied gradually until a peak was reached within a given period [80].

7.1.4.3 - Contact analysis

Currently, solid models are developed from imaging technologies, such as CT, μCT or MR images. The objects in these images are segregated by identifying interfaces, which is possible through sequential 2D sliced or through segmentation of 3D objects. In this way, the interfaces between different bodies are precisely identified through common nodes, called coincident nodes, between the different objects in the contact area. This makes the simulation more realistic, allowing to simulate, for example, the interface between the bone and an implant [16].

Barone et al. (2016) studied the use of removable thermoplastic appliances (RTAs) to treat moderate malocclusion problems. This was a study of contact and displacement imposition once the relationship between teeth and RTA had to be defined and rotation movements were analysed [70]. Han et al. (2016) study the biomechanical performance of different osseointegration patterns on cortical bone/implant interface, which were determined by the quantity of integrated nodes at the bone margin [81]. Gerami et al. (2016) simulate the contact between teeth, their adjacent structures and multi-strand wire with composite through contact elements, in a way to study how the inclination of the lower anterior teeth can affect displacement and change the direction of occlusal loads exerted to dental and its supporting tissues [82].

7.1.5 - Materials

Several investigators have studied the relationship between the elastic properties of composite dental restorations and restored tooth stiffness.

Farah, Hood and Craig (1975) studied an axisymmetric model of a molar with a class I amalgam restoration. In this study, the cement bases, which support the restoration, were varying in material and thickness. The authors were trying to understand the effect of the base on the stresses obtained in amalgam restorations [60].

Other studies focused on the effect of different restorative materials, or different material combinations, on the stress-distribution [83,71].

Some authors study dental restorations to understand not only the influence of the use of different restorative materials on stress distribution but also the influence of the quantity of remaining dental tissues. To do so, different adhesive layers that varied in thickness and rigidity (Young's modulus) were tested [84], or the thickness and materials of endocrowns were varied and tested [85].

Ausiello et al. (2001), performed different tests on a maxillary premolar with a class II MOD (Mesial/Occlusal/Distal) restoration, in which a significant amount of dentin and enamel were lost, compromising the integrity of the structure. This study focused on the use of resin-based composites. These materials are being widely employed in restorative dentistry. However, present a major disadvantage, the polymerization contraction and the mismatch that occurs during hardening and that leads to polymerization shrinkage stresses and interfacial stress concentrations. The aim of this study was to understand the influence of the shrinkage characteristics and composite rigidity on the cusps displacement, evaluating stresses arising from polymerization shrinkage and from shrinkage in combination with vertical occlusal loading [86].

Toparli, Gökay and Aksoy (2000), focused on the influence of temperature on the behaviour of different restorations, using a 3D model of a restored maxillary second premolar subjected to thermal loads, simulating the presence of hot and cold liquids in the mouth. Two types of restorative materials - amalgam and composite resin - were studied. Critical points of the model were chosen, and the temperature and stress distribution were analysed at these points [65]. Thus, Tulimar et al. (2010), focused not only on the effect of mechanical loads on the behaviour of dental restorations, but also on the effects of temperature, simulating the ingestion of hot and cold foods. In this way, the authors combined effects of temperature variations and mastication loads [33]. For this, the authors developed a model of a mandibular second molar, including mandibular bone in the model and considering two types of restoration, one consisting

of resin and another one of porcelain. For a selected point at the interface between the dentin and the restoration, the stress-distribution caused by temperature changes in normal and restored teeth was analysed, as well as, the stress-distribution caused by the combined effects of temperature variations and mastication loads, also in teeth normal and restored [33].

Is possible to conclude that the study of dental restorations and the materials used is a subject of high interest and the conclusions taken by each author vary widely, which only proves the complexity of studying dental structures, in which several factors can be responsible for this disparity in results.

7.1.6 - FEM and dental bridges

In section 3.2 of this manuscript were presented several types of dental bridges. If, using *Scopus* database, the search is narrowed to manuscripts dealing with different types of dental restoration (dental bridges), the number of published works decreases considerably, as it is possible to visualize in Figure 7.8. This observation indicates that this is an area that has not yet been widely studied, with many unanswered questions.
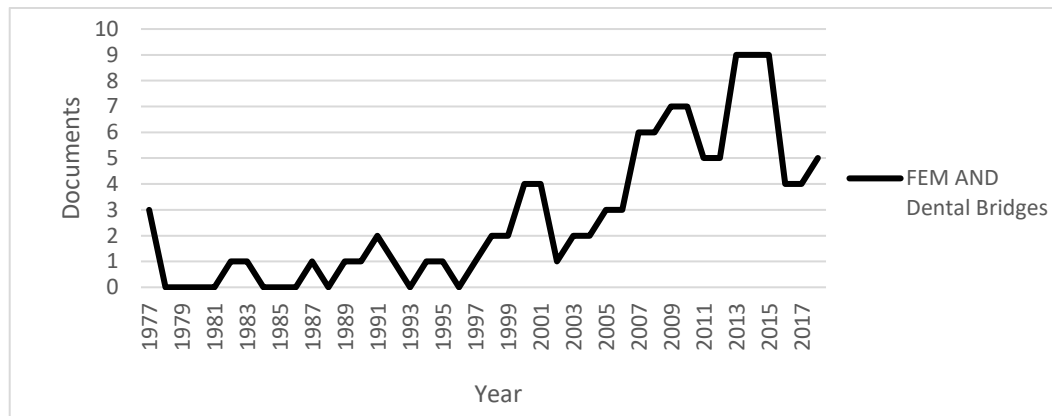
Figure 7.8 - Number of documents published through the years, in the subjects indicated. The data was obtained through a research on *Scopus* database (www.scopus.com) assuming as keywords the subjects indicated in the graph.

7.1.6.1- Conventional dental bridges

7.1.6.1.1 - Cantilever bridges

Many authors studied cantilever bridges and several variations were made, however most of these authors have drawn similar conclusions. One of the conclusions is that most of the stresses are transmitted to the tooth closest to the pontic, which is well seen in Figure 7.9 [87,88,89].

Wang et al. (1998) concluded that changing the bridge material to more rigid materials and more extensive preparation of the tooth immediately next to the pontic does not contribute to a better stress distribution [88].

Eraslan et al. (2005) studied different morphologies and different materials of cantilever bridges, concluding that both parameters affect the stress distribution and their values in the

connectors and cervical region of distal support tooth. Again, the maximum von Mises stresses were found at the connector between the pontic and the first abutment tooth, so it becomes imperative to control the size of this connector. The right material to use varies, since the results indicated that for models with premolar cantilever the use of all-ceramic induced lower stresses, whereas for models with molar cantilever the use of metal-ceramic restorations induced lower stresses [90].
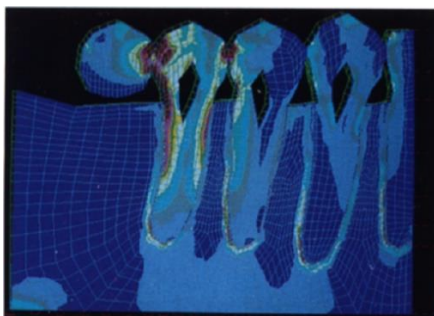
Figure 7.9 - Deflection and stress distribution of three-unit cantilever with normal level of bone support and two abutment teeth [91].

Another important conclusion, and that the authors were able to conclude by varying the number of abutments, is that when two support teeth are used, connected with each other and with the pontic tooth, the stress concentration and displacement are reduced. The use of three abutment teeth allows optimum stress reduction but the increase of supporting teeth above three does not result in reduction of stresses [91,88]. In some studies, the number of pontics is also varied concluding that increasing the number of pontics increases stresses markedly, so long cantilever bridges are not advisable [91].

Yang et al. (1996) and Wang et al. (1998) also studied the level of bone support, verifying that reduced bone support increases the stress concentration [91,88].

Natali et al. (2006), evaluated the relevance of stress states induced in cantilever bridges, supported by implants, by a misfit. Both mesial-distal and lingual-labial misfits were considered and these induced significant stress effects on the peri-implant bone tissue. Thus, to ensure the reliability of the prosthetic system, it is necessary to consider the possible misfit that may occur, and which is comparable with occlusal forces [92].

Zhang et al. (2015), studied different distributions of zirconia in cantilever bridges to increase the mechanical resistance of these bridges, thus minimizing the fracture risk. It was already mentioned the high stress concentration occurring in the connector between the pontic and the first abutment, which could potentially lead to a crack initiation in that site. As such, the authors developed optimized designs with different volume fractions of zirconia, which was gradually added in the areas of high stress concentrations. It was found that as the volume fraction increases, the peak tensile stress substantially decreases [89].

Henyš et al. (2017) studied a mandibular cantilever bridge with six units subjected to fatigue cycles verifying that in an extreme situation of a bite force of 1280 N, the bridge failed in less than one day. As such, it becomes extremely important to consider the dynamic character of bite forces and the fatigue damages, due to excessive biting force, as failure factors of dental bridges [93].

With all these studies is possible to conclude that there are many factors that can influence the success of cantilever dental bridges, such as: bone support; size of the connector; materials

used; and number of pontics and abutments. Therefore, this type of studies is relevant, because they can help to find out ways of improving dental restorations, leading to higher survival rates.

7.1.6.1.2 - Fixed-fixed bridges

Most studies regarding fixed-fixed bridges analyse bridges located in the posterior part of the mandible, since the masticatory forces applied here are very high [9,94,95,96,97]. In these studies, it was verified that connectors in FPDs are the weakest areas and responsible for failure in most cases, once this is the area with highest stress concentration, like verified in cantilever bridges. Rappelli et al. (2005) concluded that stresses are concentrated in the connector areas and in the prepared teeth. The peak stresses are at the cervical margin of the preparation [95].

It becomes imperative to optimize the design of connectors leading to higher strength and better performance of FPDs [96]. In this way, many studies focused on connector design. Chun-Li Lin et al. (2005) studied different design parameters of the bridge, to understand if any of them would influence the stress distribution at the bridge. Thus, the thickness, height and angle of the axial surface extensions were varied, as shown in Figure 7.10, concluding that the average stress values of the remaining tooth and prosthesis decreases with higher values of thickness and height. According to the authors, this phenomenon occurs because the increase of the thickness and height allow the bonding area between the enamel and the retainer to be maximized. However, no significant differences were found in the stresses with the increase of the angle since the stress transmission was concentrated in the connectors. The most relevant factor was height [9].
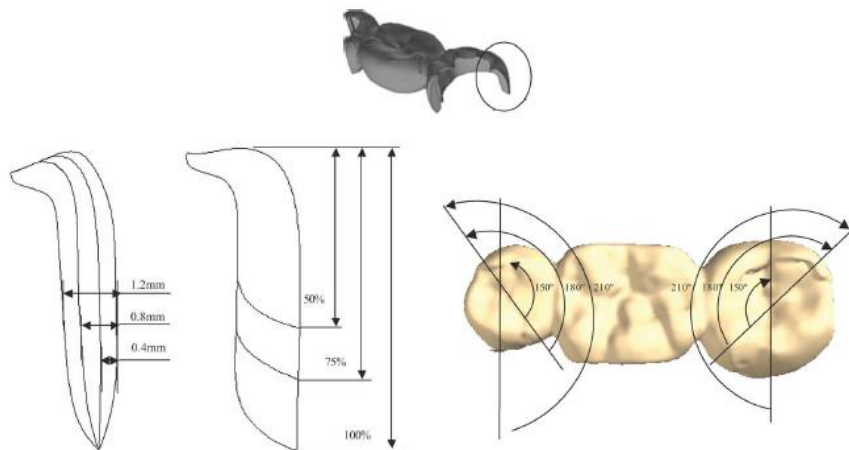
Figure 7.10 - Schema of prosthesis retainer design with different thickness, height and angle of axial surface extension (from left to right) [9].

Mokhtarikhoee et al. (2008) focused on the effect of connector width (in buccolingual direction) on stress distribution, concluding that decreasing the width of the connectors causes higher stresses. Therefore, wide connectors are highly recommended for clinical use since they reduce the risk of fracture. In this study they also verified that the stress distribution along the connector is not smooth, which means that different areas of the connector transmit different levels of stress. Thus, it is also necessary to analyse the cross section of the connector to find

its optimal shape, and it is also important to investigate the radius of curvature at the attachment point to the teeth [96].

Andrei et al. (2013) studied a fixed bridge replacing a lower first molar with the second premolar and second molar as the abutment teeth. Conclusions in this work went further than the works previously mentioned, since the authors concluded that maximum stresses and most movements occur in the mesial abutment tooth (second premolar in this case) [97]. This is because a molar is larger than a premolar and has two roots that provide better load distribution and lower stress concentration, leading to lower stress values at the connector with the molar than at the connector with the premolar [96]. For this reason, two mesial abutment teeth (first and second premolar) must be prepared so that the forces can be supported equally on both mesial and distal sides of the bridge [97].

Reimann et al. (2015) studied the effect of different connector geometries on strength of a prosthetic bridge, varying the cross-sectional area of the connectors and concluding that increasing the cross-sectional area causes a decrease in deflection and maximum stress. It was also possible to conclude that oblique forces cause higher stresses than vertical forces [98].

Some authors focused also in the materials used in FPDs. In the study of Rappelli et al. (2005) the FPD was constituted by Fibre-reinforced composite inlay, since these materials appear to have a better stress distribution than other materials, such as composites, glass ceramics, gold, alumina and zirconia. Thus, the stress concentration in this type of bridges is correlated to abutment design and, clinically, the results suggest that the inlay design of abutment teeth should provide the maximum fibre reinforcement and that, whenever possible, the cervical margin should be located on the enamel [95]. Nuno Calha et al. (2014) studied the effects of functional loading on a fixed anterior zirconia bridge since this material has very attractive aesthetic characteristics. The authors found that for loads above 200 N, the movement tends to obtain a non-linear form, which may indicate that zirconia can improve the rigidity of the bridge. However, framework design should be analysed to lower strain values and reduced micromovements under functional loads [99]. Reimann et al. (2015) studied the impact of the properties of different metal alloys on deflection of the prosthesis. The increase of the Young's modulus causes a decrease in deflection [98]. So, the deflection of the bridges depends on the cross-sectional area of the connectors and the Young's modulus of the chosen material [98].

Yang et al. (1999) studied fixed-fixed dental bridges with the aim of understand the effect of different levels of bone support and different numbers of abutment teeth on deflection and stresses generated in the teeth and their supporting structures. Similar to cantilever bridges, the loss of bone support increased the deflection and stresses generated in the constituent structures of the model. However, when the bridge was placed a reduction of stress and deflection was seen in the supporting structures. By increasing the number of abutment teeth, mesial stresses and deflection generated in the supporting structures decreased but increased in the prosthesis. As such, with this type of bridges, it was also concluded that the increase of the abutment teeth does not translate into a proportional reduction of stress in the periodontium and stress concentration is located in the connectors of the prosthesis and in the cervical dentin area [94].

Misfit of the bridge onto osseointegrated implants can also occur in FPDs, as such, Pietrabissa et al. (2000) studied the biomechanical effects induced by a misfitting bridge, using different models with different types of misfit, concluding that the method developed by them

can help to estimate the distribution of stresses in the bridge and bone as consequence of different types of misfits [100].

7.1.6.2 - Resin-bonded bridges

If the bibliographic search (using *Scopus* database) is further narrowed, searching computational FEM analyses of "resin-bonded bridges", the number of papers published is very low, as seen in Figure 7.11. The reduced number of published works may indicate that this is an area to be explored.
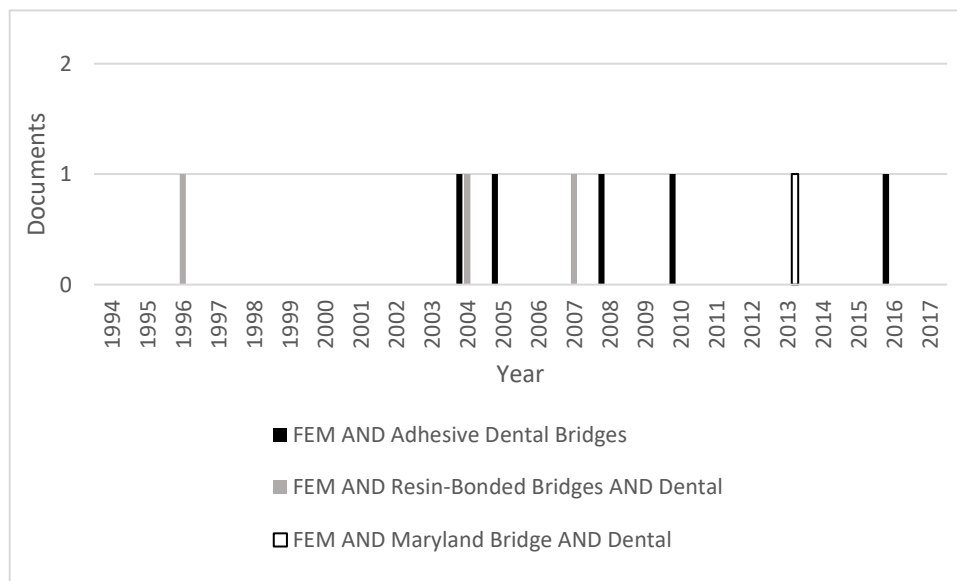
Figure 7.11 - Number of documents published through the years, in the subjects indicated. The data was obtained through a research on *Scopus* database (www.scopus.com) assuming as keywords the subjects indicated in the graph.

AFPDs can be a good alternative to traditional bridges previously discussed and analysed. However, as has been seen previously (in section 3.2.1), there are many factors that affect the success of such bridges.

One of the factors that could affect the success of AFPDs is different abutment preparation configurations. However, Magne et al. (2002) verified that no significant differences were detected between the various preparations tested, which means that more extensive preparations did not result in a better stress distribution [101].

The bridge construction also seemed to be relevant, but Śmielak et al. (2016), studied several 2D models, varying the bridge construction. The bridge was supported on crown inlays or onlays[2] and no great differences were found [11].

The materials used are one of the most relevant factors. Maryland-bridge is one of the most extensively adopted AFPDs, however as an alternative, direct FRC bridge has become a viable

---

[2] Inlays are indirect restorations fitted to a cavity inside the tooth and onlays fit around the outside portion of the tooth, incorporating a replacement for a tooth cusp.

alternative, promoting a "one-appointment" technique for temporary or midterm resin-bonded bridges [102]. That is why many authors studied FRC AFPDs.

Some authors compared FRC with other materials, concluding that in none of the cases stresses seem capable of damaging the bridge, however lower stresses were found when FRC were used [101,11].

W. Li et al. (2004), study the role of fibres in structural responses by modelling single-fibre and double-fibre designs, concluding that the design of the fibres did not influence significantly the value of the maximum principal stresses [44].

Many investigators tried to develop an optimized design, which includes thickness, position and orientation of the fibres. To do so, it is necessary to know the locations of higher stresses and directions of maximum principal stresses, with the aim of align the fibres directions with those of the maximum principal stresses, thus developing an optimized design of FRC. Therefore, it was verified that high tensile stresses can be found in the bottom of the pontic and in the connectors, that link the pontic to the abutment teeth. With these findings, the fibres should be placed in the bottom of the tooth, and not in the upper part, forming a U-shape substructure that extends into the connectors, with greater reinforcement in the connectors. The direction of the fibres should follow the principal stresses shown in Figure 7.12. With this new design, there was indeed a reduction of stresses both in the veneering composite and at the interface between the veneer and the FRC substructure. The optimized design can improve fracture resistance of FPDs by reducing some of the failure-initiating stresses [103,8].

(a)

(b)
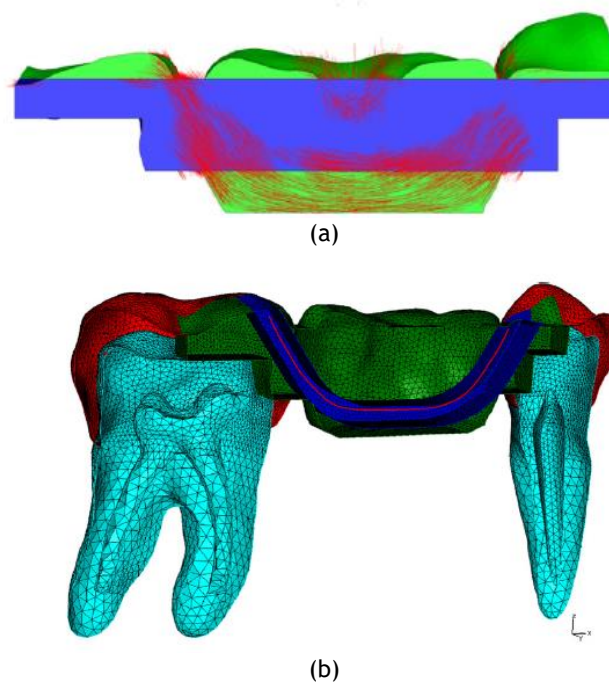
Figure 7.12 - (a) Directions of the maximum principal stresses; (b) Optimized FRC FPD design [8].

Magne et al. (2002), went even further and performed an optimized design in which contact of the fibres with the pulpal wall was avoided, leading to a better stress distribution by reducing the tensile stress peaks at the interface [101].

Nakamura et al. (2005), varied the veneering composite, using two types, one with high Young's modulus and one with low Young's modulus. The use of veneering composite with

higher Young's modulus resulted in lower tensile stresses in the FRC, thus reducing the risk of fracture [103].

Lopes et al. (2014) studied this type of bridge, but considering another type of material, all-ceramic. The bridge analysed had a zirconia framework veneered with feldspathic ceramic and the bridge design included the entire lingual surface of the abutment teeth to maximize the contact area for adhesion. The results demonstrated that the area of the connectors should be as wide as possible and that these ceramic materials are capable of withstanding occlusal loads [104].

The mechanical properties of adhesive resin cements can also affect stress distribution in AFPDs. Yokoyama et al. (2012), tested two adhesive resin cements in FRC AFPDs, one of which had a Young's modulus approximated to that of the hybrid composite that embedded the fibres, resulting in a more homogeneous and regular distribution of stresses at the bonding interfaces. So, this exhibits better stress distribution, reducing stresses in the connector area and did not create large differences in stress values at the bonding interfaces of the retainers. Therefore, it can be concluded that the mechanical properties of the adhesive resin cements play an important role in the stress distribution and as such the safety and longevity of AFPDs depends on the choice of the adhesive resin cements with the appropriate mechanical properties for each case [36].

As it can be verified, FEM has been widely used for many years. Namely in dentistry, FEM has allowed to understand complex processes and has assisted researchers in looking for better procedures to preserve oral health. The validity of this method has been a concern for decades and, as such, FEM does not replace laboratory studies since these are important to prove the validity of this method and its results. With the advancement of computing power, this will be a tool that will continue to be used and may still be associated with clinical evaluations as a diagnostic tool or treatment planning [16].

However, there are still many areas of dentistry with many unanswered questions and where new studies are required. Besides that, further developments, such as robust solid models, with increased capability to manipulate CAD objects, are still necessary and will also allow increased research [16].

Thus, computational techniques are important for studying fracture patterns, predicting the behaviour of a treatment, failure of certain restoration techniques, normal functioning, property-structure relationships, or tissue response to stress and strain [16]. FEM has followed the evolution of the technology. However, there are other numerical methods that can be applied as is the case of Meshless methods.

7.2 - Meshless

As was seen in Chapter 1 , through Figure 1.1, this advanced discrete method has not yet been widely used in dentistry.

Therefore, most of the work done so far was to validate this approach. The results obtained in different analysis - by using this advanced discretization computational technique - were compared with those obtained either experimentally or with other numeric methods. Meshless methods proved to be useful for: (1) the analysis of the biomechanical behaviour of dental prostheses [105]; (2) predicting the loads that should be applied to dental implants to maximize bone density near the implant (by combining meshless methods with bone remodelling algorithms) [106,107]; (3) predicting osseointegration around the contact area between bone

and implant [108]; (4) studying the interactions between bone tissue and an implant, which will allow to select the best clinical solution (by combining meshless methods with an elasto-plastic model) [46]; (5) predicting the biomechanical behaviour of restored teeth [45,109,110]; and (6) predicting the principal and secondary trabecular structures (by combining meshless methods with bone remodelling algorithms) [108]. Like in FEM, it is imperative to consider the presence of adjacent teeth, since these are important for the prevention of possible fractures [109].

It is also possible to apply meshless methods to the study of different properties of bone tissue - simulating different possibilities of bone behaviour - and of different restorative materials. Studying these topics showed that the increase in trabecular bone rigidity induces higher stresses in the PDL and lower stresses in the neck of the tooth. For restorative materials, materials with higher Young's modulus induce higher stresses in the artificial cap and smaller stresses in the biological structures. According to the literature, bone remodelling is stimulated by inflammatory processes in the periodontal tissues, so restorative materials with a lower Young's modulus should lead to greater bone remodelling [34].

Meshless were also used to study dental bridges, as the work done by H.M.S. Duarte et al. (2013) that analysed a cantilever bridge supported by two implants [111]. In that research work, the bar material was varied, and the bridge was subjected to two different load cases. It was possible to verify that as the stiffness of the bar material increased, the stresses in the bone tissue also increased and the stresses in the implants decreased [111].

Despite the positive results obtained, Moreira et al. (2013) analysed the behaviour of the meshless methods in the analysis of a central incisor and concluded that these advanced numerical methods are appropriate for the study of dental structures, but it is still necessary to overcome some numerical problems, like the presence of convex boundaries [112].

In my best knowledge, there are no documents regarding the study of adhesive dental bridges and meshless. Several searches were performed in *Scopus*, *ScienceDirect*, *Elsevier* and *Springer* databases of scientific and medical research, and no documents were found dealing with "adhesive dental bridges and meshless", meaning that there is a gap in this research topic, that this work intends to fulfil.

Chapter 8

Elasto-static numerical analysis

As previously mentioned, Maryland bridges can be an alternative solution to conventional bridges or even implants, but it must be guarantee the mechanical resistance of the bridge, to obtain a long and functional replacement. Therefore, in this chapter, it will be presented all the elasto-static numerical analysis performed.

First, two preliminary works are presented. The elaboration of these studies allowed to acquire competences and a proficient level in several computational mechanics software, such as Mimics, 3-Matic, FEMAP and FEMAS (Finite Element and Meshless Analysis Software, which is an academic software capable to perform several kinds of computational mechanics analysis, using both the FEM and meshless methods - more details in cmech.webs.com). With these analyses, it was possible to understand the influence of the inclusion of support structures in the analysis model. It is important to define which dental structures should be included in an analysis model, allowing to know the possible simplifications that can be implemented.

Then, a 2D model and a 3D model were developed with the main objective to study the influence of different parameters, such as the resin-cement used, the design of the bridge (two-retainer design or single-retainer design) and the thickness of the adhesive, on the mechanical resistance of an adhesive dental bridge. Moreover, three numerical methods were used (FEM, RPIM and NNRPIM), to compare them and understand the level of performance of meshless methods.

8.1 – 3D finite element analysis of maxilla model

Frist, a 3D model was developed with the purpose of testing if the abutment teeth can support the resin-bonded bridge, used in dental restorations.

The most relevant advantage of this type of bridges is the minimal required preparation of the adjacent teeth, which is healthier for these teeth that will serve as a support, since it avoids the removal of a large amount of enamel and dentin. However, these bridges can only be used when the abutment teeth are healthy or with very small fillers. This is because when using this method, the load applied on the pontic will be transmitted to the adjacent teeth trough the bridge.

The study was conducted on a 3D model of a part of maxilla where a tooth was missing, and it was used the FEM. So, it was obtained a model consisting of the maxilla bone, the central incisor and a canine, missing the lateral incisor, as seen in Figure 8.1(a). It was only considered three materials (cortical bone, trabecular bone and dentin), represented with different colours in Figure 8.1(b). In the same figure, it is also possible to observe the mesh. In the present study, it was considered the following material properties: for dentin, $E = 1.86 \cdot 10^4$ MPa and $\upsilon=0.31$; for cortical bone, $E = 1.1 \cdot 10^4$ MPa and $\upsilon=0.30$; for trabecular bone, $E=1370$ MPa and $\upsilon=0.30$ [11]. The theoretical ultimate tension stress of each material is indicated in Table 8.1.

(a)   (b)
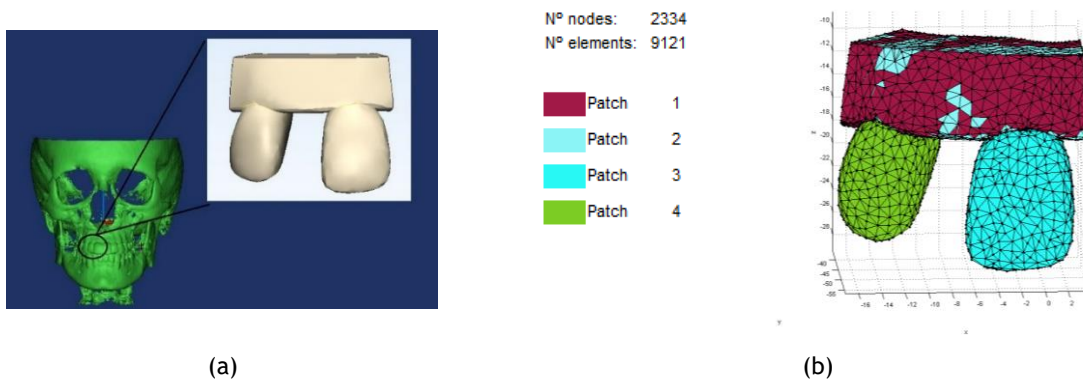
Figure 8.1 - Model used in this study with its description: (a) Model obtained; (b) Mesh and materials description. Patch 1 corresponds to cortical bone, patch 2 corresponds to trabecular bone and patch 3 and 4 to dentin.

Table 8.1 - Ultimate tension stress of each material [11,113].

Part of the model	Material	Ultimate tension stress (MPa)
Bone	Cortical Bone	300
	Trabecular Bone	150
Teeth	Dentin	105.5

For the case studied, the boundary conditions considered were applied on the top and on both sides of the bone, preventing either the rotation or the movement in any direction, as shown in Figure 8.2.
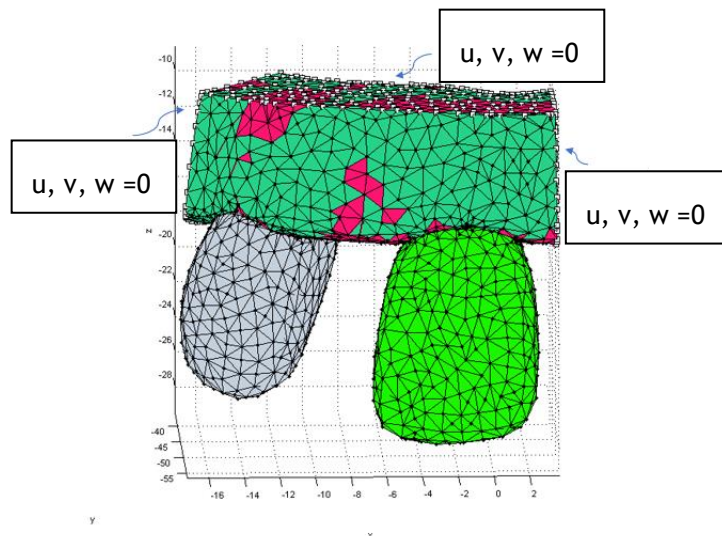
Figure 8.2 - Boundary conditions.

For the stress analysis, two sets of loads were applied: (1) the loads applied correspond to the distribution of loads applied to the pontic; and (2) the loads applied directly to each abutment tooth.

As mentioned previously, the loads applied to the pontic, because of chewing, are (in a simplistic way) uniformly distributed to the abutment teeth through the bridge. So, a bite force of 100 N, means that each abutment tooth will support 50 N. Therefore, it was applied a force of 25 N, in the direction of the Z axis, on the front and back of each tooth, as showed in Figure 8.3(a).

The abutment teeth, in addition to the loads that will be transmitted through the bridge, must also be able to withstand the loads directly applied to them. Thus, it was added to the initial forces a new set of forces, shown in Figure 8.3(b), corresponding to the force applied directly to each of the abutment teeth during a bite. According to [102], the bite force has an orientation of 26° with respect to the longitudinal axis of the abutment teeth. So, each abutment tooth was subjected to a force of 150 N.

(a)

(b)
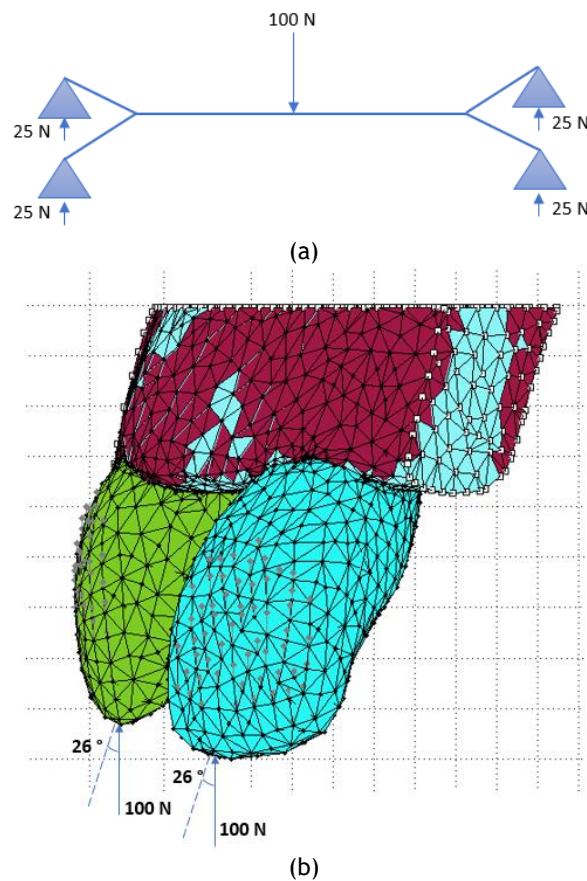
Figure 8.3 - Load cases used in the study: (a) Representative schema of the distribution of loads in case 1; (b) Additional forces applied to the model in case 2.

To facilitate the interpretation of the results obtained, the analysis was performed for each teeth and surrounding bone separately. This means that it was examined a set of two variable fields: (1) the stresses obtained in the central incisor and the bone that surrounds this tooth; and (2) the stresses obtained in the canine and the bone surrounding this tooth. Then, for each mentioned analysis, points belonging to the bone and the tooth were selected. In Figure 8.4 it is possible to visualize the results obtained.

(a)

(b)

(c)

(d)
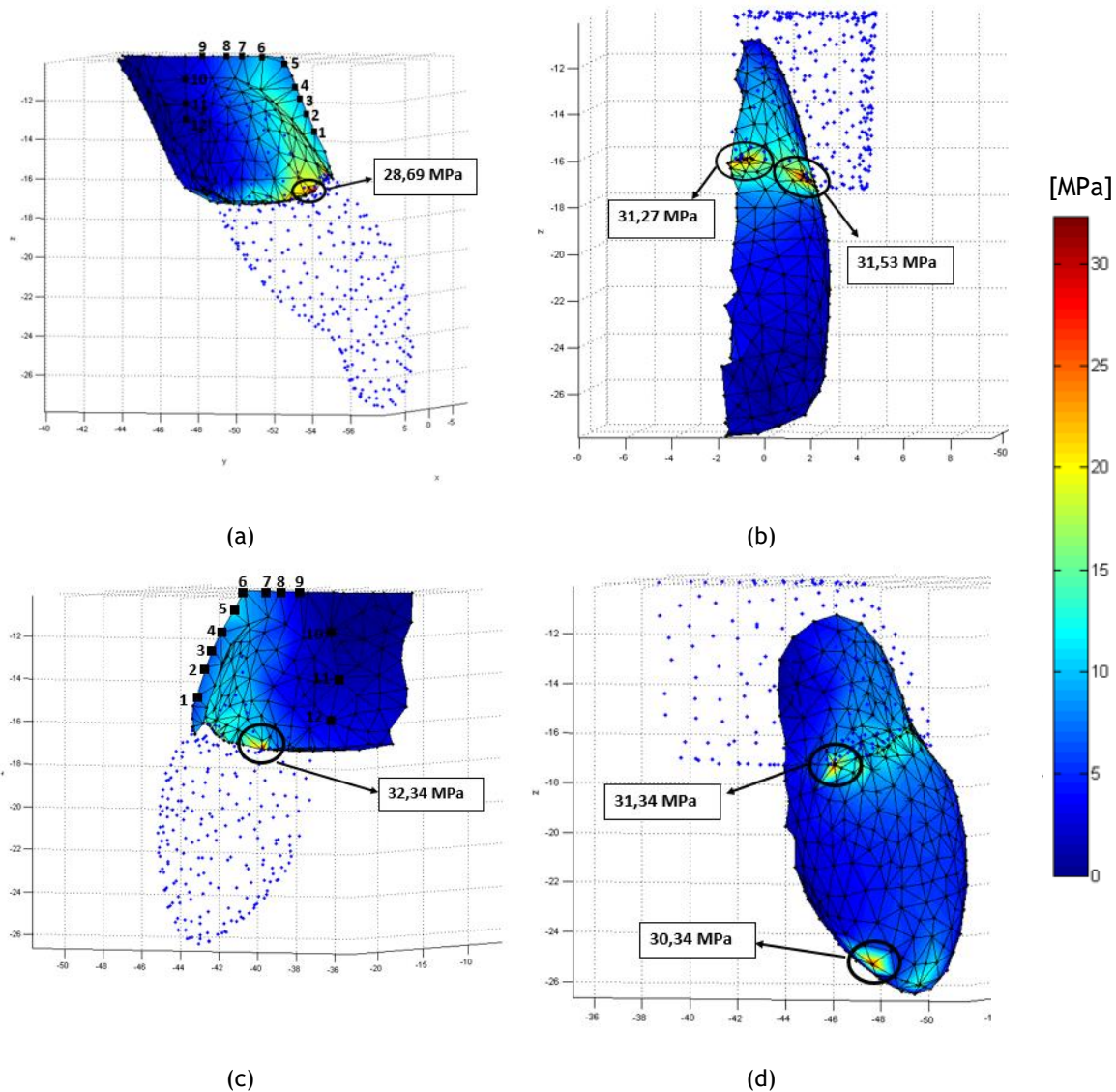
Figure 8.4 – von Mises stresses maps obtained: (a) Stress map obtained to the bone surrounding the central incisor and selected points to analyse [MPa]; (b) Stress map obtained to the central incisor with maximum stresses selected [MPa]; (c) Stress map obtained to the bone surrounding the canine with selected points to analyse and maximum stress selected [MPa]; (d) Stress map obtained to the canine with maximum stresses selected [MPa].

The obtained stresses did not exceed 33 MPa. Comparing the stresses obtained throughout the model with the theoretical ultimate tension stress of each material, indicated in Table 8.1, it can be concluded that for the numerical conditions assumed, there is no risk to the maxilla or to the abutment teeth, since the stresses obtained are much lower than the ultimate stresses tension of each material.

So, with this study, it is possible to conclude that the abutment teeth can support the loads applied, these loads will not damage the abutment teeth and the use of resin-bonded bridges seems to be a viable method for dental reconstruction.

Since the maximum stresses were found in the cervical region of the teeth and bone, a possible simplification to be implemented in an analysis model would be the removal of the support structures of the tooth, being the simplified model composed only by the teeth. This simplification would allow to create a more refined mesh in this area of interest.

8.2 - A computational strain analysis of PDL

During the development of this work, a computational strain analysis of PDL was developed with the objective to understand the computational advantages and disadvantages of include this dental structure in virtual models. Not including the PDL on the model oversimplifies the models. However, the PDL shows a very complex behaviour, being nonlinear, inhomogeneous and anisotropic [64].

The study was conducted on a 2D model of a mandibular premolar tooth. The geometry of the tooth and surrounding tissues were obtained from literature [19]. As it is possible to observe in Figure 8.5(a), the model simulates a mandibular premolar tooth inserted in trabecular bone (material 2) with a thin layer of cortical bone (material 1). Other main structures represented are: the enamel (material 4), the dentin (material 5), the pulp (material 6) and the PDL (material 3). In the present study, the following material properties were considered: for enamel, E=41000 MPa and υ=0.31; for dentin, E=18600 MPa and υ=0.31; for pulp, E=3 MPa and υ=0.45; for PDL, E=0.0689 MPa and υ=0.49; for cortical bone, E=13700 MPa and υ=0.30; for trabecular bone, E=1370 MPa and υ=0.30 [114].

(a)   (b)
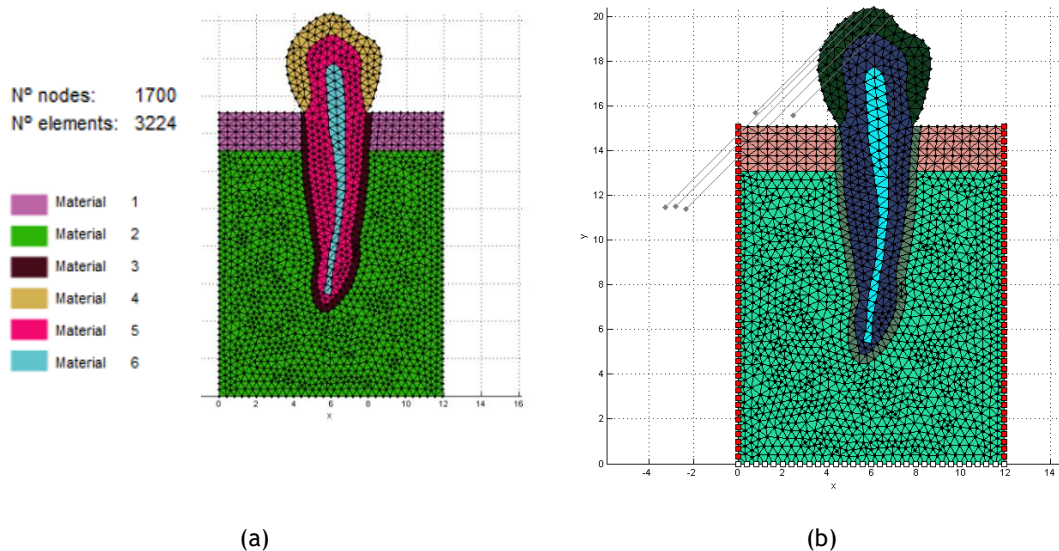
Figure 8.5 - (a) model used in this study with its description; (b) boundary conditions and load cases applied.

The bottom nodes of the model were constrained in both the Ox and Oy directions and the side nodes were only constrained in Ox direction. It was applied a load of 100 N on the top of the tooth's crown with a 45°- degree inclination with the longitudinal axis of the tooth. The load applied corresponds to a compressive force, as is possible to see in Figure 8.5(b).

The results obtained are represented in Figure 8.6. To accurately simulate the PDL, it is necessary to include incompressibility conditions and hyperelastic constitutive models. In this work, it was assumed the 2D plane strain deformation theory, which allows to impose quasi-incompressible condition by approaching the Poisson ratio to 0.5. As shown in Figure 8.6(b), by approximating the PDL Poisson ratio to 0.5, an approximated incompressible behaviour starts to occur. However, there is still a slightly deformation of dental tissues, which in reality does not occur.

(a)   (b)
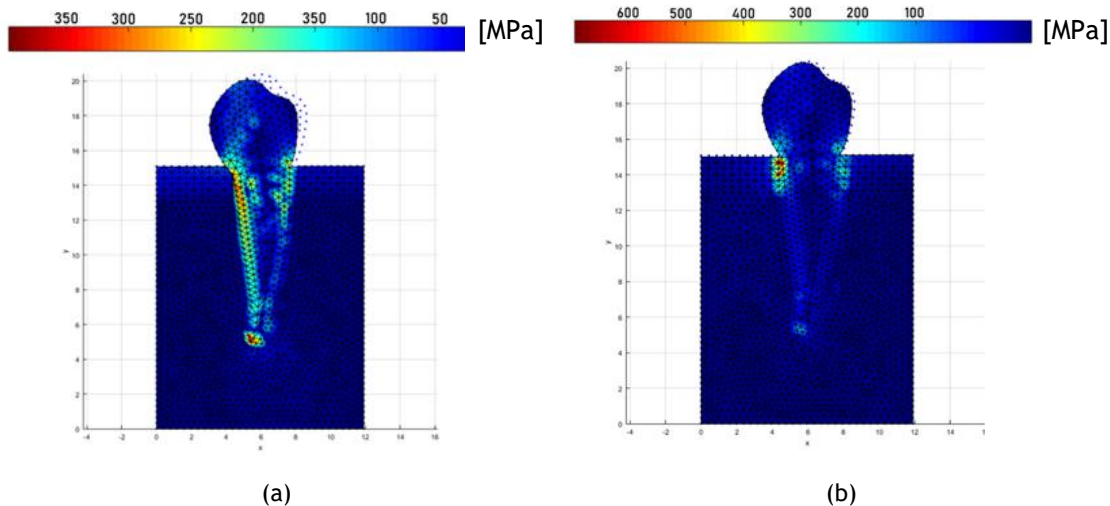
Figure 8.6 - Stress map obtained for: (a) $\nu = 0.4999$; (b) $\nu = 0.499999999$.

The software used to perform these analyses was FEMAS (program developed at FEUP and implemented in the commercial software Matlab), which does not include incompressibility conditions and hyperelastic models. Therefore, the PDL suffers volume variations, numerically penetrating the bone, which in real situations does not occurs. Thus, the inclusion of the ligament under these conditions may influence negatively the obtained results. Thus, once again, during the teeth's model construction, a simplification that could be implemented would be the disregard of the supporting structures, including only the areas of highest interest – the teeth crowns.

8.3 - 2D study of the structural response of an adhesive dental bridge

This study aimed to simulate the effect of the adhesive's thickness, as well as the adhesive material used, on the mechanical resistance of a resin-bonded dental bridge.

A single-retainer design was introduced in the beginning of the 1980s, to try to avoid the debonding of one of the retainer wings, which frequently occurred in the two-retainer design [115]. Therefore, both designs were also simulated.

A 2D model was constructed based on an orthopantomography of an unknown patient. Through this medical imaging exam and an image analysis software, it was possible to obtain the measurements and geometry of each teeth considered. Based on the results obtained in the elasto-static analysis previously mentioned, in this model only the teeth crowns were considered.

The obtained model consists of a mandibular central incision, lateral incisor and canine. In this model, the central incisor and the canine represent the abutment teeth, and the lateral incisor represents the pontic tooth. Moreover, wings were built on each side of the pontic tooth, thus simulating the presence of the adhesive, as represented in Figure 8.7.

To avoid the construction of several models with different adhesive's thicknesses, a single model was constructed in which each wing was divided into four parts, each one with 0.1 mm, as demonstrated in Figure 8.7. Therefore, the thickness of the adhesive was varied from 0.1 mm to 0.4 mm.
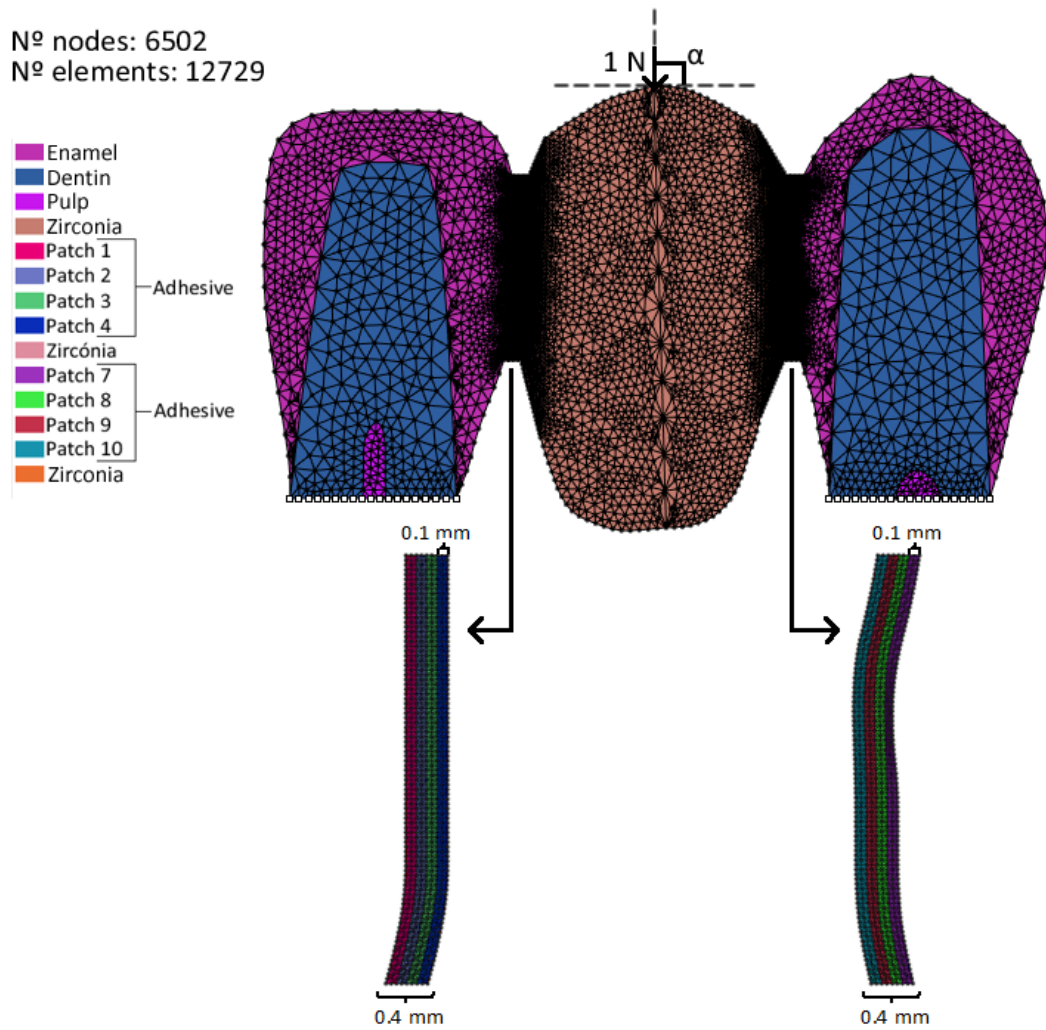
Figure 8.7 - Representation of the global 2D geometric model, boundary and load conditions considered and element mesh. The list of materials is specified, and the wings are shown with more detail.

With this generic model, it was possible to simulate eight different models, all represented in Figure 8.8, by varying the mechanical properties of the patches that compose the retainer wings. The material of the resin-cement was also varied, using the materials listed on Table 3.6, from section 3.3. Thus, considering for example the thickness of 0.1 mm and the presence of two wings: to patch 1 and 7 would be assigned the properties corresponding to the adhesive in question, and to patches 2, 3, 4, 8, 9 and 10 would be assigned the properties of zirconia (material considered for the pontic tooth). To simulate the presence of only one wing, to patches 7, 8, 9 and 10 were assigned the following properties: E=0.0841 MPa and υ=0.3, as a way of simulating the absence of the right retainer wing (notice that the elasticity modulus is much lower than any other elasticity modulus considered in the analysis).

The domain of the problem was discretized in a mesh of triangular elements, represented in Figure 8.7. In this study, only one unitary punctual load (1 N) was considered. Three load orientations, represented as α in Figure 8.7, were assumed: $\alpha = [45°, 90°, 135°]$. The bottom nodes, presented in the inferior bounds of the central incisor and the canine, were constrained in both Ox and Oy directions.
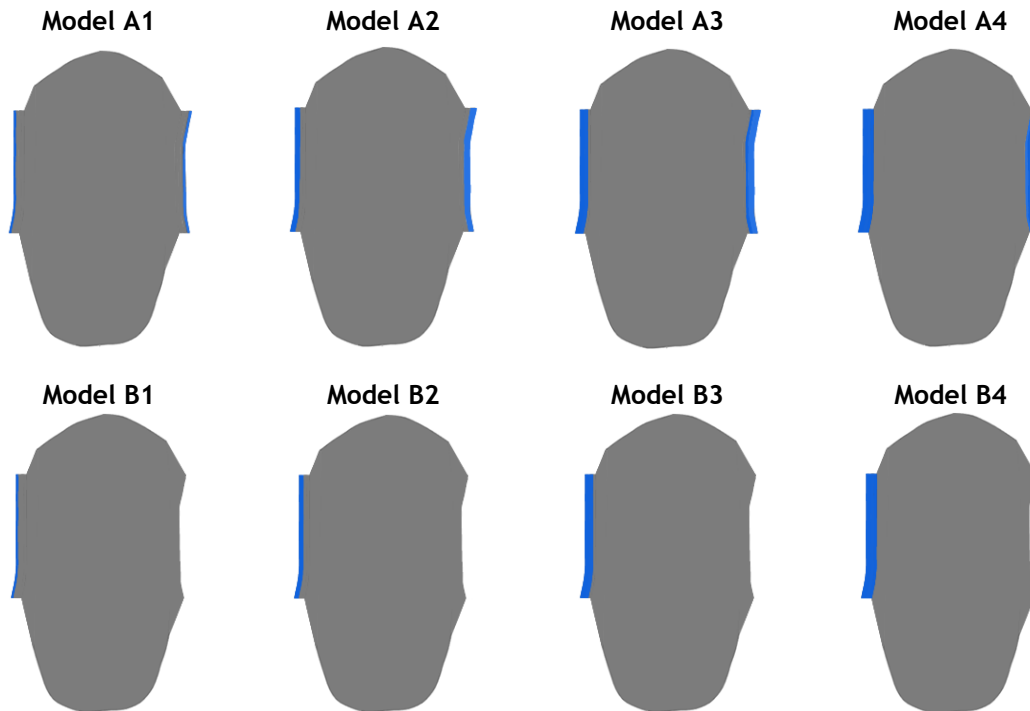
Figure 8.8 - Identification of the models used in this study. The models A represent the two-retainer design, and the models B simulate the single-retainer design. Notice the increase of the adhesive thickness from 0.1 mm to 0.4 mm, from models 1 to 4, respectively.

In this study, the materials considered have an elastic, homogeneous and isotropic linear behaviour. Thus, the properties considered were the Young's modulus and the Poisson ratio. These mechanical properties for the dental materials considered (indicated in Figure 8.7) are given in Table 3.4, from section 3.3. For the pontic, it was assigned the material Zirconia, whose properties are given in Table 3.5, from section 3.3. Lastly, for the adhesive was attributed the resin-cements presented in Table 3.6, from section 3.3. However, the resin-cements Brilliant and NC Coltène have the same linear behaviour, therefore these were considered as one resin-cement.

A static linear-elastic analysis was performed for three numerical methods: FEM, RPIM and NNRPIM. Thus, the results of all methods were compared, and their performance was evaluated.

With these analyses, it was possible to obtain the colour dispersion maps of principal stress σ_{11} of each model studied. The maps for all the models are presented in Appendix 1. In Figure 8.9 it is represented an example of these stress maps for models A4 and B4, and for the following parameters: (1) $\alpha = 90°$; (2) both resin-cements (Admira and Brilliant/NC Coltène); and (3) the three numerical methods: FEM, RPIM and NNRPIM.

As is possible to observe, the resin-cements present a similar behaviour. When using the single-retainer design, the maximum principal stress σ_{11} obtained is higher than the one obtained when using the two-retainer design. Moreover, in the two-retainer design, there is a high concentration of tensile stresses in the inferior part of the connector, in the interface between the adhesive and the pontic. This means that there is a higher probability of occur debonding between the pontic and the adhesive. While in the single-retainer design there is a high concentration of tensile stresses in the superior area of the connector, in the interface adhesive/abutment. Therefore, this is the area with higher risk of debonding. Also, for the two-retainer design, is possible to observe that the stress concentration has a U-shape, like what is verified in the literature [8].

Two-retainer design   Single-retainer design
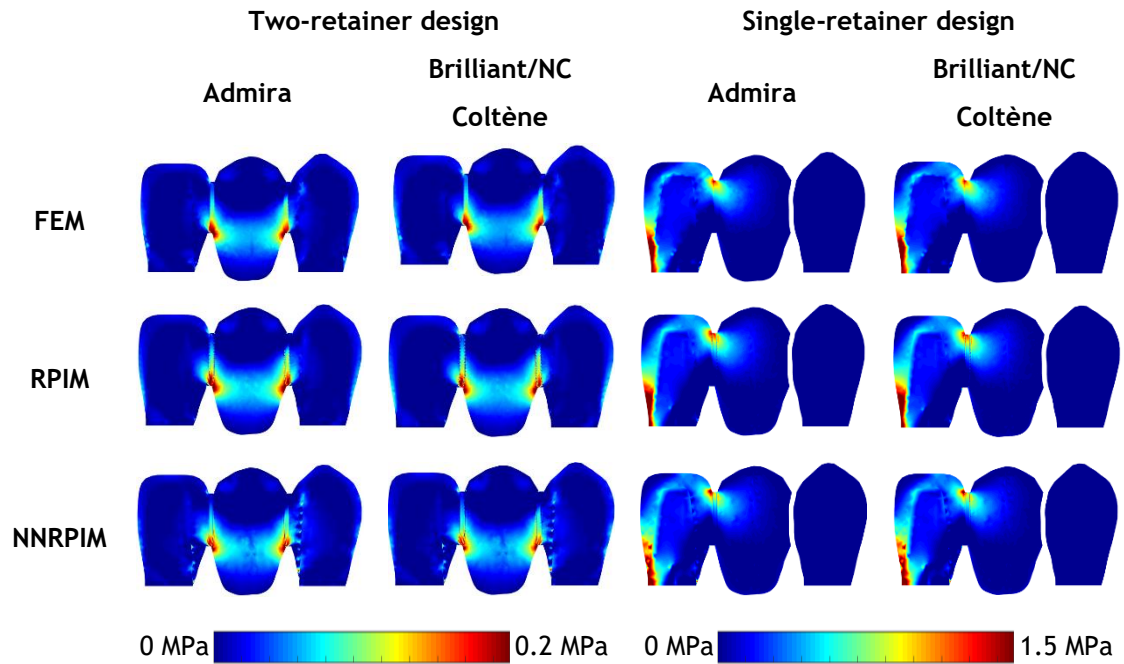
Figure 8.9 - Colour dispersion maps of principal stress σ11 for Model A4 (on the left) and B4 (on the right) and the following parameters: (1) α=90°; (2) both resin-cements (Admira and Brilliant/NC Coltène); and (3) the three numerical methods: FEM, RPIM and NNRPIM.

In Figure 8.9, for the single-retainer design, it is possible to observe a peak of stress concentration in the left inferior area of the central incisor. However, this is due to element mesh distortion and it is more evident for FEM. For the meshless methods, this mesh distortion is slightly smoothed, especially for NNRPIM.

The adhesive is the area with higher interest for this study. Therefore, to better evaluate the stress distribution along the retainer wings, it was graphically represented the principal stress σ11 and shear stress component τ_{xy} along a line of selected points from the retainer wings. The points were selected as demonstrated in Figure 8.10, thus 91 points were analysed from the top to the bottom of the adhesive, on both sides.
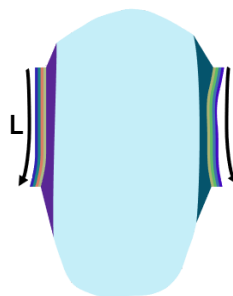
Figure 8.10 - The arrows the arrow indicates the direction in which the analysed points were collected.

The graphics for all the study cases are presented in Appendix 2 and Appendix 3. From these graphics, it was selected the ones regarding patch 1, since this patch is present in all simulations, regardless the adhesive's thickness.

In Figure 8.11 and Figure 8.12, it was analysed the σ11 and the τ_{xy} along patch 1, for α = 90°, and two-retainer design and single-retainer design, respectively. It was also varied the adhesive's thicknesses, the resin-cements and the numerical method.

Figure 8.11 - Graphic representation of principal stress σ11 and shear stress component τ_{xy}, in points along left retainer wing marked in figure as 'Patch 1', for models A1 to A4 represented in Figure 8.8 and the following parameters: (1) α=90˚; (2) both resin-cements (Admira and Brilliant/NC Coltène); and (3) the three numerical methods: FEM, RPIM and NNRPIM.

Figure 8.12 - Graphic representation of principal stress σ11 and shear stress component τ_{xy}, in points along left retainer wing marked in figure as 'Patch 1', for models B1 to B4 represented in Figure 8.8 and the following parameters: (1) α=90˚; (2) both resin-cements (Admira and Brilliant/NC Coltène); and (3) the three numerical methods: FEM, RPIM and NNRPIM.

With these figures, it was possible to observe, once again, that the resin-cements present a similar behaviour, in such way that the curves of the two resin-cements overlap each other.

For the two-retainer design it is possible to perceive that in the inferior part of the adhesive there is a concentration of tensile stresses, like it was verified in the colour maps of Figure 8.9. The shear stress component τ_{xy} is somewhat constant along the adhesive and no significant changes between thicknesses are verified.

For the single-retainer design, the superior part of the adhesive is subjected to tensile stresses, as verified in Figure 8.9. No significant changes in the values of the principal stress σ11 and the shear stress component τ_{xy} were verified along thicknesses. However, the values registered are considerably higher for the single-retainer design, especially for the τ_{xy}, which can lead to higher probability to occur debonding.

Regarding the numerical methods, important observations can be drawn. Regardless the design considered, it was possible to detect that with the increase of the adhesive's thickness, the results from the RPIM and NNRPIM approximate to the results obtained with FEM. RPIM presented more inconstant results, which was due to the lower thickness of the adhesive. Therefore, when the radial search is performed, the influence-domains of the point of interest include alternately nodes from the adhesive and the more resistant material, either enamel or zirconia, depending on the side. NNRPIM presents smoother and more precise results, when compared to FEM.

Other two load cases were analysed, for α = 45° and α = 135°. These loads intend to simulate the cases of bruxism, which is a medical condition that leads to shear overloads on teeth surface [45]. This condition can be responsible for the breakage of dental restorations, and therefore it becomes important to analyse it.

As it is possible to observe in Figure A.3, from Appendix 1, the load case α = 45° changes the stress distribution previously verified for the two-retainer design (Figure 8.9), as well as increases the maximum σ11. For the single-retainer design (Figure A.4, from Appendix 1), there is a concentration of tensile stresses in the inferior part of the connector and compressive stresses in the upper part of the connector. For the load case α = 135°, demonstrated in Figure A.5 from Appendix 1, the stress distribution is identical to the one previously verified for the single-retainer design (Figure 8.9), but with higher values of σ11.

In Figure 8.13 and Figure 8.14 it was analysed the σ11 and the τ_{xy} along patch 1, for α = 45°, and two-retainer design and single-retainer design, respectively. It was also varied the adhesive's thicknesses, the resin-cements and the numerical method.

In Figure 8.15, it was analysed the σ11 and the τ_{xy} along patch 1, for α = 135°, single-retainer design, 0.1 to 0.4 mm of adhesive's thickness, both resin-cements and all numerical method. For this load case it is sufficient to analyse the single-retainer design because for the two-retainer design, the load case with α = 45° is symmetric to this one.
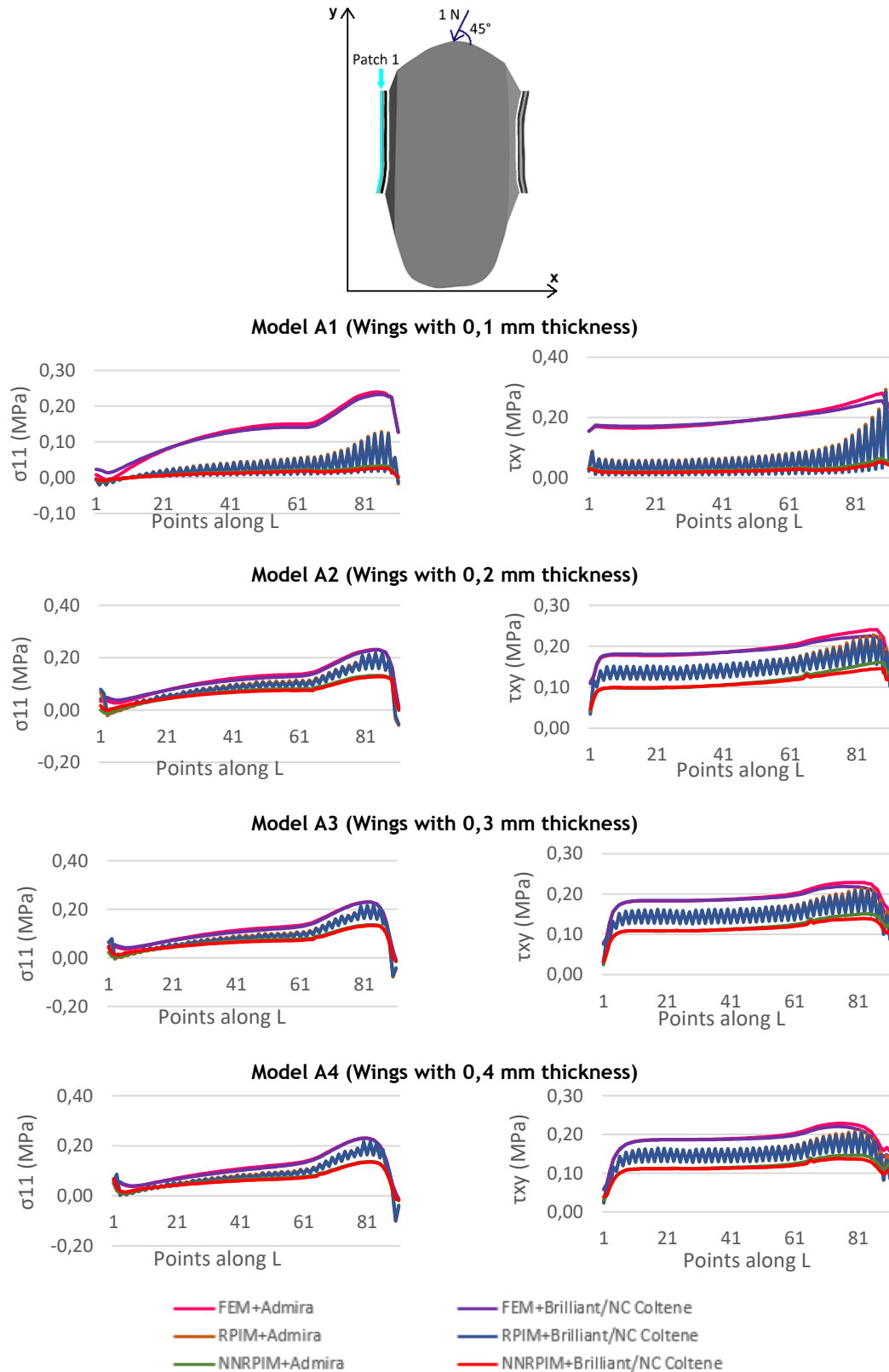
Figure 8.13 - Graphic representation of principal stress σ11 and shear stress component τ_{xy}, in points along left retainer wing marked in figure as 'Patch 1', for models A1 to A4 represented in Figure 8.8 and the following parameters: (1) α=45°; (2) both resin-cements (Admira and Brilliant/NC Coltène); and (3) the three numerical methods: FEM, RPIM and NNRPIM.
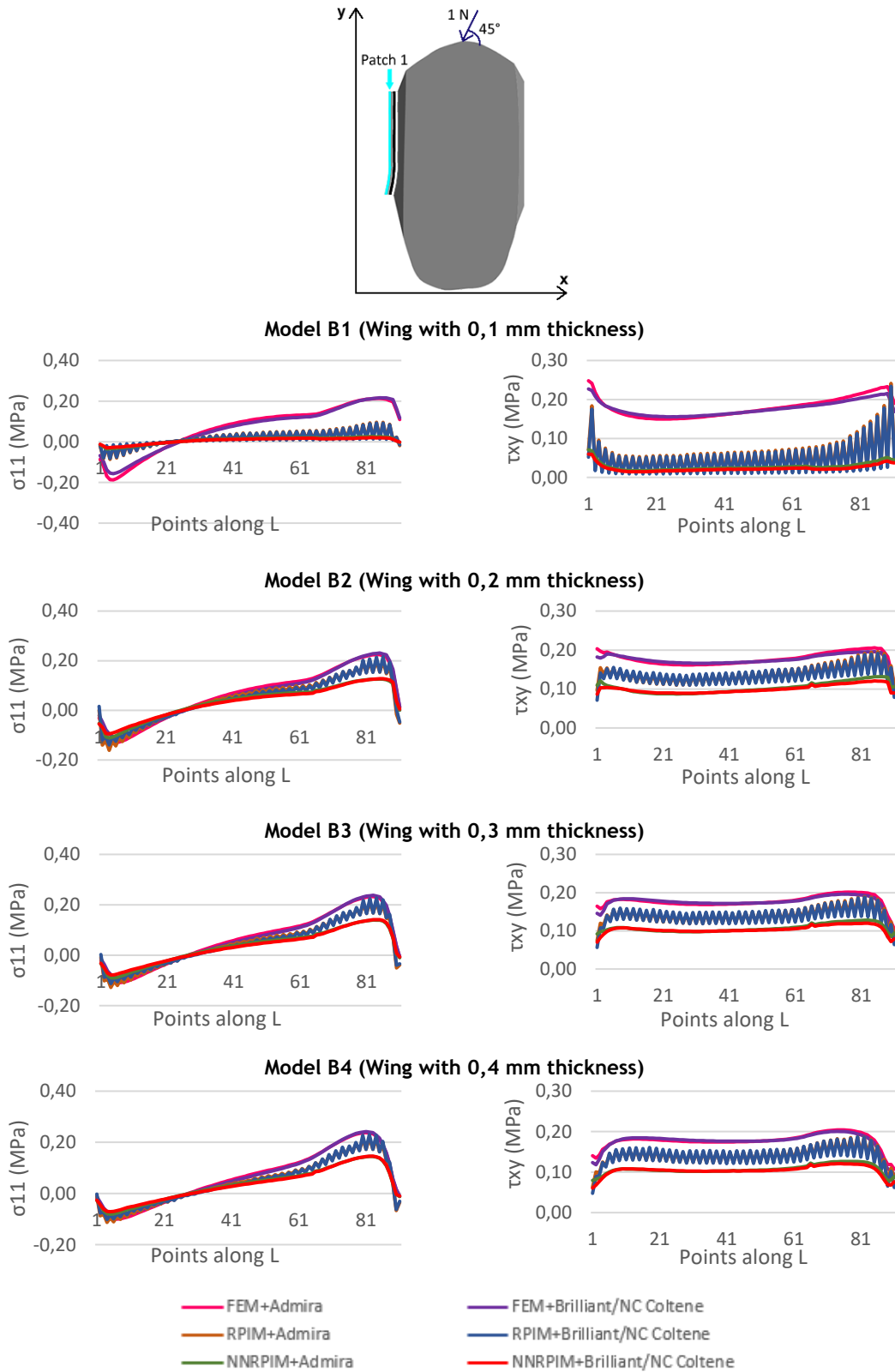
Figure 8.14 - Graphic representation of principal stress σ11 and shear stress component τ_{xy}, in points along left retainer wing marked in figure as 'Patch 1', for models B1 to B4 represented in Figure 8.8 and the following parameters: (1) α=45°; (2) both resin-cements (Admira and Brilliant/NC Coltène); and (3) the three numerical methods: FEM, RPIM and NNRPIM.

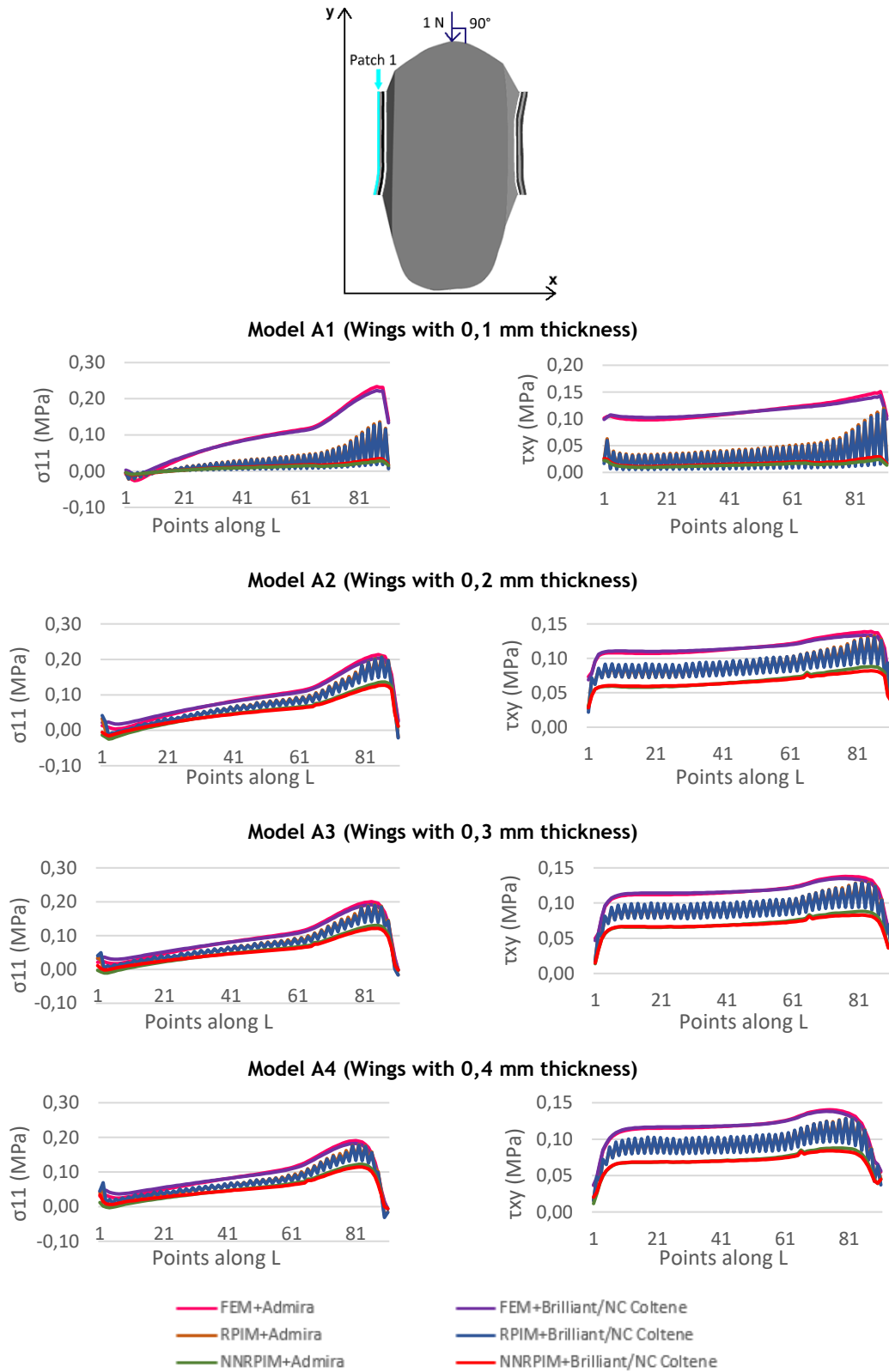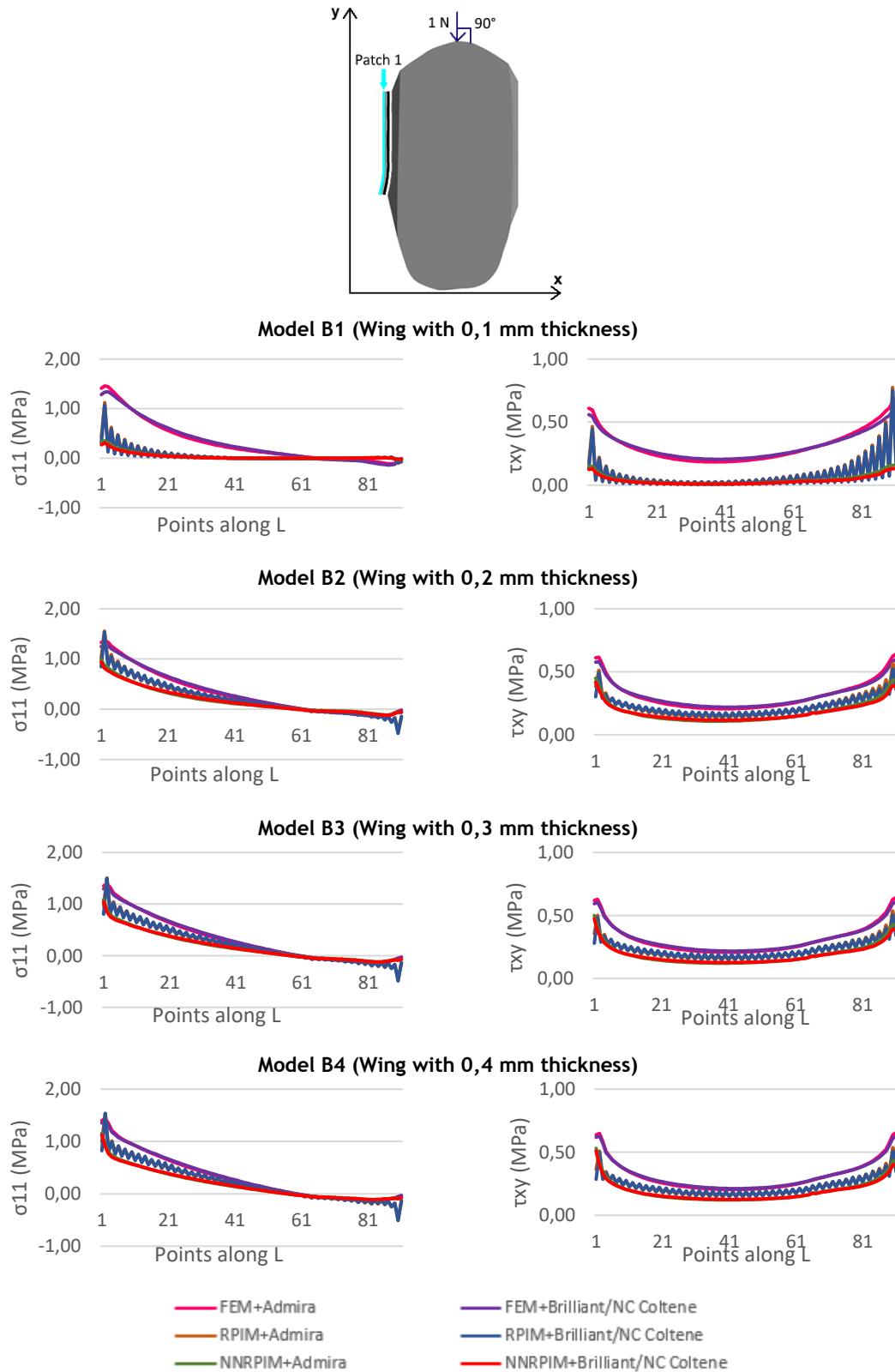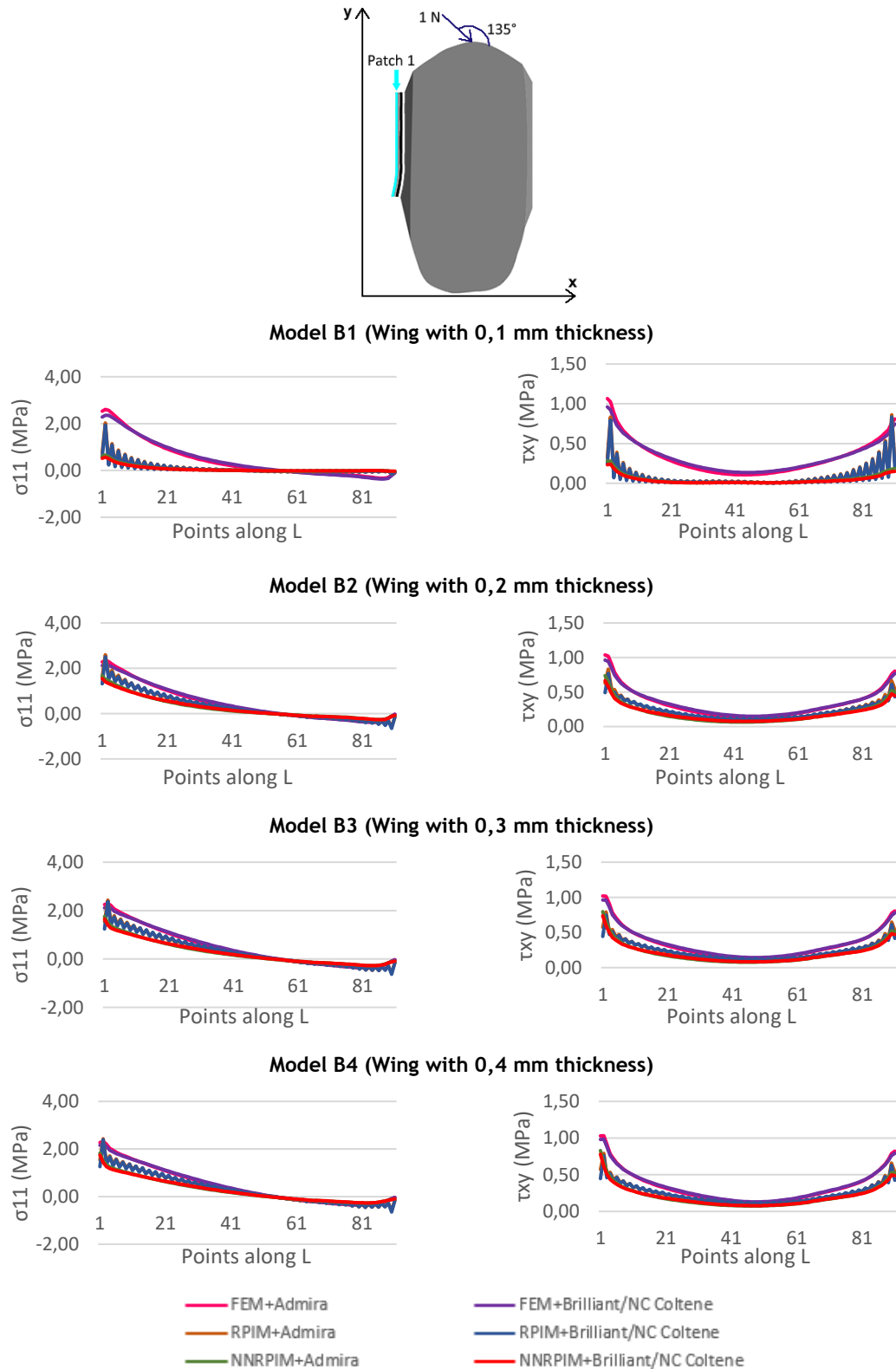**Figure 8.15** - Graphic representation of principal stress σ11 and shear stress component τ_{xy}, in points along left retainer wing marked in figure as 'Patch 1', for models B1 to B4 represented in Figure 8.8 and the following parameters: (1) α=135˚; (2) both resin-cements (Admira and Brilliant/NC Coltène); and (3) the three numerical methods: FEM, RPIM and NNRPIM.

It Is possible to verify that the two-retainer design presents a similar behaviour when subjected to the load α = 90° or α = 45°. The same happens for the single-retainer design that exhibits a similar behaviour for the load α = 90° and α = 135°. However, the main difference from the load case with α = 90° to the load cases with α = 45°/135° is in the values of σ11 and τ_{xy}, being this higher for the load cases with α = 45°/135°. This observation corroborates the hypothesis that bruxism increases the probability of dental prostheses failure once the higher values of τ_{xy} can be an indicator of higher probability to occur debonding.

The analysis of the σ11 and the τ_{xy} along patch 1 for all the study cases allowed to verify that single-retainer seems to increase the risk of debonding. Regarding the numerical methods, the same observations previously mentioned continue to be observed.

With the tables presented in Appendix 4, Figure 8.16 and Figure 8.17 were assembled.
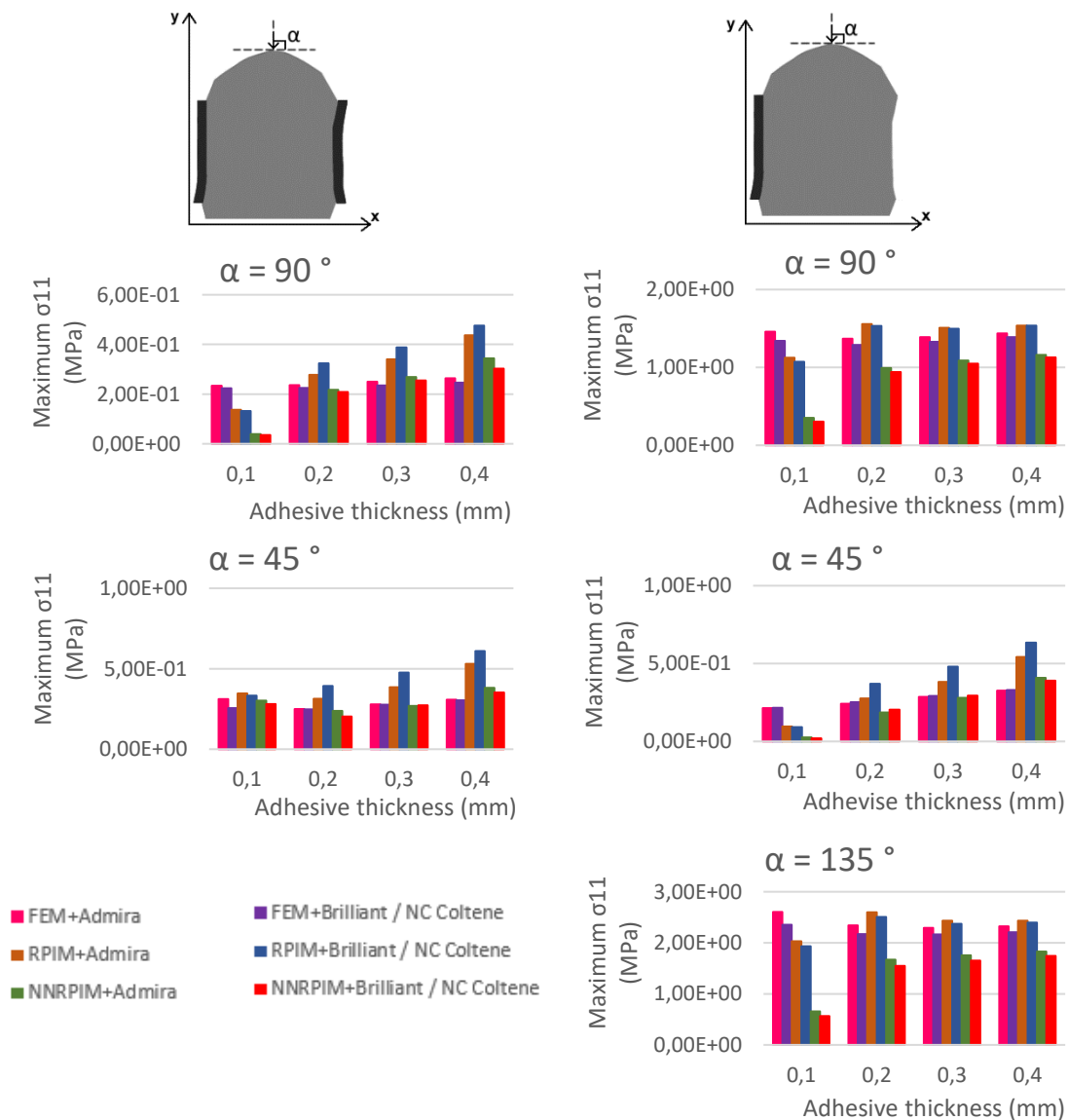
Figure 8.16 - Histograms representation of $\sigma11_{max}$ found in retainer wing for all study cases.

The maximum principal stress ($\sigma11_{max}$) should not depend on the adhesive's thickness. In Figure 8.16, when comparing the $\sigma11_{max}$ obtained for the different adhesive's thicknesses and the same load case and numerical method, it is possible to observe that in fact this is somewhat

constant, being this observation valid for FEM. However, this does not occur with meshless methods. The principal stress increases with the place of loading, therefore the load case α = 45° presents higher maximum principal stresses then the load case α = 90°. RPIM is the method with more irregular results.
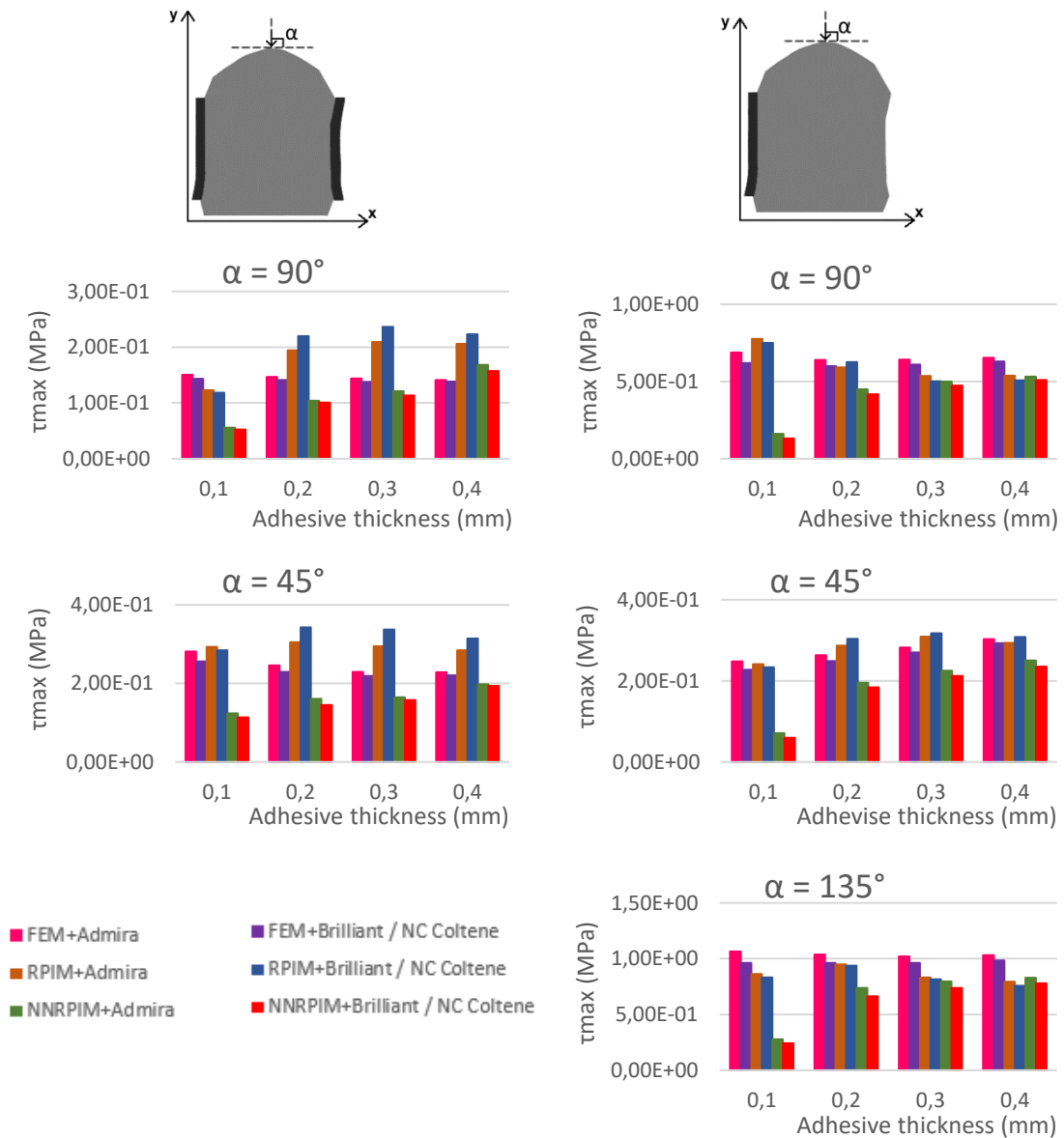
Figure 8.17 - Histograms representation of τ_{max} found in retainer wing for all study cases.

Once again, the maximum shear stress (τ_{max}) should not depend on the adhesive's thickness, being this observation evident in Figure 8.17 for FEM. The τ_{max} is higher for the load case α = 45° and for the single-retainer design. The two adhesive tested present similar behaviour.

In Figure 8.16 and Figure 8.17, there is a remarkable difference between the adhesive's thicknesses, but only for the RPIM and NNRPIM. This is due to the radial search that is performed during the analysis. As previously mentioned, with lower thicknesses, the influence-domains of the interest point (an integration point near the material interface) include alternately nodes from the adhesive and the more resistant material, either enamel or zirconia, depending on the side.

Combining the data of the graphs presented in Appendix 2 and Appendix 3 with the table presented in Appendix 4, is possible to realize that for the two-retainer design, the maximum principal stress is recorded on the left wing, closest to the pontic. While for the single-retainer design, the maximum principal stress is recorded in patch 1, regardless the adhesive's thickness considered. These findings are in concordance with Figure 8.9 and reinforce the previously expressed ideas that single-retainer design increases the probability of debonding in abutment/adhesive interface, whereas the two-retainer design increases the possibility of debonding at the adhesive/pontic interface.

With the analysis of the $\sigma11_{max}$ and the τ_{max}, it was possible to determine the locations with higher stress concentration and reinforce the previous mentioned conclusion that the single-retainer design increases the $\sigma11_{max}$ obtained. It was also possible to predict the total displacement (δ_{total}) of the pontic, measured on a node positioned in the lower part of the pontic (marked in Figure 8.18), for the conditions considered in this study. Therefore, the table presented in Appendix 5 was assembled, allowing to obtain the histograms represented in Figure 8.18.
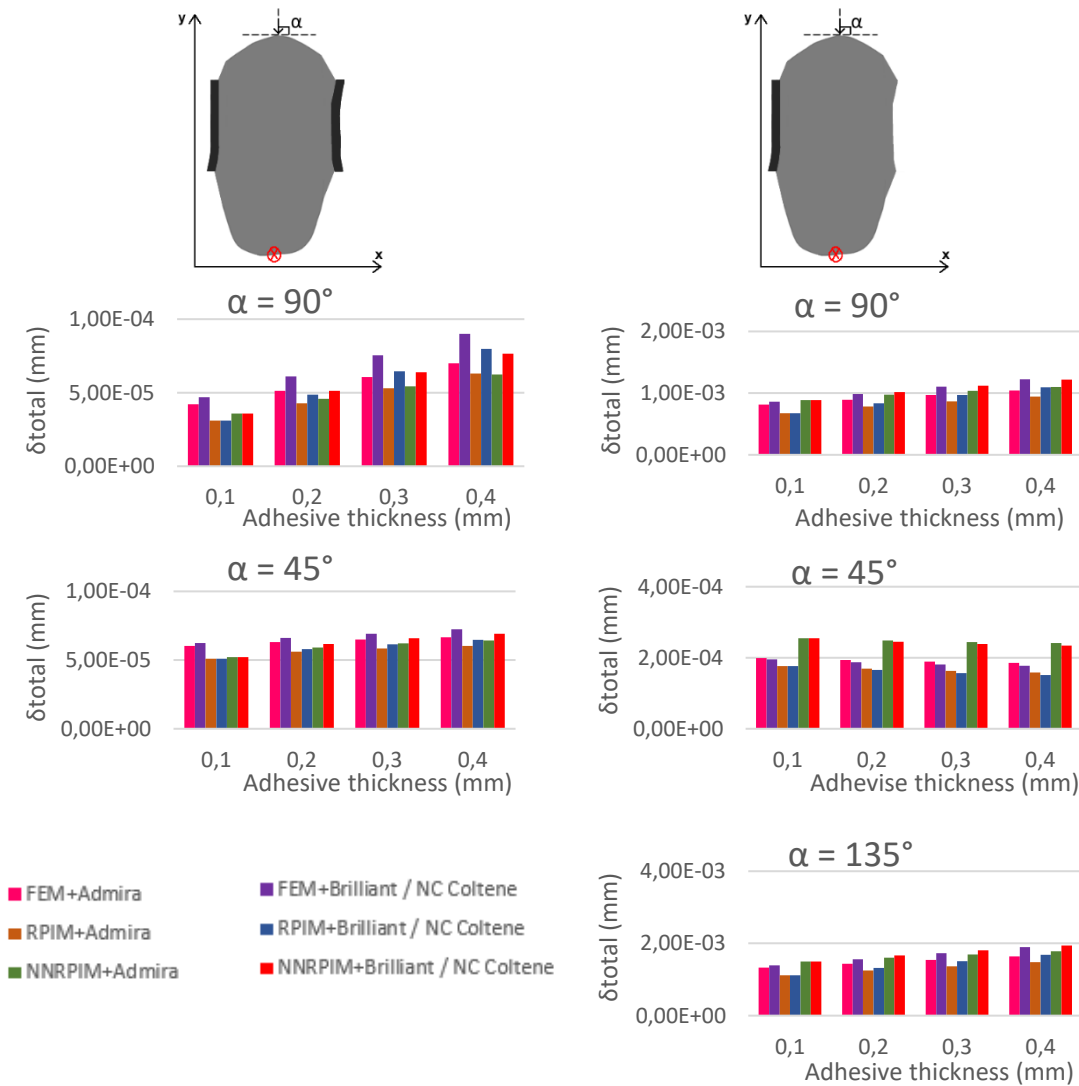
Figure 8.18 - Histograms representation of δ_{total} for the point marked with a cross on figures on the top, for all study cases.

It is possible to verify that the δ_{total} depends on the adhesive's thickness, i.e. with the increase of the adhesive's thickness, the δ_{total} of the pontic also increases. From the point of view of dental medicine, a smaller displacement of the pontic represents greater comfort for the patient and may even prevent the replacement of the fixed dental prosthesis. Therefore, lower thicknesses represent more advantages than higher thicknesses.

To better understand the influence of the adhesive material on the mechanical resistance of the dental bridge, it was evaluated the maximum force that the bridge could support for all the study cases.
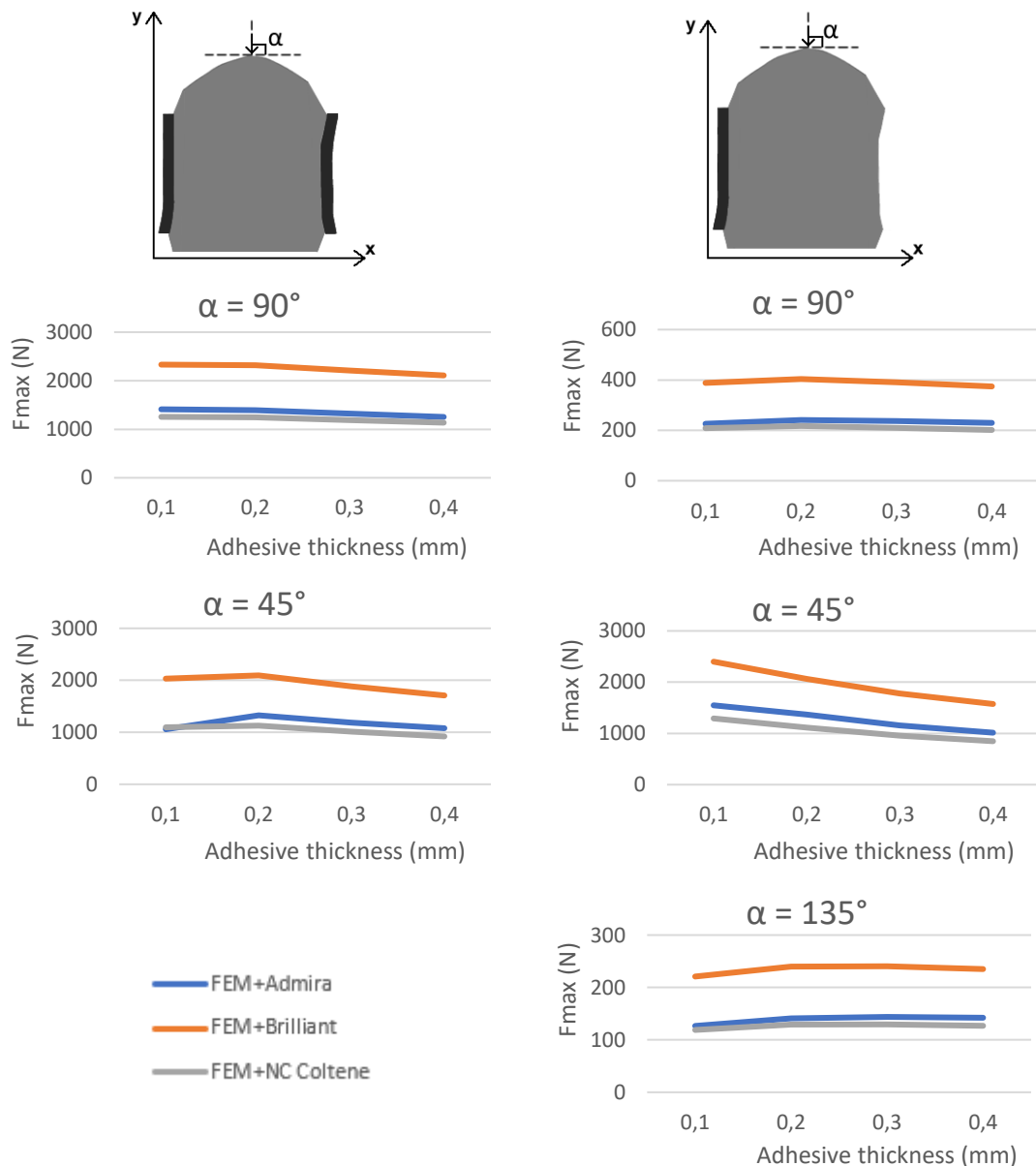
Figure 8.19 - Graphic representation of F_{max} for all study cases and numerical method FEM.

In the present study it was applied a unitary force of 1N. For such unitary force, it was possible to obtain in each analysis a maximum principal stress $\sigma 11_{max}$ (values presented in Table A.1 from Appendix 4). Since, the present study considers small strains and the material with a linear-elastic behaviour, it is possible to expect that the ultimate stress, σ_{ult}, is reached with a maximum force F_{max}. Notice that σ_{ult} of each material is presented in Table 3.6 from

section 3.3. Thus, 1N leads to $\sigma11_{max}$, and F_{max} leads to σ_{ult}. By a simple rule of proportion, it is possible to estimate F_{max} with: $F_{max} = (\sigma11_{max} \cdot \sigma_{ult})/1.0$.

The obtained maximum force F_{max} are represented in Figure 8.19, based on Table A.4 from Appendix 6. For all the study cases, the resin-cement Brilliant is the one that supports the higher F_{max}. Therefore, this resin-cement increases the mechanical resistance of the dental bridge.

Finally, was also assessed the maximum displacement (δ_{max}) of the pontic, measured in the point marked in Figure 8.20, due to the F_{max} that the bridge could support.
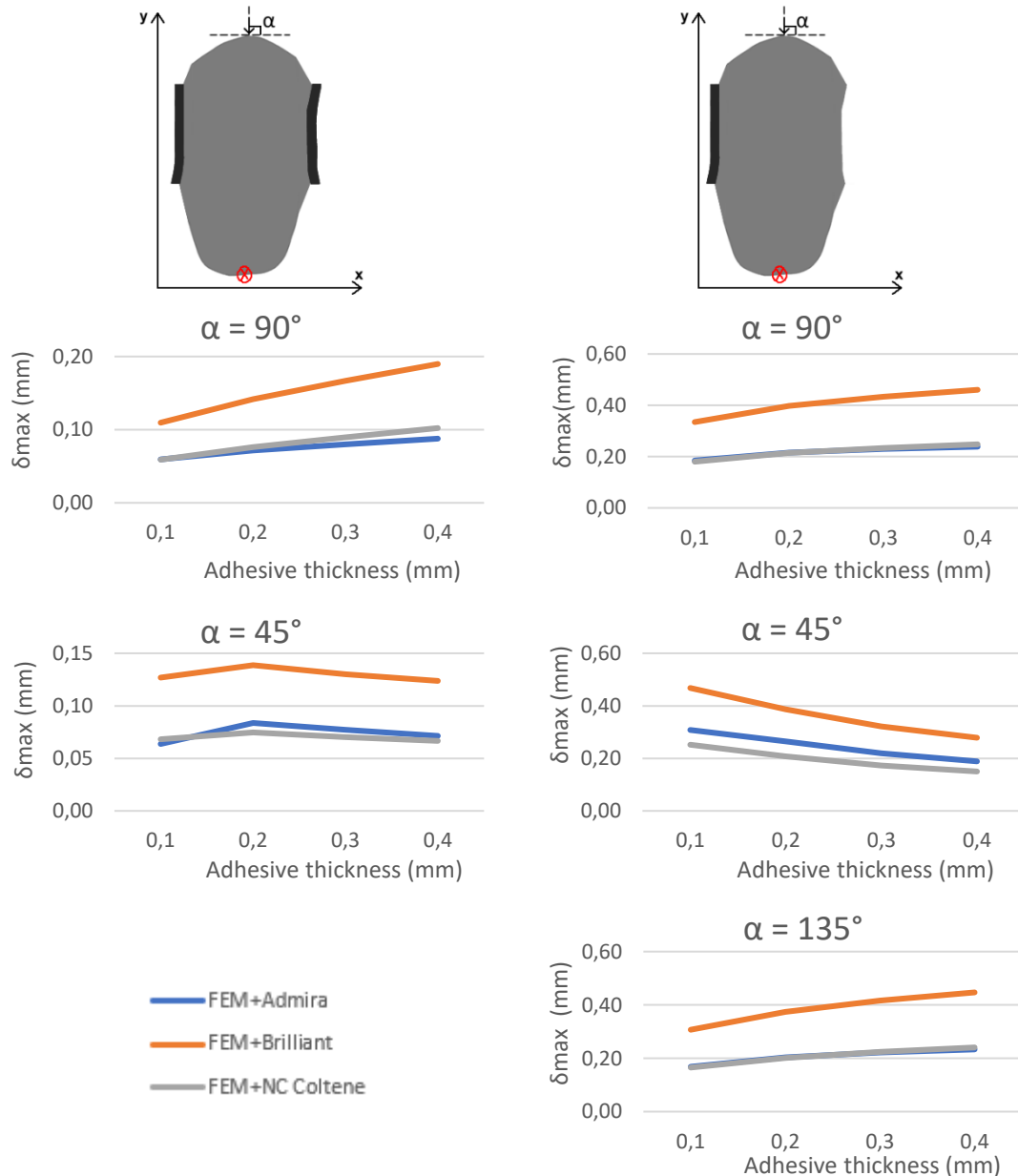
Figure 8.20 - Graphic representation of δ_{max} for all study cases and numerical method FEM.

Once again, since a unitary force of 1N produces a local displacement δ_{total}, then a maximum force F_{max} would produce a maximum displacement δ_{max}. Thus, by a simple rule of proportion, it is possible to estimate δ_{max} with: $\delta_{max} = (F_{max} \cdot \delta_{total})/1.0$. Notice that F_{max}

corresponds to the maximum force (data presented in Table A.4 from Appendix 6.) and δ_{total} corresponds to the local displacement (values presented in Table A.3 from Appendix 5).

In Figure 8.20 it is possible to observe that the resin-cement Brilliant presents the higher maximum displacement for all the cases studied, once this is obtained from the maximum force supported by the adhesive. Admira and NC Coltène present similar behaviours. For the vertical load, the maximum displacement increases with the adhesive's thickness, for both designs and for all the adhesives, as would be expected. For the load case $\alpha = 45°$, the results are not as predictable as those of vertical loading, because there are rotations involved. Like demonstrated in Figure 8.21, for $\alpha = 45°$ the geometrical centre of the adhesive is closest to the load action line, therefore the moments (and consequently, the rotations) caused by the load $\alpha = 45°$ are smaller than the ones caused by the load $\alpha = 135°$. In the latter, the geometrical centre of the adhesive is more distant from the load action line and therefore the moment and the rotation are higher, leading also to higher displacements.
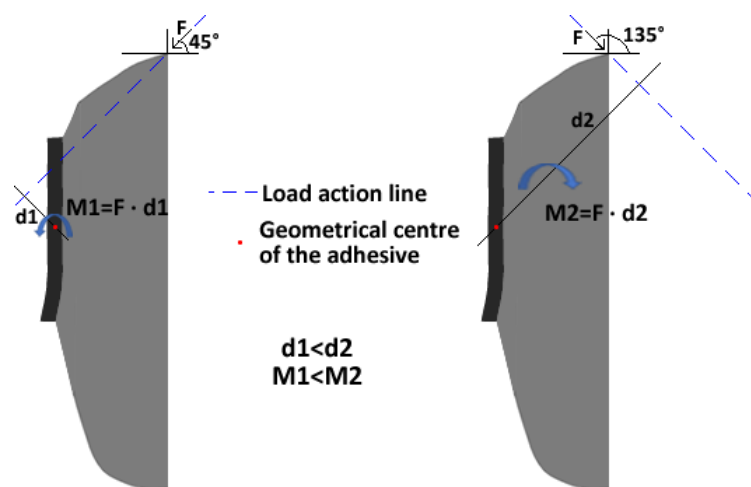
Figure 8.21 - Schematic representation of the moment of the diagonal forces.

In summary, with this elasto-static 2D study, it was possible to verify that from a medical and mechanical point of view, the use of one retainer wing increases the probability of debonding and the adhesive's thickness of 0.1 mm appears to be the most favourable. Regarding the adhesive material, the three tested materials demonstrate a similar behaviour, being Brilliant the one that stands out once it supports higher forces. The study of the representative loads of bruxism allowed to verify that this is a medical condition that may lead to failure of dental prostheses, and its analysis is more complex since the behaviour of the adhesive, when subjected to this type of loads, does not correspond to the expected. Finally, the meshless methods can approach the FEM solution as the adhesive's thickness increases.

8.4 - 3D study of the structural response of an adhesive dental bridge

This work aimed to evaluate the effect of different resin-cements on the structural response of an adhesive dental bridge.

Although in the previously presented study it was demonstrated that the thickness of 0.1 mm seems to be more medically appropriated, in this study the adhesive's thickness was not

varied, being constant and equal to 0.4 mm. This decision was due to computational limitations because, as previously shown, RPIM and NNRPIM showed less reliable results for lower thicknesses, when compared to FEM. To increase the accuracy of these advanced discretization methods it would be necessary to develop a denser element mesh in the adhesive area. However, it is difficult to analyse a dense mesh and maintain a reduced computational power.

Once again, due to computational limitations, it is not possible to analyse a complete model of the mandible (or even of the area of the missing tooth). So, simplifications were implemented. In Figure 8.22, it is considered a three-unit dental bridge with two abutments, one on each side of the pontic. This figure corresponds to a schematic representation of an incisal view of this three-unit bridge, i.e. the two-abutment design. This design was chosen based on the results of the previous study, that demonstrated that the single-retainer design increases the probability of occur debonding. It is possible to observe that, for all teeth, there is a horizontal and vertical symmetry. This symmetry can be represented through boundary conditions. Thus, only the area surrounded by the boundary conditions was modelled, obtaining a model of an adhesive with 0.4 mm of thickness and 9.5 mm of height. This height was chosen based on the height of a mandibular lateral incisor [19], therefore considering that the resin-cement covers all the posterior surface of the tooth. Only one quarter of the pontic was modelled and the interior was considered empty, as shown in Figure 8.23(a), as a way of reducing the mesh size.
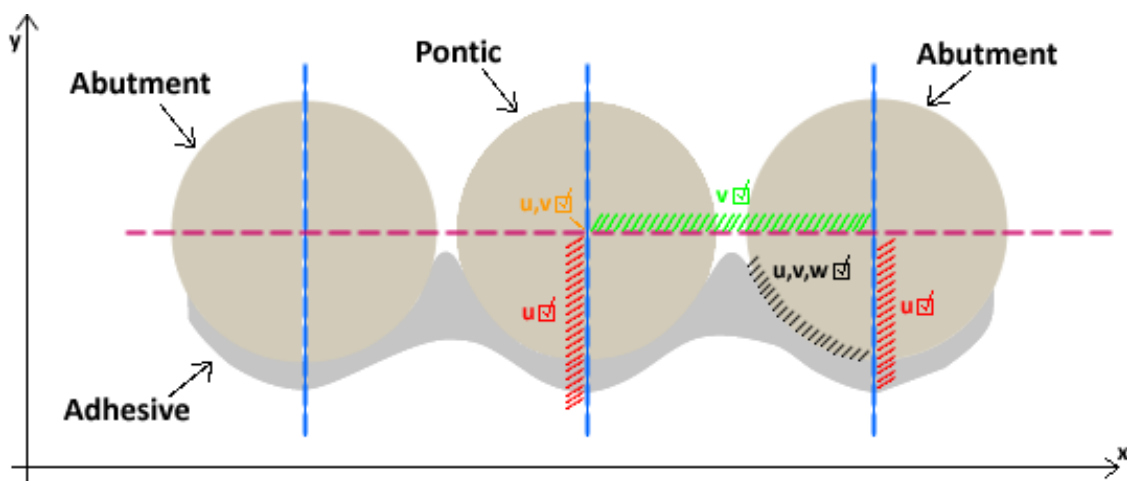
Figure 8.22 - Schematic representation of an incisal view of a three-unit dental bridge with two abutments.

The final model and the element mesh are represented in Figure 8.23(a). The essential boundary conditions are represented in Figure 8.23(b), in which the nodes marked in red are constrained in Ox, the nodes marked in yellow are constrained in Oy and Ox and the nodes marked in green are constrained in Oy. It was assumed that there was a perfect mechanical and chemistry bond between the adhesive and the abutment, hence there are also nodes marked in white, which are constrained in all directions, i.e. in Ox, Oy and Oz. As a natural boundary condition, it was considered a 1 N load, applied in the z direction (Figure 8.23(b)).

In this study, the materials considered have an elastic, homogeneous and isotropic linear behaviour. As seen in Figure 8.23, the model is composed by two patches: (1) the pontic, for which was assigned the material Zirconia and whose properties are given in Table 3.5 from

section 3.3; and (2) the adhesive, for which was attributed the resin-cements presented in Table 3.6 from section 3.3. The resin-cements Brilliant and NC Coltène have the same linear behaviour, therefore these were considered as one resin-cement.

(a)   (b)
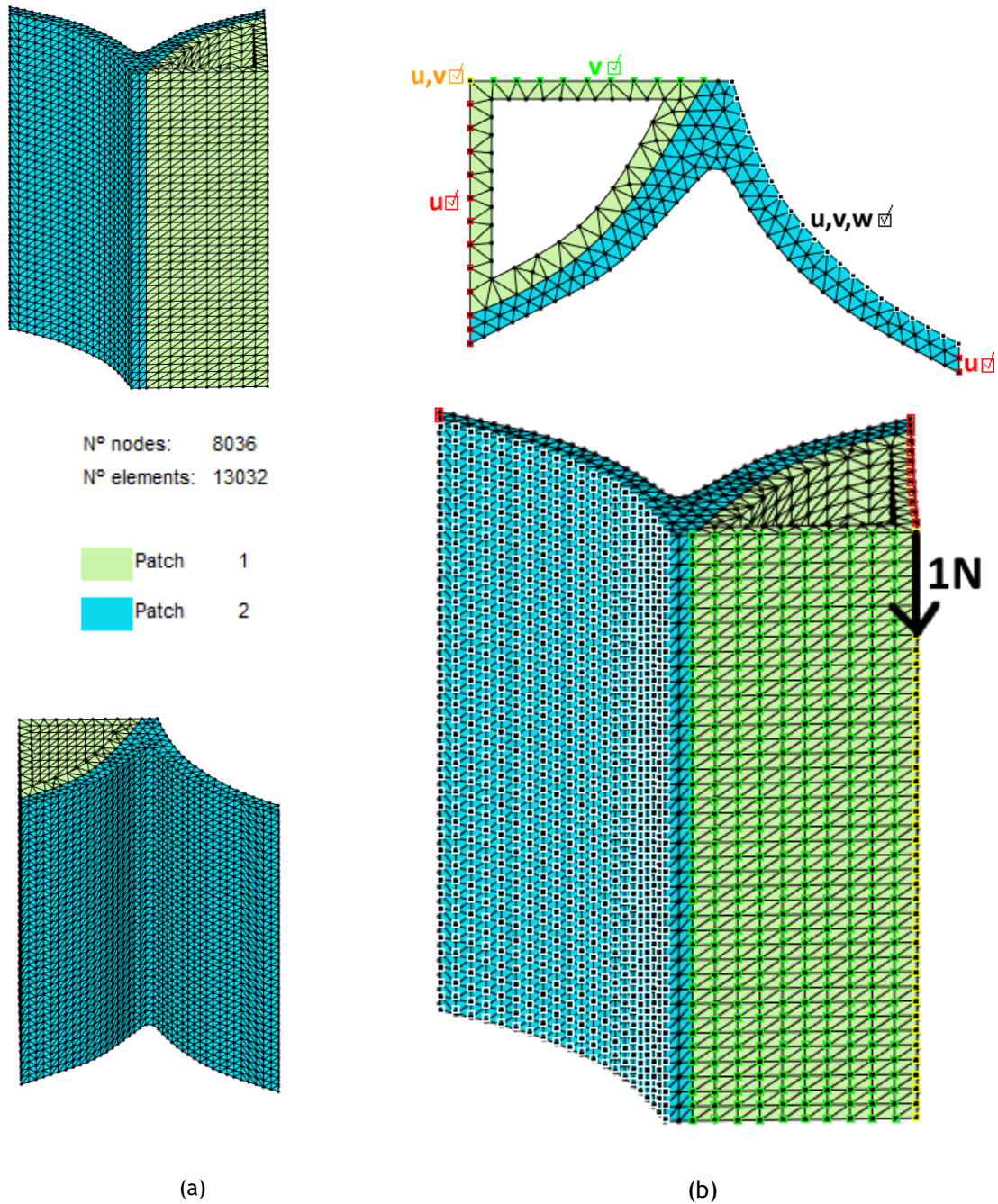
Figure 8.23 - Representation of the global 3D geometric model, boundary and load conditions considered and element mesh.

A static linear-elastic analysis was performed for three numerical methods - FEM, RPIM and NNRPIM - obtaining the colour dispersion maps of principal stress σ11 and the shear stress component τ_{zx} represented in Figure 8.24 and Figure 8.25.

Admira   **Brilliant / NC Coltène**

FEM

RPIM

NNRPIM

[MPa]
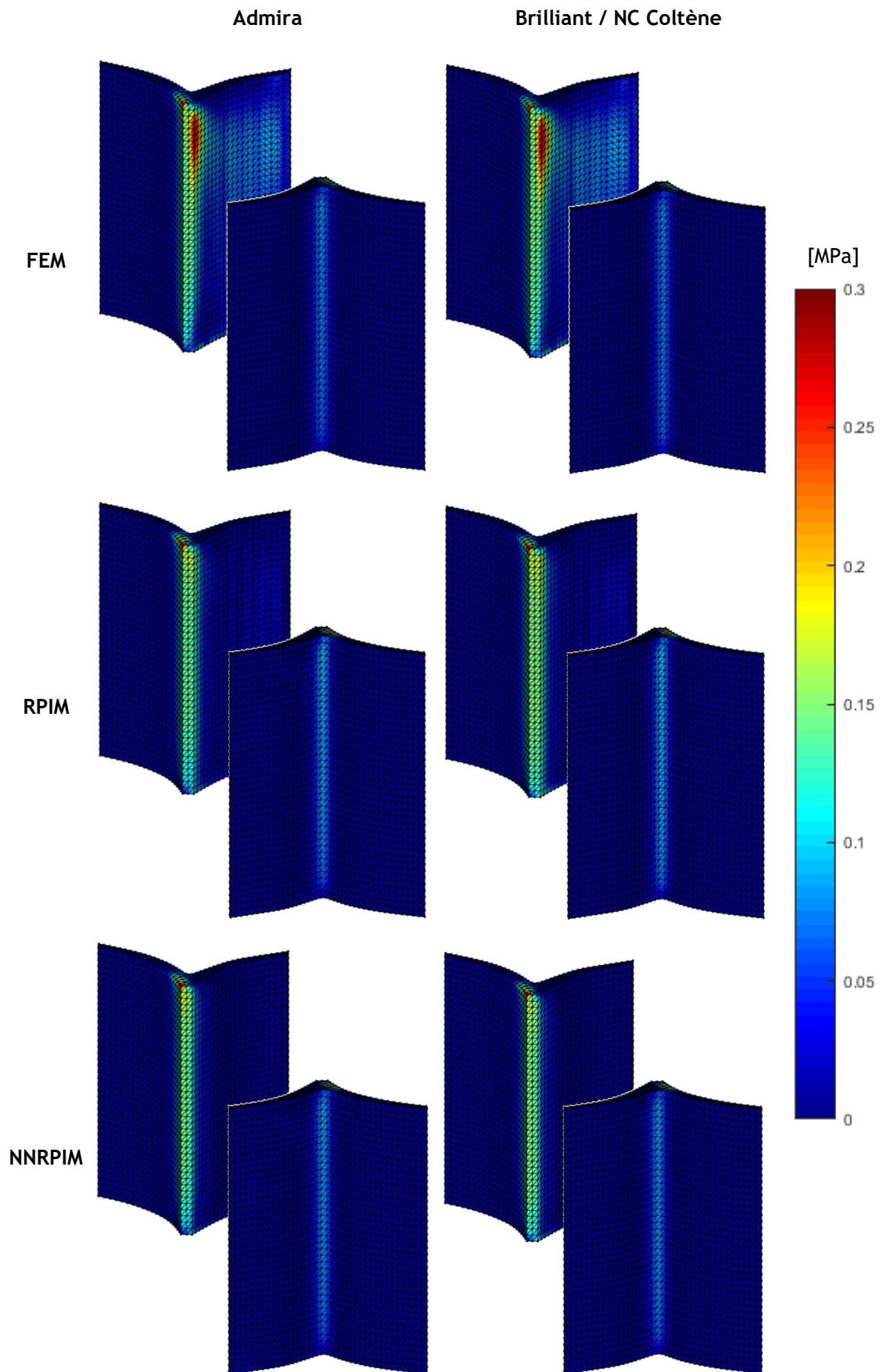
Figure 8.24 - Colour dispersion maps of principal stress σ11 for all the study cases.

Admira　　　　　　　**Brilliant / NC Coltène**
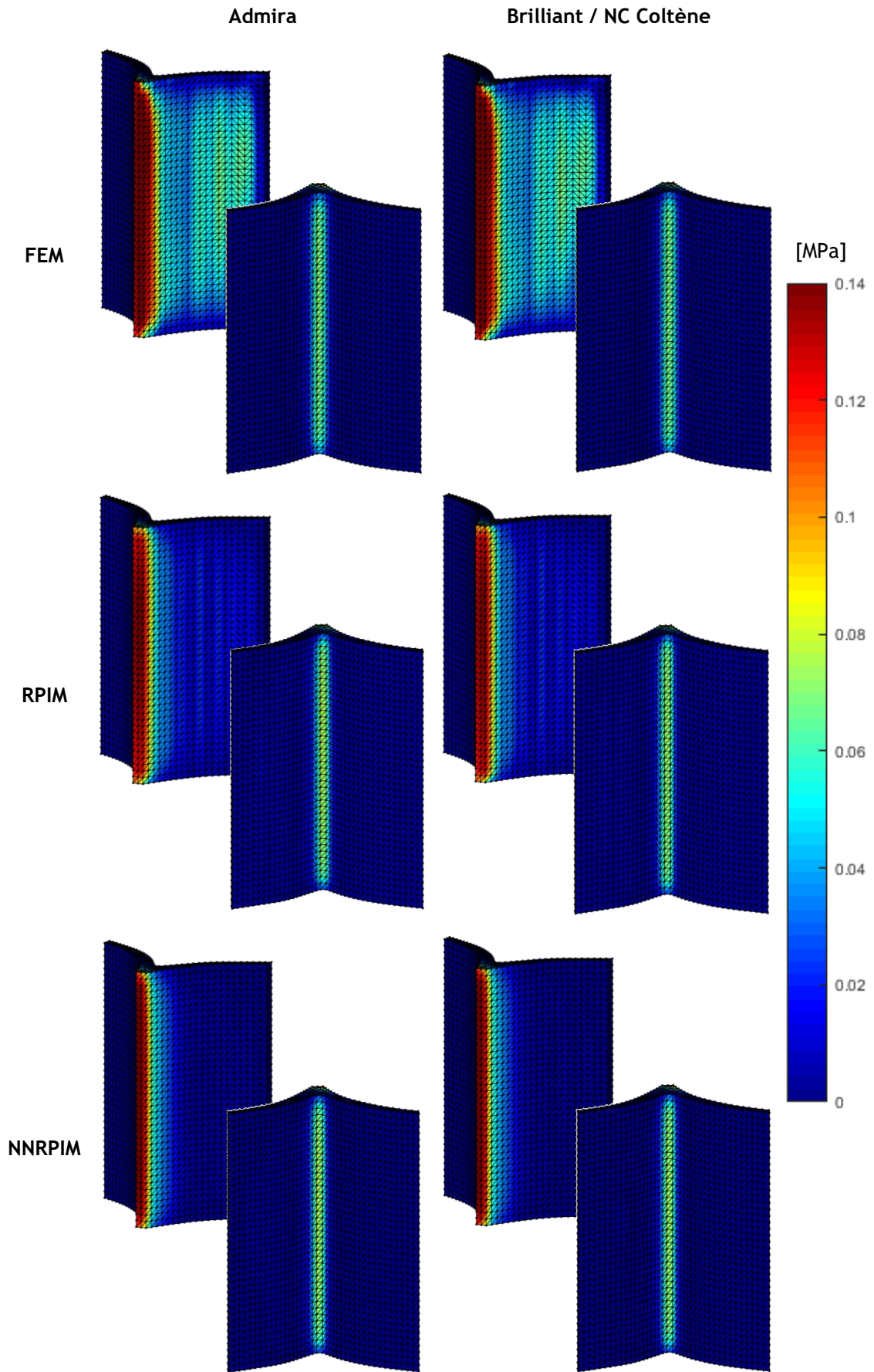
Figure 8.25 - Colour dispersion maps of shear stress component τ_{zx} for all the study cases.

With the previous figures presented, it is possible to observe that the area of the adhesive that is at risk is the one between the abutment and the pontic. Therefore, here could be the initial point of crack propagation, leading to breakage of the adhesive, and consequently the entire dental prosthesis. The adhesive in contact with the abutment does not exhibit tensions due to the assumptions made that the adhesive is perfectly bonded to the abutment tooth. The two adhesives appear to have a similar behaviour. Regarding the numerical methods, there is a clear smoothing of the solution for the meshless methods.

In Figure 8.25, it is possible to verify that the shear stress has a nearly parabolic distribution along the adhesive, with the minimum stresses at the edges and maximum at the centre, as expected.

To better understand the stress distribution along the adhesive, and consequently the differences between the resin-cements tested, and to better evaluate the numerical methods performance, the principal stress σ11 and the shear stress component τ_{zx} were examined in a line at the interface between the adhesive and the abutment (line 1, marked in Figure 8.26), a line at the interface between the adhesive and the pontic (line 2, marked in Figure 8.27) and in a line at the interior of the adhesive (line 3, marked in Figure 8.28).

Analysing the principal stress σ11, a somewhat similar pattern is identified in the stress distribution along the three lines. At the bottom of each line are found the minimum stresses that increase towards the centre until a certain point, from which the stresses begin to stabilize. Then, the stresses begin to increase, reaching their maximum at the top of each line. The maximum stress σ11 is obtained for line 1, which for FEM and Admira is equal to $3.21 \cdot 10^{-1}$ MPa, and for FEM and Brilliant/NC Coltène is equal to $2.98 \cdot 10^{-1}$ MPa. This values are approximated to the ones found in the previous study (section 8.3), presented in Figure 8.16, whose values are in Table A.1, from Appendix 4 (FEM + Admira = $2.63 \cdot 10^{-1}$ MPa; FEM + Brilliant/NC Coltène = $2.47 \cdot 10^{-1}$ MPa). Therefore, it is possible to verify that the 2D and 3D studies presented similar results and that although the differences are almost imperceptible, with adhesive Brilliant/ NC Coltène slightly lower tensile stresses are obtained.

Examining the shear stress component τ_{zx} , it is again identified the almost parabolic distribution of this stress, a previously verified behaviour in section 8.3, from Figure 8.11 to Figure 8.15. Hence, it is perceptible that this becomes more accentuated from line 1 to line 3. Despite this, line 1 is again the one presenting the maximum shear stress. It is possible to observe that the two resin-cements present a similar behaviour and for the shear stress no significant differences were found.

Regarding the numerical methods, it is possible to observe that NNRPIM is the advanced discretization method that can better approximate the FEM solution.
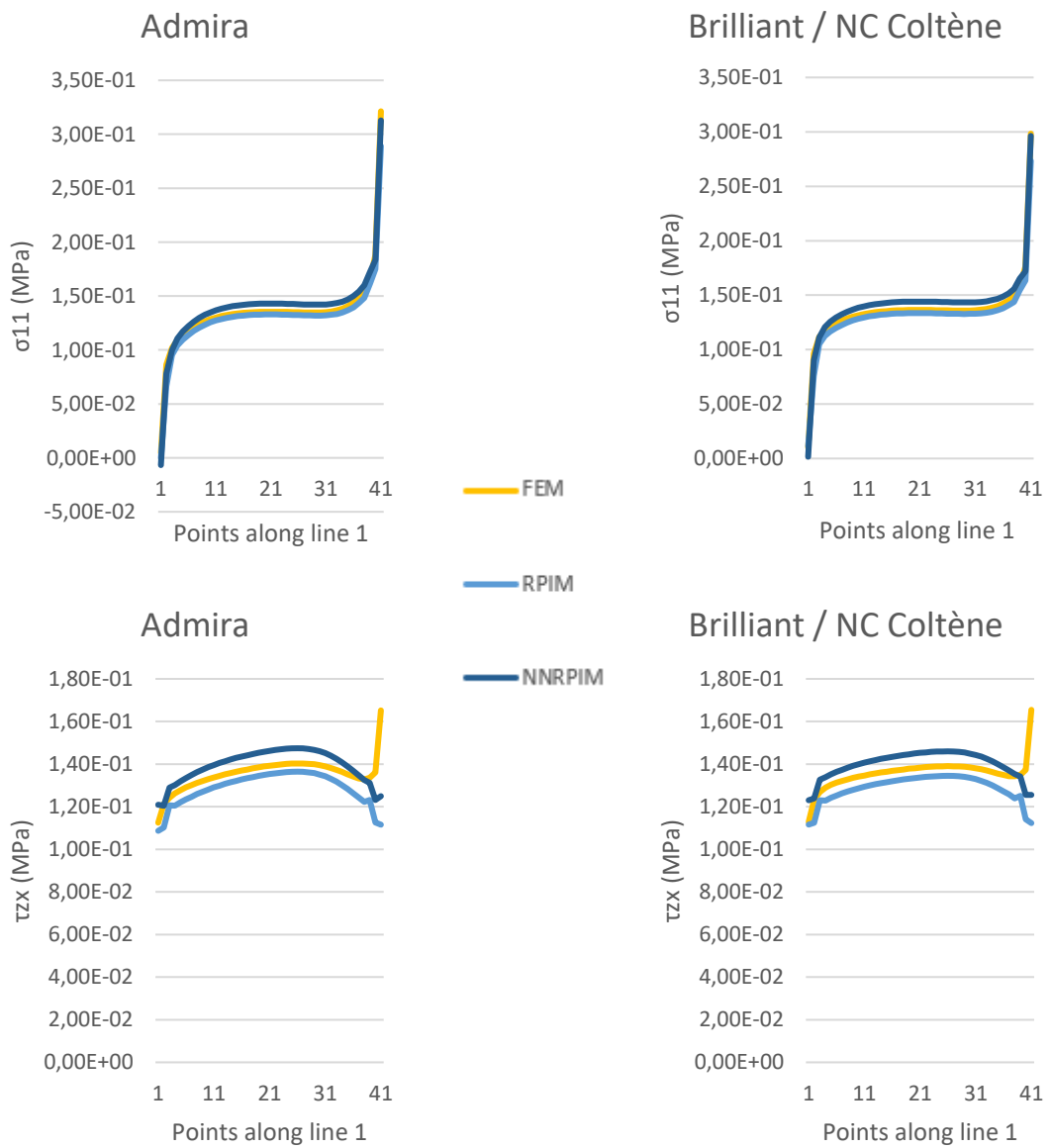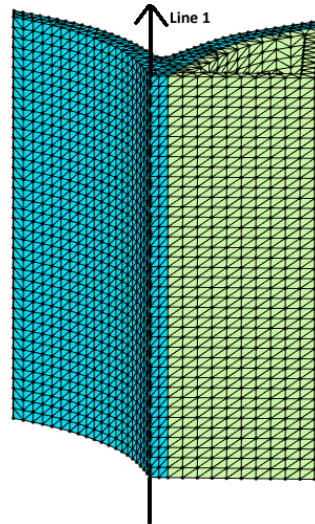
Figure 8.26 - Graphic representation of principal stress σ11 and shear stress component τ_{zx}, in points along line 1, for all study cases.
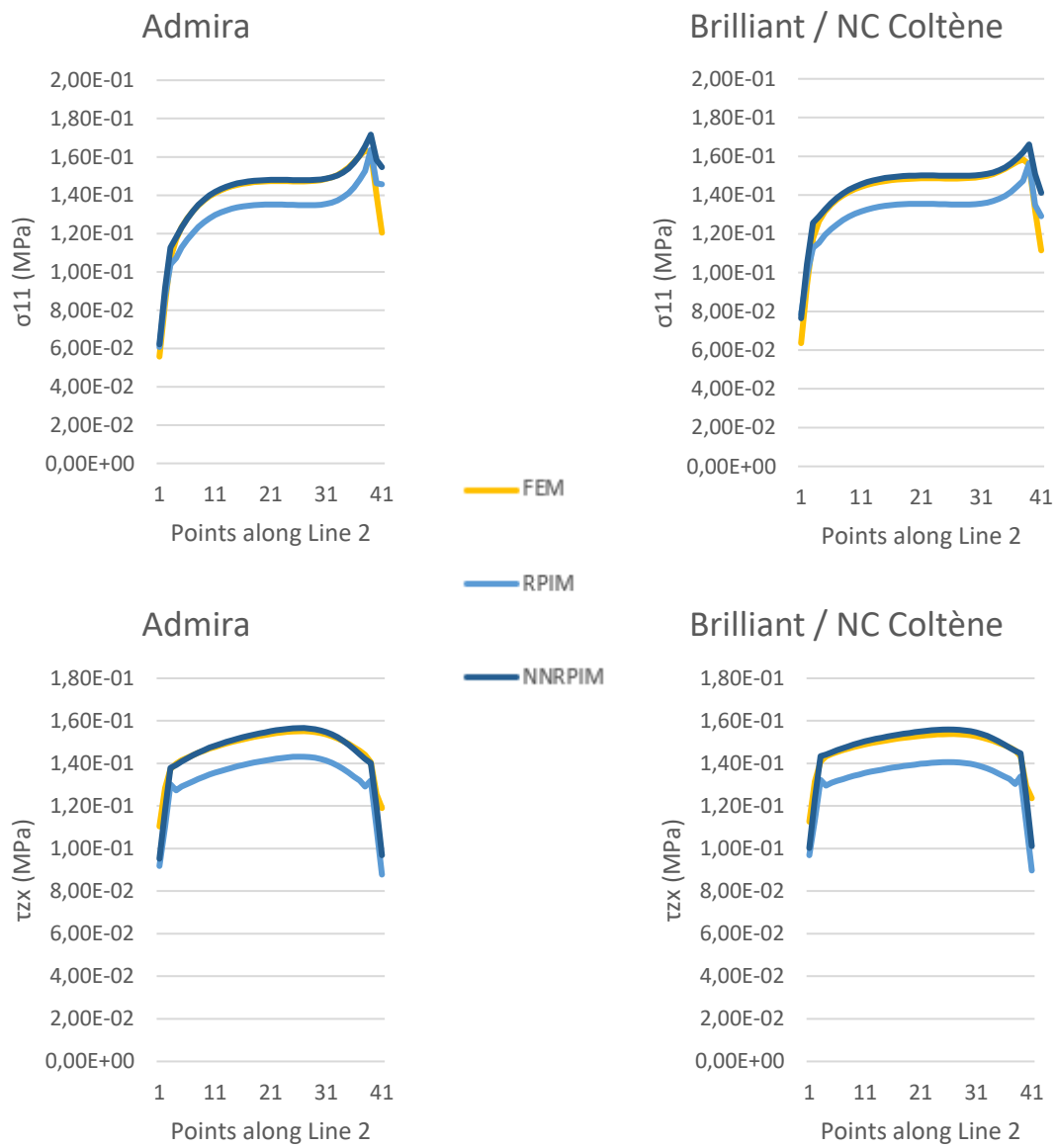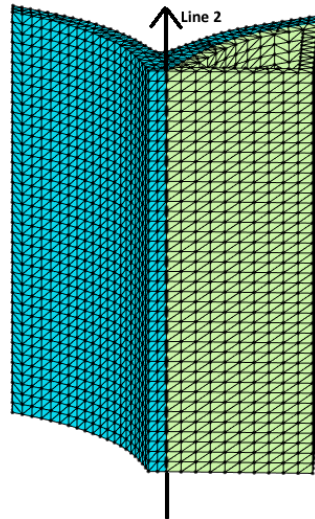
Figure 8.27 - Graphic representation of principal stress σ11 and shear stress component τ_{zx}, in points along line 2, for all study cases.
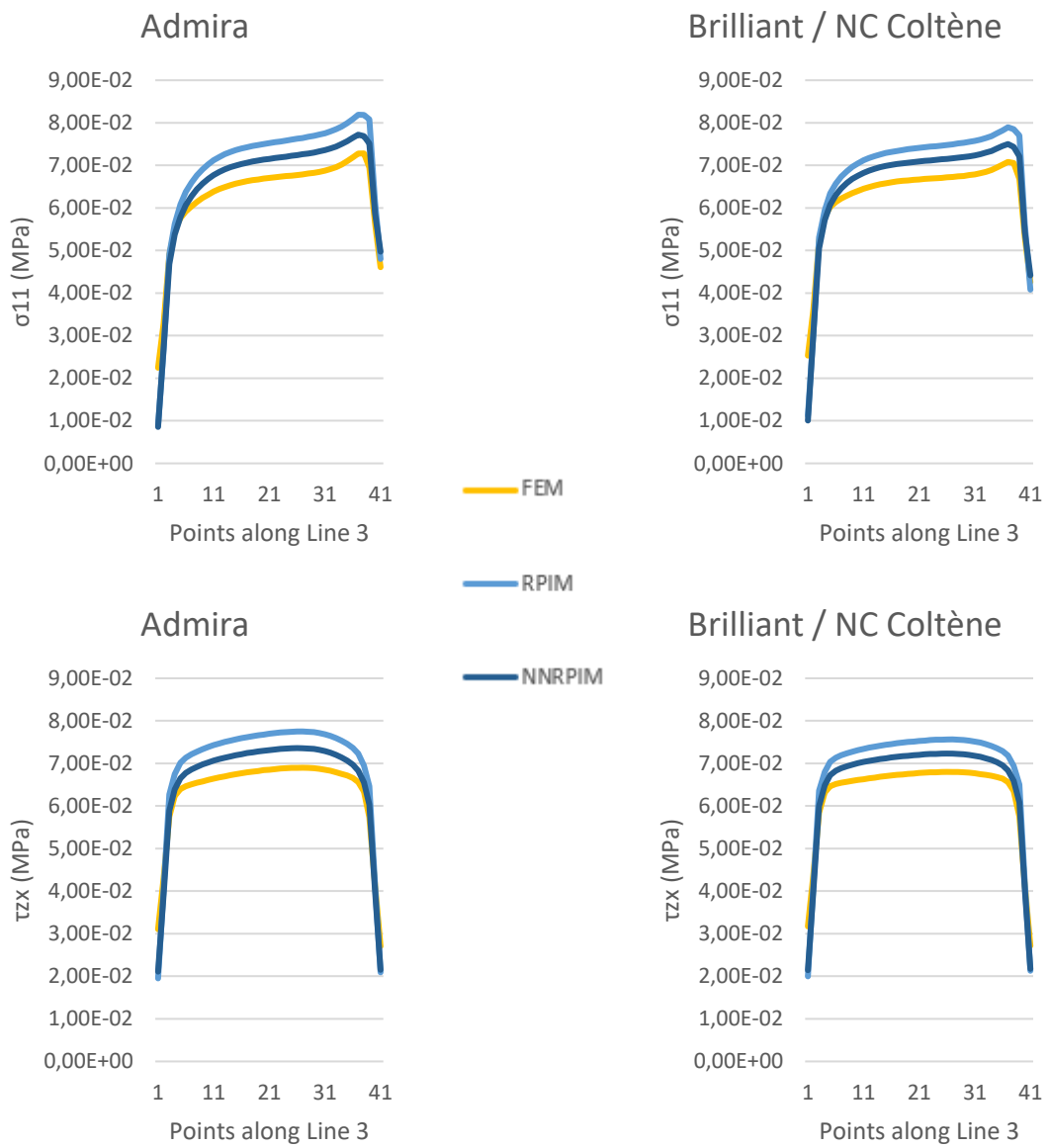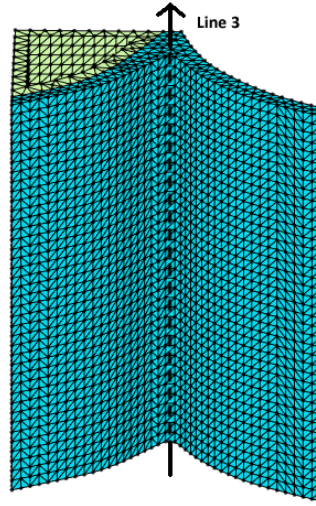
Figure 8.28 - Graphic representation of principal stress σ11 and shear stress component τ_{zx}, in points along line 3, for all study cases.

Analysing a point of the pontic, it was possible to investigate the total displacement of the pontic (Figure 8.29). The values obtained are in the same order of magnitude found in section 8.3, in Figure 8.18, and also presented in Table A.3 from Appendix 5. When comparing the two resin-cements, it is possible to observe that Brilliant and NC Coltène present higher displacements, which can represent a less comfortable situation for the patient. This finding was also verified in Figure 8.18. The three numerical methods achieved identical solutions.
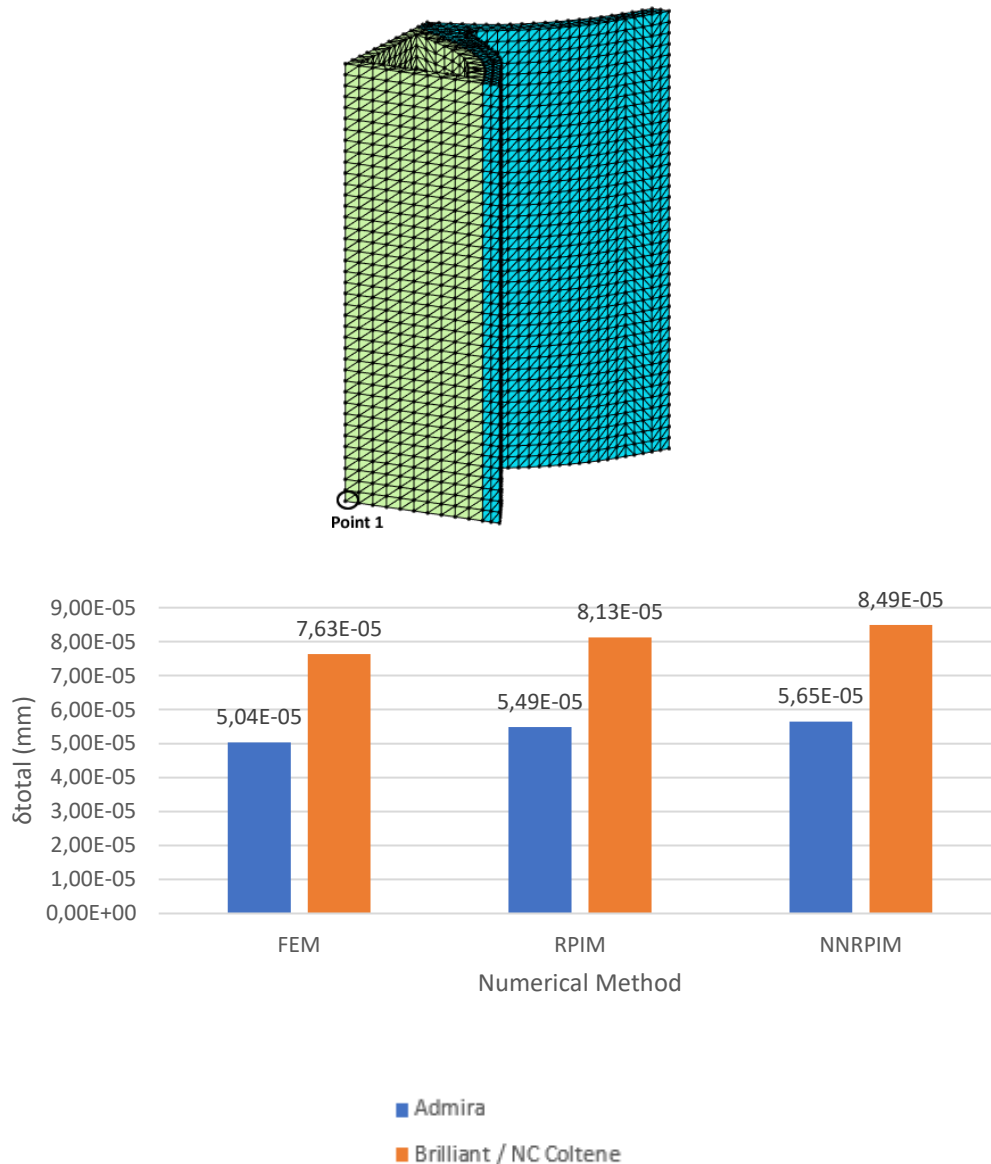
Figure 8.29 - Histogram representation of total displacement for the point marked on the bottom of the pontic, for all study cases.

This 3D study was in concordance with the previously 2D study presented and allow to identify the area of the adhesive at higher risk.

Despite the resin-cement NC Coltène presented lower tensile and shear stresses, which could indicate lower probability to occur debonding, it also presented higher displacements of the pontic, which can represent a less comfortable situation to the patient. Therefore, at this point, both resin-cement represent a valid solution.

Chapter 9

Elasto-plastic numerical analysis

After exceeding yield strength, the materials enter in the plastic range, for which its rigidity changes. The behaviour of the material in the plastic state is different and unloading can leave permanent deformations. The elasto-static numerical analysis does not account for material non-linearity. Therefore, to accurately analyse the resin-cements behaviour, 2D and 3D analysis models were developed, and elasto-plastic numerical analyses were performed using three numerical methods (FEM, RPIM and NNRPIM). With the results obtained, it was possible to acquire relevant practical conclusions about the resin-cement influence on the mechanical resistance of the adhesive dental bridge and regarding the level of performance of meshless methods, when compared to FEM.

9.1 - 2D study of the structural response of an adhesive dental bridge

This study was developed with the objective of simulating the effect of the adhesive material used and the bridge design on the mechanical resistance of the resin-bonded dental bridge. The 2D model used was based on the model presented in Figure 8.7, from section 8.3. However, due to computational limitations, simplifications had to be implemented. Therefore, the previously presented model was cut, being this new model composed by the left adhesive wing and half of the mandibular lateral incisor, which corresponded to the pontic tooth, as presented in Figure 9.1(a). The adhesive's thickness was constant and equal to 0.4 mm.

To simulate the presence of one or two retainer wings, different essential boundary conditions were applied, as demonstrated in Figure 9.1(b) and Figure 9.1(c), respectively. The main difference between the two designs is the essential boundary conditions applied in the pontic tooth, constraining the nodes in Ox direction, present only in the two-retainer design (Figure 9.1(c)). For the single-retainer design, this area is free in all directions (Figure 9.1(b)). As a natural boundary condition, it was considered a 1 N load aligned with the longitudinal axis of the tooth, applied on the top of the pontic.

N° nodes: 2885
N° elements: 5570

Patch   1
Patch   2

(a)

1N

u,v ☑

(b)

1N

u,v ☑   u ☑

(c)
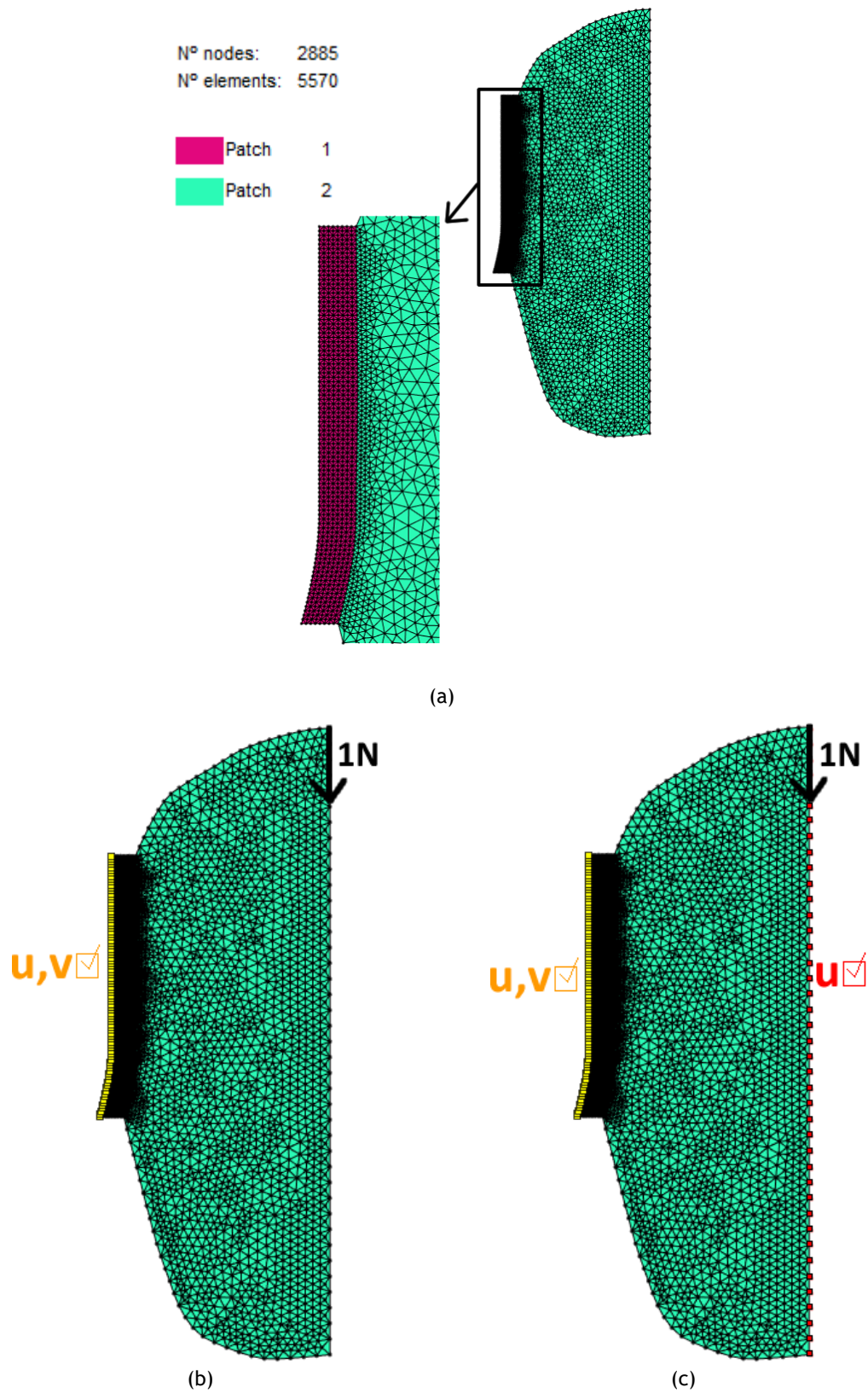
Figure 9.1 – (a) Representation of the global 2D geometric model and element mesh; (b) boundary and load conditions considered for the single-retainer design; and (c) boundary and load conditions considered for the two-retainer design.

The domain of the problem was discretized in a mesh of triangular elements, as shown in Figure 9.1(a). In this study, the considered materials have a bi-linear elasto-plastic, homogeneous and isotropic behaviour. Thus, the properties considered were the Young's modulus, the Poisson ratio, the yield stress and the plastic tangent modulus. This model was composed by two patches: (1) the adhesive, for which was attributed the resin-cements and the respective mechanical properties presented in Table 3.6 from section 3.3; and (2) the pontic, for which was assigned the material Zirconia, whose properties are given in Table 3.5 from section 3.3, and for the yield stress and the plastic tangent modulus was attributed the values of $12 \cdot 10^{14}$ MPa and 24.5 GPa, respectively, as a way of guarantee that this material would not reach the plastic regime. In this way, was possible to analyse only the behaviour of the adhesive. However, the resin-cement Brilliant was not analysed in this study because its plastic tangent modulus is higher than the Young's modulus, which is not supposed to happen. As a material is deformed, internal force act in opposition to the applied forces. While the material is in the elastic range, these internal forces can completely resist to the applied force, therefore when unloading the material can return its original form. After the material enter in the plastic state, its rigidity decreases, and a larger applied force may lead to a state of permanent deformation. The Young's modulus and the plastic tangent modulus are measurements of the stiffness of the material in the elastic and plastic range, respectively. Therefore, if the material loses rigidity when enters the plastic range, its plastic tangent modulus should be lower than the Young's modulus. This inconsistency may be due to errors in experimental tests. Therefore, only two resin-cements were analysed: Admira and NC Coltène.

A nonlinear-elasto-plastic analysis was performed for three numerical methods: FEM, RPIM and NNRPIM. With this, it was possible to obtain the colour dispersion maps of the principal stress σ11 and the shear stress component τ_{xy} for the last increment of the nonlinear-elasto-plastic analysis, i=10 (corresponding to different force levels), represented in Figure 9.2 and Figure 9.3, respectively. In the colour maps, it is only represented the adhesive, which allowed to examine the stress distribution along this area of high interest.

With Figure 9.2 and Figure 9.3, the evaluation of meshless methods performance is not clear, due to the different force levels between numerical methods. Nevertheless, is possible to observe a common pattern between the three numerical methods, for both principal stress and shear stress distribution along the adhesive.

The maximum tensile stresses and shear stresses found were lower for NC Coltène, however for inferior force levels. Therefore, with these colour maps the differences between the two resin-cements are also imperceptible.

When comparing the two designs tested is possible to verify that the single-retainer design increases stresses on the adhesive, therefore, it increases the probability of occur debonding.
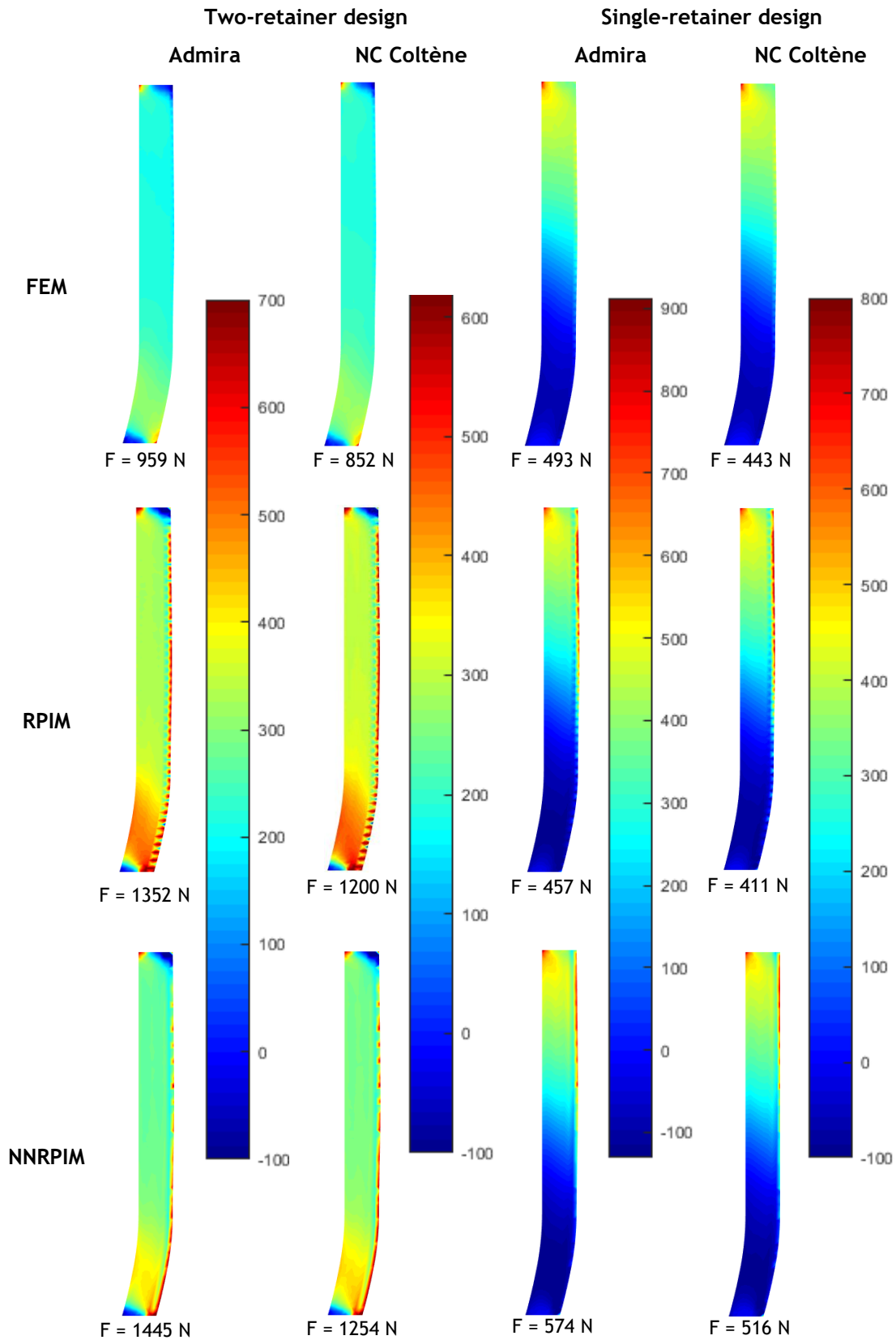
Figure 9.2 - Colour dispersion maps of principal stress σ11 for patch 1 (adhesive) and all study cases. Colour maps represent the values of σ11 in [MPa] and are presented for different force levels.
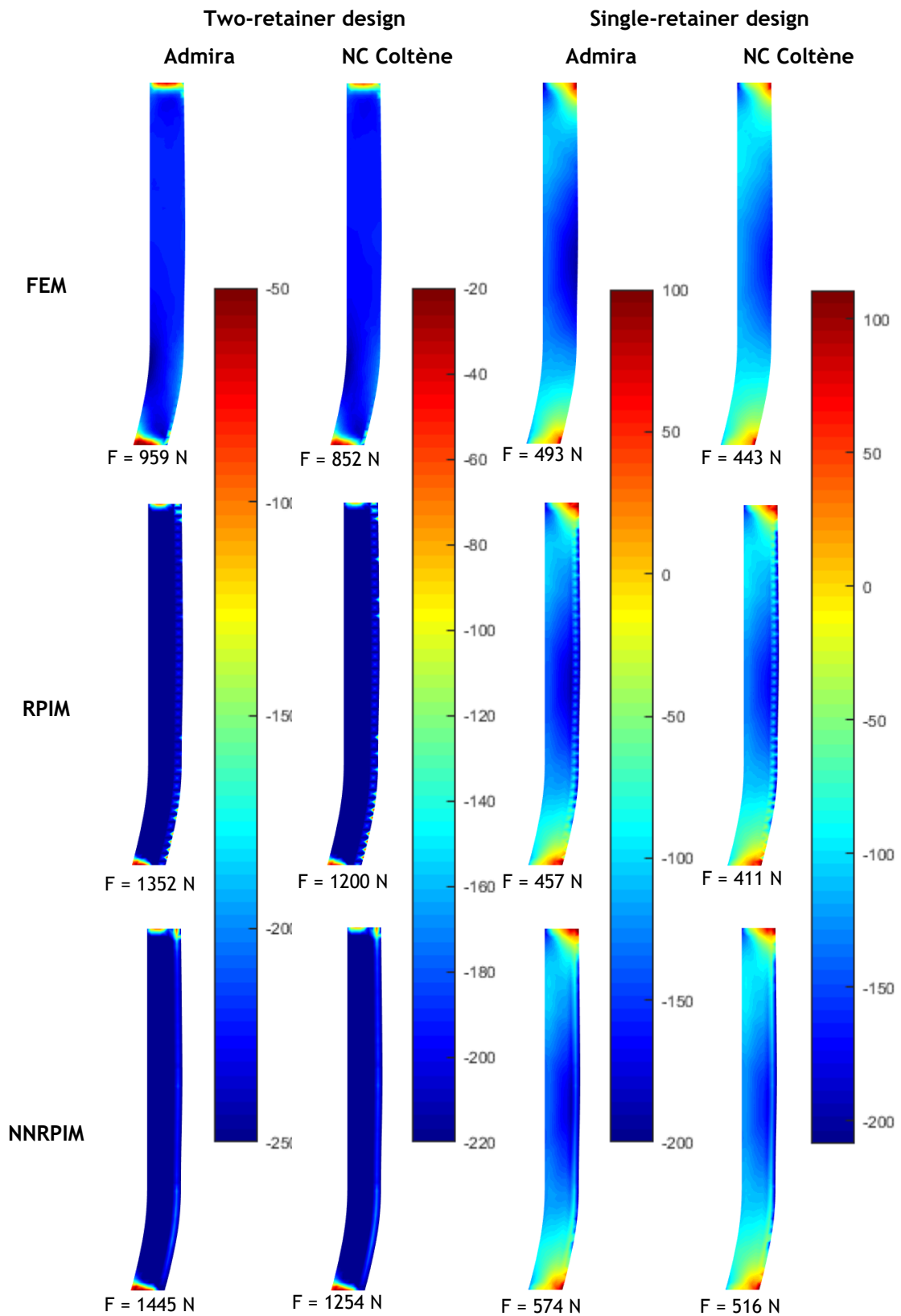
Figure 9.3 - Colour dispersion maps of shear stress component τ_{xy} for patch 1 (adhesive) and all study cases. Colour maps represent the values of τ_{xy} in [MPa] and are are presented for different force levels.

The elasto-plastic behaviour of the resin-cements analysed was documented and then shown in the graphs presented in Figure 9.4 and Figure 9.5.

Figure 9.4 - Graphic representation of stress/strain curve in a point of the adhesive.

In the graphs of Figure 9.4 a point of the adhesive, marked in red in the figure, was analysed for both designs. Comparing the two resin-cements, it is verified that both present similar behaviour, however NC Coltène reaches the elastic limit for lower stresses and higher deformations. This observation is also valid for the single-retainer design, although the plastic behaviour is less noticeable. The comparison between the two designs is not entirely conclusive

through these graphs, since in both designs the adhesives enter the plastic regime nearly for the same stresses and deformations. On the other hand, the results of the meshless methods approximate the FEM solution in such way that the curves overlap.
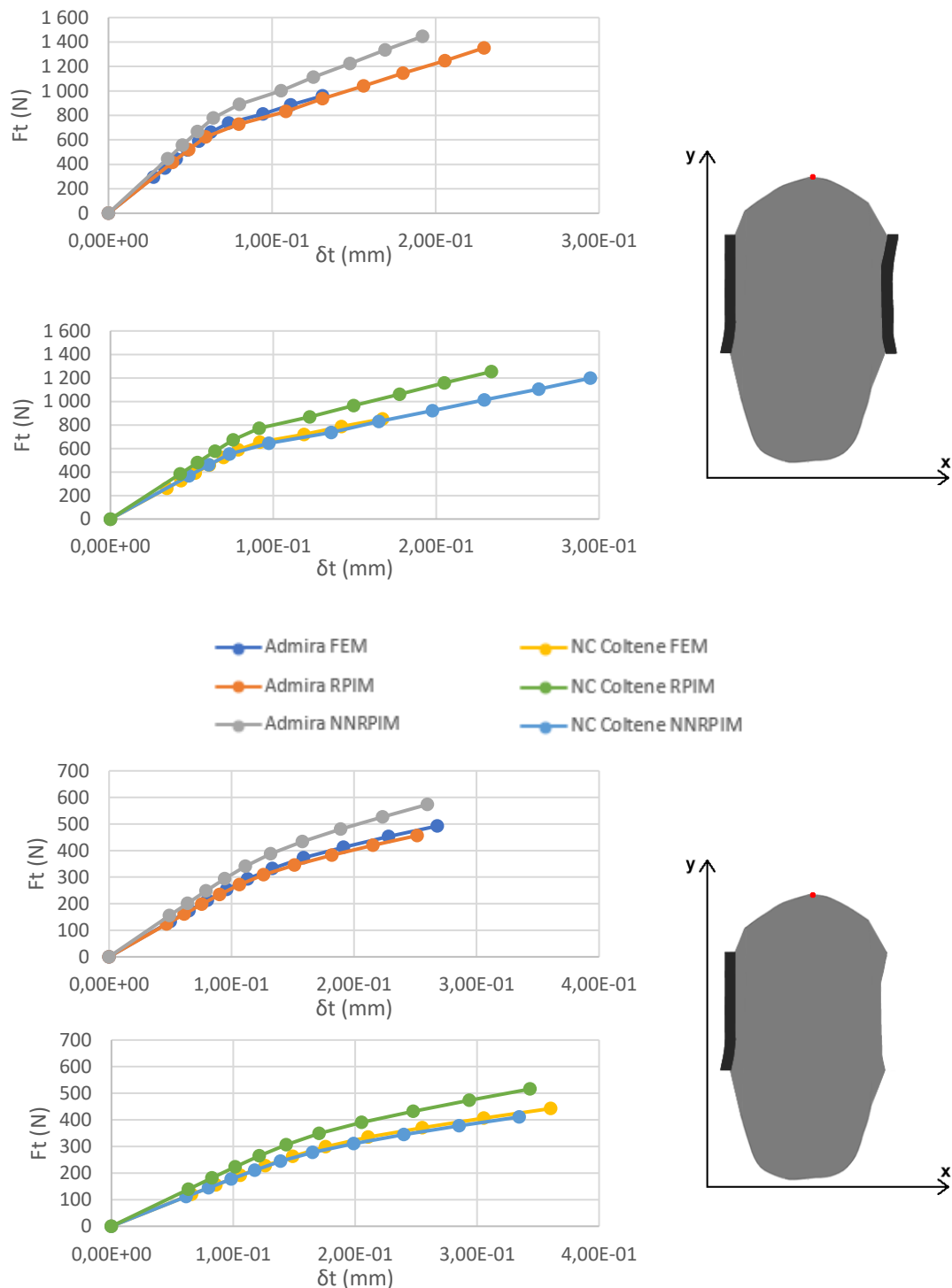
Figure 9.5 - Graphic representation of force/displacement curve in a point of the pontic.

To more accurately evaluate the difference between the two designs, the graphs depicted in Figure 9.5 were assembled. In these graphs a point of the pontic, marked in red, was analysed for both designs as a way of evaluating the total displacement of the pontic obtained with the

force applied. Comparing the two resin-cements, it is verified that both present similar behaviour, however NC Coltène reaches the elastic limit for lower forces, which is in concordance with the previous findings. This observation is also valid for the single-retainer design, although once again the plastic behaviour is less noticeable. Comparing the two designs, it is verifiable that the single-retainer leads to higher displacement of the pontic, which can lead to higher discomfort for the patient.

This study demonstrated that in fact the previously presented elasto-static studies were ignoring the non-linear behaviour that these adhesives present. However, two similar conclusions were withdrawals: (1) the single-retainer design leads to higher displacement of the pontic, which can represent a higher discomfort for the patient, and to higher stress concentration, which can be an indicator of high probability to occur debonding; (2) for 0.4 mm of adhesive's thickness, meshless methods can approach the FEM solution. Although the two resin-cements showed similar behaviour, NC Coltène undergoes irreversible deformations for lower forces, between 200 and 300 N. These force levels are easily reached during the daily activities. Therefore, NC Coltène presents itself as a less viable solution.

9.2 - 3D study of the structural response of an adhesive dental bridge

This study was developed with the objective of simulating the effect of the adhesive material on the mechanical resistance of the resin-bonded dental bridge.

The 3D model used was the same as the previously presented in section 8.4. Recalling, for the development of this model, it was considered an adhesive bridge with two retainer wings, one on each side of the pontic, with 0.4 mm of thickness and 9.5 mm of height. The final model corresponds to a portion of the complete bridge/teeth system (Figure 8.21). Once again, zirconia was considered as the pontic material and two resin-cements were analysed: Admira and NC Coltène. Brilliant was not studied due to inconsistencies in the material's properties. In addition, the pontic was considered empty inside, thus reducing the element mesh. A complete description of the model, mesh, materials, essential and natural boundary conditions is introduced in section 8.4 and observed in Figure 8.22.

In this study, the considered materials have a bi-linear elasto-plastic, homogeneous and isotropic behaviour. Thus, the properties considered were the Young's modulus, the Poisson ratio, the Yield stress and the plastic tangent modulus. The material's properties considered can be found in section 3.3.

A nonlinear-elasto-plastic analysis was performed for three numerical methods: FEM, RPIM and NNRPIM. With this, it was possible to obtain the colour dispersion maps of the principal stress σ11 and the shear stress component τ_{zx} for the last increment of the nonlinear-elasto-plastic analysis, i=10 (corresponding to different force levels), represented in Figure 9.6 and Figure 9.7, respectively. In the colour maps is only represented the adhesive, which allowed to examine the stress distribution along this area of high interest.
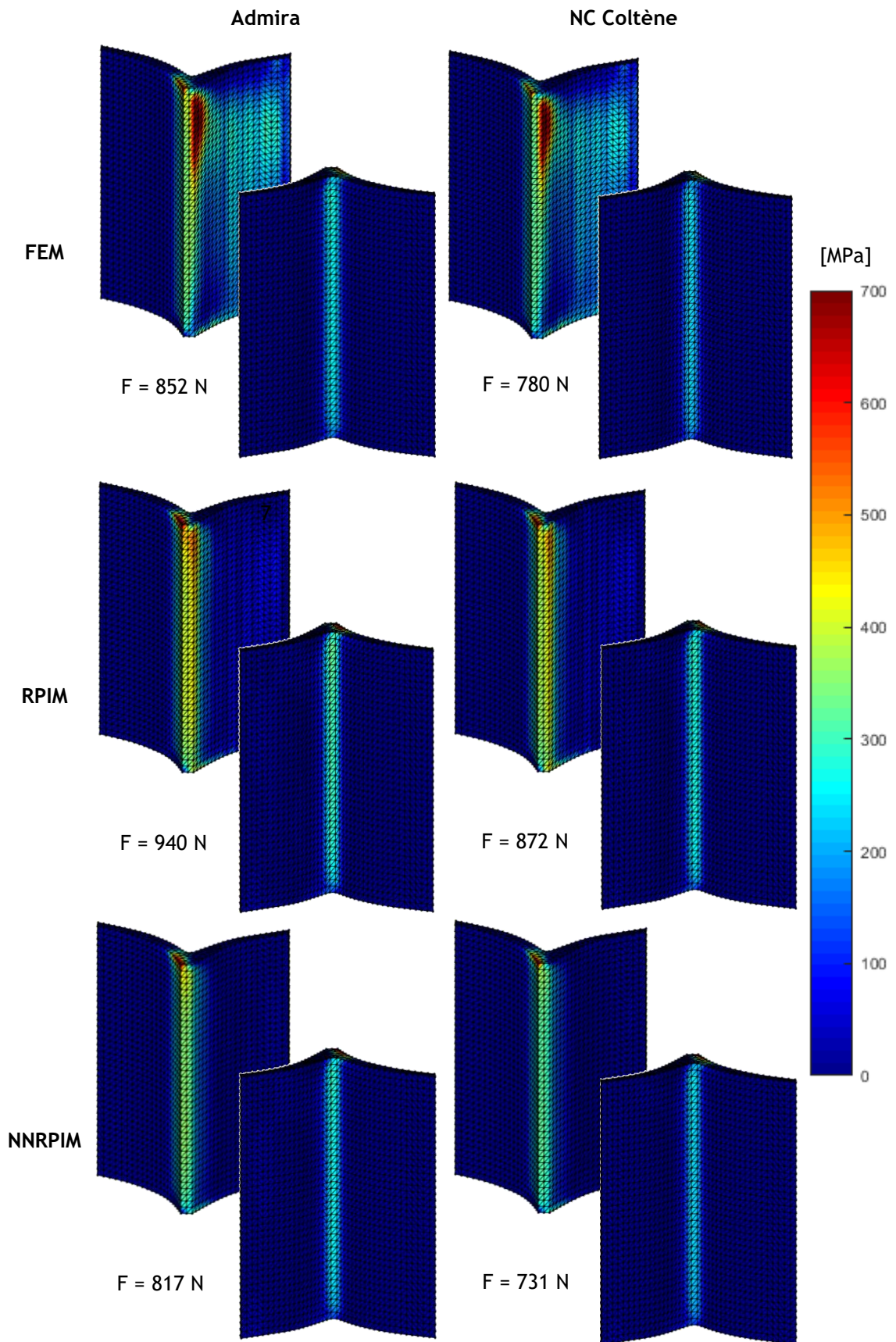
Figure 9.6 - Colour dispersion maps of principal stress σ11 for all the study cases and for different force levels.

Admira   **NC Coltène**

FEM

F = 852 N   F = 780 N

RPIM

F = 940 N   F = 872 N

NNRPIM

F = 817 N   F = 731 N
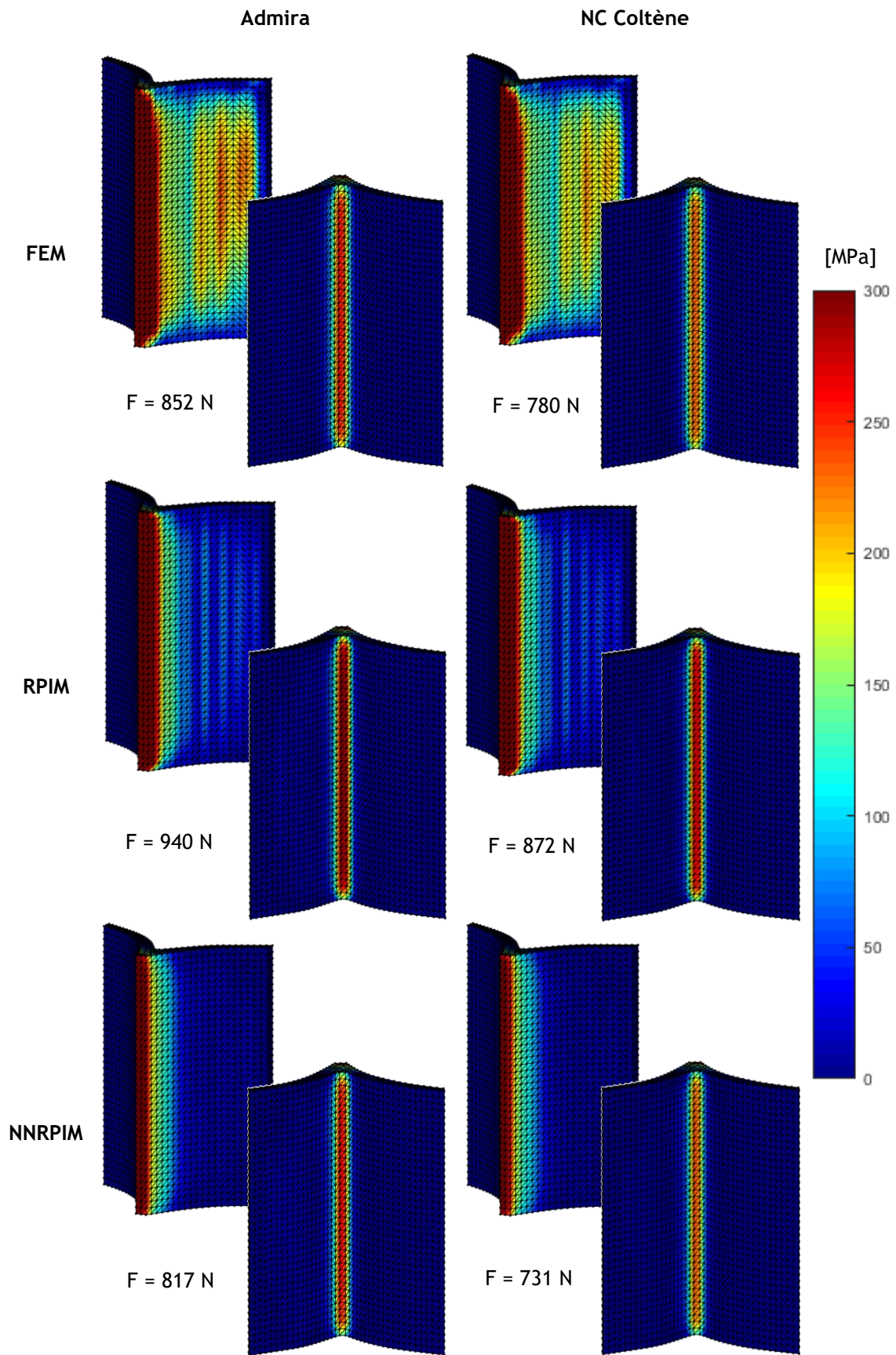
Figure 9.7 - Colour dispersion maps of shear stress component τ_{zx} for all the study cases and for different force levels.

With Figure 9.6 and Figure 9.7, the evaluation of meshless methods performance is not clear, due to the different force levels. Nevertheless, it is possible to observe a common pattern between the three numerical methods, for both principal stress and shear stress distribution along the adhesive. This pattern is consistent to the one found for the elasto-static analysis, presented in section 8.4 (Figure 8.24 and Figure 8.25). It is important to underline the nearly parabolic distribution along the adhesive observed for the shear stress, also previously verified in Figure 8.25. The patterns disclosed in the principal stress and shear component demonstrate that this is the area of the adhesive at higher risk of debonding, leading to failure of the dental prosthesis.

With these colour maps the differences between the two resin-cements are also unclear, once again because they are subjected to different force levels.

The elasto-plastic behaviour of the resin-cements analysed was recorded in the graphs presented in Figure 9.8 and Figure 9.9.
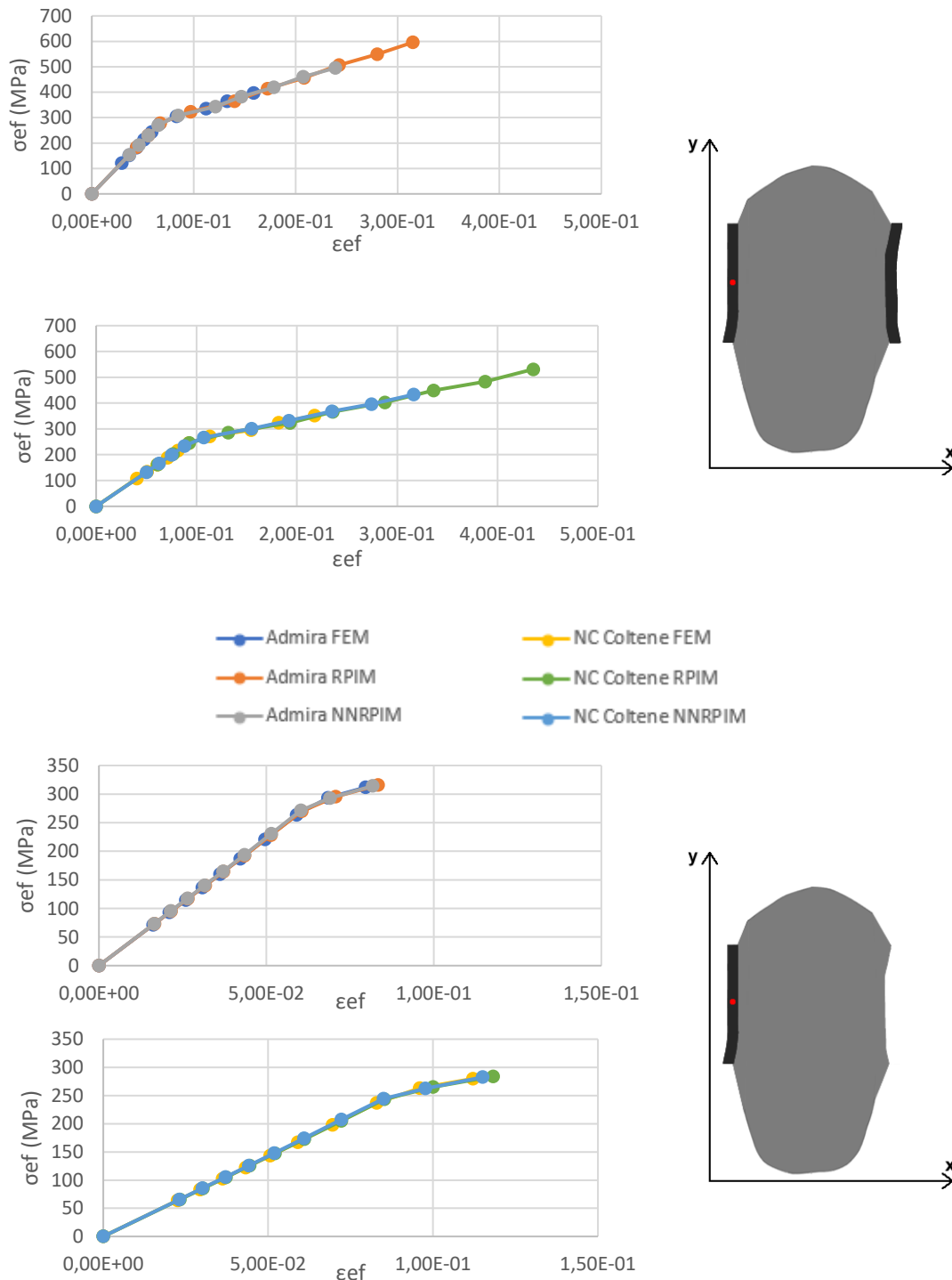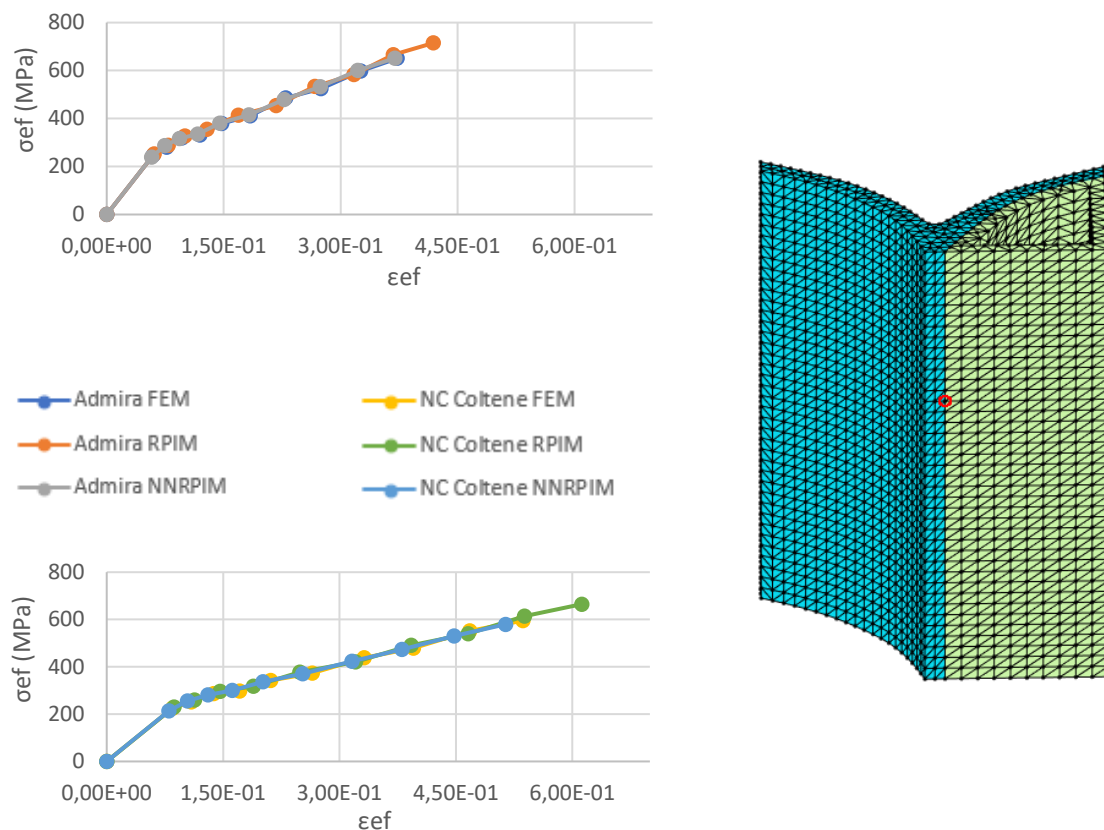

Figure 9.8 - Graphic representation of stress/strain curve in a point of the adhesive.

In Figure 9.8, for a point of the adhesive, marked in red in the figure, it was analysed the stress/strain curve, being possible to compare the behaviour of the two resin-cements studied. It is verified that NC Coltène reaches the elastic limit for lower stresses and higher deformations. Regarding the numerical methods used, the results of the meshless methods approximate the FEM solution in such way that the curves overlap.
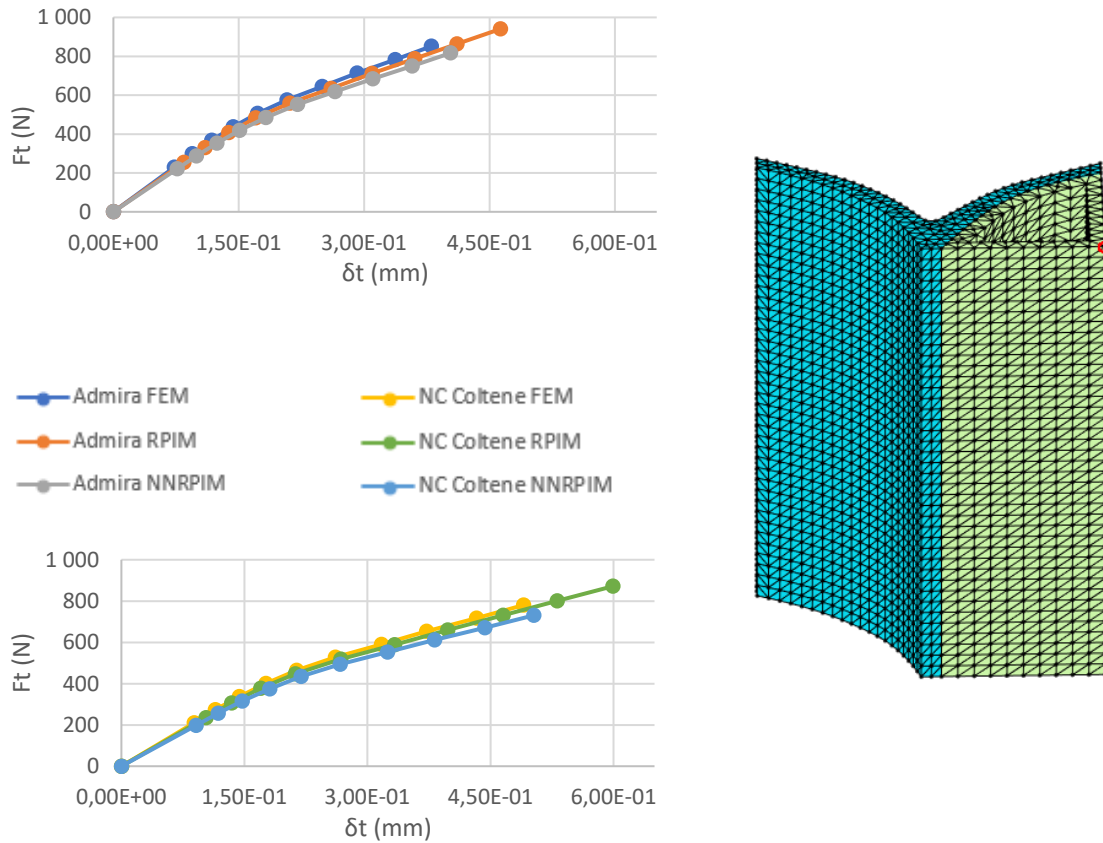
Figure 9.9 - Graphic representation of force/displacement curve in a point of the pontic.

In the graphs of Figure 9.9 a point of the pontic, marked in red, was analysed evaluating the total displacement of the pontic obtained with the force applied. Comparing the two resin-cements it is verified that both present similar behaviour, however NC Coltène reaches the elastic limit for lower forces, which is in concordance with the previous findings in Figure 9.8.

Once again, it was demonstrated that in fact the previously presented elasto-static studies were ignoring the non-linear behaviour that these adhesives present.

This 3D nonlinear-elasto-plastic study allowed to verify that meshless methods can accurately approach to the FEM solution and NC Coltène undergoes permanent deformations for lower forces. The latter is an indicator that this resin-cement can lead to higher discomfort for the patient, increasing the probability of prosthesis failure and replacement.

The conclusions of this study are in total agreement with the previous study, in section 9.1.

Chapter 10

Conclusions and future work

The loss of teeth has a negative impact on the individual's quality of life, affecting performance at work and in daily activities. In my best knowledge, there are no documents regarding the study of adhesive dental bridges and meshless. Therefore, in this work the use of the Radial Point Interpolation Method (RPIM) and the Natural Neighbour Radial Point Interpolation Method (NNRPIM) was extended for the analysis of adhesive dental bridges in 2D and 3D models, being the first time that meshless methods have been used for this purpose.

The main objectives of this thesis were to perform elasto-static and nonlinear-elasto-plastic analysis of adhesive dental bridges using FEM and meshless methods and with these, study the effect of different adhesive's thicknesses, bridge designs and resin-cements on the mechanical behaviour of the dental prosthesis. It was also aimed to compare FEM and meshless methods performances.

Relevant practical conclusions were obtained. It was demonstrated that higher adhesive's thicknesses increases the bridge punctual displacement. Regarding the bridge design, for the single-retainer, higher displacements of the pontic were registered, which can represent a higher discomfort for the patient. It was also verified that the single-retainer design increases stresses on the adhesive, therefore increases the probability of occur debonding. Thus, the use of two retainer wings, adhesively bonded with an adhesive's thickness of 0.1 mm, appears to be the most favourable combination.

With the data obtained through the elasto-static analysis, the effect of the resin-cement on the mechanical resistance of the bridge was unclear. The results of the 2D elasto-static study permitted to obtain the maximum force that the bridge could support under de conditions of the study, allowing to conclude that Brilliant was the resin-cement that supports higher forces. After, the 3D elasto-static analysis demonstrated that Brilliant and NC Coltène presented lower stresses, which could indicate lower probability to occur debonding. However, these two adhesives also presented higher displacements of the pontic, which can represent a less comfortable situation to the patient. These results were in concordance with the behaviour verified in the experimental phase (observed in Figure 3.17), which allowed to observe that Brilliant exhibited a low ductility, that is, it behaves in a fragile way, so it breaks without warning. With this information, the use of this adhesive becomes somewhat less appealing.

On the other hand, the nonlinear-elasto-plastic analysis demonstrated that the elasto-static studies were ignoring the non-linear behaviour that the tested adhesives present. Hence, with

these studies, it was possible to draw more precise conclusions: NC Coltène undergoes permanent deformations for lower forces, which is an indicator that this resin-cement can lead to higher discomfort for the patient, increasing the probability of prosthesis failure and replacement. According to the literature, the occlusal force during chewing peanuts is 35.57 Kg [116], about 350 N. NC Coltène suffers permanent deformations for about 200 N (Figure 9.8 and Figure 9.9). This means that in a daily activity, such as simply eating, the adhesive bridge is suffering irreversible and accumulative deformations, and using the resin-cement NC Coltène, the patient will need to replace the prosthesis earlier.

Two secondary conclusions were also draw: (1) the study of the representative loads of bruxism allowed to verify that this medical condition may lead to failure of dental prostheses; and (2) the 3D studies allowed to observe that the area of the adhesive that is at risk is the one between the abutment and the pontic, therefore here could be an initial point of crack propagation, leading to breakage of the adhesive. It is important to consider that, in all the studies performed, the loads applied were unitary (1 N), thus in real situations all the obtained stresses and displacements have to be multiplied by a factor equal to the magnitude of the realistic applied load.

The use of meshless methods also proved to be adequate, as shown by the significant and recurring overlay of results between these methods and the well-known FEM (mostly in the elasto-plastic numerical analysis, presented in Chapter 9). In the 2D elasto-static study were found abrupt variations in the stress plots for the RPIM, which was due to a lack of mesh and influence-domains refinement. However, in general, meshless methods revealed smoother results, without abrupt variations of stress values (particularly NNRPIM), when compared to FEM results. Furthermore, the literature shows that meshless methods are capable to deliver more accurate solutions [10]. However, there is no exact solution available for the problem analysed. Therefore, the mentioned advantage could not be verified. Nevertheless, one verifiable disadvantage is the higher computational cost, once the analysis time of meshless methods was always superior to the analysis time of FEM (about 2 to 4 times higher).

While this work reached all the proposed objectives, it also had some limitations. Firstly, for the 2D elasto-static study of the adhesive bridge (section 8.3), there were some inconsistencies in the results of the three numerical methods, and it was verified that the solution of the meshless methods moved away from the FEM solution for lower thicknesses. These findings are mainly due to the radial research, once the influence-domains of the point of interest include alternately nodes from the adhesive and the more resistant material, as previously explained. These could be prevented by decreasing the size of the influence-domain, or by increasing the density of the mesh discretization. However, the first solution would reduce the accuracy of the meshless analysis and the second solution would increase even more its computational cost.

Secondly, the development of more realistic models could represent better the complete tooth/restoration system, leading to more accurate results. However, the hardware available limited the level of discretization that could be achieved, hence the necessity to analyse simplified models.

As a future further work, it could be used a real case study to obtain the exact geometry of the dental bridge, as well as the application of complex loads. A more realistic model and natural boundary conditions, allied with a denser element mesh and a nonlinear-elasto-plastic analysis, could lead to more accurate results. A complete experimental phase would be useful for a better mechanical characterization of the resin-cements analysed. Last, the study of the

retainer wing, namely different retainer areas or volumes (depending on the model used) could also be interesting, which could be achieved by varying the retainer's parameters such as height, width and thickness.

References

[1]   C. E. Misch, "Rationale for Dental Implants," in *Dental Implant Prosthetics*, Second Edi., Elsevier Inc., 2014, pp. 1–25.

[2]   C. M. Allen and C. Camisa, "The Challenge of Oral Disease," *Second Edition*. p. 13, 2015.

[3]   S. Listl, J. Galloway, P. A. Mossey, and W. Marcenes, "Global economic impact of dental diseases," *J. Dent. Res.*, vol. 94, no. 10, pp. 1355–1361, 2015.

[4]   J. A. Hobkirk, R. M. Watson, and L. J. J. Searson, *Introducing Dental Implants*, 1st Editio. Churchill Livingstone, 2003.

[5]   A. D. Walmsley *et al.*, *Restorative Dentistry*, Second Edi. Churchill Livingstone, 2007.

[6]   K. A. Durey, P. J. Nixon, S. Robinson, and M. F. W. Y. Chan, "Resin bonded bridges: Techniques for success," *Br. Dent. J.*, vol. 211, no. 3, pp. 113–118, 2011.

[7]   P. K. Vallittu and C. Sevelius, "Resin-bonded, glass fiber-reinforced composite fixed partial dentures: a clinical study.," *J. Prosthet. Dent.*, vol. 84, no. 4, pp. 413–418, 2000.

[8]   L. Shi and A. S. L. Fok, "Structural optimization of the fibre-reinforced composite substructure in a three-unit dental bridge," *Dent. Mater.*, vol. 25, no. 6, pp. 791–801, 2009.

[9]   C. L. Lin, K. W. Hsu, and C. H. Wu, "Multi-factorial retainer design analysis of posterior resin-bonded fixed partial dentures: A finite element study," *J. Dent.*, vol. 33, no. 9, pp. 711–720, 2005.

[10]   J. Belinha, "Meshless Methods in Biomechanics: Bone Tissue Remodelling Analysis," in *Lecture Notes in Computational Vision and Biomechanics*, Springer, 2014.

[11]   B. Śmielak, J. Świniarski, E. Wołowiec-Korecka, and L. Klimek, "2D-finite element analysis of inlay-, onlay bridges with using various materials," *Int. Sci. J.*, vol. 79, no. 2, pp. 71–78, 2016.

[12]   G. J. Tortora and B. Derrickson, *Introduction to the Human Body*, Eighth Edi. Wiley, John & Sons, Incorporated, 2010.

[13]   C. E. Misch, "Bone Density: A Key Determinant for Treatment Planning," in *Dental Implant Prosthetics*, Second Edi., Elsevier Inc., 2014, pp. 237–252.

[14]   A. Gulsahi, "Bone Quality Assessment for Dental Implants," in *Implant Dentistry - The Most Promising Discipline of Dentistry*, I. Turkyilmaz, Ed. InTech, 2011.

[15]   R. C. van Staden, H. Guan, and Y. C. Loo, "Application of the finite element method in dental implant research," *Comput. Methods Biomech. Biomed. Engin.*, vol. 9, no. 4, pp. 257–270, 2006.

[16]   D. Moratal, *Finite Element Analysis: From Biomedical Applications to Industrial Developments*, Second Edi. InTech, 2016.

[17]   Ds. Susan Standring, PhD, "Gray's Anatomy 40th edition," *Churchill Livingstone*. 2009.

[18]   P. Heasman, Ed., *Master dentistry. Volume 2: restorative dentistry, paediatric dentistry and orthodontics*. Churchill Livingstone, 2013.

[19]   S. Nelson, *Wheeler's Dental Anatomy, Physiology, and Occlusion*, 9th Editio. Elsevier Health Sciences, 2009.

[20]   C. M. Abraham, "A Brief Historical Perspective on Dental Implants, Their Surface Coatings and Treatments," *Open Dent. J.*, vol. 8, no. 1, pp. 50–55, 2014.

[21]   P. E. Petersen, D. Bourgeois, H. Ogawa, S. Estupinan-day, and C. Ndiaye, "Policy and

Practice The global burden of oral diseases and risks to oral health," *Bull. World Health Organ.*, vol. 83, no. 9, pp. 661–669, 2005.

[22]   F. Müller, M. Naharro, and G. E. Carlsson, "What are the prevalence and incidence of tooth loss in the adult and elderly population in Europe?," *Clin. Oral Implants Res.*, vol. 18, no. SUPPL. 3, pp. 2–14, 2007.

[23]   Observatório da saúde oral, "Barómetro Da Saúde Oral," *Ordem dos Médicos Dent.*, vol. 3ªEdição, 2017.

[24]   R. Patel, "The state of oral health in Europe.," *Rep. Comm. by Platf. better oral Heal. Eur.*, pp. 1–20, 2012.

[25]   F. McCord and R. Smales, "Oral diagnosis and treatment planning: Part 7. Treatment planning for missing teeth," *Br. Dent. J.*, vol. 213, no. 7, pp. 341–351, 2012.

[26]   A. W. G. Walls, F. S. A. Nohl, and R. W. Wassell, "Crowns and other extra-coronal restorations: Resin-bonded metal restorations," *Br. Dent. J.*, vol. 193, no. 3, pp. 135–142, 2002.

[27]   M. Miettinen and B. J. Millar, "A review of the success and failure characteristics of resin-bonded bridges," *Br. Dent. J.*, vol. 215, no. 2, pp. 76–77, 2013.

[28]   A. Gupta, R. K. Yelluri, and A. K. Munshi, "Fiber-reinforced Composite Resin Bridge: A Treatment Option in Children.," *Int. J. Clin. Pediatr. Dent.*, vol. 8, no. 1, pp. 62–65, 2015.

[29]   R. G. Craig and J. M. Powers, Eds., *Restorative Dental Materials*, Eleventh E. Mosby, 2002.

[30]   I. Ahmad, *Protocols for Predictable Aesthetic Dental Restorations*. John Wiley & Sons, 2008.

[31]   M. Sasse and M. Kern, "All-ceramic resin-bonded fixed dental prostheses: treatment planning, clinical procedures, and outcome," *Quintessence Int.*, vol. 45, no. 4, pp. 291–7, 2014.

[32]   R. De Santis, L. Ambrosio, and L. Nicolais, "Mechanical Properties of Tooth Structures," in *Integrated Biomaterials Science*, Springer US, 2002, pp. 589–599.

[33]   T. P. M. Cornacchia, E. B. Las Casas, C. A. Cimini, and R. G. Peixoto, "3D finite element analysis on esthetic indirect dental restorations under thermal and mechanical loading," *Med. Biol. Eng. Comput.*, vol. 48, no. 11, pp. 1107–1113, 2010.

[34]   S. F. Moreira, J. Belinha, L. M. J. S. Dinis, and R. M. N. Jorge, "A global numerical analysis of the ' central incisor / local maxillary bone ' system using a meshless method," *Mol. Cell. Biomech.*, vol. 11, no. 3, pp. 151–184, 2014.

[35]   A. A. A. Mahmoud, N. Wakabayashi, and H. Takahashi, "Prediction of permanent deformation in cast clasps for denture prostheses using a validated nonlinear finite element model," *Dent. Mater.*, vol. 23, no. 3, pp. 317–324, 2007.

[36]   D. YOKOYAMA, A. SHINYA, H. GOMI, P. K. VALLITTU, and A. SHINYA, "Effects of mechanical properties of adhesive resin cements on stress distribution in fiber-reinforced composite adhesive fixed partial dentures," *Dent. Mater. J.*, vol. 31, no. 2, pp. 189–196, 2012.

[37]   A. Della Bona, T. A. Donassollo, F. F. Demarco, A. A. Barrett, and J. J. Mecholsky, "Characterization and surface treatment effects on topography of a glass-infiltrated alumina/zirconia-reinforced ceramic," *Dent. Mater.*, vol. 23, no. 6, pp. 769–775, 2007.

[38]   P. F. Manicone, P. Rossi Iommetti, and L. Raffaelli, "An overview of zirconia ceramics: Basic properties and clinical applications," *J. Dent.*, vol. 35, no. 11, pp. 819–826, 2007.

[39]   P. Magne, "Efficient 3D finite element analysis of dental restorative procedures using micro-CT data," *Dent. Mater.*, vol. 23, no. 5, pp. 539–548, 2007.

[40]   J.-P. Geng, K. B. C. Tan, and G.-R. Liu, "Application of finite element analysis in implant dentistry: A review of the literature," *J Prosthet Dent*, vol. 85, no. 6, pp. 585–598, 2001.

[41]   S. Trivedi, "Finite element analysis: A boon to dentistry," *J. Oral Biol. Craniofacial Res.*, vol. 4, no. 3, pp. 200–203, 2014.

[42]   A. Srirekha and K. Bashetty, "Infinite to finite: An overview of finite element analysis," *Indian J. Dent. Res.*, vol. 21, no. 3, p. 425, 2010.

[43]   S. K. Parashar and J. K. Sharma, "A review on application of finite element modelling in bone biomechanics," *Perspect. Sci.*, vol. 8, pp. 696–698, 2016.

[44]   W. Li, M. V. Swain, Q. Li, J. Ironside, and G. P. Steven, "Fibre reinforced composite dental bridge. Part II: Numerical investigation," *Biomaterials*, vol. 25, no. 20, pp. 4995–5001, 2004.

[45]   C. Tavares, J. Belinha, L. Dinis, and R. N. Jorge, "The numerical analysis of a restored tooth using meshless methods," *Proc. - 2015 IEEE 4th Port. Meet. Bioeng. ENBENG 2015*, 2015.

[46]   C. S. S. Tavares, J. Belinha, L. M. J. S. Dinis, and R. M. Natal Jorge, "The elasto-plastic response of the bone tissue due to the insertion of dental implants," *Procedia Eng.*, vol. 110, pp. 37–44, 2015.

[47]   L. M. J. S. Dinis, R. M. Natal Jorge, and J. Belinha, "Analysis of 3D solids using the natural neighbour radial point interpolation method," *Comput. Methods Appl. Mech. Eng.*, vol. 196, pp. 2009–2028, 2007.

[48]   R. Sibson, "A vector identity for the dirichlet tessellation," *Math. Proc. Cambridge Philos. Soc.*, vol. 87, no. 1, pp. 151–155, 1980.

[49]   J. Belinha, L. M. J. S. Dinis, and R. M. Natal Jorge, "The analysis of the bone remodelling around femoral stems: A meshless approach," *Math. Comput. Simul.*, vol. 121, pp. 64–94, 2016.

[50]   J. G. Wang and G. R. Liu, "A point interpolation meshless method based on radial basis functions," *Int. J. Numer. Methods Eng.*, vol. 54, no. 11, pp. 1623–1648, 2002.

[51]   R. L. Hardy, "Multiquadric Equations of Topography and Other Irregular Surfaces," *J. Geophys. Res.*, vol. 76, no. 8, pp. 1905–1915, 1971.

[52]   G. R. Liu, S. S. Quek, G. R. Liu, and S. S. Quek, "2 – Introduction to mechanics for solids and structures," in *Finite Element Method*, 2003, pp. 12–34.

[53]   S. F. Moreira, J. Belinha, L. M. J. S. Dinis, and R. M. N. Jorge, "The anisotropic elasto-plastic analysis using a natural neighbour RPIM version," *J. Brazilian Soc. Mech. Sci. Eng.*, vol. 39, no. 5, pp. 1773–1795, 2017.

[54]   D. R. J. Owen and E. Hinton, *Finite Elements in Plasticity: Theory and Practice*, Pineridge. 1980.

[55]   E. M. LIFSHITZ, A. M. KOSEVICH, and L. P. PITAEVSKII, *Theory of Elasticity*, Elsevier. 1986.

[56]   R. Hill, *The mathematical Theory of Plasticity*. Clarendon Press, 1998.

[57]   M. A. Crisfield, *Non-linear Finite Element Analysis of Solids and Structures: Essentials*. Wiley, 1991.

[58]   J. W. Farah, R. G. Craig, and D. L. Sikarskie, "Photoelastic and Finite Element Stress Analysis of a Restored Axisymmetric First Molar," *J. Biomech.*, vol. 6, no. 5, pp. 511–520, 1973.

[59]   R. W. Thresher and G. E. Saito, "The stress analysis of human teeth.," *J. Biomech.*, vol. 6, pp. 443–449, 1973.

[60]   J. W. Farah, J. A. A. Hood, and R. G. Craig, "Effects of Cement Bases on the Stresses in Amalgam Restorations," *J. Dent. Res.*, vol. 55, no. 1, 1975.

[61]   A. L. Yettram, K. W. J. Wright, and H. M. Pickard, "Finite Element Stress Analysis of the Crowns of Normal and Restored Teeth," *J. Dent. Res.*, vol. 55, no. 6, pp. 1004–1011, 1976.

[62]   R. A. Reinhardt, R. F. Krejci, Y. C. Pao, and J. G. Stannard, "Dentin Stresses in Post-reconstructed Teeth with Diminishing Bone Support," *J. Dent. Res.*, vol. 62, no. 9, pp. 1002–1008, 1983.

[63]   S. C. Khera, V. K. Goel, R. C. S. Chen, and S. A. Gurusami, "A Three-dimensional Finite Element Model," *Oper. Dent.*, vol. 13, pp. 128–137, 1988.

[64]   T. W. P. Korioth and A. Versluis, "Modeling the Mechanical Behavior of the Jaws and Their Related Structures By Finite Element (FE) Analysis," *Crit. Rev. Oral Biol. Med.*, vol. 8, no. 1, pp. 90–104, 1997.

[65]   M. Toparli, N. Gökay, and T. Aksoy, "An investigation of temperature and stress distribution on a restored maxillary second premolar tooth using a three-dimensional finite element method.," *J. Oral Rehabil.*, vol. 27, pp. 1077–1081, 2000.

[66]   M. L. Jones, J. Hickman, J. Middleton, J. Knox, and C. Volp, "A validated finite element method study of orthodontic tooth movement in the human subject," *J. Orthod.*, vol. 28, no. 1, pp. 29–38, 2001.

[67]   N. Verdonschot, W. M. M. Fennis, J. Stolk, C. M. Kreulen, and N. H. J. Creugers,

"Generation of 3-D Finite Element Models of Restored Human Teeth Using Micro-CT Techniques," *Int J Prosthodont*, vol. 14, no. 4, pp. 310–315, 2001.

[68] K. Akça, Y. Cavusoglu, E. Sagirkaya, B. Aybar, and M. C. Cehreli, "CAD/CAM glass ceramics for single-tooth implant crowns: A finite element analysis," *Implant Dent.*, vol. 22, no. 6, pp. 623-626, 2013.

[69] A. Chen, X. Feng, Y. Zhang, R. Liu, and L. Shao, "Finite element analysis to study the effects of using CAD/CAM glass-fiber post system in a severely damaged anterior tooth," *Biomed. Mater. Eng.*, vol. 26, pp. S519-S525, 2015.

[70] S. Barone, A. Paoli, A. V. Razionale, and R. Savignano, "Computer aided modelling to simulate the biomechanical behaviour of customised orthodontic removable appliances," *Int. J. Interact. Des. Manuf.*, vol. 10, no. 4, pp. 387-400, 2016.

[71] P. Ausiello, S. Ciaramella, M. Martorelli, A. Lanzotti, A. Gloria, and D. C. Watts, "CAD-FE modeling and analysis of class II restorations incorporating resin-composite, glass ionomer and glass ceramic materials," *Dent. Mater.*, 2017.

[72] C. Field *et al.*, "Mechanical responses to orthodontic loading: A 3-dimensional finite element multi-tooth model," *Am. J. Orthod. Dentofac. Orthop.*, vol. 135, no. 2, pp. 174-181, 2009.

[73] P. F. Hübsch, J. Middleton, J. S. Rees, and P. H. Jacobsen, "An adaptive finite-element approach for the analysis of dental restorations," *J. Biomed. Eng.*, vol. 15, no. 5, pp. 401–408, 1993.

[74] M. M. Winkler, J. Chen, H. Qian, D. W. Hamula, T. J. Carlson, and T. R. Katona, "Experimental validation of a finite element model of light-activated polymerization shrinkage," *J Biomed Mater Res*, vol. 53, no. 5, pp. 554-559, 2000.

[75] D. Palamara, J. E. A. Palamara, M. J. Tyas, and H. H. Messer, "Strain patterns in cervical enamel of teeth subjected to occlusal loading," *Dent. Mater.*, vol. 16, no. 6, pp. 412-419, 2000.

[76] C. M. A. Mattos, E. B. Las Casas, I. G. R. Dutra, H. A. Sousa, and S. M. G. Guerra, "Numerical analysis of the biomechanical behaviour of a weakened root after adhesive reconstruction and post-core rehabilitation," *J. Dent.*, vol. 40, no. 5, pp. 423–432, 2012.

[77] I. Z. Oskui, M. N. Ashtiani, A. Hashemi, and H. Jafarzadeh, "Effect of thermal stresses on the mechanism of tooth pain," *J. Endod.*, vol. 40, no. 11, pp. 1835-1839, 2014.

[78] P. Ausiello, P. Franciosa, M. Martorelli, and D. C. Watts, "Numerical fatigue 3D-FE modeling of indirect composite-restored posterior teeth," *Dent. Mater.*, vol. 27, no. 5, pp. 423–430, 2011.

[79] P.-J. RODRíGUEZ-CERVANTES, J.-L. SANCHO-BRU, C. GONZÁLEZ-LLUCH, A. PÉREZ-GONZÁLEZ, A. BARJAU-ESCRIBANO, and L. FORNER-NAVARRO, "Premolars restored with posts of different materials: fatigue analysis," *Dent. Mater. J.*, vol. 30, no. 6, pp. 881–886, 2011.

[80] B. R. da Silva, J. J. S. Moreira Neto, J. I. da Silva, and A. S. W. de Aguiar, "Three-dimensional finite element analysis of the maxillary central incisor in two different situations of traumatic impact," *Comput. Methods Biomech. Biomed. Engin.*, vol. 16, no. 2, pp. 158-164, 2013.

[81] J. Han, Y. Sun, and C. Wang, "Effect of Integration Patterns Around Implant Neck on Stress Distribution in Peri-Implant Bone: A Finite Element Analysis," *J. Prosthodont.*, vol. 26, no. 6, pp. 549-558, 2017.

[82] A. Gerami, S. Dadgar, V. Rakhshan, P. Jannati, and F. Sobouti, "Displacement and force distribution of splinted and tilted mandibular anterior teeth under occlusal loads: an in silico 3D finite element analysis," *Prog. Orthod.*, vol. 17, no. 1, 2016.

[83] P. Ausiello, S. Rengo, C. L. Davidson, and D. C. Watts, "Stress distributions in adhesively cemented ceramic and resin-composite class II inlay restorations: A 3D-FEA study," *Dent. Mater.*, vol. 20, no. 9, pp. 862-872, 2004.

[84] P. Ausiello, A. Apicella, and C. . Davidson, "Effect of adhesive layer properties on stress distribution in composite restorations—a 3D finite element analysis," *Dent. Mater.*, vol. 18, no. 4, pp. 295-303, 2002.

[85] J. Zhu, Q. Rong, X. Wang, and X. Gao, "Influence of remaining tooth structure and restorative material type on stress distribution in endodontically treated maxillary premolars: A finite element analysis," *J. Prosthet. Dent.*, vol. 117, no. 5, pp. 646-655,

2017.

[86] P. Ausiello, A. Apicella, C. L. Davidson, and S. Rengo, "3D-finite element analyses of cusp movements in a human upper premolar, restored with adhesive resin-based composites," *J. Biomech.*, vol. 34, no. 10, pp. 1269–1277, 2001.

[87] H. A. Awadalla, M. Azarbal, Y. H. Ismail, and W. El-Ibiari, "Three-dimensional finite element stress analysis of a cantilever fixed partial denture," *J. Prosthet. Dent.*, vol. 68, no. 2, pp. 243–8, 1992.

[88] C. H. Wang, H. E. Lee, C. C. Wang, and H. P. Chang, "Methods to improve a periodontally involved terminal abutment of a cantilever fixed partial denture a finite element stress analysis.," *J. Oral Rehabil.*, vol. 25, no. 4, pp. 253–7, 1998.

[89] Z. Zhang, S. Zhou, E. Li, W. Li, M. V. Swain, and Q. Li, "Design for minimizing fracture risk of all-ceramic cantilever dental bridge," *Biomed. Mater. Eng.*, vol. 26, pp. S19–S25, 2015.

[90] O. Eraslan, M. Sevimay, A. Usumez, and G. Eskitascioglu, "Effects of cantilever design and material on stress distribution in fixed partial dentures – a finite element analysis," *J. Oral Rehabil.*, vol. 32, no. 4, pp. 273–278, 2005.

[91] H.-S. Yang, H.-J. Chung, and Y.-J. Park, "Stress analysis of a cantilevered fixed partial denture with normal and reduced bone support," *J. Prosthet. Dent.*, vol. 76, no. 4, pp. 424–430, 1996.

[92] A. N. Natali, P. G. Pavan, and A. L. Ruggero, "Evaluation of stress induced in peri-implant bone tissue by misfit in multi-implant prosthesis," *Dent. Mater.*, vol. 22, no. 4, pp. 388–395, 2006.

[93] P. Henyš, M. Ackermann, L. Čapek, T. Drahorád, A. Šimůnek, and M. Exnerová, "Stress and fatigue analysis of cantilevered bridge during biting: a computer study," *Comput. Methods Biomech. Biomed. Engin.*, vol. 20, no. sup1, pp. 103–104, 2017.

[94] H. Yang, L. Lang, and D. Felton, "Finite element stress analysis on the effect of splinting in fixed partial dentures," *J Prosthet Dent*, vol. 81, no. 6, pp. 721–728, 1999.

[95] G. Rappelli, L. Scalise, M. Procaccini, and E. P. Tomasini, "Stress distribution in fiber-reinforced composite inlay fixed partial dentures," *J. Prosthet. Dent.*, vol. 93, no. 5, pp. 425–432, 2005.

[96] S. Mokhtarikhoee, A. Jannesari, H. Behroozi, and S. Mokhtarikhoee, "Effect of connector width on stress distribution in all ceramic fixed partial dentures (a 3D finite element study)," in *Conference proceedings : 30th Annual International IEEE EMBS Conference*, 2008, pp. 1829–1832.

[97] O.-C. Andrei, M. N. Dina, R. Margarit, and M. H. Tierean, "3D Finite Elements Analysis of Stresses in a 3 unit Mandibular Metal-ceramic Bridge," *Metal. Int.*, vol. 18, no. 3, pp. 132–137, 2013.

[98] Ł. Reimann, J. Żmudzki, and L. A. Dobrzański, "Strength analysis of a three-unit dental bridge framework with the Finite Element Method," *Acta Bioeng. Biomech.*, vol. 17, no. 1, pp. 51–59, 2015.

[99] N. Calha, T. Rodrigues, A. Messias, L. Roseiro, P. Nicolau, and M. A. Neto, "Effects of micromovement on the strain distribution of an implant supported zirconia dental bridge structure during loading: A 3D digital image correlation and 3D finite element analysis," in *Biodental Engineering III - Proceedings of the 3rd International Conference on Biodental Engineering*, 2014, pp. 97–101.

[100] R. Pietrabissa, R. Contro, V. Quaglini, M. Soncini, L. Gionso, and M. Simion, "Experimental and computational approach for the evaluation of the biomechanical effects of dental bridge misfit," *J. Biomech*, vol. 33, no. 11, pp. 1489–1495, 2000.

[101] P. Magne, N. Perakis, U. C. Belser, and I. Krejci, "Stress distribution of inlay-anchored adhesive fixed partial dentures: A finite element analysis of the influence of restorative materials and abutment preparation design," *J Prosthet Dent*, vol. 87, no. 5, pp. 516–527, 2002.

[102] W. Li, M. V Swain, Q. Li, and G. P. Steven, "Towards automated 3D finite element modeling of direct fiber reinforced composite dental bridge," *J. Biomed. Mater. Res. Part B Appl. Biomater.*, vol. 74B, no. 1, pp. 520–528, 2005.

[103] T. Nakamura, T. Ohyama, T. Waki, and S. Kinuta, "Finite Element Analysis of Fiber-reinforced Fixed Partial Dentures," *Dent. Mater. J.*, vol. 24, no. 2, pp. 275–279, 2005.

[104] I. Lopes *et al.*, "All-ceramic CAD-CAM Maryland bridge - a numerical stress analysis,"

in *Biodental Engineering III - Proceedings of the 3rd International Conference on Biodental Engineering*, 2014, pp. 291–294.

[105] J. R. Andrade, J. Belinha, L. M. J. S. Dinis, and R. M. Natal Jorge, "Analysis of dental implant using a meshless method," in *Biodental Engineering II - Proceedings of the 2nd International Conference on Biodental Engineering*, 2013, pp. 145–150.

[106] J. Belinha, L. M. J. S. Dinis, and R. M. N. Jorge, "The bone tissue remodelling analysis in dentistry using a meshless method," in *Biodental Engineering III - Proceedings of the 3rd International Conference on Biodental Engineering*, 2014, pp. 213–220.

[107] J. Belinha, L. M. J. S. Dinis, and R. M. Natal Jorge, "Mandible bone tissue remodelling analysis using a new numerical approach," in *Biodental Engineering II - Proceedings of the 2nd International Conference on Biodental Engineering*, 2013, pp. 151–157.

[108] J. Belinha, L. M. J. S. Dinis, and R. M. N. Jorge, "The Mandible Remodeling Induced By Dental Implants: a Meshless Approach," *J. Mech. Med. Biol.*, vol. 15, no. 04, pp. 1550059-1–31, 2015.

[109] C. S. Tavares, J. Belinha, L. Dinis, and R. Natal, "The biomechanical response of a restored tooth due to bruxism : a mesh- less approach," in *BioMedWomen: Proceedings of the International Conference on Clinical and Bioengineering for Women's Health*, 2016, pp. 49–56.

[110] C. S. S. Tavares, J. Belinha, L. M. J. S. Dinis, and R. M. Natal Jorge, "Numerical analysis of a teeth restoration: A meshless method approach," in *Biodental Engineering III - Proceedings of the 3rd International Conference on Biodental Engineering*, 2014, pp. 207–211.

[111] H. M. S. Duarte, J. Belinha, L. M. J. S. Dinis, and R. M. Natal Jorge, "Analysis of a bar-implant using meshless method," in *Biodental Engineering II - Proceedings of the 2nd International Conference on Biodental Engineering*, 2013, pp. 139–144.

[112] S. F. Moreira, J. Belinha, L. M. J. S. Dinis, and R. M. Natal Jorge, "A meshless method analysis of maxillary central incisor," in *Biodental Engineering II - Proceedings of the 2nd International Conference on Biodental Engineering2*, 2013, pp. 159–161.

[113] J. Tavares and N. Jorge, Eds., *Lectures Notes in Computational Vision and Biomechanics*. 2012.

[114] S. Belli, O. Eraslan, and G. Eskitascioglu, "Effect of Root Filling on Stress Distribution in Premolars with Endodontic-Periodontal Lesion: A Finite Elemental Analysis Study," *J. Endod.*, vol. 42, no. 1, pp. 150–155, 2016.

[115] C. Hopkins, "An immediate cantilever Rochette bridge.," *Br. Dent. J.*, vol. 151, no. 9, pp. 292–295, Nov. 1981.

[116] S. B. G. C H Gibbs, P E Mahan, H C Lundeen, K Brehnan, E K Walsh, S L Sinkewiz, "Occlusal forces during chewing- influences of biting strength and food consistency," *J. Prosthet. Dent.*, vol. 46, no. 5, pp. 561–567, 1981.

Appendix 1

Each figure represents a colour dispersion map of the principal stress σ11 for a specific adhesive's thickness, resin-cement, design, load case and numerical method. Thus, 120 different images are shown.

Figure A.1 - Colour dispersion maps of principal stress σ11 for the following parameters: (1) Two-retainer design; (2) all adhesive's thicknesses; (3) α=90°; (4) both resin-cements (Admira and Brilliant/NC Coltène); and (5) the three numerical methods: FEM, RPIM and NNRPIM.

Figure A.2 - Colour dispersion maps of principal stress σ11 for the following parameters: (1) Single-retainer design; (2) all adhesive's thicknesses; (3) α=90˚; (4) both resin-cements (Admira and Brilliant/NC Coltène); and (5) the three numerical methods: FEM, RPIM and NNRPIM.

FEM

RPIM

NNRPIM

Admira — Brilliant / NC Coltène — Admira — Brilliant / NC Coltène — Admira — Brilliant / NC Coltène

Model A1

Model A2

Model A3

Model A4

Min = 0 MPa   Max = 0.3 MPa

Figure A.3 - Colour dispersion maps of principal stress σ11 for the following parameters: (1) Two-retainer design; (2) all adhesive's thicknesses; (3) α=45°; (4) both resin-cements (Admira and Brilliant/NC Coltène); and (5) the three numerical methods: FEM, RPIM and NNRPIM.

Figure A.4 - Colour dispersion maps of principal stress σ11 for the following parameters: (1) Single-retainer design; (2) all adhesive's thicknesses; (3) α=45˚; (4) both resin-cements (Admira and Brilliant/NC Coltène); and (5) the three numerical methods: FEM, RPIM and NNRPIM.
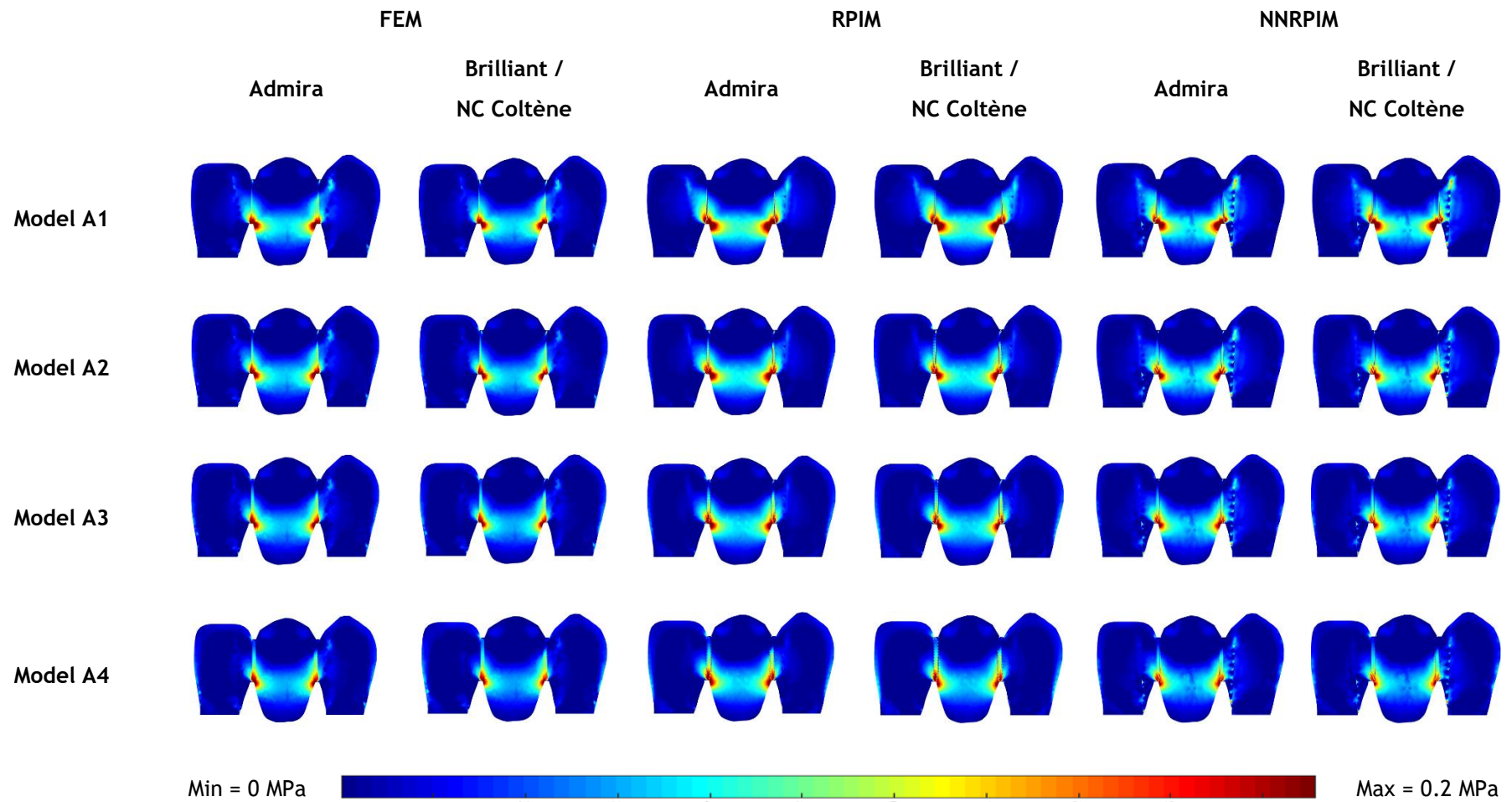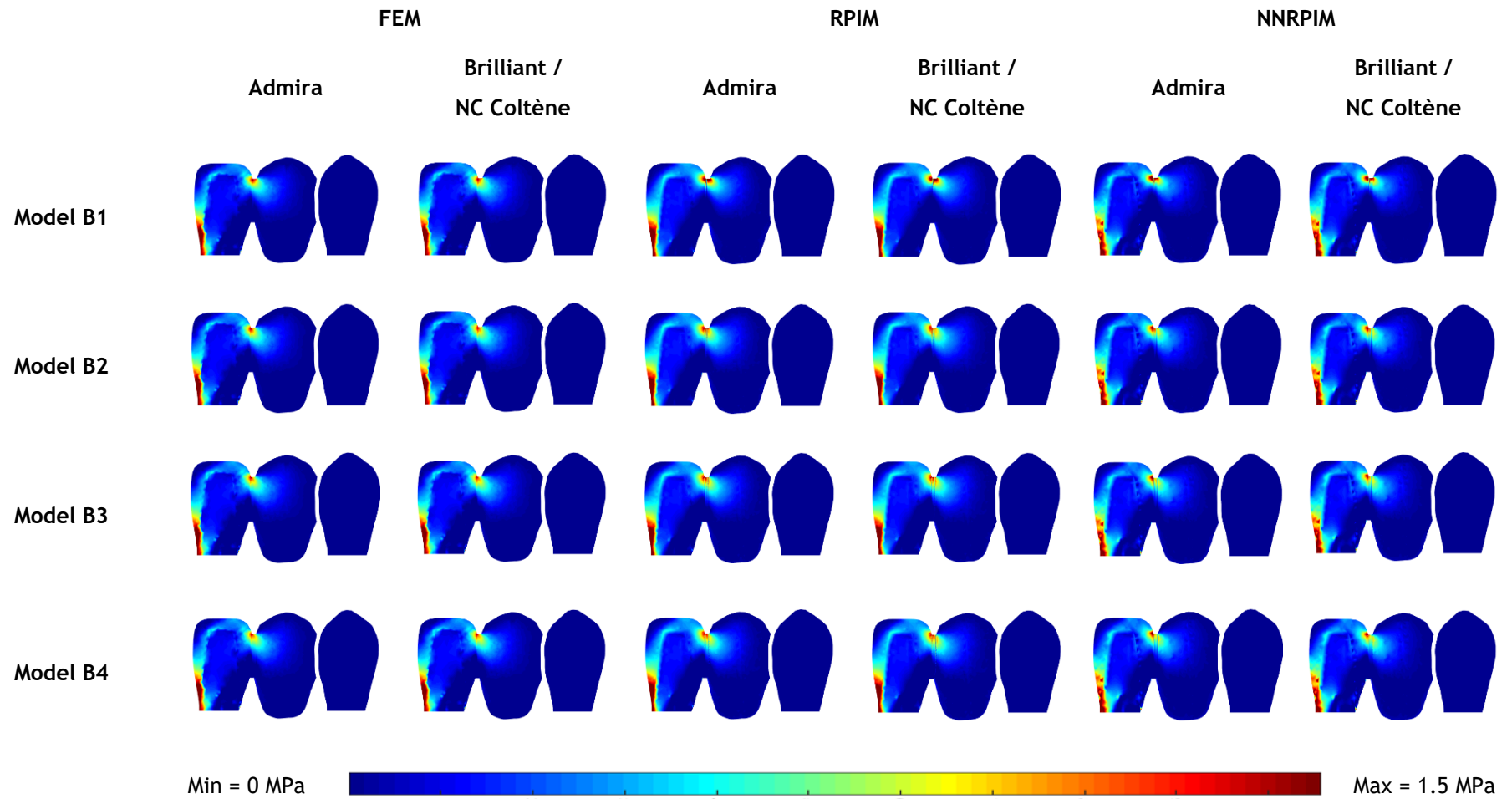
Figure A.5 - Colour dispersion maps of principal stress σ11 for the following parameters: (1) Single-retainer design; (2) all adhesive's thicknesses; (3) α= 135˚; (4) both resin-cements (Admira and Brilliant/NC Coltène); and (5) the three numerical methods: FEM, RPIM and NNRPIM.

Appendix 2

In this Appendix, it is presented the analysis of the principal stress σ11 for all studied cases. This analysis is performed for the limit patches, i.e. for the patches of the adhesive that are in the boundary between the abutment and the adhesive and between the adhesive and the pontic. Therefore, each graphic represents a specific patch, adhesive's thickness, design and load case. Each curve on the graphics represents a resin-cement and numerical method. Thus, there are 49 graphics grouped in 5 figures.

Figure A.6 - Graphic representation of principal stress σ11, in points along the left and right retainer wings for the following parameters: (1) Two-retainer design; (2) all adhesive's thicknesses; (3) α=90°; (4) both resin-cements (Admira and Brilliant/NC Coltène); and (5) the three numerical methods: FEM, RPIM and NNRPIM.

Figure A.7 - Graphic representation of principal stress σ11, in points along the left retainer wing for the following parameters: (1) Single-retainer design; (2) all adhesive's thicknesses; (3) α=90°; (4) both resin-cements (Admira and Brilliant/NC Coltène); and (5) the three numerical methods: FEM, RPIM and NNRPIM.
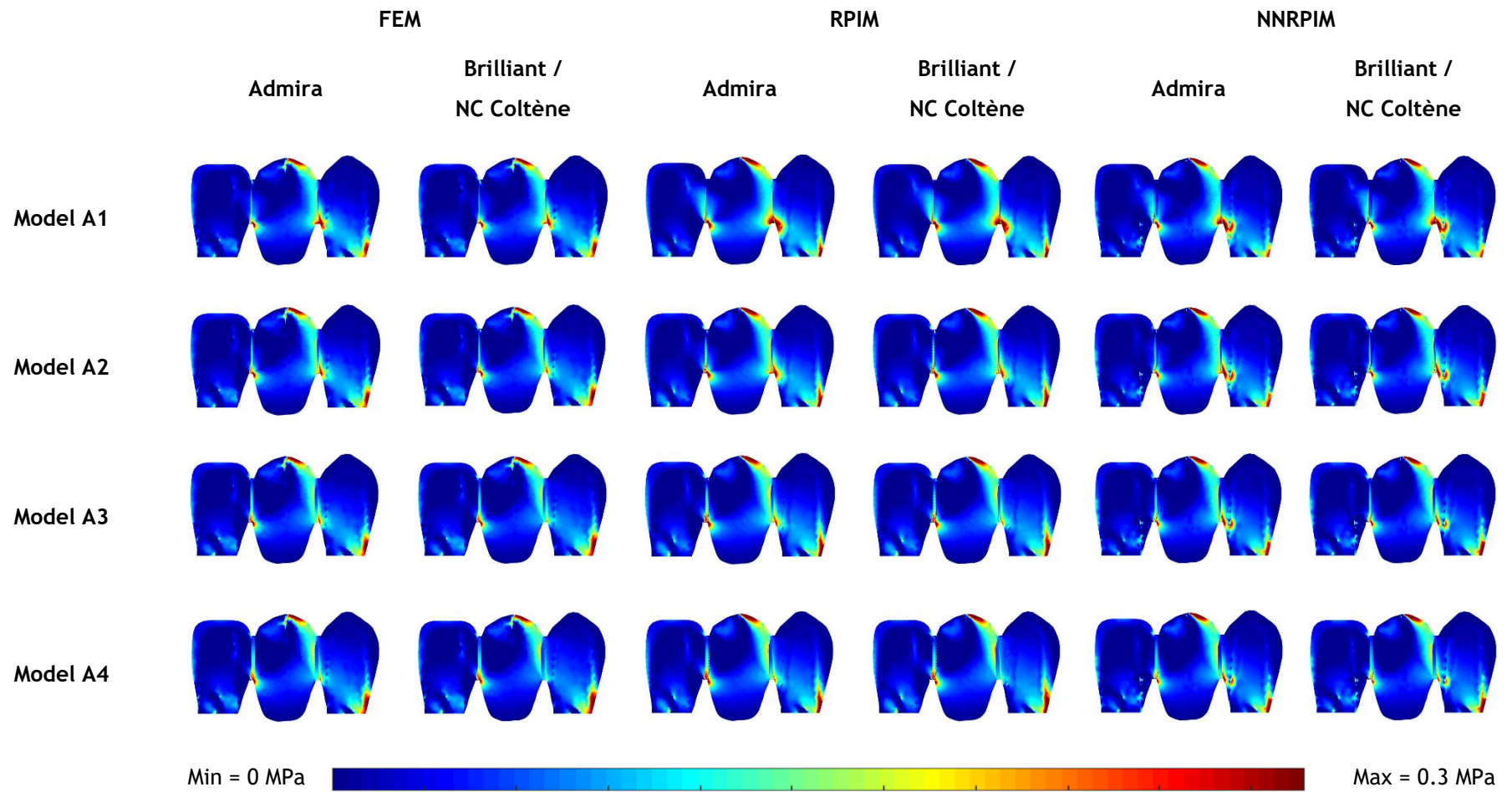
Figure A.8 - Graphic representation of principal stress σ11, in points along the left and right retainer wings for the following parameters: (1) Two-retainer design; (2) all adhesive's thicknesses; (3) α=45°; (4) both resin-cements (Admira and Brilliant/NC Coltène); and (5) the three numerical methods: FEM, RPIM and NNRPIM.
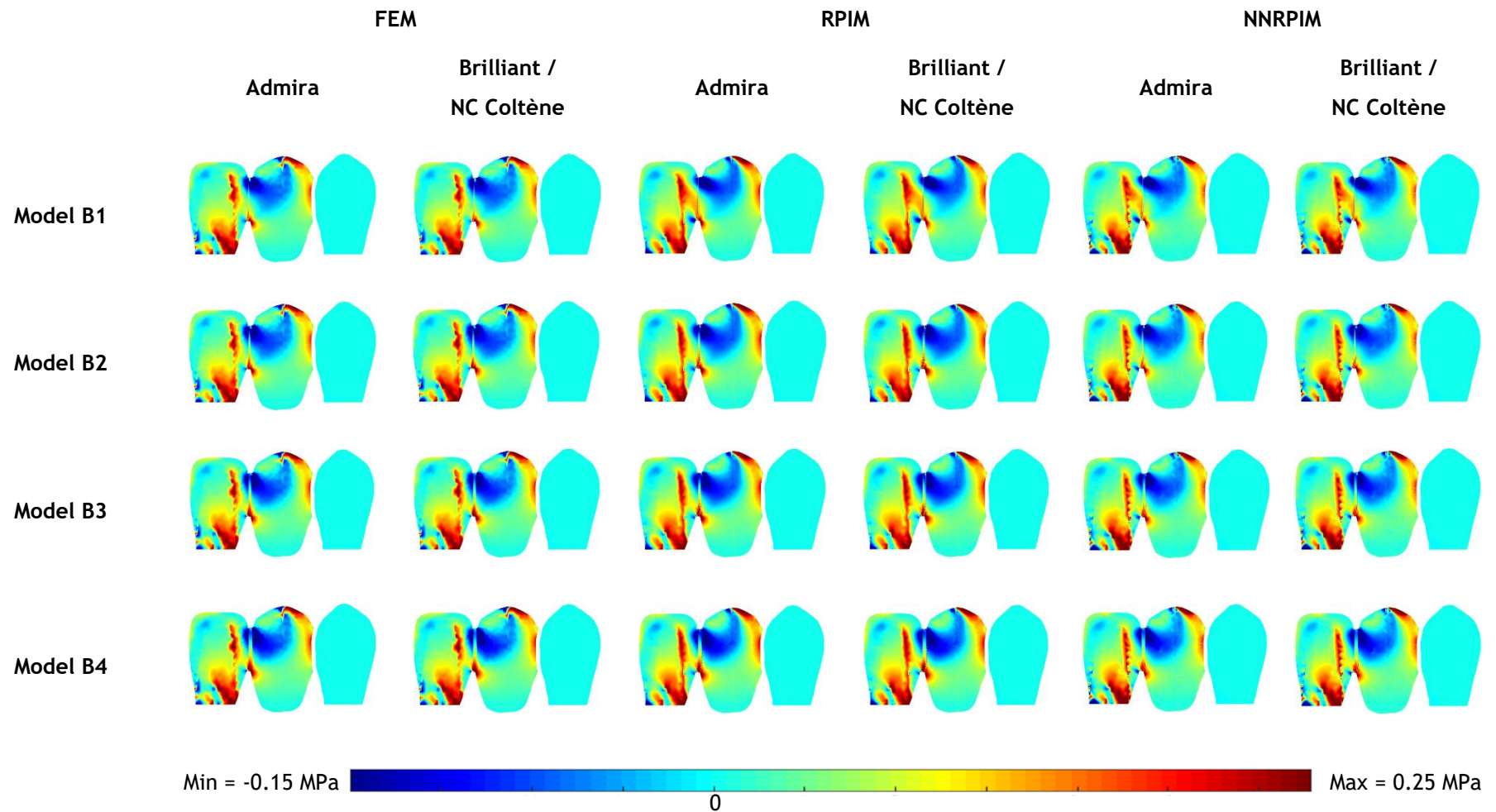
Figure A.9 - Graphic representation of principal stress σ11, in points along the left retainer wings for the following parameters: (1) Single-retainer design; (2) all adhesive's thicknesses; (3) α=45˚; (4) both resin-cements (Admira and Brilliant/NC Coltène); and (5) the three numerical methods: FEM, RPIM and NNRPIM.
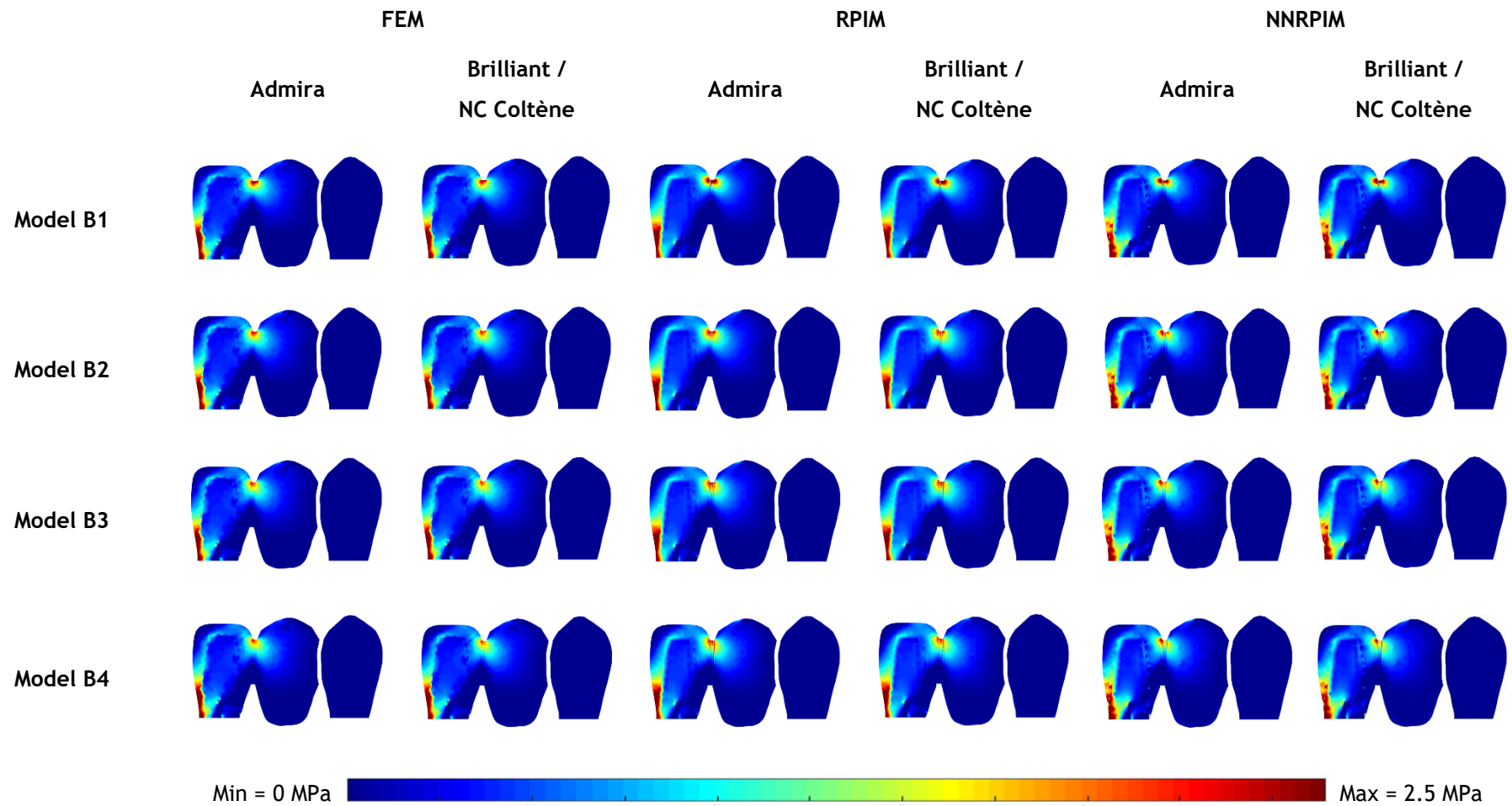
Figure A.10 - Graphic representation of principal stress σ11, in points along the left retainer wing for the following parameters: (1) Single-retainer design; (2) all adhesive's thicknesses; (3) α= 135˚; (4) both resin-cements (Admira and Brilliant/NC Coltène); and (5) the three numerical methods: FEM, RPIM and NNRPIM.

Appendix 3

In this Appendix, it is presented the analysis of the shear stress component τ_{xy} for all the study cases. This analysis is performed for the limit patches, i.e. for the patches of the adhesive that are in the boundary between the abutment and the adhesive and between the adhesive and the pontic. Therefore, each graphic represents a specific patch, adhesive's thickness, design and load case. Each curve on the graphics represents a resin-cement and numerical method. Thus, there are 49 graphics grouped in 5 figures.
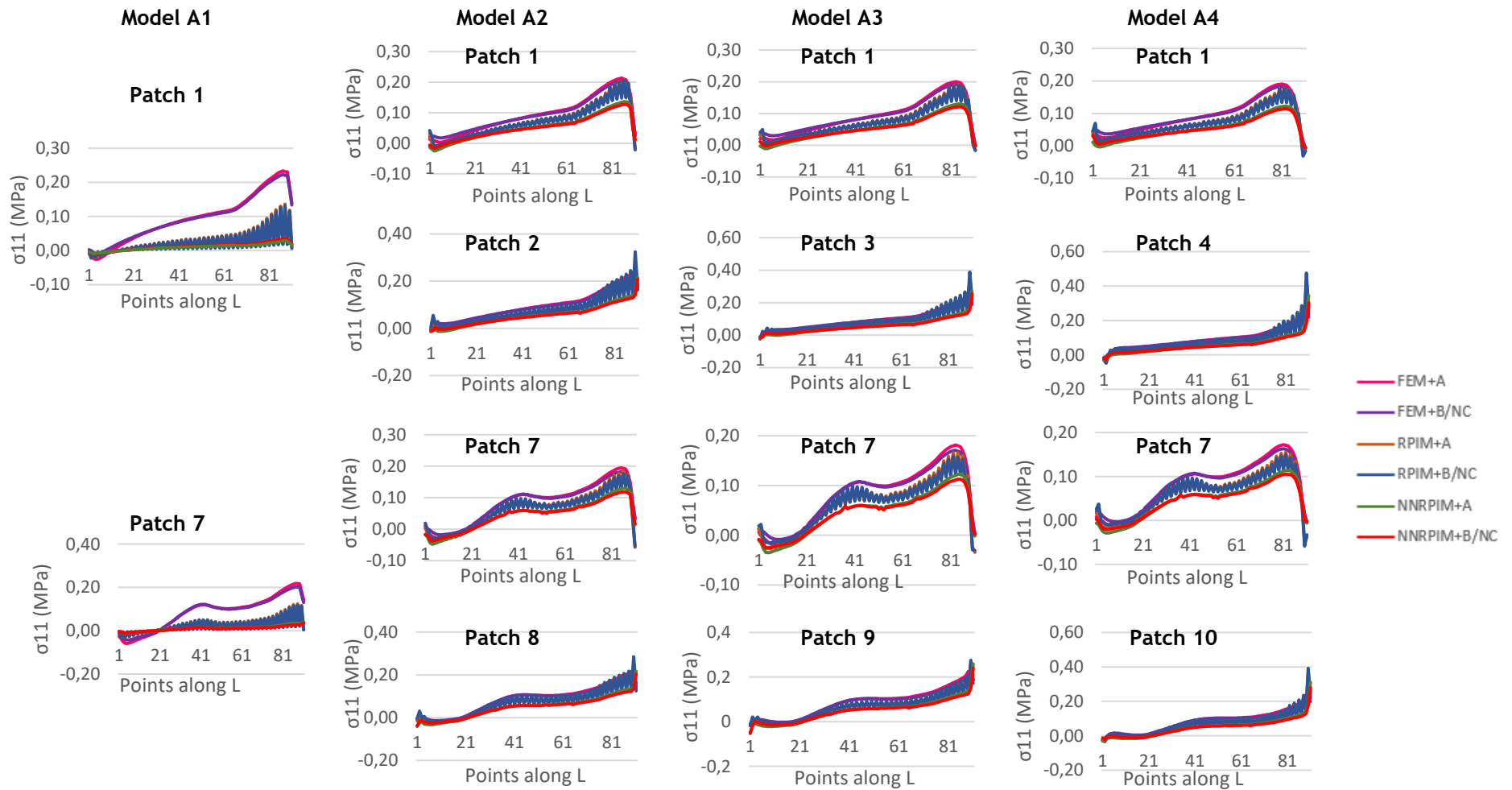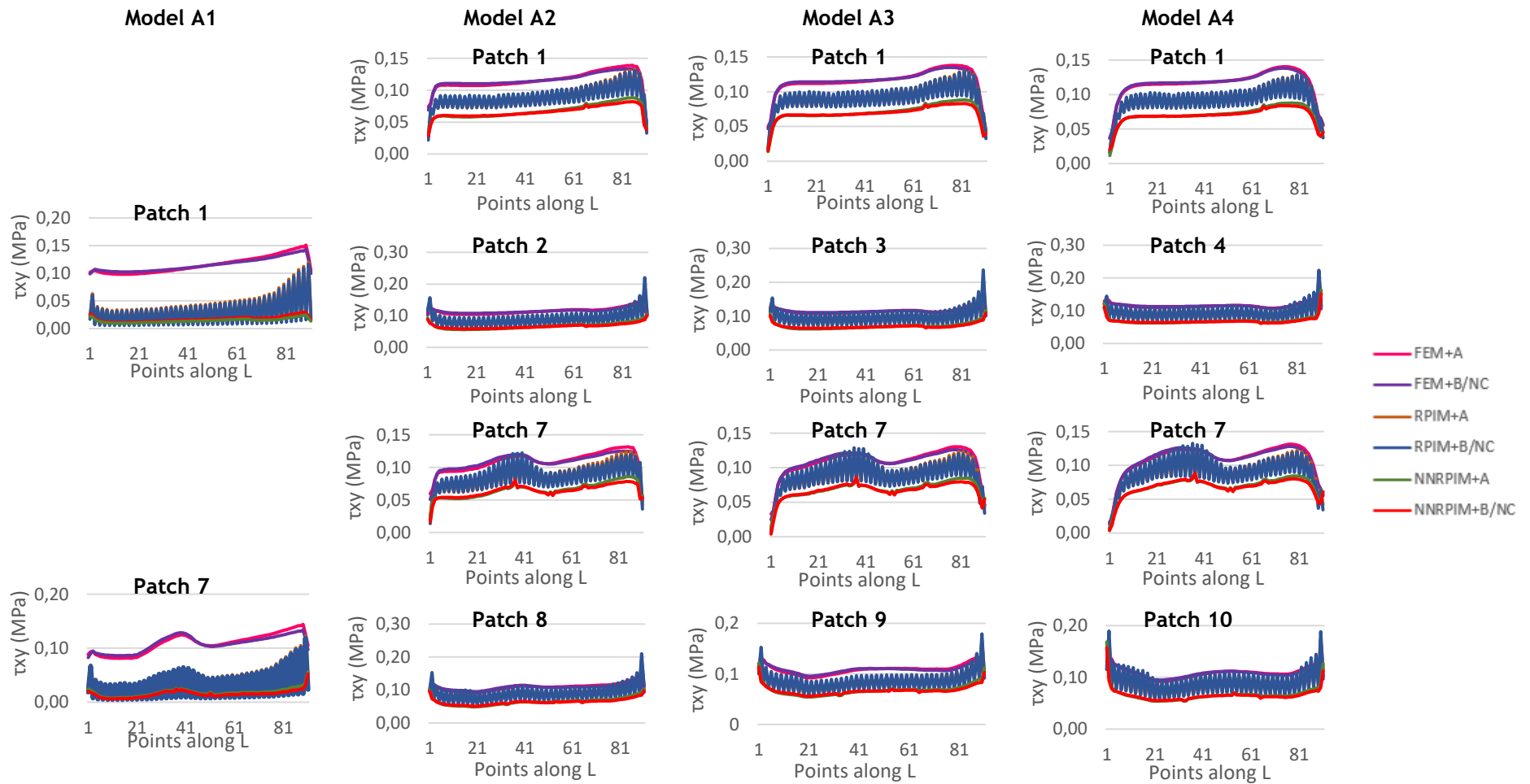
Figure A.11 - Graphic representation of shear stress component τ_{xy}, in points along the left and right retainer wings for the following parameters: (1) Two-retainer design; (2) all adhesive's thicknesses; (3) α= 90˚; (4) both resin-cements (Admira and Brilliant/NC Coltène); and (5) the three numerical methods: FEM, RPIM and NNRPIM.
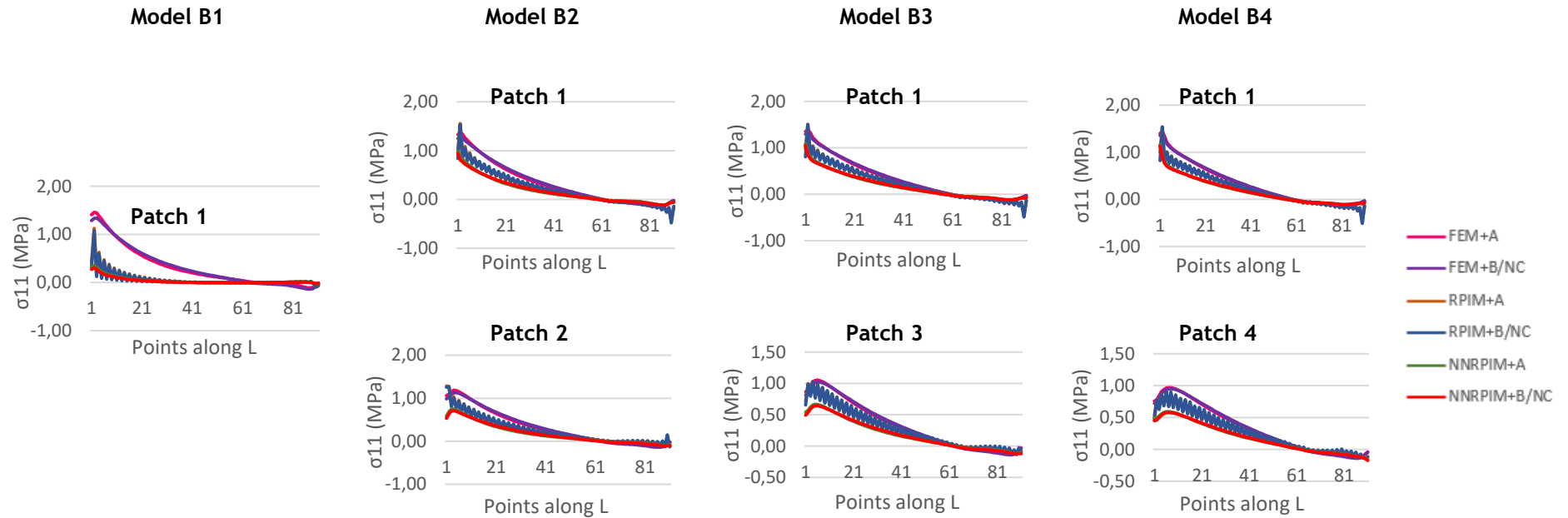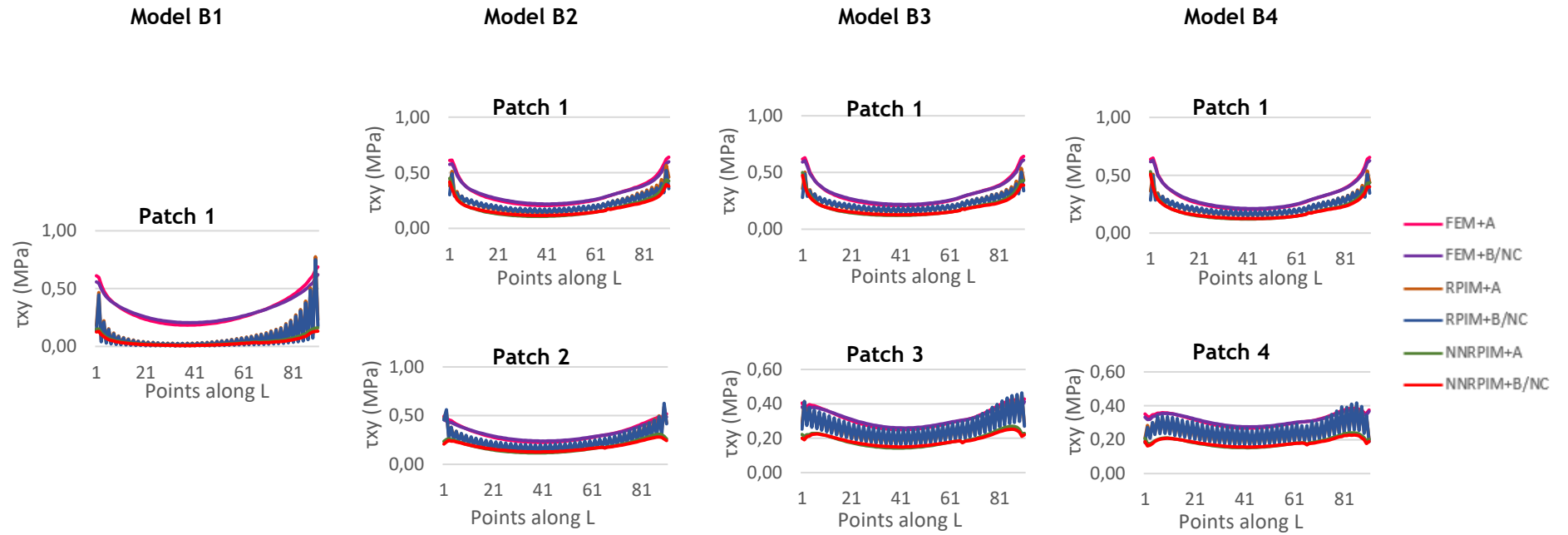
Figure A.12 - Graphic representation of shear stress component τ_{xy}, in points along the left retainer wing for the following parameters: (1) Single-retainer design; (2) all adhesive's thicknesses; (3) α= 90˚; (4) both resin-cements (Admira and Brilliant/NC Coltène); and (5) the three numerical methods: FEM, RPIM and NNRPIM.
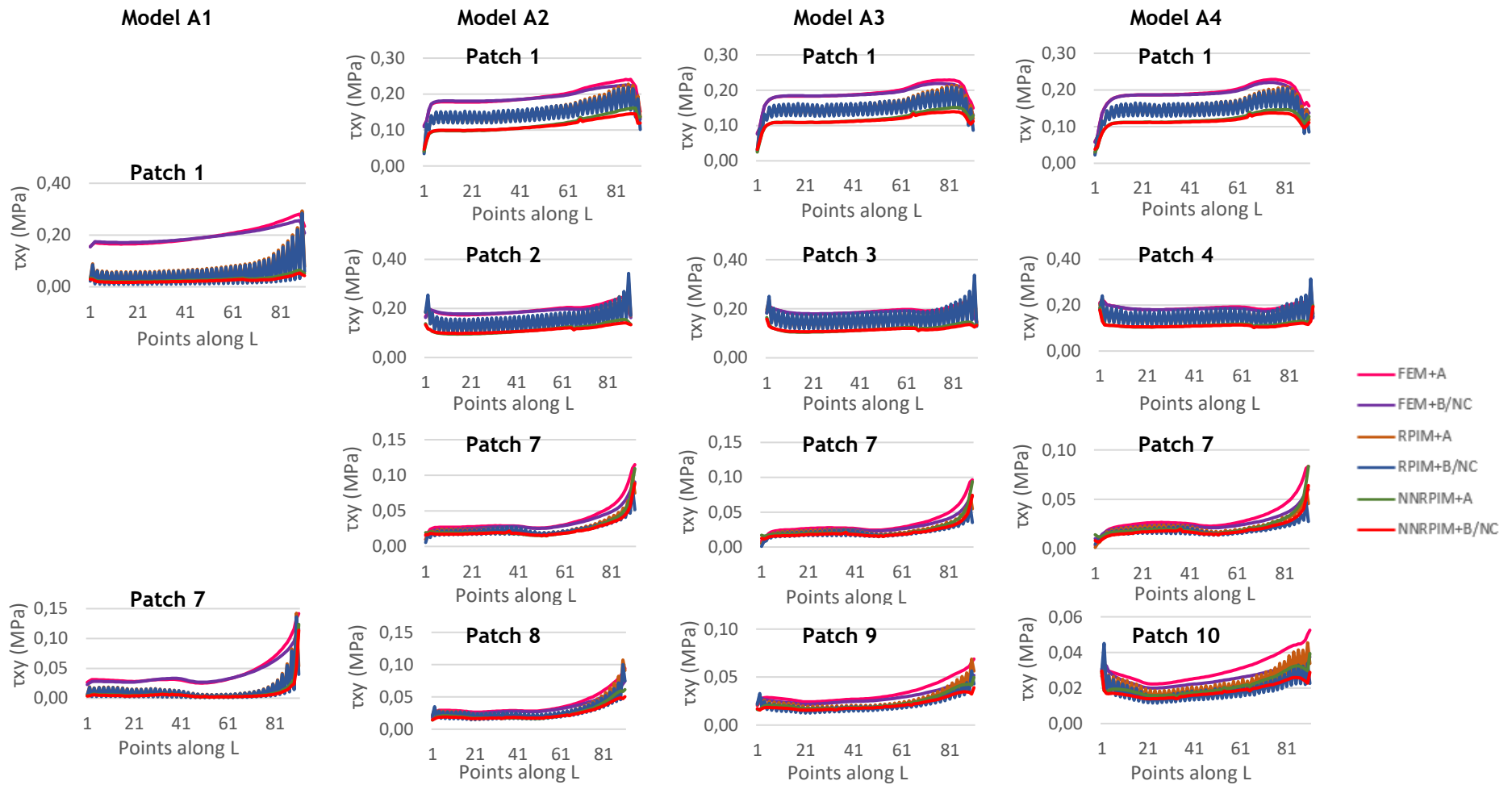
Figure A.13 - Graphic representation of shear stress component τ_{xy}, in points along the left and right retainer wings for the following parameters: (1) Two-retainer design; (2) all adhesive's thicknesses; (3) α= 45°; (4) both resin-cements (Admira and Brilliant/NC Coltène); and (5) the three numerical methods: FEM, RPIM and NNRPIM.
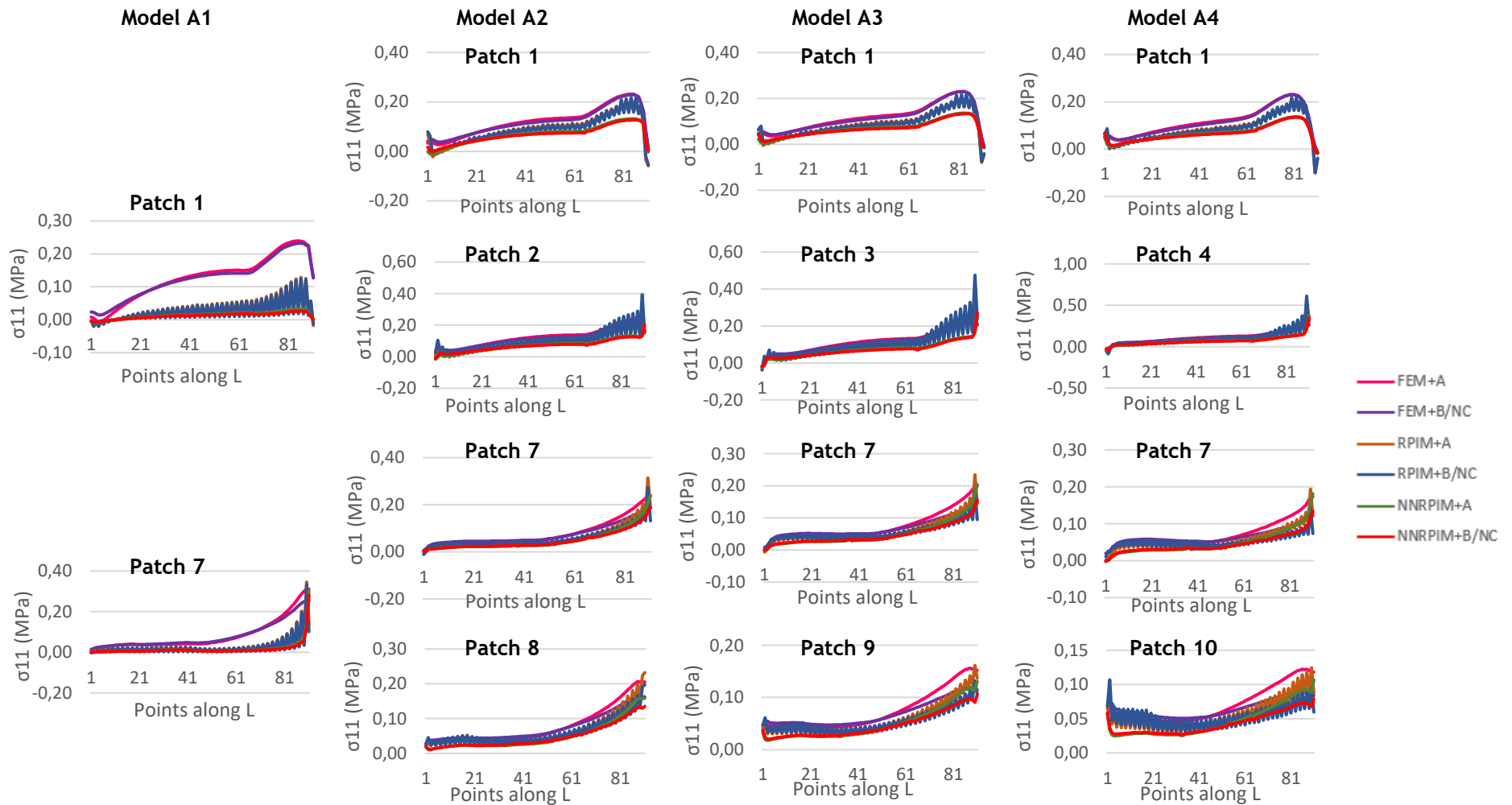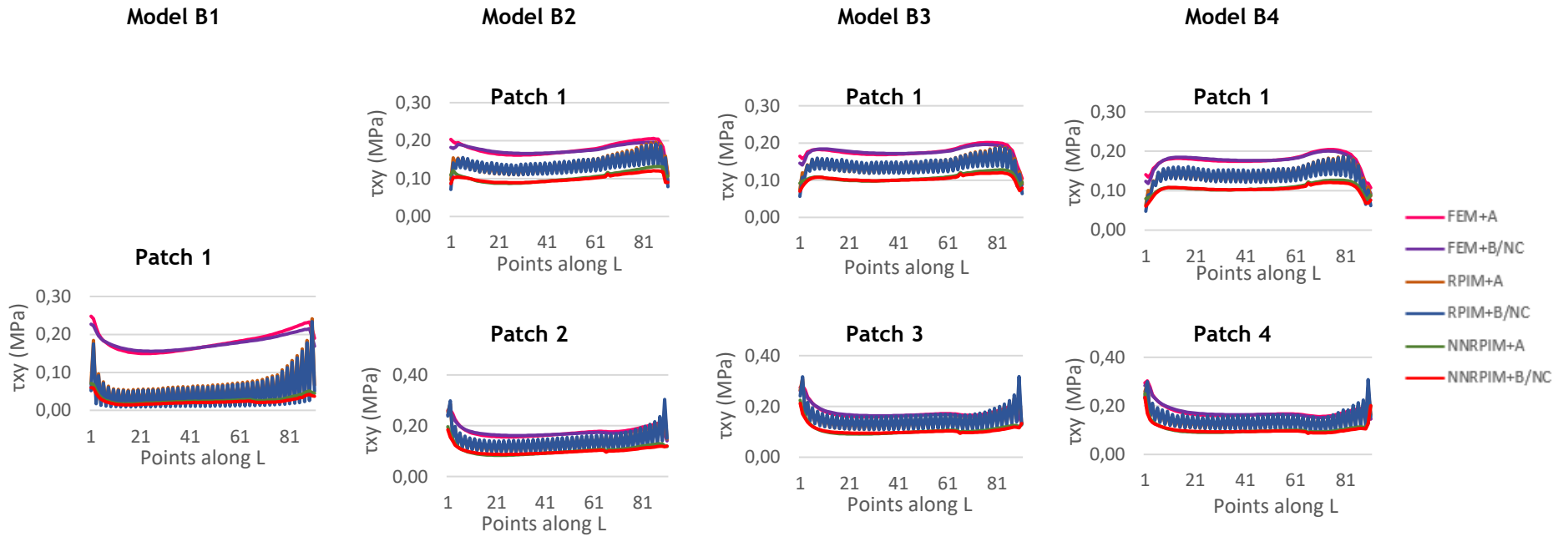
Figure A.14 - Graphic representation of shear stress component τ_{xy}, in points along the left retainer wing for the following parameters: (1) Single-retainer design; (2) all adhesive's thicknesses; (3) α= 45°; (4) both resin-cements (Admira and Brilliant/NC Coltène); and (5) the three numerical methods: FEM, RPIM and NNRPIM.
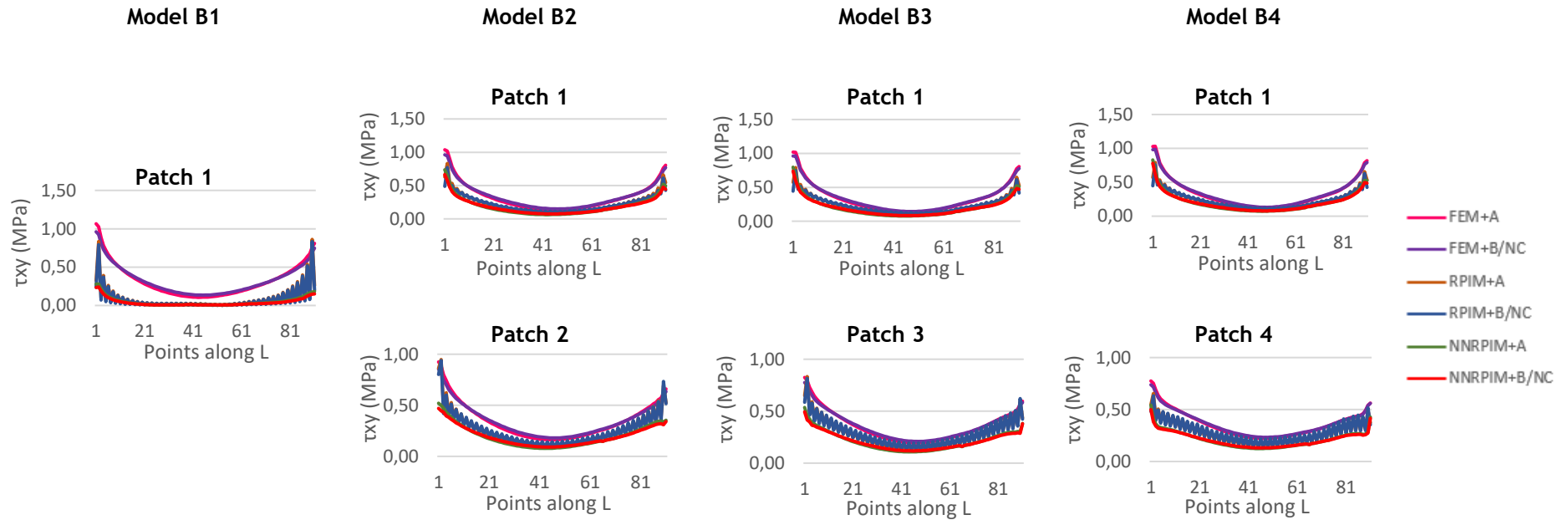
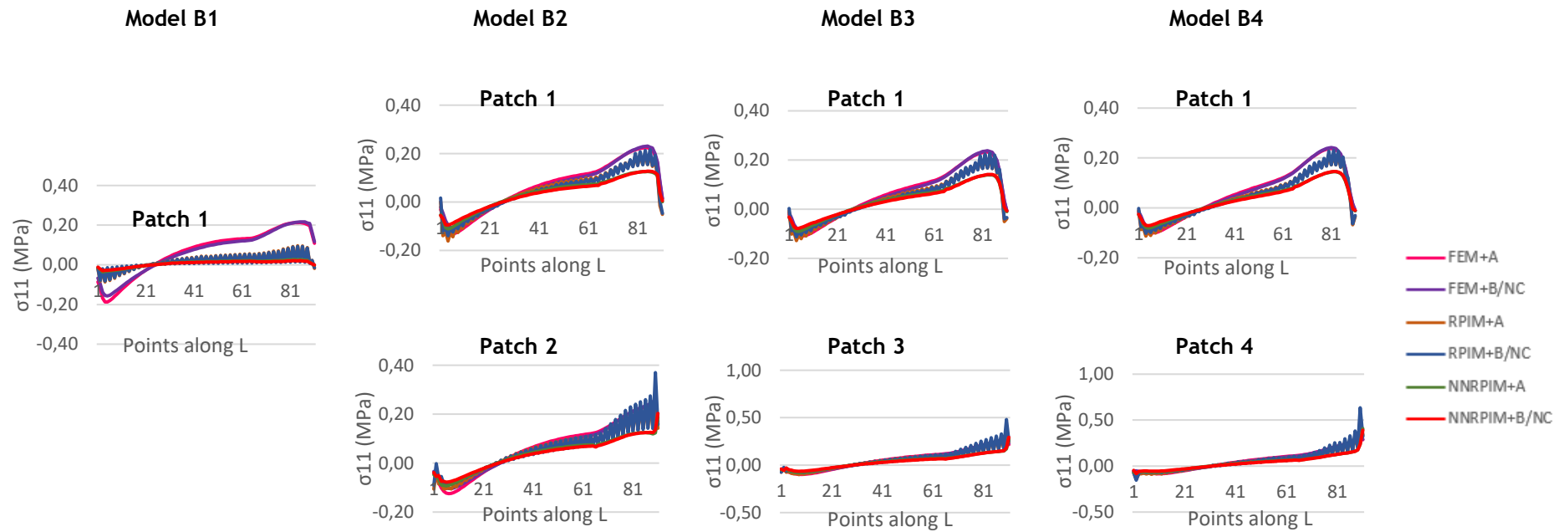**Figure A.15** - Graphic representation of shear stress τ_{xy}, in points along the left retainer wing for the following parameters: (1) Single-retainer design; (2) all adhesive's thicknesses; (3) α= 135˚; (4) both resin-cements (Admira and Brilliant/NC Coltène); and (5) the three numerical methods: FEM, RPIM and NNRPIM.
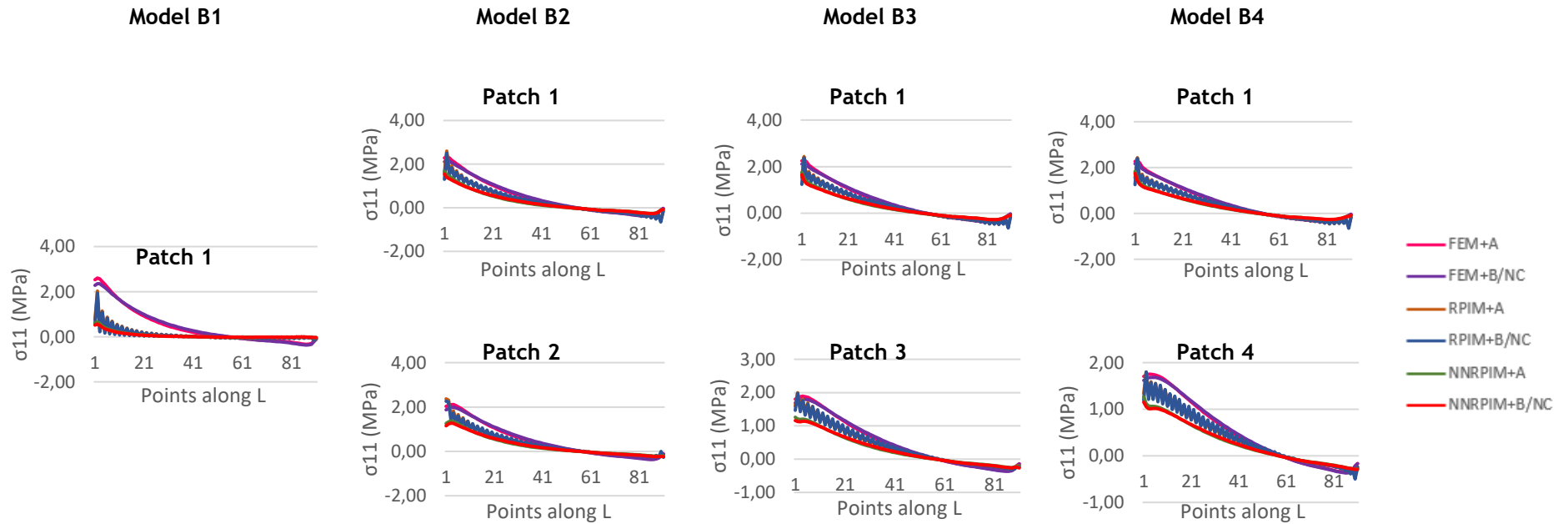
Appendix 4

In this Appendix, it is presented the analysis of the maximum principal stress σ11 ($\sigma 11_{max}$) and maximum shear stress (τ_{max}) registered for all the study cases. This analysis is independent on the area of the adhesive, where these maximum stresses were found, being registered only the maximum value for each adhesive's thickness, design, resin-cement and numerical method.

Table A.1 - Maximum principal stress σ11 found in retainer wing for all study cases.

Force Angle	Adhesive	Number of wings	Numerical Method	$\sigma11_{max}$ (MPa)			
				Adhesive's thickness (mm)			
				0.1	0.2	0.3	0.4
90°	Admira	2	FEM	2.34E-01	2.36E-01	2.50E-01	2.63E-01
			RPIM	1.36E-01	2.77E-01	3.40E-01	4.37E-01
			NNRPIM	3.93E-02	2.17E-01	2.68E-01	3.44E-01
		1	FEM	1.46E+00	1.37E+00	1.39E+00	1.44E+00
			RPIM	1.12E+00	1.56E+00	1.51E+00	1.54E+00
			NNRPIM	3.53E-01	9.94E-01	1.09E+00	1.16E+00
	Brilliant/NC Coltène	2	FEM	2.23E-01	2.24E-01	2.35E-01	2.47E-01
			RPIM	1.32E-01	3.24E-01	3.88E-01	4.76E-01
			NNRPIM	3.55E-02	2.09E-01	2.54E-01	3.03E-01
		1	FEM	1.34E+00	1.29E+00	1.33E+00	1.39E+00
			RPIM	1.07E+00	1.53E+00	1.50E+00	1.54E+00
			NNRPIM	3.04E-01	9.41E-01	1.05E+00	1.13E+00
45°	Admira	2	FEM	3.12E-01	2.49E-01	2.78E-01	3.07E-01
			RPIM	3.46E-01	3.14E-01	3.86E-01	5.31E-01
			NNRPIM	3.02E-01	2.38E-01	2.68E-01	3.81E-01
		1	FEM	2.13E-01	2.42E-01	2.85E-01	3.26E-01
			RPIM	9.63E-02	2.76E-01	3.82E-01	5.42E-01
			NNRPIM	2.60E-02	1.86E-01	2.79E-01	4.07E-01
	Brilliant/NC Coltène	2	FEM	2.56E-01	2.48E-01	2.76E-01	3.04E-01
			RPIM	3.32E-01	3.93E-01	4.76E-01	6.11E-01
			NNRPIM	2.81E-01	2.03E-01	2.72E-01	3.53E-01
		1	FEM	2.17E-01	2.52E-01	2.92E-01	3.30E-01
			RPIM	9.24E-02	3.70E-01	4.81E-01	6.35E-01
			NNRPIM	2.06E-02	2.03E-01	2.94E-01	3.90E-01
135°	Admira	1	FEM	2.61E+00	2.34E+00	2.30E+00	2.32E+00
			RPIM	2.03E+00	2.60E+00	2.43E+00	2.43E+00
			NNRPIM	6.57E-01	1.67E+00	1.76E+00	1.83E+00
	Brilliant/NC Coltène	1	FEM	2.35E+00	2.17E+00	2.16E+00	2.21E+00
			RPIM	1.93E+00	2.50E+00	2.37E+00	2.40E+00
			NNRPIM	5.67E-01	1.55E+00	1.65E+00	1.74E+00

Table A.2 - Maximum shear stress (τ_{max}) found in retainer wing for all study cases.

Force Angle	Adhesive	Number of wings	Numerical Method	τ_{max} (MPa) Adhesive's thickness (mm)			
				0.1	0.2	0.3	0.4
90°	Admira	2	FEM	1.51E-01	1.47E-01	1.44E-01	1.41E-01
			RPIM	1.23E-01	1.95E-01	2.09E-01	2.06E-01
			NNRPIM	5.61E-02	1.04E-01	1.21E-01	1.69E-01
		1	FEM	6.87E-01	6.40E-01	6.43E-01	6.55E-01
			RPIM	7.75E-01	5.92E-01	5.37E-01	5.37E-01
			NNRPIM	1.61E-01	4.49E-01	5.00E-01	5.31E-01
	Brilliant/NC Coltène	2	FEM	1.43E-01	1.41E-01	1.38E-01	1.38E-01
			RPIM	1.19E-01	2.20E-01	2.36E-01	2.23E-01
			NNRPIM	5.23E-02	1.01E-01	1.14E-01	1.57E-01
		1	FEM	6.21E-01	5.99E-01	6.09E-01	6.30E-01
			RPIM	7.50E-01	6.26E-01	5.03E-01	5.09E-01
			NNRPIM	1.32E-01	4.18E-01	4.74E-01	5.09E-01
45°	Admira	2	FEM	2.81E-01	2.46E-01	2.29E-01	2.29E-01
			RPIM	2.93E-01	3.05E-01	2.95E-01	2.85E-01
			NNRPIM	1.24E-01	1.61E-01	1.65E-01	1.98E-01
		1	FEM	2.48E-01	2.63E-01	2.82E-01	3.03E-01
			RPIM	2.41E-01	2.87E-01	3.09E-01	2.94E-01
			NNRPIM	7.09E-02	1.96E-01	2.25E-01	2.50E-01
	Brilliant/NC Coltène	2	FEM	2.56E-01	2.30E-01	2.19E-01	2.20E-01
			RPIM	2.84E-01	3.43E-01	3.37E-01	3.15E-01
			NNRPIM	1.14E-01	1.45E-01	1.58E-01	1.94E-01
		1	FEM	2.27E-01	2.49E-01	2.70E-01	2.93E-01
			RPIM	2.34E-01	3.04E-01	3.18E-01	3.08E-01
			NNRPIM	5.98E-02	1.84E-01	2.12E-01	2.35E-01
135°	Admira	1	FEM	1.07E+00	1.04E+00	1.02E+00	1.03E+00
			RPIM	8.62E-01	9.48E-01	8.33E-01	7.92E-01
			NNRPIM	2.79E-01	7.37E-01	7.97E-01	8.30E-01
	Brilliant/NC Coltène	1	FEM	9.61E-01	9.62E-01	9.61E-01	9.84E-01
			RPIM	8.33E-01	9.38E-01	8.15E-01	7.58E-01
			NNRPIM	2.41E-01	6.64E-01	7.38E-01	7.79E-01

Appendix 5

In this Appendix, it is presented the total displacement of the pontic (δ_{total}), measured on a node positioned in the lower part of the pontic (marked in Figure 8.18), for the conditions considered in the study.

Table A.3 - Total displacement of the pontic for all study cases.

Force Angle	Adhesive	Number of wings	Numerical Method	δ_{total} (mm)			
				Adhesive's thickness (mm)			
				0.1	0.2	0.3	0.4
90°	Admira	2	FEM	4.21E-05	5.13E-05	6.06E-05	7.00E-05
			RPIM	3.11E-05	4.28E-05	5.31E-05	6.30E-05
			NNRPIM	3.58E-05	4.59E-05	5.42E-05	6.25E-05
		1	FEM	8.17E-04	8.94E-04	9.70E-04	1.04E-03
			RPIM	6.76E-04	7.81E-04	8.66E-04	9.46E-04
			NNRPIM	8.87E-04	9.73E-04	1.04E-03	1.10E-03
	Brilliant/NC Coltène	2	FEM	4.70E-05	6.11E-05	7.54E-05	9.00E-05
			RPIM	3.12E-05	4.88E-05	6.45E-05	7.97E-05
			NNRPIM	3.58E-05	5.12E-05	6.39E-05	7.65E-05
		1	FEM	8.63E-04	9.85E-04	1.11E-03	1.23E-03
			RPIM	6.77E-04	8.35E-04	9.70E-04	1.10E-03
			NNRPIM	8.87E-04	1.02E-03	1.12E-03	1.22E-03
45°	Admira	2	FEM	6.02E-05	6.31E-05	6.50E-05	6.65E-05
			RPIM	5.10E-05	5.62E-05	5.85E-05	6.02E-05
			NNRPIM	5.22E-05	5.90E-05	6.21E-05	6.43E-05
		1	FEM	1.99E-04	1.94E-04	1.89E-04	1.86E-04
			RPIM	1.76E-04	1.69E-04	1.63E-04	1.59E-04
			NNRPIM	2.55E-04	2.48E-04	2.44E-04	2.41E-04
	Brilliant/NC Coltène	2	FEM	6.24E-05	6.62E-05	6.92E-05	7.24E-05
			RPIM	5.10E-05	5.80E-05	6.14E-05	6.48E-05
			NNRPIM	5.22E-05	6.17E-05	6.59E-05	6.91E-05
		1	FEM	1.95E-04	1.87E-04	1.81E-04	1.77E-04
			RPIM	1.76E-04	1.65E-04	1.57E-04	1.51E-04
			NNRPIM	2.55E-04	2.45E-04	2.39E-04	2.34E-04
135°	Admira	1	FEM	1.33E-03	1.44E-03	1.54E-03	1.64E-03
			RPIM	1.11E-03	1.25E-03	1.37E-03	1.48E-03
			NNRPIM	1.50E-03	1.61E-03	1.69E-03	1.78E-03
	Brilliant/NC Coltène	1	FEM	1.39E-03	1.56E-03	1.73E-03	1.90E-03
			RPIM	1.11E-03	1.32E-03	1.51E-03	1.69E-03
			NNRPIM	1.50E-03	1.67E-03	1.81E-03	1.94E-03

Appendix 6

In this Appendix, it is presented the maximum force (F_{max}) that the bridge could support for all the study cases and the maximum displacement of the pontic (δ_{max}), due to the maximum force.

Table A.4 - Maximum force that the bridge could support for all the study cases and numerical method FEM.

Force Angle	Adhesive	Number of wings	F_{max} (N) Adhesive's thickness (mm)			
			0.1	0.2	0.3	0.4
90°	Admira	2	1.41E+03	1.40E+03	1.32E+03	1.25E+03
		1	2.26E+02	2.41E+02	2.37E+02	2.30E+02
	Brilliant	2	2.33E+03	2.32E+03	2.21E+03	2.11E+03
		1	3.88E+02	4.04E+02	3.91E+02	3.74E+02
	NC Coltène	2	1.26E+03	1.25E+03	1.19E+03	1.14E+03
		1	2.09E+02	2.17E+02	2.11E+02	2.02E+02
45°	Admira	2	1.06E+03	1.33E+03	1.19E+03	1.08E+03
		1	1.55E+03	1.36E+03	1.16E+03	1.01E+03
	Brilliant	2	2.03E+03	2.09E+03	1.88E+03	1.71E+03
		1	2.40E+03	2.07E+03	1.78E+03	1.57E+03
	NC Coltène	2	1.09E+03	1.13E+03	1.01E+03	9.20E+02
		1	1.29E+03	1.11E+03	9.58E+02	8.48E+02
135°	Admira	1	1.27E+02	1.41E+02	1.44E+02	1.42E+02
	Brilliant	1	2.21E+02	2.40E+02	2.40E+02	2.35E+02
	NC Coltène	1	1.19E+02	1.29E+02	1.29E+02	1.27E+02

Table A.5 - Maximum displacement of the pontic, due to the maximum force, for all study cases and numerical method FEM.

Force Angle	Adhesive	Number of wings	δ_{max} (mm) Adhesive's thickness (mm)			
			0.1	0.2	0.3	0.4
90°	Admira	2	5.94E-02	7.16E-02	8.00E-02	8.78E-02
		1	1.85E-01	2.16E-01	2.30E-01	2.39E-01
	Brilliant	2	1.10E-01	1.42E-01	1.67E-01	1.90E-01
		1	3.35E-01	3.98E-01	4.34E-01	4.60E-01
	NC Coltène	2	5.90E-02	7.62E-02	8.97E-02	1.02E-01
		1	1.80E-01	2.14E-01	2.34E-01	2.48E-01
45°	Admira	2	6.37E-02	8.37E-02	7.72E-02	7.15E-02
		1	3.08E-01	2.65E-01	2.19E-01	1.89E-01
	Brilliant	2	1.27E-01	1.39E-01	1.30E-01	1.24E-01
		1	4.68E-01	3.86E-01	3.22E-01	2.79E-01
	NC Coltène	2	6.83E-02	7.47E-02	7.01E-02	6.66E-02
		1	2.52E-01	2.08E-01	1.73E-01	1.50E-01
135°	Admira	1	1.68E-01	2.03E-01	2.21E-01	2.33E-01
	Brilliant	1	3.07E-01	3.74E-01	4.16E-01	4.47E-01
	NC Coltène	1	1.65E-01	2.01E-01	2.24E-01	2.41E-01